University of Strathclyde

Department of Physics

Variations in Modelled and Measured Hyperspectral Remote Sensing Reflectance

Lorraine Hay

Supervisor: Dr. Alex Cunningham

A thesis presented in fulfilment of the requirements for the degree of Doctor of Philosophy

2006

Declaration of Authors Rights

Abstract

Measurements of hyperspectral surface reflectance, with a spectral range of 350-800nm and sampling interval of 3.3nm, were made in Scottish coastal waters, the Bristol Channel and the Atlantic Ocean.

Analysis of the shape of these spectra by normalisation and differentiation revealed three prominent features: (1) the magnitude of the integral between 400-455nm, (2) the width of a trough occurring between 560-615nm, and (3) the peak to trough height between 660-750nm. The characteristics of these features were not determined by individual seawater constituents, but they proved useful as a tool for water type classification. The sign of the integral between 400-455nm discriminated between open ocean and coastal waters, and coastal sub-types could be distinguished by applying cluster analysis to the other three features.

The hyperspectral data were integrated over appropriate bandwidths to generate multi-band surface reflectance values which were used to assess the performance of remote sensing algorithms in coastal water. All the chlorophyll algorithms tested (SeaWiFS OC4V4, MODIS Chlor_a_2 and Chlor_a_3, and MERIS OC4E) overestimated the values measured *in situ*. The MODIS algorithm for absorption by phytoplankton, $a_{phyto}(675)$, performed poorly, but the MODIS algorithm for the absorption by coloured dissolved organic material, $a_{CDOM}(400)$, provided accurate values of the absorption coefficient ($R^2 = 0.91$). Algorithm performance was improved when turbid stations, identified using cluster analysis, were removed.

Hyperspectral radiometry was also used to investigate variations in chlorophyll fluorescence line height (FLH) with chlorophyll concentration, solar irradiation and seawater composition. FLH and chlorophyll *a* concentration were not correlated in the coastal waters sampled and variations in the photosynthetically available radiation (PAR), CDOM and suspended sediment concentrations affected the magnitude of FLH observed. A study of (FLH/Chl) under natural, fluctuating irradiances allowed the onset of adaptive non-photochemical quenching to be monitored *in situ*.

Acknowledgements

There are far too many people to thank for their help, support and assistance over the time I have spent in higher education, my frazzled brain can no longer cope! But here goes anyway…

First of all to my supervisor Dr Alex Cunningham, without his encouragement, support and discussions none of this work would have been completed. Though I am sad to say I still like Oban! Even though it rains all the time!

To Dr David McKee who's friendship and knowledge have been invaluable. I am just glad I didn't scratch any of the instrument windows. I hope you have many more happy coffee filled years of research.

To past and present members of the Environmental Optics group –Agnes, Leanne, Laura and Ian- cheers!

A special thank you has to go to Iain ("Shabba") Carrie and Justyna ("Beetroot and Cabbage") Zawadazka for there morale support, friendship, advice, company on boats and questionable humour. I can't thank you guys enough. Long live cake Friday's!

To my mum and dad for never making me do my homework and for basically putting up with me! To David for keeping my mum and dad in order! I hope you realise how well your tax payer pounds have been put to good use. I can't begin to thank you for your unwavering support throughout the years it means more than I could ever tell you.

A big tear-filled thank you to Elaine, David, Debbie and Angus. Some of the best friends anyone could ever wish for.

Lastly but most importantly to Thomas. There were times when doing a PhD was extremely hard but Thomas was always there to pick me up. I don't think I could ever properly thank you, you always mange to make me smile again and your belief in me was enough to keep me going. Thank you just doesn't seem enough.

Contents

Chapter 1: Introduction

1. 1. Ocean Colour

Remote sensing reflectance is a parameter commonly used to measure ocean colour (Morel and Prieur, 1977; Mobley, 1999). When sunlight enters the ocean it is spectrally modified due to the attenuating effects of the water and the components contained within it. Light that escapes from the water body, due to scattering, can reveal information on the contents of the water body (Siegel *et al*, 2005(a)).

1. 1. 1. Variation in Ocean Colour

Sunlight entering the water body can undergo one of two effects, it can either be scattered or absorbed. The coefficients of absorption and scattering are known as inherent optical properties (IOPs) and it is the IOPs which govern ocean colour. In open ocean water (Morel and Maritorena, 2001) the main optically important components which can modulate the light field are, apart from the water itself, phytoplankton and its associated breakdown products. The reflectance from the ocean should therefore be strongly correlated with the concentration of phytoplankton. Phytoplankton contain an array of pigments (e.g. chlorophylls *a*, *b* and *c*, the caroteniods and the billiproteins) in order to absorb light for photosynthesis (Kirk, 1986). Different species of phytoplankton have different optical properties due to variations in absorption and scattering between species. The primary pigment found in all phytoplankton is chlorophyll *a*, which is used as an indicator of the abundance of phytoplankton. Many algorithms exist which have been developed to retrieve chlorophyll *a* concentration from radiometric parameters (O'Reilly *et al*, 1998; He *et al*, 2000; Sathyendranath *et al*, 2001; Darecki *et al*, 2005).

In coastal waters the interaction of sunlight and the water body is complicated by the presence of other optically important constituents (Lee *et al*, 1994; Siegel *et al*,

2005(b)). In addition to phytoplankton, colour dissolved organic matter (CDOM) and suspended particulate materials (SPM) are found. CDOM, also known as yellow substance or gelbstoff, results from the degradation of plant tissue (e.g. from the breakdown of phytoplankton) or from the run-off of heavily wooded regions or from regions of rich organic soil. For example, in Scottish fjords high concentrations of CDOM are typically the result of fresh water run-off from the surrounding peat laden hills. Absorption by CDOM is assumed to be exponential in nature, highest in the blue and decreasing into the red. CDOM is also assumed to be non-scattering in nature (Aas, 2000). SPM includes all suspended matter (e.g. minerals). SPM concentrations tend to be highest in coastal regions. Wave, wind and current actions can re-suspend sediments in shallower coastal areas and in land water bodies. Estuaries and other areas where tidal effects are important can have their optical properties strongly influenced by the re-suspension of sediments. The term suspended particulate material applies to a wide range of material, each with its own absorbing and scattering properties.

1. 1. 2. Importance of Monitoring Ocean Colour

Measurements of ocean colour have an important role in oceanography as it helps monitor the marine environment. Phytoplankton play a pivotal role in the exchange of gases (e.g. carbon dioxide and oxygen) between the ocean and the atmosphere which helps regulate global climate (Raven and Falkowski, 1999; Demchak, 2005). The quantity of atmospheric carbon fixed by phytoplankton each year is roughly equal to the amount that is fixed by the tropical rainforests. Phytoplankton photosynthesis, in addition to influencing the exchange of gases between the ocean and atmosphere, is also the basis of the vast majority of marine food chains. The different species of animals that live in the sea (e.g. zooplankton and fish) congregate in regions of high phytoplankton abundance. The ability to calculate the abundance of phytoplankton in the oceans, using chlorophyll *a* as an index, is important for models of primary productivity (Geider *et al*, 2001; Weston *et al*, 2005). Monitoring of different types of water masses, for example phytoplankton blooms, sediment plumes and pollutants, is important in coastal regions as these are the sites of the

majority of the world's fisheries and are also important for social and recreational uses. Approximately 60% of the global population live in the coastal zone area which accounts for only 18% of global surface area (Field *et al*, 2002). The stress on the coastal zone area and surrounding shelf sea due to, for example, pollution, urbanisation, tourism, over-fishing and eutrophication is immense (Sathyendranath *et al*, 2000). Therefore, careful monitoring of these areas is key to maintaining there sustainability for both industrial and environmental purposes.

1. 2. Monitoring Ocean Colour

Measurements of ocean colour can be conducted by deploying *in situ* instrumentation or by remote sensing techniques.

1. 2. 1. *In situ* and Surface Measurements of Ocean Colour

Ocean colour can be measured by deploying radiometric systems from ships to measure radiance or reflectance as it leaves the surface of the water body. Profiling instrumentation also exists which allows radiometric parameters to be depth resolved. *In situ* measurements of the underwater and surface leaving light field have certain advantages over remote sensing techniques, being free from the attenuating effects of the atmosphere and also from the effects of surface glare and reflection. Profiling instrumentation allows depth resolved measurements of the light field to be collected whereas remote sensors are restricted to processes occurring within the first optical depth, from which 90% of the water leaving photons originate (Mobley, 1994). Over the years the spectral coverage of *in situ* instrumentation has developed from a small number of discrete bandwidths to full spectral coverage (hyperspectral). Hyperspectral radiometers, which are now widely available, allow continuous spectral measurements to be made over a broad wavelength range, typically from 350 to 800nm, with better than 10nm resolution (Chang *et al*, 2003).

1. 2. 2. Remote Sensing of Ocean Colour

The temporal and spatial coverage offered by remote sensing satellites is far superior to that offered by *in situ* measurements which are severely limited in geographical range. However, remotely sensed data is affected by the atmosphere (Clark *et al*, 1997; Gordon, 1997; Gordon, 2003; Stamnes *et al*, 2005), with 90% of the light received by a satellite originating from scattering effects taking place in the Earth's atmosphere. It is therefore necessary to validate remote sensing measurements using *in situ* techniques. Ground truth measurements can be used to correct for the effects of the atmosphere (Bulgorelli and Zibordi, 2003; Lavender *et al*, 2004). The presence of other material in addition to phytoplankton in the water can have a deleterious effect on remote sensing algorithms (Carder *et al*, 1989; Dall'Olmo *et al*, 2005). Therefore, developing new algorithms for the retrieval of optical parameters of the water body (e.g. component concentration) also requires that ground truth measurements be conducted.

As with *in situ* instrumentation remote sensing satellites have been developed to include more spectral channels and improved resolution and sensitivity. The first dedicated ocean colour satellite was the Coastal Zone Colour Scanner (CZCS).

In the section below a brief description of the first ocean colour satellite (CZCS) is given, along with some current satellites whose bandwidths and algorithms will be discussed in later chapters.

i. CZCS

The Coastal Zone Colour Scanner, or CZCS, was the first dedicated ocean colour satellite. It was launched on board the Nimbus 7 satellite in October 1978 and was designed to map chlorophyll concentration, sediment distribution, gelbstoff concentration, with an infra-red channel used to determine the temperature of coastal water and ocean currents.

CZCS had four channels between 400 and 700nm each with a 20nm bandwidth and provided a scan width of 1556km. The CZCS project showed that ocean colour measurements could successfully be carried out from space. This helped provide justification for future ocean colour missions such as SeaWiFS and MODIS. CZCS continued to collect data intermittently until it was switched off in December 1986.

ii. SeaWiFS

Until 1996 CZCS was the only ocean colour satellite to be sent into space. Its successor was the Sea-viewing Wide Field-of-view Sensor, SeaWiFS, launched on the 1st of August 1997 on board the SeaStar satellite. SeaWiFS has 6 wavebands occurring in the visible centred on 412, 443, 490, 510, 555, and 670nm, each with full width half maximum of 20nm. It operates in a sun synchronous orbit, it passes over the same point on the Earth's surface at the same time each day, at a height of 705km with a swath width of 2800km and resolution of 1.1km. SeaWiFS offered improved calibration, sensor characterization, spectral bands and radiometric sensitivity over its predecessor, CZCS.

The SeaWiFS programme goals are outlined in Hooker *et al* (1992); its main aim was stated as being the "acquirement of data critical for study of the role of ocean primary productivity in global biogeochemistry, including the exchange of critical elements and gases between the atmosphere and ocean".

Today SeaWiFS is still providing ocean colour data, well exceeding its initial five year mission.

iii. MODIS Terra and Aqua

In December of 1999 NASA launched the Moderate Resolution Imaging Spectroradiometer (MODIS) ocean colour satellite onboard the Terra Platform. This was followed by the launch of a second MODIS instrument on board the Aqua platform in May 2002. Both satellites are in orbit at 705km and operate in a sun synchronous, circular, near polar orbit with a swath width of 2330km, and a resolution of 1km. MODIS Terra's orbit around the Earth is timed so that it passes from north to south across the equator in the morning (10:30am), while Aqua passes south to north over the equator in the afternoon (1:30pm). Both instruments have 36 channels, 9 of which are dedicated to ocean colour and biogeochemistry. MODIS was designed with similar ocean colour wavebands to that of SeaWiFS, though the MODIS wavebands are narrower to allow for enhanced atmospheric correction. MODIS also has improved signal to noise ratio over its predecessors and was

designed to include quantitative measurements of solar stimulated chlorophyll fluorescence (Esaias *et al*, 1998).

iv. MERIS

The Medium Resolution Imaging Spectrometer, MERIS was launched during 2002 onboard the European Space Agency's (ESA) Envisat Satellite. MERIS is a 68.5^0 field-of-view pushbroom imaging spectrometer that measures the solar radiation reflected by the Earth, at a ground spatial resolution of 300m, in 15 spectral bands, programmable in width and position, in the visible and near infra-red. As stated by Bezy *et al* (2000) MERIS aims to contribute data to the study of the upper layers of the ocean by providing information on:

- the measurement of photosynthetic potential by detection of phytoplankton (algae)
- the detection of yellow substance (dissolved organic material)
- the detection of suspended matter (re-suspended or river borne sediments)

MERIS also has the ability to measure solar stimulated chlorophyll fluorescence (Bricaud *et al*, 1999; Gower, 1999).

1. 3. Hyperspectral Measurements

When discussing hyperspectral measurements we are talking about an instrument capable of providing continuous spectral measurements over a broad wavelength range, typically from 350 to 800nm. Until recently most hyperspectral instrumentation used in oceanography was limited to laboratory bench top spectrophotometers (Chang *et al*, 2003). For example, high resolution (hyperspectral) data has already proven useful for identification of phytoplankton pigments from absorption spectra (Aguirre-Gomez *et al*, 2001(a); Aguirre-Gomez *et al*, 2001(b)). However, due to electronic and computational improvements hyperspectral instrumentation now exists for the collection of data at sea, for example, the TriOS RAMSES radiometers, the Satlantic HyperPro, HOBI Labs HydroRad and the WetLabs AC-S. These instruments allow the collection of hyperspectral radiometric and IOP parameters. The application of hyperspectral

technology to airborne and remote sensing instrumentation still proves troublesome due to low sensitivity (Levin *et al*, 2005). In fact one advantage that multispectral sensors have over hyperspectral instruments is an improved signal to noise ratio due to the fact that they are integrating over a larger bandwidth, thus collecting more photons. However, as hyperspectral sensors are developed the sensitivity of these instruments continues to improve.

Optical oceanographers have shown that selected bands and band ratios, obtained using multispectral instrumentation, can be useful for the retrieval of information on the water body (Lee and Carder, 2000; Blondeau-Patissier *et al*, 2004). However, when band ratio algorithms designed for use in open ocean waters are applied to coastal or shelf sea water the algorithms can cease to provide reliable data (Lee and Carder, 2002). This is due to the increase in optical complexity in such areas owing to the occurrence of other optically important constituents, such as CDOM and SPM, in addition to phytoplankton. In coastal environments spatial and temporal variability is also increased. Using hyperspectral instrumentation in such areas may help provide more information on the water body than traditional multispectral sensors by providing more degrees of freedom for algorithm development (e.g. tuning of regional remote sensing algorithms) and for modelling of more optically complex water. Hyperspectral measurements may also prove useful for improving atmospheric correction in coastal areas and classifying optically complex water types. Data from hyperspectral instrumentation can also be appropriately binned for comparison with any multispectral satellite, for example, SeaWiFS, MODIS and MERIS, without having to interpolate between wavebands. It has also been suggested that hyperspectral backscattering measurements can be used to discriminate phytoplankton populations from other in-water constituents due to the fact that wavelength dependence of backscattering from phytoplankton is different from other particles (Bricaud *et al*, 1983; Stramski *et al*, 2001).

Hyperspectral instrumentation offers improvement in the amount of data available to oceanographers, which may help increase their understanding of optically complex waters such as coastal or shelf sea water. Hyperspectral measurements increase the number of wavelengths available that can be used in analysis of relationships such as component concentration and ocean colour.

1. 4. Aims of Research

Multispectral radiometers have been successfully used to measure the *in situ* light field and water leaving signals. This research aims to assess the performance of profiling and surface floating hyperspectral radiometers, which have limited sensitivity, in comparison to their multispectral equivalents and to test the hypothesis that hyperspectral data contains features, not illustrated in the widely spaced multi-band spectra, which can be used to reveal information on the content of the water body. In addition to this the higher resolution offered by hyperspectral radiometers will be utilized to resolve the chlorophyll fluorescence peak. Chlorophyll fluorescence line height (FLH) measurements in coastal water, an area of current interest, will be used to test the hypothesis that FLH is related to chlorophyll concentration in coastal water. However, as chlorophyll fluorescence is an inelastic scattering process detail contained in the spectra prior to the fluorescence peak would be useful in any investigation into this feature.

Chapter 2: Optical Theory

In order to understand the nature of the underwater light field and the associated water leaving signals, it is important to have knowledge of the parameters used to quantify and describe the optics involved. The object of this chapter is to define the terms most commonly used for this purpose. A more detailed explanation of these terms can be found in Preisendorfer (1976), Kirk (1986) and Mobley (1994).

2. 1. Radiometry

2. 1. 1. Radiance

Radiance (L) is a measure of the radiant flux (Φ) in a given direction per unit solid angle $(d\omega)$ per unit area (dS) perpendicular to the direction of propagation. It is defined as:

$$L(\theta,\varphi) = \frac{d^2\Phi}{dS\cos\theta\, d\omega} \tag{2.1}$$

Radiance, a function of the zenith (θ) and azimuth (φ) angle, is measured in units of $W\,m^{-2}\,sr^{-1}$. Spectral radiance, $L(\lambda)$ is defined as the radiance per unit wavelength interval at a given wavelength, λ.

$$L(\lambda) = \frac{L(\theta,\varphi)}{d\lambda} \tag{2.2}$$

where $L(\lambda)$ is the spectral radiance measured in units of $W\,m^{-2}\,nm^{-1}\,sr^{-1}$. All other radiometric parameters can be derived from radiance by integration over an appropriate range of solid angles.

2. 1. 2. Irradiance

The most commonly measured radiometric parameter is irradiance. Irradiance (E) is defined as the radiant flux (Φ) incident on an infinitesimal element of a surface, divided by the area:

$$E = \frac{d\Phi}{dS} \tag{2.3}$$

Irradiance is measured in units of $W\,m^{-2}$.

Downwelling irradiance (E_d) and upwelling irradiance (E_u) are the values of irradiance on the upper and lower faces, respectively, of a horizontal surface. If a detector fitted with a horizontal diffusing disk is pointed vertically upwards then photons from the upper hemisphere can reach the detector and give a measure of the spectral downward plane irradiance (E_d). The detector is not equally sensitive to all downwelling photons. Photons striking a plane surface have an irradiance response that is proportional to the cosine of the angle between the photon direction and the normal to the collector surface.

The spectral downward plane irradiance, measured in $W\,m^{-2}\,nm^{-1}$, is defined as:

$$E_d = \int_{2\pi} L(\lambda)\cos\theta\, d\omega \tag{2.4}$$

Changing the orientation of the detector so that the collector was pointing vertically downwards would measure the upwelling spectral plane irradiance, in $W\,m^{-2}\,nm^{-1}$.

$$E_u = -\int_{-2\pi} L(\lambda)\cos\theta\, d\omega \tag{2.5}$$

The scalar irradiance (E_o) is the integral of the radiance distribution over all angles, defined as:

$$E_o = \int_{4\pi} L(\lambda) d\omega \tag{2.6}$$

The downwelling scalar irradiance and upwelling scalar irradiance are then defined as:

$$E_{od} = \int_{2\pi} L(\lambda) d\omega \tag{2.7}$$

$$E_{ou} = \int_{-2\pi} L(\lambda) d\omega \tag{2.8}$$

All scalar irradiances are measured in units of $W\,m^{-2}\,nm^{-1}$.

2. 2. Inherent Optical Properties

Inherent optical properties (IOPs) depend only upon the composition of the medium, and are independent of the ambient light field. When a photon enters the water it can undergo one of two processes, it can either be absorbed or scattered. The absorption and scattering properties of the water body, for light at any wavelength, are specified in terms of the absorption coefficient, scattering coefficient and volume scattering function (also known as the scattering phase function).

If we consider a small volume of water (Δv), of thickness Δr, illuminated by a narrow collimated beam of light of a single wavelength with radiant power $\phi_i(\lambda)$, then some part of the incident power $\phi_i(\lambda)$ is absorbed $(\phi_a(\lambda))$ within the volume of water, some part is scattered $(\phi_s(\lambda))$ out of the volume of water at angle θ and the remainder is transmitted $(\phi_t(\lambda))$ through the volume of water without change in direction. Assuming no inelastic scattering processes occur (e.g. no photon undergoes a change in wavelength) then by conservation of energy:

$$\phi_i(\lambda) = \phi_a(\lambda) + \phi_s(\lambda) + \phi_t(\lambda) \tag{2.9}$$

Radiant powers are measured in $W\,nm^{-1}$.

The spectral absorptance, $A(\lambda)$, is defined as the fraction of incident power absorbed within the volume:

$$A(\lambda) \equiv \frac{\phi_a(\lambda)}{\phi_i(\lambda)} \tag{2.10}$$

Similarly, the spectral scatterance, $B(\lambda)$, is defined as the fraction of incident power scattered out of the beam:

$$B(\lambda) \equiv \frac{\phi_s(\lambda)}{\phi_i(\lambda)} \tag{2.11}$$

and the spectral transmittance is:

$$T(\lambda) \equiv \frac{\phi_t(\lambda)}{\phi_i(\lambda)} \tag{2.12}$$

where,

$$A(\lambda) + B(\lambda) + T(\lambda) = 1 \tag{2.13}$$

The spectral absorption and scattering coefficients are the spectral absorbance and scatterance per unit distance in the medium. The spectral absorption coefficient is defined as:

$$a(\lambda) \equiv \lim_{\Delta r \to 0} \frac{A(\lambda)}{\Delta r} \tag{2.14}$$

and the spectral scattering coefficient as:

$$b(\lambda) \equiv \lim_{\Delta r \to 0} \frac{B(\lambda)}{\Delta r} \tag{2.15}$$

The spectral beam attenuation coefficient is defined as:

$$c(\lambda) = a(\lambda) + b(\lambda) \tag{2.16}$$

The absorption, scattering and attenuation coefficients are measured in units of m^{-1}.

The above definitions of IOPs are examples of total IOPs which include the effect of the water and any dissolved or suspended material. For example, the total absorption coefficient can be obtained from summing the absorption due to the optically significant components:

$$a(\lambda) = a_w(\lambda) + a_{phy}(\lambda) + a_{CDOM}(\lambda) + a_{MSS}(\lambda) \qquad (2.17)$$

where $a_w(\lambda)$ is the absorption due to water, $a_{phy}(\lambda)$ is the absorption due to phytoplankton, $a_{CDOM}(\lambda)$ is the absorption due to coloured dissolved organic matter (CDOM) and $a_{MSS}(\lambda)$ is the absorption due to mineral suspended sediment (MSS).

The absorption coefficient for each individual component varies with wavelength, λ. The absorption due to water is tabulated in Pope and Fry (1997). Water is most strongly absorbing in the ultraviolet, due to electronic transitions, and infra-red regions, due to vibrational transitions, of the spectrum. Vibrational transitions start to occur around 500nm due the stretching of the OH (oxygen-hydrogen) bond in the water molecule. Absorption by phytoplankton is due to the photosynthetic pigments, of which chlorophyll is the most distinctive. Chlorophyll absorbs most strongly in the blue and red, with peaks around 430 and 665nm respectively for chlorophyll *a*, with very little absorption occurring in the green. CDOM absorption is high in the blue and decreases towards the red. Traditionally, an exponential function (Jerlov, 1976; Bricaud *et al*, 1981) is used to model the absorption due to CDOM. In West of Scotland coastal waters, high CDOM levels are the result of fresh water runoff from the surrounding hills. However, in oceanic waters CDOM originates from the breakdown products of phytoplankton. The absorption due to MSS is also thought to be exponential increasing towards shorter wavelengths (Roesler *et al*, 1989; Bricaud and Stramski, 1990). Figure 2.1 illustrates the default absorption spectra for water, chlorophyll, CDOM and minerals supplied in the Hydrolight computer package.

Scattering can also be quantified in terms of its components:

$$b(\lambda) = b_w(\lambda) + b_{phy}(\lambda) + \ b_{CDOM}(\lambda) + b_{MSS}(\lambda) \qquad (2.18)$$

where $b_w(\lambda)$ is the scattering due to water, $b_{phy}(\lambda)$ is the scattering due to phytoplankton, $b_{CDOM}(\lambda)$ is the scattering due to coloured dissolved organic matter (CDOM) and $b_{MSS}(\lambda)$ is the scattering due to mineral suspended sediment (MSS). It is generally assumed that the scattering due to CDOM is negligible as the absorption coefficient is much greater than the scattering coefficient at all wavelengths within the ultraviolet and visible spectral regions (Aas, 2000).

The final IOP parameter to consider is the volume scattering function, $\beta(\theta,\lambda)$:

$$\beta(\theta)=\frac{d\Phi(\theta)}{\Phi_0\, d\omega\, dr} \tag{2.19}$$

It is defined as the light flux Φ, per unit solid angle $d\omega$, scattered in the direction θ, per unit length dr, expressed as a proportion of incident flux Φ_0, with units of $m^{-1}\,sr^{-1}$.

Integrating over all directions gives the total scattered power per unit incident irradiance and unit volume of water, e.g. the scattering coefficient:

$$b(\lambda)=2\pi\int_0^{\pi}\beta(\theta,\lambda)\sin\theta\, d\theta \tag{2.20}$$

Dividing this equation into the forward $\left(0\le\theta\le\frac{\pi}{2}\right)$ and backward $\left(\frac{\pi}{2}\le\theta\le\pi\right)$ scattering coefficients gives:

$$b_f(\lambda)=2\pi\int_0^{\frac{\pi}{2}}\beta(\theta,\lambda)\sin\theta\, d\theta \tag{2.21}$$

$$b_b(\lambda)=2\pi\int_{\frac{\pi}{2}}^{\pi}\beta(\theta,\lambda)\sin\theta\, d\theta \tag{2.22}$$

The normalised volume scattering function or phase function, $\tilde{\beta}(\theta,\lambda)$, gives a measure of the angular distribution of the scattered photons. It is defined as:

$$\tilde{\beta}(\theta,\lambda)=\frac{\beta(\theta,\lambda)}{b(\lambda)} \tag{2.23}$$

$\tilde{\beta}(\theta,\lambda)$ has units of sr^{-1}.

2. 3. Apparent Optical Properties

Apparent optical properties (AOPs) are quantities that depend more strongly upon the composition of the medium (the IOPs) than on the geometrical structure of the incident light field. Specific ratios of radiometric quantities have been shown to be relatively insensitive to changes in factors such as sea state and cloud cover and are stable enough to be useful when comparing different water bodies. Spatial derivatives of radiometric quantities with depth may also be used as AOPs.

2. 3. 1. Average Cosines

Average cosines, $\bar{\mu}$, are useful parameters for measuring the angular structure of the upwelling and downwelling light fields. They are defined as follows:

$$\bar{\mu}_u=\frac{E_u(z,\lambda)}{E_{ou}(z,\lambda)} \tag{2.24}$$

$$\bar{\mu}_d=\frac{E_d(z,\lambda)}{E_{od}(z,\lambda)} \tag{2.25}$$

$$\bar{\mu}(z,\lambda)=\frac{E_d(z,\lambda)-E_u(z,\lambda)}{E_o(z,\lambda)} \tag{2.26}$$

where z is the depth in metres. The value of $\bar{\mu}$ can vary from 0, for an isotropic radiance distribution, to 1, for a collimated beam of light.

2. 3. 2. Remote Sensing Reflectance

The most commonly used reflectance in this thesis is the radiance reflectance or remote sensing reflectance. The remote sensing reflectance, R_{rs}, is measured in units of sr^{-1} and defined as:

$$R_{rs}(\theta,\varphi,\lambda)=\frac{L_w(\theta,\varphi,\lambda)}{E_d(0^+,\lambda)} \tag{2.27}$$

where $L_w(\theta,\varphi,\lambda)$ is the water leaving radiance and $E_d(0^+,\lambda)$ is the downwelling irradiance just above the sea surface. The remote sensing reflectance just above the sea surface is represented by $R_{rs}(0^+)$. If the upwelling radiance is measured just below the sea surface then suitable corrections (i.e. immersion coefficients and the n^2 law for radiance) must be applied before it can be used in equation (2.27). Application of the corrections to $L_u(0^-)$ measurements is discussed in Chapter 3, section 3.1.6. Reflectances are important oceanographic quantities as they yield information on the ability of the water body to return light to the surface.

2. 3. 3. Diffuse Attenuation Coefficients

In a typical oceanographic water body radiance and irradiance decrease approximately exponentially with depth. For example, the depth dependence of $E_d(z,\lambda)$ can be written as:

$$E_d(z,\lambda)\equiv E_d(0,\lambda)\exp\left[-K_d(z,\lambda)z\right] \tag{2.28}$$

where $E_d(0,\lambda)$ is the downwelling irradiance at $z=0\,\mathrm{m}$ and $K_d(z,\lambda)$ is the average diffuse attenuation coefficient over the depth interval from 0 to z metres. Solving this equation for $K_d(z,\lambda)$ gives:

$$K_d(z,\lambda)=-\frac{d\ln E_d(z,\lambda)}{dz}=-\frac{1}{E_d(z,\lambda)}\frac{dE_d(z,\lambda)}{dz} \tag{2.29}$$

Other diffuse attenuation coefficients, such as K_u, K_{od}, K_{ou} and $K(\theta,\varphi)$ (which refers to the diffuse attenuation for radiance) can be written similarly. Diffuse attenuation coefficients are measured in units of m^{-1}.

The distinction between the beam attenuation coefficient, $c(\lambda)$, and the diffuse attenuation coefficient, $K_d(\lambda)$, is important. $c(\lambda)$ refers to the radiant power lost from a collimated light beam traversing an infinitesimally thin section of fluid. $K_d(z,\lambda)$ describes the reduction with depth of the ambient downwelling irradiance, $E_d(z,\lambda)$, which is a property of the diffuse light field. $K_d(z,\lambda)$ depends upon the geometrical structure of the incident light field and is therefore defined as an AOP.

2. 3. 4. Optical Depth

The optical depth of a water body is defined as:

$$\zeta = K_d z \tag{2.30}$$

It is a measure of the reduction of irradiance with depth. For water bodies of differing optical properties one optical depth corresponds to different physical depths but the same reduction of irradiance. Approximately 90% of the light reflected from a water body emanates from within the first optical depth (Dickey *et al*, 2006). Optical depths with values of 2.3 and 4.6 correspond to attenuation of downward irradiance of 10% and 1% respectively. These values are conventionally taken to indicate the midpoint and lower limit of the euphotic zone, within which photosynthesis takes place.

2. 4. Radiance Transfer Theory

Radiance transfer theory provides the link between the IOPs and AOPs of a water body. The radiance transfer equation describes the changes in radiance along a given directional path. For example, a beam of light passing through an element of

medium with thickness dr, in the direction (θ,ϕ), loses photons by scattering out of the path and absorption within the element while photons are gained by scattering of light originally travelling in another direction, (θ',ϕ'). Ignoring fluorescent emission within the water and assuming the water body is vertically stratified then the radiance transfer equation can be written as:

$$\frac{dL(z,\theta,\phi)}{dr} = -c(z)L(z,\theta,\phi) + L^{*}(z,\theta,\phi) \qquad (2.31)$$

The term on the left hand side of this expression is the rate of change of radiance with distance along the path specified by the zenith and azimuthal angles (θ,ϕ) at depth z. The first term on the right hand side deals with the loss of radiance from the path by attenuation, e.g. by absorption or scattering, and the second term deals with the gain in radiance from scattering into the path. The second term requires knowledge of the angular distribution of the light field, i.e. the volume scattering function, and the distribution of radiance $L(z,\theta',\phi')$, represented by:

$$L^{*}(z,\theta,\phi) = \int_{4\pi} \beta(z,\theta,\phi;\theta',\phi') L(z,\theta',\phi') d\omega(\theta',\phi') \qquad (2.32)$$

By integrating this equation using the method of Gershun (1936) we get:

$$a = K_E \bar{\mu} \qquad (2.33)$$

where a is the absorption coefficient, K_E is the diffuse attenuation coefficient for net irradiance $\left(\bar{E} = E_d - E_u\right)$ and $\bar{\mu}$ is the average cosine, thus providing a link between IOPs and AOPs.

2. 5. Hydrolight

Hydrolight is a commercial software package which numerically solves the radiance transfer equation and calculates the time independent radiance distribution within and leaving a water body. Inputs to the software include the absorbing and scattering

properties of different in-water constituents such as chlorophyll, CDOM and minerals. The input can also include the sky irradiance conditions and models can include inelastic scattering effects such as Raman scattering, chlorophyll and CDOM fluorescence.

The spectral radiance determines the behaviour of the light field at depth, z, in direction (θ,φ) and at wavelength λ. All other quantities of interest, such as the various irradiances, reflectances and diffuse attenuation coefficients, can be derived once the spectral radiance is known. Hydrolight predicts the spectral radiance by solving the integro-differential radiative transfer equation along with its boundary conditions (Mobley, 1994). These equations have to be solved numerically, due to their complexity, for any realistic situation. Hydrolight solves the radiative transfer equation numerically by partitioning it into segments and averaging over direction and depth.

2. 6. Chlorophyll Fluorescence

Phytoplankton cells contain an array of pigments used to absorb photons and provide the light energy necessary for photosynthesis (Lawlor, 1993; Campbell *et al*, 1987). Photosynthesis can be considered as two classes of processes, the light and dark reactions, each with multiple steps. In order to understand the origin of chlorophyll fluorescence we need only concern ourselves with the light reactions.

The most abundant pigment found in phytoplankton cells is chlorophyll *a*, which has two main absorption bands located in the red and the blue. In fact, chlorophyll *a* is often used as an indicator of the amount of biomass present in oceanic waters. Other important pigments commonly found in phytoplankton include chlorophyll *b, c* and the carotenoids.

There are two subsystems of photosynthetic pigment know as photosystem 1 (PS1) and photosystem 2 (PS2). Associated with each photosystem are special types of chlorophyll *a* molecules bound in a protein matrix known as the reaction centres. The reaction centres are the site of the first light-driven chemical reactions of photosynthesis. Other pigments found in the photosystems (chlorophylls *a*, *b* and *c* and the carotenoids) act as light harvesting complexes (LHCs) which channel the

absorbed light energy to the reaction centres of the photosystem. The number and variety of pigment molecules allow the photosystem to gather light over a larger surface area and over a greater portion of the spectrum than a single pigment would allow (Kirk, 1986).

The absorbed light energy, known as excitation energy, is then used to fuel the primary charge separation event of the photosynthetic process at the PS2 reaction centre (Krause and Weis, 1991). An electron excited to a higher energy level in the reaction centre of PS2 is captured by a primary electron acceptor and the photoexcited electron then passes from PS2 to PS1 via an electron transport chain which includes the plastoquinone pool. We can think of the plastoquinone pool as acting like a capacitor that is charged up by the photoexcited electrons of PS2 and discharged by the photochemical processes taking place at PS1 (Genty *et al*, 1989; Cunningham, 1996; Laisk and Oja, 2000). The plastoquinone pool is said to be charging when the PS2 reaction centres are open and transferring photoexcited electrons to the plastoquinone pool. When the pool is fully charged, i.e. there are no more primary electron acceptors available, then the PS2 reaction centres close. Light absorbed by the LHCs is funnelled to the PS2 reaction centre regardless of the state of the reaction centre and this energy must be dissipated (Horton and Bowyer, 1990).

In solution chlorophyll *a* exhibits a fluorescent yield, the ratio of the number of photons absorbed to the number emitted as fluorescence, of approximately 30%. In the intact photosynthetic apparatus the maximum yield is found to be approximately 3% (Krause and Weis, 1991) and occurs when all PS2 reaction centres are closed. When all reaction centres are open this yield reduces to approximately 0.6% due to quenching by photochemistry.

There are a large number of quenching mechanisms that compete with chlorophyll fluorescence and have been the subject of many reviews (Krause and Weis, 1991; Baker and Horton, 1987). These quenching mechanisms can be split into two groups, namely photochemical and non-photochemical quenching. When the PS2 reaction centres are open and able to transfer photoexcited electrons to PS1 then photochemical quenching is high. However, if the PS2 reaction centres are closed (typically this occurs under high irradiance conditions) then photochemical quenching is low and the fluorescence yield increases. Non-photochemical

quenching processes do not depend upon the state of the reaction centres (Horton and Bowyer, 1990) and include photoinhibitory quenching, state transitions and energy dependent quenching. The variability in the quantum yield of fluorescence is therefore due to quenching mechanisms with differing responses to increased illumination. For example, photochemical quenching decreases and non-photochemical quenching increases with increasing irradiance. In addition these quenching processes have different response times to changing irradiances. Photochemical quenching reaction times are typically less than one second while for non-photochemical quenching the reaction times are of the order of tens of minutes.

In oceanic waters the light re-emitted as fluorescence by phytoplankton in a unit volume of water, $F_f\left(W\,m^{-3}\right)$, depends upon the amount of flux absorbed, A_{ex} $\left(W\,m^{-3}\right)$, and the quantum yield of fluorescence, ϕ_f.

$$F_f = \phi_f\, A_{ex} \tag{2.34}$$

The flux absorbed by phytoplankton at depth z is represented by:

$$A_{ex} = Chl \int_{700nm}^{400nm} a^{*}_{Chl}(\lambda) E_o(\lambda)\, d\lambda \tag{2.35}$$

where Chl is the chlorophyll concentration$\left(mg\,m^{-3}\right)$, $a^{*}_{Chl}(\lambda)$ is the chlorophyll specific absorption coefficient $\left(m^2\,mg^{-1}\right)$ and $E_o(\lambda)$ is the scalar irradiance$\left(W\,m^{-2}\,nm^{-1}\right)$. The integral is performed over the photosynthetically available radiation (PAR) range. Equation (2.34) can then be written (Maritorena *et al*, 2000; Morrison, 2003):

$$F_f = Chl\,\phi_f \int_{700nm}^{400nm} a^{*}_{Chl}(\lambda) E_o(\lambda)\, d\lambda \tag{2.36}$$

In order to include chlorophyll fluorescence in the radiance transfer equation Hydrolight has to construct an appropriate volume inelastic scattering function, β^f.

$$\beta^f(z,\lambda' \rightarrow \lambda) \equiv a^f(z,\lambda') f^f(\lambda' \rightarrow \lambda) \tilde{\beta}^f \qquad (2.37)$$

Measured in units of $m^{-1} sr^{-1} nm^{-1}$.

The term $a^f(z,\lambda')$ describes the light absorbed by the fluorescing substance, in this case chlorophyll, as a function of depth and excitation wavelength, λ'.

$f^f(\lambda' \rightarrow \lambda)$ is the wavelength redistribution function. It is composed of several terms which are described in equation (2.38).

$$f^f(\lambda' \rightarrow \lambda) \equiv \phi_f \, g_c(\lambda') h_c(\lambda) \frac{\lambda'}{\lambda} \qquad (2.38)$$

where ϕ_f is the quantum yield of fluorescence, $g_c(\lambda')$ is a function which specifies the spectral interval over which light can excite chlorophyll fluorescence, $h_c(\lambda)$ is a function which describes the chlorophyll fluorescence emission and $\frac{\lambda'}{\lambda}$ is the ratio of the excitation wavelength to the emission wavelength used to convert photon counts to energy. In Hydrolight $h_c(\lambda)$ is approximated by a Gaussian function with a centre wavelength of 685nm and a full width half maximum of 25nm.

The final term in equation (2.37) is the phase function for the emitted light. The phase function is assumed to be isotropic, for example:

$$\tilde{\beta}^f = \frac{1}{4\pi} sr^{-1} \qquad (2.39)$$

In Hydrolight wavelengths between 370*nm* and 630*nm* can excite chlorophyll fluorescence.

2. 7. Other Inelastic Scattering Processes

In addition to chlorophyll fluorescence there are two other important inelastic scattering processes that can take place in the water column. These are Raman scattering and CDOM fluorescence.

2. 7. 1. Raman Scattering

Raman scattering is a process which can take place in solids, liquids and gasses. Sugihara *et al* (1984) found that Raman scattering by water molecules provides a mechanism for scattering light inelastically from shorter wavelengths to longer wavelengths. When an incident photon excites a molecule into a higher rotational or vibrational quantum state then the excited molecule can emit a photon of a longer wavelength than that of the incident photon. In oceanic waters the Raman scattered photons usually appear as a signal in the spectral irradiance at depths greater than a few tens of metres. Wavelengths of light greater than 550nm are unable to penetrate deeply into the water column due to strong absorption by water. However, wavelengths less than 550nm are able to penetrate more deeply into the water column. At depth it is these wavelengths, in the blue to green part of the spectrum, that are Raman scattered to longer wavelengths in the yellow to red region of the spectrum. These Raman scattered photons provide an internal source of non-solar radiation due to inelastic scattering effects. Raman scattering is a process which occurs at all depths in the water column. However, at shallow depths the Raman scattered photons are usually negligible compared to the ambient solar radiation. Further information on the contribution of Raman scattering to the underwater light field can be found in Marshall and Smith (1990), Hu and Voss (1997), Bartlett *et al* (1998), Gordon (1999) and Schroeder *et al* (2003).

2. 7. 2. CDOM Fluorescence

CDOM fluorescence is another inelastic scattering effect that takes place in the water column. However, due to the variation in compounds which make up CDOM its fluorescence emission is more complicated. Generally, light absorption in the ultra violet, between 300 to 400nm, can result in a broad band fluorescence emission occurring between 310nm to 600nm. Further information on CDOM fluorescence can be found in Chen and Bada (1992), Green and Blough (1994) and Vodacek *et al* (1994).

2. 8. Summary

a. Radiometric parameters such as radiance and irradiance are used to describe the characteristics of the incident, underwater and water leaving light field.

b. IOPs depend upon the composition of the water body and can be split into contributions from the *in situ* components (water, phytoplankton, CDOM and MSS).

c. AOPs depend strongly upon the composition of the water body but also upon the geometrical structure of the incident light field.

d. IOPs and AOPs can be linked together by radiance transfer theory and the radiance transfer equation is used to describe the change in radiance along a given directional path. The radiative transfer computer package known as Hydrolight can be used to model the water leaving radiance and underwater light field.

e. Chlorophyll fluorescence is a deactivation pathway for the light-harvesting chlorophyll *a* antenna of PS2. The quantum yield of fluorescence is the ratio of the amount of photons emitted as fluorescence to the amount of photons absorbed. Variability in the quantum yield of fluorescence is due to photochemical and non-photochemical quenching mechanisms.

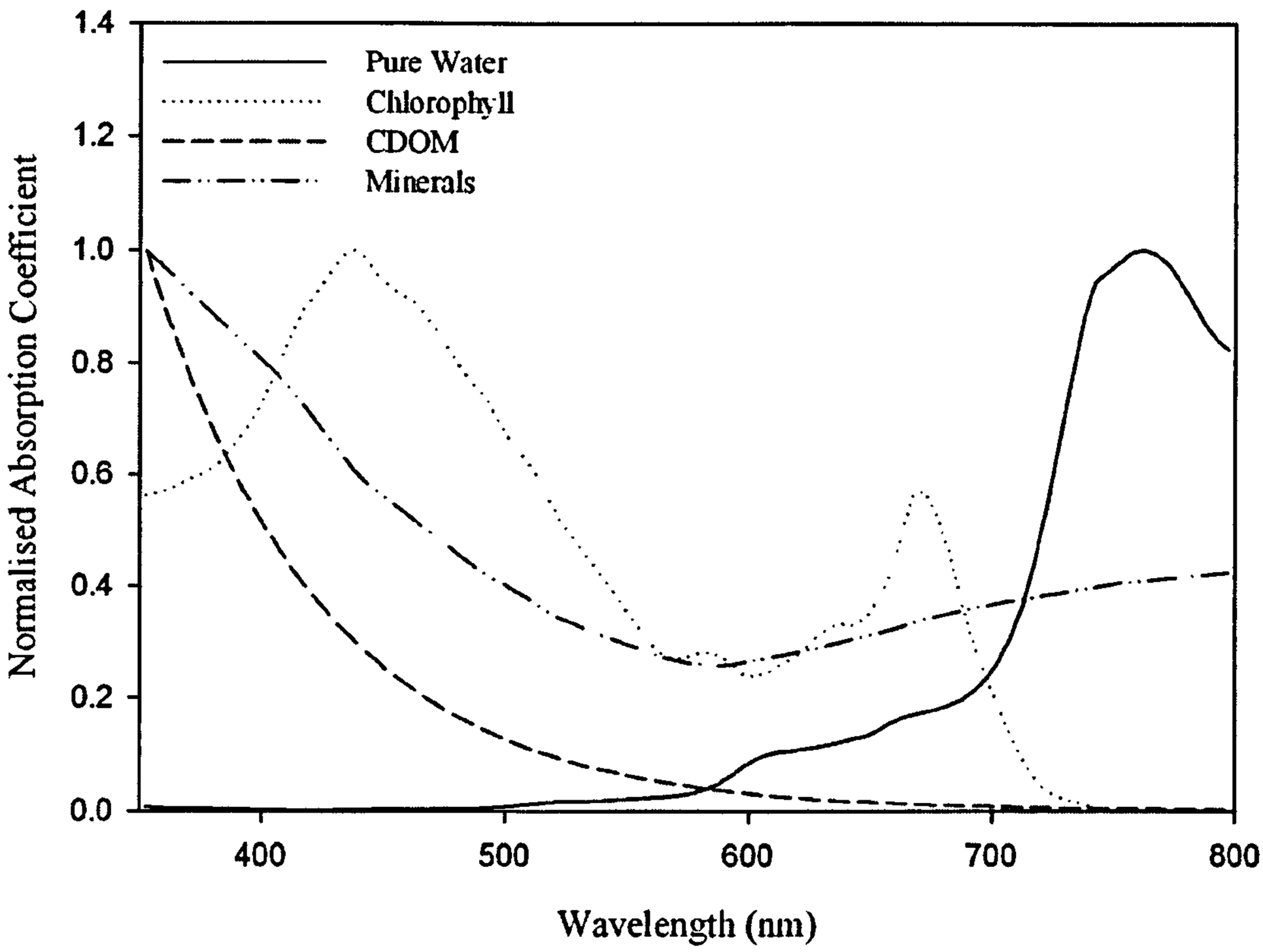

Figure 2.1. Normalised absorption spectra for water, chlorophyll, CDOM and minerals taken from the default examples in Hydrolight. Spectra were normalised by their peak value to allow comparison between the spectral shapes of the four main optically significant components.

Chapter 3: Instrumentation, and Analytical Methods for Determining Seawater Composition

Field measurements of inherent and apparent optical properties (IOPs and AOPs) were carried out during five research cruises by deploying a suite of optical instruments. Samples of seawater were collected and measurements of the concentrations of chlorophyll, suspended particulate matter (SPM), coloured dissolved organic matter (CDOM) and filter pad absorption were made.

3. 1. Profiling Instrumentation

This section describes the instrumentation used to gather data on the optical and hydrographic properties of the water body, calibration procedures, and methods used to perform corrections on field measurements.

3. 1. 1. Sea-Bird SBE 19Plus CTD

The Sea-Bird CTD is a profiling instrument that measures hydrographic features of the water column. A micro machined silicon strain gauge pressure sensor measures depth, a Wein-Bridge oscillator generates a frequency output in response to changes in conductivity and an ultra stable thermistor is used to measure temperature.

Calibration of the CTD was not possible in our laboratory, however cross comparison with the British Antarctic Survey's (BAS) CTD system, which is subject to rigorous calibration standards (Ward and Thorpe, 2005), during a cruise to South Georgia in December 2004 was carried out. Table 3.1 contains information on the correlation between the temperature, salinity and density measurements made by the BAS CTD and the University of Strathclyde's CTD. It can be seen from the gradient

and high R^2 values that the University of Strathclyde's CTD system remained within acceptable error limits.

3. 1. 2. WET Labs AC9

The WET Labs AC9 measures the absorption coefficient, $a(\lambda)$, and beam attenuation coefficient, $c(\lambda)$, of materials other than water at nine wavelengths: 412, 440, 488, 510, 532, 555, 650, 676 and 715nm (10nm Full Width Half Maximum). The AC9 is a dual path meter with each 25cm path containing its own source, optics and detector. The attenuation flow tube has a blackened inner surface to absorb any scattered light and prevent it from contributing to the transmitted light, and the detector has a small collection angle. Light passing through the tube is therefore subject to both absorption and scattering by the enclosed sample. The absorption flow tube works on the principle of total internal reflection where light that is scattered in the pathlength is reflected back into the sample volume, and the detector has a large collection angle. The flow tube comprises of a clear quartz tube surrounded by a volume of air. In this tube, light is absorbed by particulate matter, CDOM and water. The absorption measurements made by the AC9 must have a scattering correction applied as reflecting tube absorption meters do not collect all of the scattered light, due to the geometry of the reflecting tube and losses at the reflective surface. This can result in an overestimation of the absorption coefficient. The method used to correct for the overestimation in the absorption coefficient is described by Zaneveld *et al*, 1994.

Before applying the scattering correction to the absorption data it was first necessary to correct for the effects of temperature and salinity on the absorption and attenuation measurements using the method of Pegau *et al*, 1997. These effects are most pronounced in the infrared and near-infrared regions of the spectrum

By calibrating the AC9 using a pure fresh water blank, measurements of the total absorption and attenuation coefficients relative to water were obtained. For example:

$$a(\lambda)_{measured} = a(\lambda)_{total} - a(\lambda)_{water} \qquad (3.1)$$

$$c(\lambda)_{measured} = c(\lambda)_{total} - c(\lambda)_{water} \qquad (3.2)$$

The temperature and salinity problems result from the fact that the calibration is conducted using fresh water at room temperature but field measurements are carried out in saline water of a different temperature than the water used in the calibration. By measuring the temperature of the reference (calibration) and sample water and the salinity of the sample water the effects of temperature and salinity on the field measurements can be corrected as follows:

$$a(\lambda)_{mts} = a(\lambda)_m - \left[\Psi_t(t - t_r) + \Psi_s(s)\right] \qquad (3.3)$$

where $a(\lambda)_{mts}$ is the measured absorption coefficient corrected for the effects of temperature and salinity, $a(\lambda)_m$ is the uncorrected measured absorption coefficient, t and t_r are the temperatures of the sample and reference water, s is the salinity of the sampled water and Ψ_t and Ψ_s are the values of the linear slopes of the temperature and salinity dependences (supplied by the manufacturer).

Once the temperature and salinity corrections were applied it was possible to apply the scattering correction to the absorption data. The scattering correction assumes that there is a reference wavelength where the absorption due to particulate material and CDOM is zero and that the volume scattering function is independent of wavelength. The scattering correction applied was as follows:

$$a(\lambda)_{ac9} = a(\lambda)_m - \left[a(715)_{mts} \frac{c(\lambda)_m - a(\lambda)_m}{c(715)_{mts} - a(715)_{mts}}\right] \qquad (3.4)$$

where $a_{ac9}(\lambda)$ is the corrected (temperature, salinity and scattering) absorption coefficient, $a(\lambda)_m$ is the uncorrected measured absorption coefficient, $a(715)_{mts}$ is the temperature and salinity corrected absorption coefficient measured at 715nm, $c(\lambda)_m$ is the attenuation measured at wavelength and $c(715)_{mts}$ is the temperature and salinity corrected attenuation coefficient measured at 715nm.

It should be noted that the accuracy of attenuation measurements is limited by the finite acceptance angle of the detector, since incomplete rejection of scattered light causes the attenuation coefficient to be underestimated. Correcting attenuation measurements for errors caused by collection of scattered light is difficult and of questionable benefit (Pegau *et al*, 1995).

Corrected data was averaged over 1m depth intervals and the scattering coefficient $\left(b(\lambda)\right)$ was obtained by subtracting the absorption coefficient from the attenuation coefficient:

$$b_{ac9}(\lambda) = c_{ac9}(\lambda) - a_{ac9}(\lambda) \tag{3.5}$$

where $a_{ac9}(\lambda)$, $b_{ac9}(\lambda)$ and $c_{ac9}(\lambda)$ are measured in reciprocal metres$\left(m^{-1}\right)$.

The AC9 measures the absorption and attenuation coefficients relative to water. If total coefficients are required then the absorption and attenuation of water must be added (Pope and Fry, 1997). For example:

$$a_{ac9}(\lambda) = a_{part}(\lambda) + a_{CDOM}(\lambda) \tag{3.6}$$

$$a_{tot}(\lambda) = a_{ac9}(\lambda) + a_{w}(\lambda) \tag{3.7}$$

where $a_{part}(\lambda)$ is the absorption coefficient due to particulate material, $a_{CDOM}(\lambda)$ is the absorption coefficient due to CDOM, $a_{w}(\lambda)$ is the absorption coefficient due to water and $a_{tot}(\lambda)$ is the total absorption coefficient, all measured in reciprocal metres$\left(m^{-1}\right)$.

The AC9 was calibrated by measuring optical blanks using ultra pure Millipore water treated with ultraviolet light. Calibrations of the absorption and attenuation channels demonstrated that the instrument remained within the manufacturer's specification of $\pm 0.005 m^{-1}$.

3. 1. 3. HOBI Labs HydroScat-2

The HydroScat-2 is an *in situ* optical backscattering sensor. It has two channels that measure the total backscattering coefficient $\left(b_b(\lambda)\right)$ at 470 and 676nm: each channel has separate source and receiver optics. Light emitting diodes (LEDs) produce source beams that enter the water and silicon photodiodes detect the backscattered light. In addition to the backscattering measurement the HydroScat-2 is capable of measuring fluorescence excited by the 470nm source and detected by the 676nm receiver. The optical principles of HydroScat-2 measurements can be found in Maffione and Dana, 1997. Data was binned into 1m depth intervals and corrected for any loss of signal due to attenuation effects occurring between the instrument window and sensing volume. This is known as the sigma correction and is represented by equation (3.8):

$$b_b = \sigma b_{bu} \tag{3.8}$$

where b_b is the corrected backscattering coefficient$\left(m^{-1}\right)$, b_{bu} is the uncorrected backscattering coefficient $\left(m^{-1}\right)$ and σ is the correction factor given by:

$$\sigma = k_0 + k_1 K_{bb} + k_2 K_{bb}^2 \tag{3.9}$$

In equation (3.9) k_0, k_1 and k_2 are calibration constants supplied by the manufacturer and K_{bb} is the attenuation coefficient of the water contained within the sensors measurement geometry$\left(m^{-1}\right)$.

Using data recorded by the AC9, K_{bb} can be estimated as follows (Twardowski *et al,* 2001):

$$K_{bb} = a + 0.75b \tag{3.10}$$

Since calibration of the HydroScat-2 is not possible in our laboratory it was assumed that the manufacturer's calibration remained valid.

3. 1. 4. SeaWiFS Profiling Multi-channel Radiometer (SPMR)

The Satlantic SPMR is a freefalling radiometer that consists of two sensor heads that profile downwelling irradiance, E_d, and upwelling radiance, L_u, at seven wavelengths: 412, 443, 490, 510, 554, 665 and 700nm (10nm FWHM). The SPMR was deployed a distance of at least 15m from the ship to avoid the effects of ship shadow. The filters employed in the optical sensors are designed to match the 10nm bandwidths required by SeaWiFS calibration and validation protocols. Signal detection is by silicon photodiodes. The SPMR sensors were calibrated before cruises using a 100-W standard lamp. A full description of the method used is given in section 3. 1. 7. Data from the instrument was processed using ProSoft, a MatLab data analysis package. The steps involved included the application of calibration files, depth binning into 1m intervals and derivation of additional products such as the diffuse attenuation coefficient for downwelling irradiance, K_d, and the water leaving radiance, L_w.

3. 1. 5. Satlantic HyperPro Profiling Radiometer

The Satlantic HyperPro is a freefalling hyperspectral optical profiler that measures downwelling irradiance, E_d, and upwelling radiance, L_u. It uses silicon photodiode array detection systems to provide 256 channels in the spectral region between 350 and 800nm with a spectral resolution of 10nm and spectral sampling of 3.3nm/pixel. Details on the method used to calibrate the HyperPro E_d and L_u sensors can be found in section 3. 1. 7. The ProSoft computer package was used to apply calibration files, bin data as either a function of time or depth and derive additional products such as diffuse attenuation coefficients.

3. 1. 6. TriOS Hyperspectral Radiometers

The TriOS hyperspectral radiometer system consists of three irradiance sensors which record E_{od} (downwelling scalar irradiance), E_u (upwelling planar irradiance) and E_d (downwelling planar irradiance), and a radiance sensor that records L_u

(upwelling radiance). Light is detected by an optical fibre bundle made up of 30 single fibres. Sampled light is dispersed by a holographic grating and detected by a 256 channel silicon photodiode array. The wavelength range of the sensors is 320 to 950nm with a spectral sampling of 3.3nm/pixel. The TriOS radiometers can be used in profiling mode or as a sea surface detection system depending upon the deployment configuration.

When the TriOS radiometers were deployed in surface penetrating mode the radiance sensor measured subsurface upwelling radiance, $L_u\left(0^-\right)$. In order to calculate the remote sensing reflectance $L_u\left(0^-\right)$ signals had to be converted to water leaving radiance, L_w, signals. This required the application of the n^2 law for radiance to extrapolate through the air-water interface (Mobley, 1994). However, as the TriOS L_u sensor was calibrated in air it was necessary to apply immersion coefficients before extrapolating from water to air (Ohde and Siegel, 2003). The application of the immersion coefficients is a necessary correction in calculating the correct values of $L_u\left(0^-\right)$, regardless of whether or not one wishes to extrapolate through the air-water interface. The wavelength dependent immersion coefficients are required as the solid angle viewed by the sensor when submerged in water is reduced, and the glass-water refractive indices are better matched and so reflective losses at the window will be reduced (Mueller and Austin, 1995). According to Austin (1976) the wavelength dependent immersion coefficient is given by:

$$F_i(\lambda)=\frac{n_w(\lambda)\left(n_w(\lambda)+n_g(\lambda)\right)^2}{\left(1+n_g(\lambda)\right)^2} \tag{3.11}$$

where $F_i(\lambda)$ is the wavelength dependent immersion coefficient, $n_w(\lambda)$ is the wavelength dependent refractive index of seawater and $n_g(\lambda)$ is the wavelength dependent refractive index of the glass window in the radiance sensor.

According to Austin and Halikas (1976) the refractive index of seawater, $n_w(\lambda)$, can be expressed as follows:

$$n_w(\lambda)=1.325147+\frac{6.6096}{\lambda-137.1924} \tag{3.12}$$

where λ is the wavelength (*nm*).

The wavelength dependent refractive index of the radiance sensor glass window was found to be (Ohde and Siegel, 2003):

$$n_g(\lambda)=1.4424+\frac{7.1661}{\lambda-144.7170} \tag{3.13}$$

Once the immersion coefficients had been applied to the L_u data the n^2 law for radiance was applied to extrapolate from seawater to air. Applying the n^2 law for radiance gives:

$$\frac{L_w(\lambda)}{n_{air}(\lambda)^2}=t(\theta,n)\frac{L_u(0^-,\lambda)}{n_w(\lambda)^2} \tag{3.14}$$

where $L_w(\lambda)$ is the water leaving radiance $\left(W\,m^{-2}\,nm^{-1}\,sr^{-1}\right)$, $n_{air}(\lambda)$ is the wavelength dependent refractive index of air, $L_u(0^-,\lambda)$ is the upwelling radiance just below the sea surface $\left(W\,m^{-2}\,nm^{-1}\,sr^{-1}\right)$, $n_w(\lambda)$ is the wavelength dependent refractive index of seawater and $t(\theta,n)$ is the transmittance of the air-water interface. For $\theta=0^o$ (normal incidence) $t(\theta,n)$ has a value of 0.98 which is not significantly wavelength dependent and for air $n_{air}(\lambda)=1$. Equation (3.14) can therefore be rewritten as:

$$L_w(\lambda)=0.98\frac{L_u(0^-,\lambda)}{n_w(\lambda)^2} \tag{3.15}$$

Using this value of $L_w(\lambda)$ the remote sensing reflectance could be calculated:

$$R_{rs}(0^+,\lambda)=\frac{L_w(\lambda)}{E_d(\lambda)} \tag{3.16}$$

During 2005 the TriOS radiometers were recalibrated in the manufacturer's laboratory and calibration files for use in air and seawater were provided, therefore the immersion coefficient correction was only applied to data that was collected prior to 2005.

3. 1. 7. Radiometer Calibrations

Before deployment on a research cruise the irradiance and radiance sensors were calibrated in the laboratory at the University of Strathclyde.

i. Irradiance Sensor Calibration

The experimental set-up is illustrated in Figure 3.1. The irradiance sensor was mounted in a dark tent 0.5m from the front surface of a Bentham CL2 lamp bracket. The Bentham CL2 100W standard lamp generated a known spectral irradiance at 0.5m. The irradiance sensor and lamp were aligned along the same optical axis and the lamp was operated from a DC power supply with a constant current of 8.5A. Before commencing the calibration measurements the lamp was allowed a period of 30 minutes in which to stabilize. The output intensity from the lamp is described by an inverse square law:

$$E_r(\lambda)=\frac{E_l(\lambda)r_o^2}{r^2} \tag{3.17}$$

where $E_r(\lambda)$ is the measured irradiance at wavelength λ and distance r, $E_l(\lambda)$ is the known irradiance at the calibration distance $r_0 = 0.5m$. If the irradiance sensor is placed a distance of $0.5m$ from the lamp equation (3.17) simplifies to:

$$E_r(\lambda)=E_l(\lambda) \tag{3.18}$$

As the TriOS radiometers were recalibrated in 2005 in the manufacturer's laboratory, subject to National Institute for Standards and Technology (NIST) levels, it was decided that the TriOS radiometers would be used as a transfer standard. The Bentham lamp was recalibrated using the newly calibrated TriOS radiometer

response when the sensor was placed a distance of 0.5m from the lamp. In addition to the recalibration of the TriOS instruments, modifications were made to improve the way in which the irradiance and radiance sensors were mounted in the calibration tent. Figure 3.2 illustrates the spectral irradiance provided in the Bentham lamp file and the signal measured by the recalibrated TriOS irradiance sensors. A fifth order polynomial was fitted to the TriOS signal and used to recalibrate the Bentham lamp. The recalibrated lamp data was then applied to previous cruise calibration data. Figure 3.3 panels (A) to (D) illustrate the comparison between the expected irradiance values and the measured signal for calibrations carried out for the (A) Oban 2003, (B) Sound of Jura 2004, (C) AMT 15 and (D) Bristol Channel 2005 cruises.

The ratio between the expected value and the signal measured by the sensor was then calculated (i.e. the expected value was divided by the measured value) for wavelengths, λ. The calculated values were then used to correct the field measurements recorded.

ii. Radiance Sensor Calibration

The radiance sensor calibrations were carried out by illuminating a Spectralon plate with the Bentham standard lamp. The Spectralon plate has highly Lambertian properties, i.e. it reflects equal intensities in all directions, and has a known spectral reflectance. The experimental set-up for the radiance calibration is illustrated in Figure 3.4. If the irradiance striking the Spectralon plate is known then the radiance from the plate detected by a sensor can be calculated from:

$$L(\lambda)=\frac{E_r(\lambda)\rho}{\pi} \tag{3.19}$$

where $L(\lambda)$ is the radiance, $E_r(\lambda)$ is the irradiance at distance r and ρ is the spectral reflectance of the plate. The Spectralon plate used in the calibration procedure has a ρ of 0.99 between 300 and 800nm. By setting r equal to 0.5m the irradiance striking the plate should be equal to the values of $E(\lambda)$ given in the lamp calibration file. Therefore, using equation (3.19) values of $L(\lambda)$ expected can be

calculated and compared with the measured signal. As with the irradiance measurements the lamp was allowed a period of 30 minutes to stabilize prior to measurements being recorded and was operated at 8.5A from the DC power supply. Figure 3.5 panels (A) to (D) illustrate the comparisons between expected and measured $L(\lambda)$ values for the (A) Oban 2003, (B) Sound of Jura 2004, (C) AMT 15 and (D) Bristol Channel 2005 cruises.

The ratio between the expected values and the measured signal was calculated and used to correct field measurements.

3. 2. Analytical Methods for Determining Seawater Composition

In this section the procedures used to determine the concentration of the in-water constituents, such as SPM, chlorophyll and CDOM, are discussed. The method used to determine absorption by particulate material concentrated on glass fibre filters is also included.

3. 2. 1. Gravimetric Determination of Suspended Particulate Material

The concentration of suspended particulate material was determined by the method described in Parsons *et al* (1992). Prior to a cruise 90mm GF/F filters were numbered with a water insoluble pen, wrapped in aluminium foil and dried at $75^{o}C$. The dried filters were weighed three times and the average was recorded, B_{ave}. On the cruise a volume of seawater was filtered (for Scottish fjords a typical sample volume was 5l), the filter was rinsed with ultra pure water (approximately 100ml) and frozen for transport to the laboratory. Once in the laboratory the filters were dried in the oven at $75^{o}C$ for three hours and weighed three times with the average value being recorded, W_{ave}. The filters were then ashed in the furnace at $500^{o}C$ for three hours to burn off the organic particulate component and allow discrimination

between the algal (organic) and non-algal (inorganic) components. Each filter was then weighed three times and the average value was recorded, R_{ave}.

The organic and inorganic components were calculated as follows:

$$TSS = \frac{W_{ave} - B_{ave}}{V} \tag{3.20}$$

$$MSS = \frac{R_{ave} - B_{ave}}{V} \tag{3.21}$$

$$OSS = TSS - MSS \tag{3.22}$$

where W_{ave}, B_{ave} and R_{ave} are measured in milligrams (mg), V is the volume of seawater filtered in litres (l) and TSS, MSS and OSS are total, mineral and organic suspended solid concentrations measured in milligrams per litre ($mg\ l^{-1}$).

3. 2. 2. Filter Pad Absorption Measurements

Samples were collected by concentrating particulate material onto 25mm GF/F filter by filtering a known volume of sample (Yentsch, 1962). Filters were immediately frozen and stored in darkness to reduce pigment photodegradation. The optical density of the total particulate matter $\left(OD_p\right)$ was measured using a spectrophotometer. The filter, moistened with a few drops of filtered seawater, was placed on a glass microscope slide in front of a diffusing disk and adjacent to the PMT (photomultiplier tube) detector. The filter was then scanned, using a monochromatic light source, at 2nm intervals between 400 and 750nm, with a clean moistened 25mm GF/F filter scanned as a reference. The optical density was then calculated:

$$OD_p = \log\left(\frac{I_0}{I}\right) \tag{3.23}$$

where I_0 is the reference signal and I is the sample signal.

After the total particulate measurements were carried out the filter pad was left to soak in 90% acetone for 24 hours to extract the pigmented material (Parsons *et al*, 1992), before analysing the bleached filter to determine the absorption due to detritus. The optical density of the bleached filter pads, OD_d, was measured in the same manner as the total particulate filter pad.

Using the optical density information collected for the total particulate and detrital filter pad measurements the absorption coefficients of these two components could be calculated (Kishino *et al*, 1985; Bricaud and Stramski, 1990):

$$a(\lambda) = \frac{2.303 \times OD_{p/d}(\lambda) \times s}{V_f \times \beta(\lambda)} \tag{3.24}$$

where a is the absorption coefficient $\left(m^{-1}\right)$ for total particulate/detrital component at wavelength λ, s is the clearance area of the filter pad $\left(m^2\right)$, V_f is the volume filtered $\left(m^3\right)$ and $\beta(\lambda)$ is the pathlength amplification factor (*dimensionless*) (see section 3. 2. 3.).

The absorption due to phytoplankton was then calculated by subtracting the detrital absorption from the total particulate absorption:

$$a_{phy}(\lambda) = a_p(\lambda) - a_d(\lambda) \tag{3.25}$$

where $a_{phy}(\lambda)$ is the absorption coefficient of phytoplankton $\left(m^{-1}\right)$ at wavelength λ.

3. 2. 3. The Pathlength Amplification Factor

Equation (3.24) introduces the pathlength amplification factor, $\beta(\lambda)$, defined as the ratio of the optical to the geometrical pathlength, which occurs due to multiple scattering within the glass fibre filter on which particulate material is concentrated. This can lead to an overestimation in measured absorption values (Butler, 1962). Work has been carried out by a number of investigators to determine a pathlength amplification correction scheme.

Kishino *et al* (1985) found that β varied between 2.4 and 4.7 depending on particle type and geometrical configuration. Mitchell and Kiefer (1988) found that β varied as a function of optical density measured on the filter $\left(OD_f\right)$ and derived an inverse relationship to describe this. Mitchell (1990) also showed that β varied between different types of filters as well as between different lots of filters. Bricaud and Stramski (1990) used the data gathered by Mitchell and Kiefer (1988) and fitted a power function to it in order to describe the relationship between β and OD_f on Whatman GF/F filters. Allali *et al* (1995) suggested the use of the fast-transfer-freeze (FTF) technique which eliminates the need to correct for the pathlength amplification factor. In the FTF technique particles concentrated onto a Nucleopore filter are transferred to a glass microscope slide using liquid nitrogen freezing. Tassan and Ferrari (1998) suggested that some of the variability observed in β between different species may be attributed to incomplete collection of scattered light. Roesler (1998) suggested that, on a theoretical basis, the pathlength amplification factor is equal to the inverse of the average cosine of a perfectly diffuse irradiance field (i.e. $\beta = 2$) as light passing through a glass fibre filter becomes uniformly diffuse. Lohrenz (2000) also used a theoretical approach to correct the β factor for filters of different sample loading.

The approach used here to determine the pathlength amplification factor was to compare filter pad absorption measurements with absorption values measured *in situ* using an AC9. As the AC9 measures the absorption of particulates and CDOM, the CDOM values measured using the spectrophotometer were added to the filter pad measurements to ensure like for like comparison. In addition to this the absorption value at 715nm was subtracted from the entire spectrum to ensure that the value at 715nm was equal to zero as is the case with the AC9 measurements.

The power function of Bricaud and Stramski (1990) was applied to the filter pad measurements:

$$\beta(\lambda) = 1.63\left[OD_f(\lambda)\right]^{-0.22} \tag{3.26}$$

where $OD_f(\lambda)$ is the optical density of the filter pad at wavelength λ and the measured CDOM absorption added.

Figure 3.6 shows the results of linear regressions between the β corrected filter pad plus CDOM absorption values and the AC9 *in situ* values. The coefficients of equation (3.26) were then altered by ±10% but no significant improvement was found. For West of Scotland coastal water the Bricaud and Stramski (1990) power function with coefficient values of 1.63 and -0.22 was therefore a suitable choice of correction for the pathlength amplification factor.

The same procedure was carried out for samples collected in the Bristol Channel during the cruise conducted in 2005. This analysis was carried out by Laura Waite, University of Strathclyde, and it was found that the best fit between the AC9 data and filter pad plus CDOM data was achieved using the Bricaud and Stramski (1990) power law with the following coefficients:

$$\beta(\lambda)=1.26\left[OD_f(\lambda)\right]^{-0.1} \qquad (3.27)$$

The fact that the coefficients required to correct the Bristol Channel data are different from those used in the Oban 2003, Oban 2004 and Sound of Jura 2004 data is probably due to the fact that the filter pads were analysed in a different spectrophotometer. The spectrophotometers used for the filter pad analysis have different optical set-ups and this may be responsible for the change in coefficients observed. However, it is also possible that variations in particle type and size could have an effect on the values of coefficients used in equations (3.26) and (3.27).

3. 2. 4. Chlorophyll, Carotenoid and Phaeopigment Concentrations

Chlorophyll samples were obtained by filtering a sample volume through 25mm GF/F filters and extracting the pigments by soaking the filters for 24 hours in 90% acetone buffered with magnesium carbonate (Parsons *et al*, 1992). The filters were centrifuged for 5 minutes at 6000rpm and the supernatant was carefully decanted into a 1cm pathlength glass cuvette. The absorbance of the decanted centrifuge extract was then measured in a spectrophotometer against a blank that consisted of a 1cm

glass cuvette containing 90% acetone. The absorbance spectra of the chlorophyll pigment extract was converted to chlorophyll concentrations (chlorophyll *a, b* and c) using the trichromatic equations set out by Jeffery and Humphery (1975).

$$C_a = 11.85A_{664} - 1.54A_{647} - 0.08A_{630} \tag{3.28}$$

$$C_b = 21.03A_{647} - 5.43A_{664} - 2.66A_{630} \tag{3.29}$$

$$C_c = 24.52A_{630} - 1.67A_{664} - 7.60A_{647} \tag{3.30}$$

where A_λ is the absorbance (*dimensionless*) at the specified wavelength corrected for turbidity at 750nm.

The concentration of carotenoids present can be calculated as follows:

$$C_p = 7.6\left(A_{480} - 1.49A_{510}\right) \tag{3.31}$$

The concentration of the different pigments (C_a, C_b , C_c and C_p) , measured in milligram per metre cubed $\left(mg\,m^{-3}\right)$, is then given by:

$$Concentration\left(mg\,m^{-3}\right) = \frac{C\ \ v}{V} \tag{3.32}$$

where v is the volume of acetone extract decanted (ml) and V is the volume of seawater filtered (l).

The trichromatic equations assume that no chlorophyll degradation products are present, for example phaeopigments. However, in natural samples the quantity of phaeopigments present can form a significant part of the total plant pigment. In the presence of such degradation products, the trichromatic equations will overestimate the concentration of the chlorophyll *a, b* and *c* pigments (Parsons *et al,* 1992; Jeffery *et al*, 1997).

The absorption of phaeopigment is lower in the 665nm region of the spectrum than the parent molecule. By measuring the absorbance at 665nm before and after

acidification with 10% hydrochloric acid, which breaks down all of the chlorophyll *a* into phaeopigments, the concentration of phaeopigment originally present can be measured (Lorenzen, 1967). Using the Lorenzen technique the chlorophyll *a* concentration was calculated as follows:

$$C_a = \frac{26.7\left(665_b - 665_a\right)\times v}{V \times l} \tag{3.33}$$

and the concentration of phaeopigments is given by:

$$C_{phaeo} = \frac{26.7\left(1.7\left(665_a\right) - 665_b\right)\times v}{V \times l} \tag{3.34}$$

where l is the pathlength of the cuvette(cm).

3. 2. 5. *In Vivo* Chlorophyll *a* Specific Absorption Coefficient

The chlorophyll *a* specific absorption coefficient $\left(a^*(\lambda)\right)$ was determined by dividing the absorption coefficient of phytoplankton by the chlorophyll *a* concentration:

$$a^*(\lambda) = \frac{a_{phy}(\lambda)}{C_a} \tag{3.35}$$

where $a^*(\lambda)$ is the chlorophyll *a* specific absorption coefficient ($m^2\ mg^{-1}$).

3. 2. 6. Coloured Dissolved Organic Matter (CDOM)

CDOM samples were obtained by filtering seawater through a $0.2\mu m$ nucleopore membrane filter and the filtrate was stored in sterile bottles and kept refrigerated until analysed. The CDOM samples were allowed to adjust to room temperature, in order to avoid condensation forming on the glass cuvette, before being carefully decanted into a 10cm pathlength glass cuvette and placed in the spectrophotometer against a diffusing disk. CDOM samples were scanned between 400 and 750nm in

5nm intervals, with cuvettes containing ultra pure water scanned as a blank. The absorption of the CDOM samples is given by:

$$a_{CDOM}(\lambda) = \frac{2.303 \times OD(\lambda)}{r} \qquad (3.36)$$

where $OD(\lambda)$ is the optical density at wavelength λ and r is the pathlength of the cuvette in metres.

The absorption coefficient of CDOM at 440nm is conventionally used as an indicator of CDOM concentration, represented as g_{440}.

3. 3. Summary

a. *In situ* data was collected by deploying a number of instruments to measure different properties of the water column. The CTD measured hydrographic profiles of salinity, temperature and depth. The IOPs were measured using an AC9 and HydroScat-2. The AC9 yielded information on the absorption and attenuation profiles, and the HydroScat-2 on the backscattering profile. The SPMR and HyperPro generated profiles of the in-water light field at discrete wavebands and in hyperspectral mode. Hyperspectral radiometry was obtained at the sea surface using TriOS radiometers.

b. Seawater composition was determined by gravimetrically measuring SPM and using a spectrophotometer to measure absorption by different *in situ* components. Total particulate and detrital absorption measurements were conducted and used to calculate the absorption due to phytoplankton. Chlorophyll, carotenoid and phaeopigment concentrations were determined spectrophotometrically by employing the techniques set out by Jeffery and Humphery (1975) and Lorenzen (1967). CDOM absorption was also measured spectrophotometrically and the value at 440nm was used as an indicator of concentration.

	GRADIENT	OFFSET	R^2
Temperature (^0C)	0.9806	0.01	0.9941
Salinity (*PSU*)	1.0155	-0.2408	0.9939
Density ($kg\,m^{-3}$)	1.006	0.0654	0.9942

Table 3.1. Cross calibration between British Antarctic Survey, plotted along the y axis, and University of Strathclyde's, plotted along the x axis, CTD systems.

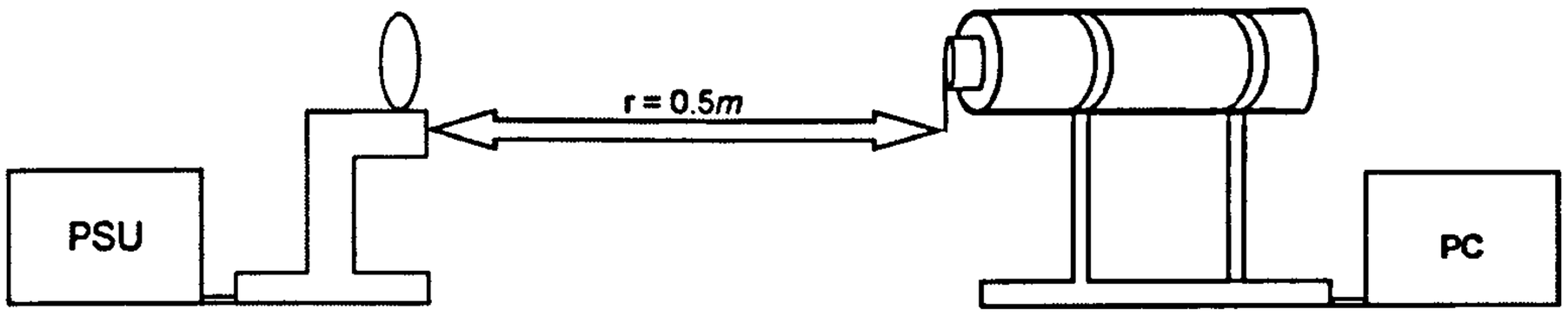

Figure 3.1. Irradiance sensor calibration. The lamp and irradiance sensor were placed on the same optical axis 0.5*m* apart. The lamp was allowed to stabilize for 30 minutes prior to any measurement being carried out.

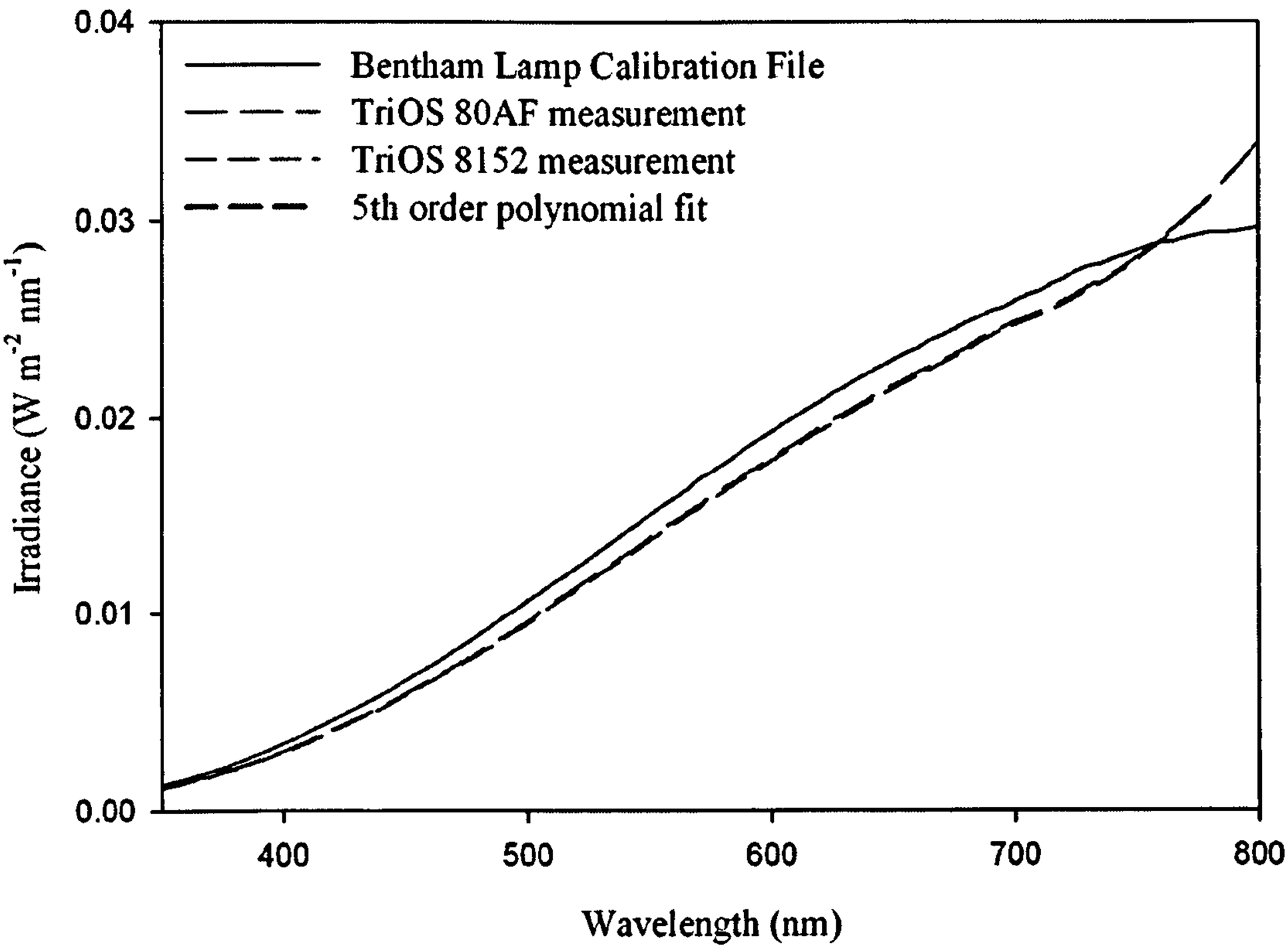

Figure 3.2. Comparison between Bentham standard lamp calibration file and the measured TriOS irradiance signal when sensors placed at r = 0.5m from lamp. TriOS sensors were recalibrated in the manufacturer's laboratory in 2005 to NIST standards. A 5th order polynomial function was fitted to the TriOS 8152 irradiance data and used to recalibrate the Bentham lamp.

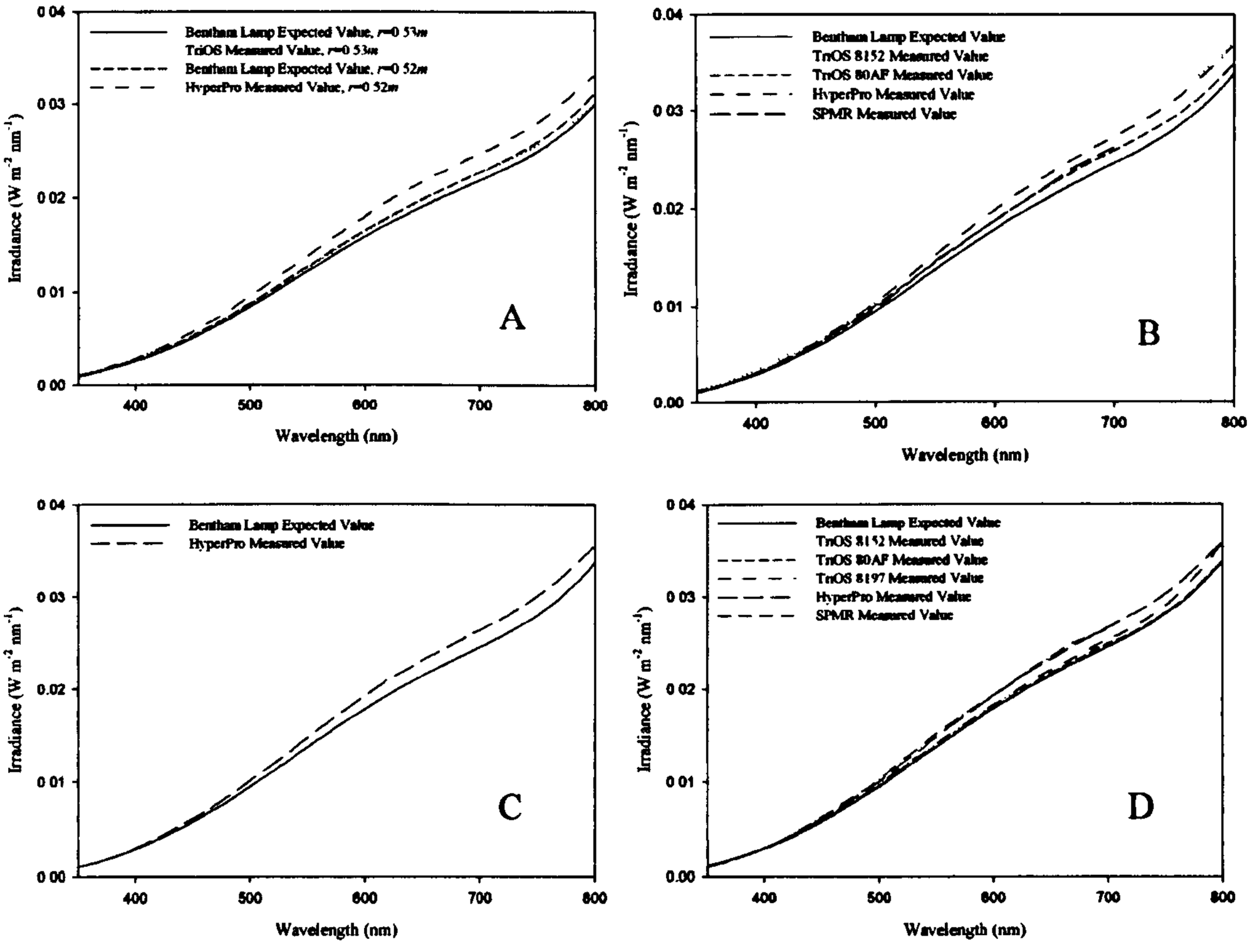

Figure 3.3. Irradiance sensor calibration for (A) Oban 2003, (B) Sound of Jura 2004, (C) AMT 15 and (D) Bristol Channel 2005. For the Oban 2003 calibration the distance between the sensor and lamp was $r=0.53m$ for the TriOS calibration and $r=0.52m$ for the HyperPro calibration, the expected Bentham lamp (see Figure 3.2) values were adjusted using equation (3.17). For all other cruise calibrations $r=0.5m$.

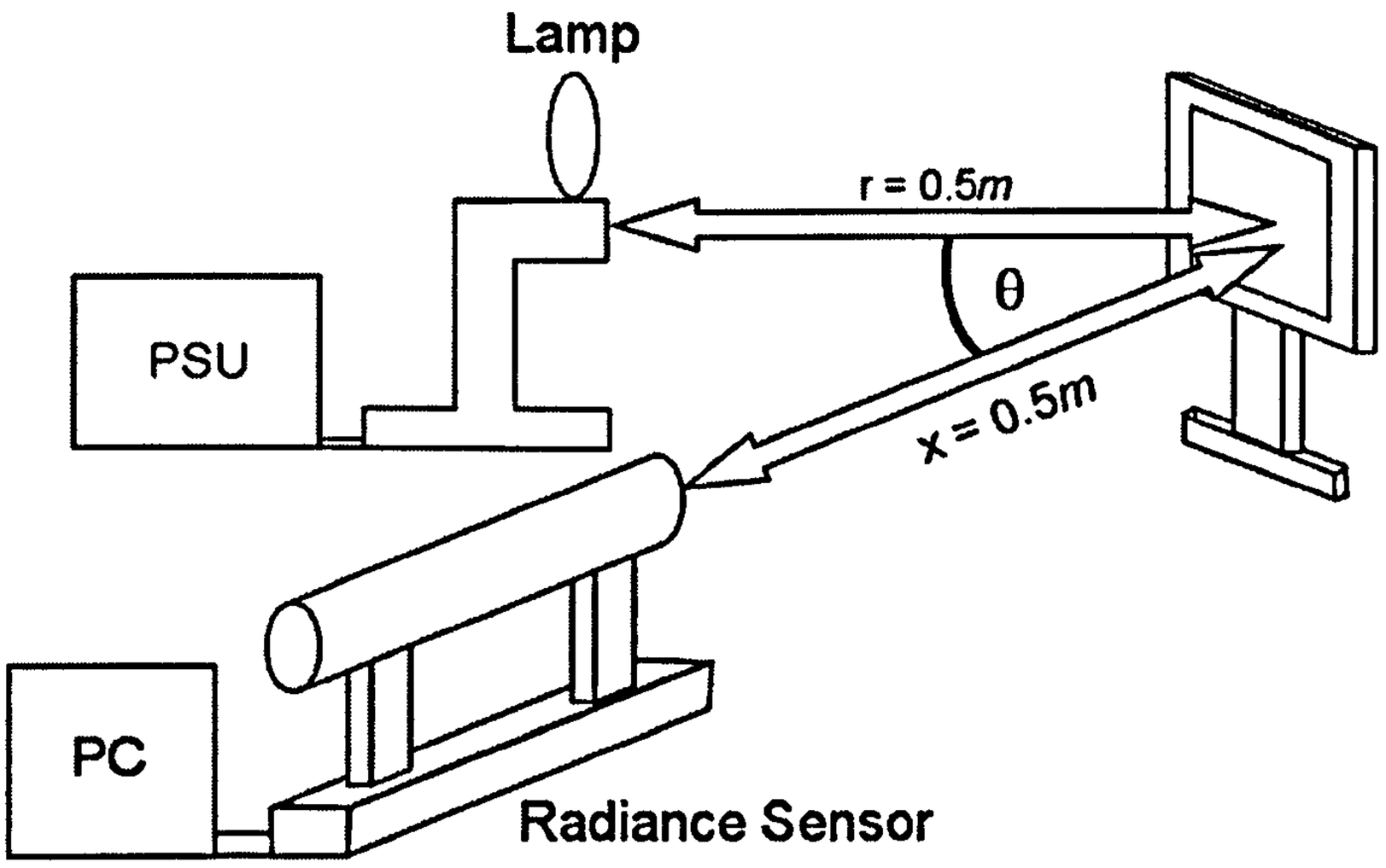

Figure 3.4. Radiance sensor calibration. The lamp and Spectralon plate were placed on the same optical axis 0.5*m* apart. The radiance sensor was then aligned to the centre of the Spectralon plate and the lamp was allowed to stabilize for 30 minutes prior to any measurement being carried out.

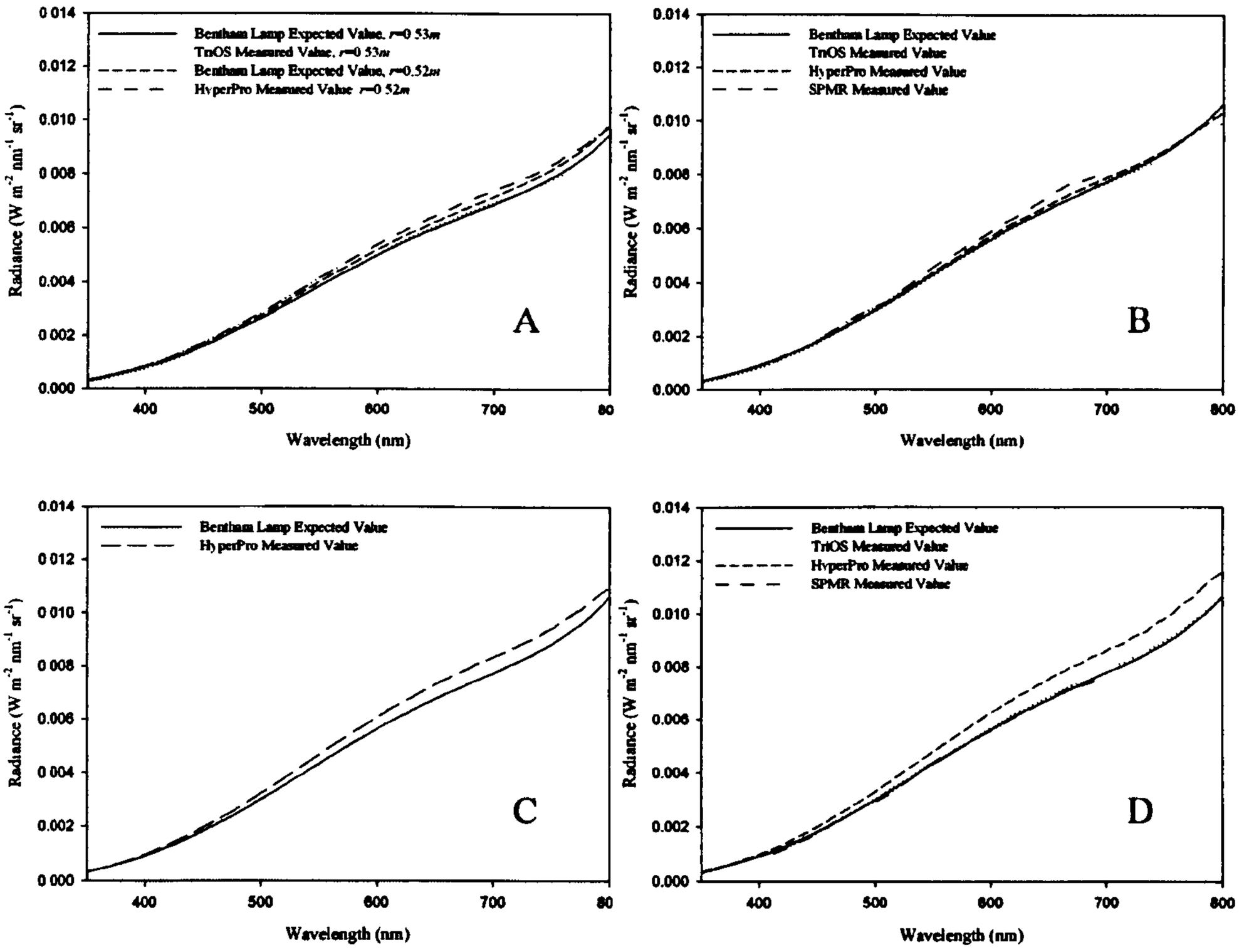

Figure 3.5. Radiance sensor calibration for (A) Oban 2003, (B) Sound of Jura 2004, (C) AMT 15 and (D) Bristol Channel 2005. The expected radiance values were obtained by substituting the expected lamp irradiance values into equation (3.19). For the Oban 2003 calibration the distance between the sensor and lamp was $r=0.53m$ for the TriOS calibration and $r=0.52m$ for the HyperPro calibration, the expected Bentham lamp values were adjusted using equation (3.17) before being substituted into equation (3.19). For all other cruise calibrations $r=0.5m$.

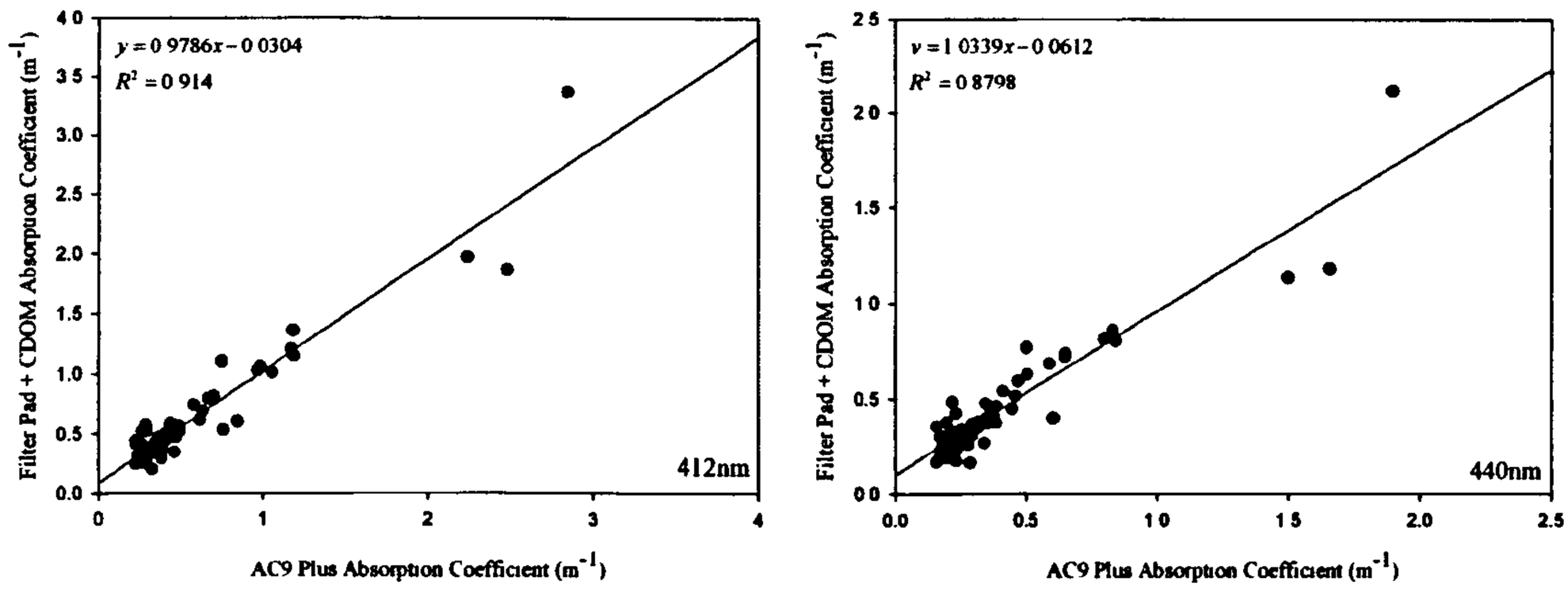

Figure 3.6. (i) Pathlength amplification factor for West of Scotland coastal waters. The above diagrams show the regression achieved when filter pad plus CDOM absorption values were plotted against AC9 absorption measured *in situ*. The filter pad measurements have the Bricaud and Stramski (1990) expression, $\beta(\lambda)=1.63\left[OD_f(\lambda)\right]^{-0.22}$, applied to correct for the effect of pathlength amplification within the filter.

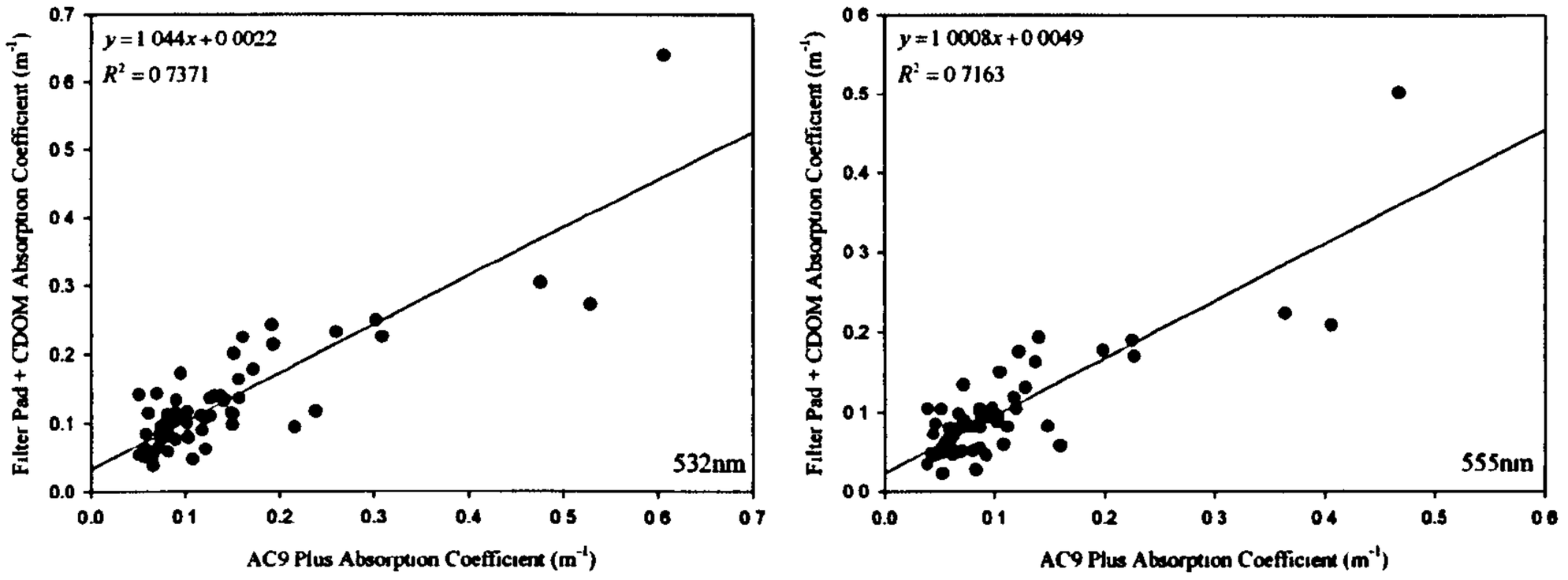

Figure 3.6. (ii). Pathlength amplification factor for West of Scotland coastal waters. The above diagrams show the regression achieved when filter pad plus CDOM absorption were plotted against AC9 absorption measured *in situ*. The filter pad measurements have the Bricaud and Stramski (1990) expression, $\beta(\lambda)=1.63\left[OD_f(\lambda)\right]^{-0.22}$, applied to correct for the effect of pathlength amplification within the filter.

Chapter 4: Cruise Schedule, Field Measurements and Distribution of In-water Constituents

Field data were collected on five research cruises between April 2003 and May 2005. Cruises were carried out in the coastal waters of the West of Scotland, the Irish Sea and the Bristol Channel. In addition participation in an Atlantic Meridional Transect (AMT) cruise was made possible by an invitation from Dr Samantha Lavender, University of Plymouth.

This chapter includes a description of the instruments deployed and a discussion of the methodology used to obtain hyperspectral radiometry measurements for each research cruise. The distribution of the concentrations of the optically significant seawater components (chlorophyll, suspended particulate matter and CDOM) is also discussed.

4. 1. Cruise 1 - Oban, April 2003

The first research cruise consisted of a four day survey carried out onboard the *RV Calanus* between the 22nd and 25th of April 2003. Figure 4.1 illustrates the location of stations sampled during this cruise. An instrument cage containing a Sea-Bird CTD, HOBI Labs HydroScat-2, WET Labs AC9 and AC9 Plus was deployed in profiling mode to measure the hydrographic and inherent optical properties of the water column. The AC9 had a $0.2\,\mu m$ filter attached to its input to remove particulate matter and allow the absorption due to coloured dissolved organic matter (CDOM) to be measured. The AC9 Plus was deployed in its normal configuration to measure absorption relative to water $(a_{tot} - a_w)$. The underwater light field was measured using the Satlantic HyperPro, which profiled downwelling irradiance

(E_d) and upwelling radiance(L_u), and a raft containing two TriOS hyperspectral radiometers, measuring downwelling irradiance just above the surface, $E_d(0^+)$, and upwelling radiance just below the surface, $L_u(0^-)$. Filter pad and CDOM absorptions were measured along with chlorophyll and suspended particulate matter (SPM) concentrations. SPM measurements were used to quantify the total, mineral and organic suspended solid concentrations occurring in the water body. Table 4.1 contains information on the station conditions and Table 4.6 on the instrumentation deployed and water samples recorded during this field trip.

The AC9Plus was used to measure particulate and dissolved absorption *in situ* and the AC9 was used to measure absorption by CDOM. It was found that the AC9 absorption measurements did not compare well with the spectrophotometer measurements of CDOM. The filter attached to the AC9 input appeared to create a problem with bubbles becoming trapped in the flow tubes and having a detrimental effect on the absorption and attenuation measurements made. The TriOS radiometers were used to measure hyperspectral $E_d(0^+)$ and $L_u(0^-)$ as no depth sensor was available at the time these measurements were conducted. The HyperPro was used as a freefalling instrument to obtain hyperspectral profiles of E_d and L_u in the water column.

4. 2. Cruise 2 - Oban, April 2004

This cruise involved three days of sampling onboard the *RV Seol Mara* between the 14th and 16th of April 2004. Stations sampled during this cruise are illustrated in Figure 4.2. The instrument cage deployed contained a Sea-Bird CTD, HydroScat-2 and AC9 Plus. On this cruise the TriOS raft system included an additional hyperspectral radiometer that measured upwelling irradiance just below the sea surface $\left(E_u(0^-)\right)$ in addition to $E_d(0^+)$ and $L_u(0^-)$. Filter pad absorption, CDOM absorption, chlorophyll and SPM concentration measurements were carried out for all stations sampled during this cruise. Table 4.2 list the conditions on station and Table 4.6 lists the measurements conducted.

The TriOS radiometers were chosen as the aim of this research cruise was to obtain water leaving remote sensing reflectance, $R_{rs}(0^+)$, spectra which contained the chlorophyll fluorescence signal.

4. 3. Cruise 3 – Sound of Jura, June 2004

Four days sampling in the Sound of Jura and Oban areas were carried out onboard the *RV Calanus* from the 21st to 25th of June 2004. Figure 4.3 illustrates the locations of the stations sampled during this cruise. As with previous cruises, an instrument cage was deployed in profiling mode to measure hydrographic and optical properties of the water column. The instrument cage contained a Sea-Bird CTD, HydroScat-2 and AC9 Plus. In addition to the cage, two profiling radiometers and the TriOS floating radiometric system were also deployed. The SeaWiFS Profiling Multi-channel Radiometer (SPMR), which measures E_d and L_u over seven wavebands, was used to profile the *in situ* light field. The TriOS raft system enabled hyperspectral measurements of subsurface E_u and L_u to be obtained, in addition to above surface measurements of E_d. Table 4.3 lists the conditions on station and Table 4.6 lists the instrumentation deployed and the sample analysis conducted.

During the Oban 2003 cruise the lead weight on the HyperPro was adjusted and extra drag added in order to control the drop velocity of the instrument and allow it a long enough time period to sample the light field. On this cruise the HyperPro was lowered to a fixed depth using the winch and held there for a period of time long enough for the light field to be well sampled. This method of deploying the HyperPro was more time consuming than using the instrument as a free falling profiler and resulted in fewer depths being sampled. As a result the SPMR was used to obtain freefalling profiles of the light field *in situ*, though this only provided radiometric data over seven wavebands.

4. 4. Cruise 4 - AMT 15, September-October 2004

The AMT programme is an ongoing series of National Environment Research Council (NERC) funded research cruises which take place biannually. The AMT programme aims to quantify the nature and causes of the ecological and biogeochemical variability in the planktonic ecosystems of the temperate and tropical Atlantic Ocean (Rees, 2004). It is hoped that the research carried out will enable scientists to investigate the long term variability of ocean biogeochemistry in order to help predict future climate and understand climate change. The AMT programme involves work on several areas of oceanography (including the structure of planktonic ecosystems, nutrient uptake, and atmosphere-ocean exchange), the work we were involved in on AMT 15 was aimed at determining *in situ* optical properties, pigment composition and photosynthetic parameters.

AMT 15 was conducted onboard the *RRS Discovery* with measurements recorded between the 19th of September and the 27th of October 2004. The cruise track for AMT 15 is illustrated in Figure 4.4.

During this cruise an optics instrument cage was deployed which contained a Sea-Bird CTD, WET Labs AC9 Plus and VSF-3 and two Satlantic radiometric sensors. In addition the Satlantic HyperPro was deployed as a surface floating radiometric system measuring $E_d(0^+)$ and $L_u(0^-)$. Seawater samples were collected from the CTD rosette to provide filter pad absorption and chlorophyll concentration data. The station conditions, instrumentation deployed and water samples collected are listed in Table 4.4 and Table 4.6.

The HyperPro was modified for use as a surface floating system on AMT 15 by adding two cylindrical floats between the fins. The HyperPro was chosen instead of the TriOS raft system as it could be deployed by hand, whereas the TriOS raft system required the use of a winch, and the time on station was limited due to the distances covered on this cruise.

4. 5. Cruise 5 – The Bristol Channel, April-May 2005

The final research cruise was carried out between the 29th of April and 3rd of May 2005 in the turbid waters of the Bristol Channel onboard the *RV Prince Madog*. As with previous cruises an instrument cage was deployed from the stern of the ship to profile the optical and hydrographical properties of the water column. The instrument cage contained the Sea-Bird CTD, HydroScat-2 and AC9. The HyperPro was deployed as a surface floating system and measured $E_d(0^+)$ and $L_u(0^-)$. Profiling measurements of the *in situ* light field were obtained using the SPMR. The TriOS system was modified to include a downwelling scalar irradiance (E_{od}) sensor in addition to the three hyperspectral sensors deployed during the Sound of Jura and Oban 2004 cruises. On this cruise the TriOS radiometers were deployed using a winch to lower the system to a fixed depth where it was held for a period of time to sample the light field. Filter pad absorption, CDOM absorption and chlorophyll concentration were sampled and analysed onboard. SPM measurements were also conducted, with samples being frozen for analysis in the laboratory at the University of Strathclyde. Figure 4.5 illustrates the station locations, Table 4.5 lists the station conditions and Table 4.6 lists the measurements made during the cruise.

On this cruise it was decided that the HyperPro would be deployed as a surface floating radiometer due to its successful deployment in this manner on AMT 15. This allowed the TriOS radiometers, which now included a downwelling scalar irradiance sensor (E_{od}) and a L_u radiometer with a depth sensor (provided courtesy of Dr Samantha Lavender, University of Plymouth), to be deployed in the method used for the HyperPro during the Sound of Jura 2004 cruise. Deploying the TriOS instruments in this manner increased the amount of radiometric data gathered on the underwater light field. As with the Sound of Jura cruise this method of deployment is time consuming and allows fewer depths to be sampled. Again the SPMR was used to obtain freefalling profiles of the light field over seven wavebands.

4. 6. Hyperspectral Sampling

During the research cruises hyperspectral radiometric measurements were made either at the sea surface or in profiling mode. There were a number of issues that had to be addressed whilst recording hyperspectral data. Where the TriOS raft system was used (Oban 2003, Oban 2004 and the Sound of Jura 2004) the raft was deployed a distance of at least 15m from the ship to ensure that the ships shadow did not cover the radiometers. Similarly on AMT 15 and the Bristol Channel cruises the floating HyperPro had to be deployed at least 15m from the ship to avoid ship shadowing effects. On these cruises the buoyancy of the HyperPro was adjusted so that the L_u sensor remained submerged whilst the E_d sensor remained above surface. It was necessary to also ensure that the tilt angle of the HyperPro remained within acceptable limits $\left(\pm 10^0\right)$, and any data measured outside this tilt limit was removed using the processing software. Using the HyperPro as a freefalling radiometer meant that the drop velocity of the instrument had to be slow enough to allow the sensor to sample the light field at depth z, i.e. the integration time had to be suitable for the light levels being sampled. The drop velocity of the instrument was controlled by adjusting a lead weight attached to the bottom of the HyperPro and adding extra drag using a plastic funnel. In the Sound of Jura 2004 and Bristol Channel 2005 the HyperPro and TriOS radiometers were lowered to a fixed depth using a winch and held there for a period of time to sample the light field, e.g. the integration time was optimized. Problems associated with this method of recording hyperspectral radiometry included near surface measurements being conducted in ship shadow, the roll of the boat changing the depth at which the instruments were being held and tilt effects. These effects were reduced as much as possible by making measurements in direct sunlight (i.e. positioning the ship for best instrument deployment) and attaching a heavy weight to the instrument to hold it vertical in the water. The pressure sensor readings also allowed the depth at which the instrument was being held to be monitored. The data retrieved by the instruments was quality controlled and any spurious measurements were removed.

4. 7. Distribution of In-water Constituents for Cruises Conducted

Before examining the relationships between the optical parameters and sea water constituents (chlorophyll, CDOM and TSS) the distribution of these constituents, sampled at a depth of 1m, for the research cruises conducted is discussed.

4. 7. 1. Distribution of Chlorophyll for Coastal Water Cruises

Figure 4.6 illustrates histograms of the distribution of chlorophyll concentrations. The Oban 2003 and 2004 cruises had chlorophyll concentrations, ranging from 1 to $10.5 mg\,m^{-3}$. The Oban 2003 cruise contained the highest concentration of chlorophyll sampled during this research project, $10.5 mg\,m^{-3}$. Both cruises were conducted around the time of the spring phytoplankton bloom in the West of Scotland sea lochs. The Sound of Jura chlorophyll values varied between 0.7 and $4 mg\,m^{-3}$ with only one station sampled having a concentration greater than $5 mg\,m^{-3}$. In the Bristol Channel only a handful of stations had a chlorophyll concentration greater than $1 mg\,m^{-3}$, with the vast majority of stations having low chlorophyll concentrations, ranging between 0.2 and $1 mg\,m^{-3}$.

4. 7. 2. Distribution of CDOM for Coastal Water Cruises

Figure 4.7 illustrates the distribution of CDOM (absorption values measured at 440nm) for (A) Oban 2003, (B) Oban 2004, (C) the Sound of Jura 2004 and (D) the Bristol Channel 2005. The Oban 2004 cruise had a wide range of CDOM concentrations with five of the stations sampled having concentrations in excess of $1 m^{-1}$. These stations occurred in Loch Creran, a Scottish fjord. The Oban 2003 stations ranged between 0.2 and $0.8 m^{-1}$, with the majority of stations having values more typical of shelf sea conditions $\left(\leq 0.6 m^{-1}\right)$. The Sound of Jura stations also had CDOM values more typical of shelf sea waters, ranging between 0.1 and $0.4 m^{-1}$.

Finally it was observed that the Bristol Channel had low CDOM values with the vast majority of stations sampled having an $a(440)$ less than $0.2 m^{-1}$.

4. 7. 3. Distribution of TSS for Coastal Water Cruises

Figure 4.8, the histograms of TSS, revealed that the Oban 2003, Oban 2004 and Sound of Jura 2004 cruises all had typical shelf sea TSS values, ranging between 2 and $4 mg l^{-1}$. However, the Bristol Channel TSS concentrations had a much wider range of values with only five of the stations sampled having TSS less than $5 mg l^{-1}$, and the majority of stations having values in excess of $10 mg l^{-1}$. The highest value recorded on this cruise was $38.6 mg l^{-1}$.

4. 7. 4. AMT 15 Concentrations

On the AMT 15 cruise it was found that, with the exception of the station sampled in the North African Upwelling, the surface chlorophyll concentration ranged between 0.01 and $1 mg m^{-3}$ (Figure 4.9). Low chlorophyll concentrations in the surface layer were expected for clear oceanic water. The station sampled in the North African Upwelling had a chlorophyll concentration of $4.5 mg m^{-3}$.

Unfortunately no data was available on the CDOM and TSS concentrations for the AMT 15 cruise.

4. 7. 5. Summary of the Distribution of In-water Constituents

The Oban 2003 and 2004 cruises had the broadest range of chlorophyll and CDOM concentrations, with the highest concentrations of each component occurring during these cruises. They also tended to have a narrow range of TSS, generally between 2 and $3 mg l^{-1}$. The Sound of Jura cruise contained stations that were more typical of shelf sea conditions, with chlorophyll ranging between 0.7 and $4 mg m^{-3}$, CDOM between 0.1 and $0.4 m^{-1}$, and TSS values generally between 3 and $4 mg l^{-1}$. The

Bristol Channel cruise was distinguished by high and varied levels of TSS and by low levels of chlorophyll and CDOM.

The AMT 15 cruise, with the exception of the upwelling station, was marked by the absence of chlorophyll in the surface layer with values less than $1 mg\,m^{-3}$, typical of open ocean conditions.

4. 8. Cluster Analysis of In-water Constituents

In the previous section the distribution of constituent material, sampled at a depth of 1m, was discussed. The cluster analysis feature of the Data Desk software programme was used to investigate whether any distinct clusters existed within the constituent concentrations for the coastal water dataset. Cluster analysis is an exploratory data analysis tool which organises observations into groups whose members share properties in common. These groups may or may not be of use for classifying objects. It is important to note that cluster analysis simply discovers structure in data but does not explain why it exists.

4. 8. 1. Constituent Concentration Cluster Analysis

As there were three constituents to consider (chlorophyll, CDOM and TSS) it was useful to imagine the data as existing as a cube, with the $\log_{10}$ transform of each of the constituent concentrations running down the x, y and z axes. Panels (A) to (C) of Figure 4.10 illustrate the three faces of the data cube. Panel (D) shows a tree diagram, obtained by performing cluster analysis, using Data Desk, on the three in-water constituents, in which a high level bifurcation can be seen. Marking data points according to the cluster analysis allowed the position of the clusters on the plots of the in-water constituents to be examined. Histograms of constituent concentration were plotted for the high level double cluster occurring in Figure 4.10 panel (D). Figure 4.11 illustrates the histograms for the cluster coloured blue in the tree diagram. From this figure it can be seen that the vast majority of stations (95%) had a TSS $\leq 4 mg\,l^{-1}$. There was a wide spread of CDOM and chlorophyll concentrations, though the majority of chlorophyll concentrations (89%) tended to be

$\geq 3 mg\, m^{-3}$. This cluster corresponded to low TSS water with higher chlorophyll concentrations and a wide variety of CDOM levels. Figure 4.12 illustrates histograms of constituent concentrations for the points coloured red in the tree diagram (Figure 4.10 panel (D)). These histograms revealed that 94% of stations in this cluster had a TSS $\geq 4 mg\, l^{-1}$. TSS concentration for this cluster tended to be high and varied, ranging up to $38.6 mg\, l^{-1}$. The CDOM and chlorophyll concentrations were low and had a tight distribution compared with the previous cluster. CDOM values remained below $0.4 m^{-1}$, with 80% of stations have a value $\leq 0.2 m^{-1}$. Chlorophyll concentrations also remained low $\left(\leq 3 mg\, m^{-3}\right)$ with 94% of stations having a concentration $\leq 2 mg\, m^{-3}$. The points coloured red on the tree diagram tended to be higher TSS stations with low levels of chlorophyll and CDOM. Points corresponding to higher levels of TSS mainly originated from the Bristol Channel 2005 cruise with the exception of six stations from the Sound of Jura. For the data points coloured blue on the tree diagram stations came from the West coast of Scotland cruises, with only one station coming from the Bristol Channel.

Cluster analysis of the in-water constituents revealed there was a tendency to have either (a) low TSS water with higher concentrations of chlorophyll and varied levels of CDOM or (b) higher TSS water with low levels of chlorophyll and CDOM. It appeared that the concentration of TSS was an important factor in clustering the stations but was not the sole contributing factor as the chlorophyll concentration also appeared to influence the clustering.

4. 8. 2. Hyperspectral $R_{rs}\left(0^{+}\right)$ Spectra of Constituent Clusters

In the previous section two constituent clusters were identified. Using the bifurcation in the cluster analysis it was possible to plot the hyperspectral $R_{rs}\left(0^{+}\right)$ spectra of the stations occurring in each of the clusters. This allowed the similarity and discrepancies in the spectra to be assessed.

Figure 4.13 illustrates the hyperspectral $R_{rs}\left(0^{+}\right)$ spectra for the two clusters. In panel (A) a fluorescence peak occurred which was consistent with the fact that this

cluster contained stations with higher chlorophyll concentrations. In panel (B) the fluorescence peak was not observed, however, the higher reflectance values after 600nm indicated the presence of turbid water with higher concentrations of TSS. Comparison of the two panels showed that the magnitude of the spectra in panel (A) was smaller compared to those contained in panel (B), illustrating that the magnitude of the spectra was driven by TSS.

Figure 4.14 contains histograms of the normalisation factors of the hyperspectral $R_{rs}(0^+)$ spectra, the normalisation factors being the maximum reflectance value for each spectrum and therefore indicative of the magnitude of the $R_{rs}(0^+)$ spectra. Comparison of the normalisation factors for the clusters revealed that the majority (95%) of stations in the low TSS cluster had a normalisation factor $\leq 0.003 sr^{-1}$, whereas in the high TSS cluster the majority of stations (94%) had a normalisation factor $\geq 0.004 sr^{-1}$. Figure 4.15 illustrates the results of normalising the spectra for the two clusters identified in the cluster analysis. In panel (A) the fluorescence peak occurred, in panel (B) the peak was missing but the raised section after 600nm was still evident.

In Figure 4.13, the hyperspectral $R_{rs}(0^+)$ spectra, there appeared to be a number of interesting features. The increase in reflectance signal after 600nm seemed to be driven by TSS. Figure 4.16 illustrates the relationship between $R_{rs}(0^+, 650nm)$ and the concentration of TSS. It can be seen that as the concentration of TSS increased the value of $R_{rs}(0^+, 650nm)$ also tended to increase. This was in keeping with findings of Binding *et al* (2003) who showed that the reflectance at 665nm was related to MSS concentration (see also Binding *et al*, 2005). However, the spectral region under 550nm in Figure 4.13 was more complicated. Normalising the spectra helped remove some of this complexity and allowed the spectral shape to be investigated. The spectral shape of normalised modelled and field spectra will be discussed in a future chapter.

4. 9. Summary

a. Five research cruises were conducted in a variety of water types. Three of these cruises were carried out in the coastal waters of the West of Scotland. The turbid, sediment dominated waters of the Bristol Channel were also sampled as were the clear oceanic waters of the Atlantic Ocean and the highly productive North African Upwelling.

b. *In situ* inherent optical properties and radiometry were obtained by deploying a range of instrumentation. Information on the seawater constituents was gathered by determining the chlorophyll, SPM and CDOM concentrations and by filter pad absorption measurements.

c. A great amount of time and effort was invested in obtaining good quality hyperspectral radiometric data. From the instrumentation deployed it became apparent that hyperspectral surface data could be successfully recorded, however, the collection of hyperspectral radiometric profiles proved to be problematic. Freefalling hyperspectral profiles were of low quality and different methods of deploying hyperspectral instruments at depth were tested. It was found that the low sensitivity of these instruments meant that they required a relatively long integration time to adequately sample the light field.

d. The Oban 2003 and 2004 cruises had a wide range of chlorophyll concentrations, typically between 1 and $10 mg\,m^{-3}$. The majority of Sound of Jura 2004 chlorophyll values ranged between 0.7 and $4 mg\,m^{-3}$. The Bristol Channel cruise was found to have low chlorophyll values, typically between 0.2 and $2 mg\,m^{-3}$. The Oban 2003 cruise had CDOM concentrations ranging between 0.2 and $0.8 m^{-1}$, while the Oban 2004 cruise had the widest range of CDOM values (0.1 to $2 m^{-1}$) and the highest CDOM concentration recorded. The Sound of Jura CDOM values were more typical of shelf sea conditions being typically less than $0.4 m^{-1}$. The Bristol Channel was also found to have

lower CDOM levels, again ranging between 0.04 and $0.4 m^{-1}$. However, the Bristol Channel did have the highest and most varied range of TSS with values ranging between 4.2 and $40 mg l^{-1}$. The Oban 2003, Oban 2004 and Sound of Jura 2004 cruises were found to have TSS ranges lying between 1 and $6 mg l^{-1}$.

e. Cluster analysis revealed that water types tended to fall into one of two categories, either (a) low levels of TSS with higher concentrations of chlorophyll and varied levels of CDOM or (b) higher levels of TSS with lower concentrations of chlorophyll and CDOM.

f. The dataset would have been improved by the inclusion of high chlorophyll waters. However, the water types sampled were limited by the availability of the research vessels.

g. The magnitude of $R_{rs}(0^+)$ spectra appeared to be driven by TSS. Normalising spectra by their peak value removed some of the complexity viewed in the hyperspectral $R_{rs}(0^+)$ spectra and will allow investigation into the spectral shape to be conducted.

STATION	DATE	TIME ON (GMT)	DEPTH (M)	CONDITIONS
1	22/04/03	11:10	110	$\frac{9}{10}$, overcast, raining, no wind, flat calm
2	22/04/03	13:28	89	$\frac{5}{10}$, bright, some direct beam, wind 5 knots, small ripples
3	22/04/03	15:07		$\frac{10}{10}$, diffuse, wind 3 knots, small waves
4	23/04/03	08:33	30	$\frac{0}{10}$, clear blue, direct sun, slight haze, no wind, flat calm
5	23/04/03	09;40	50	$\frac{0}{10}$, clear blue, direct sun, slight haze, wind 0.3 knots, flat
6	23/04/03	10:57	27	$\frac{1}{10}$, direct sun, wind 2.6 knots, small ripples
7	23/04/03	12:46	36	$\frac{0}{10}$, clear blues, direct beam, no wind, flat, glass like surface
8	23/04/03	13;47	72	$\frac{0}{10}$, clear blue, direct beam, wind 0.6 knots, flat, glass like surface
9	24/04/03	08:33	52	$\frac{0}{10}$, clear blue, direct beam, wind 8 knots, small ripples
10	24/04/03	09:55	60	High broken cloud, wind 5 knots, ripples
11	24/04/03	11:09	58	High cloud, direct beam, wind 2.5 knots, small ripples
12	24/04/03	12:50	130	Broken cloud, direct beam, wind 5 knots, ripples
13	24/04/03	13:55	106	Patchy cloud, direct beam, wind 6 knots, ripples
14	25/04/03	09:42	40	$\frac{10}{10}$, diffuse, raining, wind 9 knots, ripples
15	25/04/03	10:48	84	$\frac{10}{10}$, dull, diffuse, wind 9 knots, small waves
16	25/04/03	12:25	47	$\frac{10}{10}$, diffuse, wind 9 knots, small waves
17	25/04/03	13:30	30	$\frac{10}{10}$, dull, diffuse, wind 7 knots, ripples

Table 4.1. Cruise 1 – Oban, April 2003. The table contains information on the date and time at which the station was sampled, the depth of water and weather conditions (fractional cloud cover, general weather, wind speed and sea surface state).

STATION	DATE	TIME ON (GMT)	DEPTH (M)	CONDITIONS
1	14/04/04	10:20	20	$\frac{9}{10}$, full cloud cover, diffuse, wind 18 knots, ripples
2	14/04/04	11:20	30	$\frac{10}{10}$, full cloud cover, diffuse, wind 12 knots, ripples
3	14/04/04	12:05	7	$\frac{8}{10}$, overcast, diffuse, wind 4 knots, calm
4	14/04/04	13:10	40	$\frac{8}{10}$, overcast, diffuse, wind 10 knots, calm
5	14/04/04	13:40	34	$\frac{9}{10}$, diffuse, showers, wind 14 knots, small waves
6	14/04/04	14:20	40	$\frac{10}{10}$, diffuse, showers, wind 5 knots, ripples
7	15/04/04	10:30	23	$\frac{10}{10}$, complete cloud cover, wind 0.8 knots, calm
8	15/04/04	11:50	22	$\frac{10}{10}$, complete cloud cover, wind 7 knots, calm
9	15/04/04	12:15	50	$\frac{10}{10}$, diffuse, showers, wind 4 knots, calm
10	15/04/04	13:00	33	$\frac{10}{10}$, complete cloud cover, diffuse, wind 1 knot, ripples
11	15/04/04	14:00	51	$\frac{10}{10}$, complete cloud cover, diffuse, wind 1 knot, ripples
12	16/04/04	08:55	50	$\frac{4}{10}$, direct beam, some cloud, wind 3.5 knots, ripples
13	16/04/04	10:20	26	$\frac{4}{10}$, direct beam, some cloud, wind 9 knots, calm
14	16/04/04	10:55	48	$\frac{4}{10}$, direct beam, some cloud, wind 6.5 knots, calm

Table 4.2. Cruise 2 – Oban, April 2004. The table contains information on the date and time at which the station was sampled, the depth of water and weather conditions (fractional cloud cover, general weather, wind speed and sea surface state).

STATION	DATE	TIME ON (GMT)	DEPTH (M)	CONDITIONS
1	21/06/04	11:10	87	$\frac{3}{10}$, direct sun, wind 0.6 knots, calm
2	21/06/04	13:55	168	$\frac{3}{10}$, direct sun, wind 2 knots, calm
3	21/06/04	16:56	186	$\frac{3}{10}$, direct sun, wind 11 knots, small ripples
4	22/06/04	07:50	150	$\frac{1}{10}$, clear blue sky, direct beam, wind 1.4 knots, calm
5	22/06/04	09:25	120	$\frac{1}{10}$, clear blue sky, direct beam, wind 1 knot, calm
6	22/06/04	11:10	85	$\frac{4}{10}$, some cloud, direct beam, wind 3.5 knots, calm
7	22/06/04	12:55	80	$\frac{6}{10}$, some cloud, direct and diffuse light, wind 11 knots, small ripples
8	22/06/04	15:50	40	$\frac{5}{10}$, cloud, direct and diffuse light, wind 0.7 knots, calm
9	23/06/04	09:40	23	$\frac{10}{10}$, diffuse light, wind 16.5 knots, small ripples
10	23/06/04	10:33	40	$\frac{10}{10}$, raining, diffuse, wind 19 knots, small waves
11	23/06/04	11:25	70	$\frac{10}{10}$, raining, diffuse, wind 22 knots, small waves
12	24/06/04	08:10	40	$\frac{10}{10}$, raining, diffuse, wind 10 knots, calm
13	24/06/04	09:10	40	$\frac{10}{10}$, diffuse light, wind 16 knots, ripples
14	24/06/04	10:40	25	$\frac{10}{10}$, diffuse light, wind 12 knots, calm
15	24/06/04	11:40	50	$\frac{10}{10}$, raining, diffuse, wind 9 knots, small ripples
16	24/06/04	13:00	14	$\frac{10}{10}$, diffuse light, wind 12.5 knots, calm
17	24/06/04	14:50	42	$\frac{10}{10}$, diffuse light, wind 12.5 knots, calm
18	25/06/04	08:15	37	$\frac{2}{10}$, blue sky, direct beam, wind 7.5 knots, small ripples
19	25/06/04	09:10	36	$\frac{3}{10}$, direct beam, wind 3.5 knots, small ripples
20	25/06/04	10:05	69	$\frac{4}{10}$, some cloud, direct beam, wind 6 knots, small ripples

STATION	DATE	TIME ON (GMT)	DEPTH (M)	CONDITIONS
21	21/06/04	11:00	26	$\frac{6}{10}$, some cloud, direct and diffuse light wind 6.5 knots, calm
22	21/06/04	12:10	40	$\frac{6}{10}$, some cloud, direct and diffuse light wind 7 knots, calm
23	21/06/04	13:20	35	$\frac{5}{10}$, direct beam, wind 10.5 knots, small ripples

Table 4.3. Cruise 3 - Sound of Jura, June 2004. The table contains information on the date and time at which the station was sampled, the depth of water and weather conditions (fractional cloud cover, general weather, wind speed and sea surface state).

STATION	DATE	TIME ON (GMT)	DEPTH (M)	CONDITIONS
2	19/09/04	10:00	175	$\frac{7}{10}$, direct and diffuse light, waves,
5	21/09/04	11:00	4796	$\frac{8}{10}$, diffuse light, small waves
7	22/09/04	11:00	4062	$\frac{10}{10}$, diffuse light, small waves
9	23/09/04	11:00	2183	$\frac{10}{10}$, diffuse light, small waves
11	24/09/04	11:00	4050	$\frac{3}{10}$, high cloud, direct beam, small waves
13	25/09/04	11:00	5187	$\frac{2}{10}$, blue sky, direct beam, small ripples
15	26/09/04	11:05	4724	$\frac{4}{10}$, direct and diffuse light, small waves
17	28/09/04	11:00	3850	$\frac{3}{10}$, direct beam, small waves
19	29/09/04	11:00	4177	$\frac{5}{10}$, direct and diffuse light, small waves
21	30/09/04	12:00	66	$\frac{1}{10}$, clear blue sky, direct beam, some chop
24	01/10/04	11:30	3025	$\frac{1}{10}$, clear blue sky, direct beam, some chop
27	02/10/04	12:00	2716	$\frac{1}{10}$, clear blue sky, direct beam, flat calm
31	04/10/04	11:00	3734	$\frac{3}{10}$, direct beam, small waves
33	05/10/04	11:00	4696	$\frac{2}{10}$, blue sky, some haze, waves
35	06/10/04	11:00	4843	$\frac{4}{10}$, direct and diffuse light, some haze, calm
37	07/10/04	11:00	3387	$\frac{5}{10}$, direct and diffuse light, small waves
40	09/10/04	11:00	3115	$\frac{1}{10}$, clear blue sky, direct beam, small waves
42	10/10/04	11:00	3016	$\frac{2}{10}$, blue sky, direct beam, some chop
43	11/10/04	11:00	5296	$\frac{2}{10}$, blue sky, direct beam, small waves
47	13/10/04	11:00	6316	$\frac{2}{10}$, blue sky, direct beam, small waves
49	14/10/04	11:00	4997	$\frac{4}{10}$, direct and diffuse light, small waves

STATION	DATE	TIME ON (GMT)	DEPTH (M)	CONDITIONS
51	15/10/04	11:00	5179	$\frac{8}{10}$, diffuse light, small waves
53	16/10/04	10:00	5094	$\frac{4}{10}$, direct and diffuse light, small waves
55	17/10/04	11:00	4794	$\frac{3}{10}$, blue sky, direct beam, choppy
57	18/10/04	11:00	3749	$\frac{2}{10}$, blue sky, direct beam, small waves
59	19/10/04	11:00	3528	$\frac{4}{10}$, direct and diffuse light, small waves
61	20/10/04	11:00	4150	$\frac{5}{10}$, direct and diffuse light, calm
63	21/10/04	10:00	4441	$\frac{8}{10}$, diffuse light, calm
65	22/10/04	10:00	4306	$\frac{7}{10}$, diffuse light, calm
67	23/10/04	10:00	4060	$\frac{0}{10}$, blue sky, direct beam, calm
69	24/10/04	10:00	5131	$\frac{7}{10}$, diffuse light, calm
71	25/10/08	10:00	5378	$\frac{2}{10}$, blue sky, direct beam, big swell

Table 4.4. Cruise 4 - AMT 15, September/October 2004. The table contains information on the date and time at which the station was sampled, the depth of water and weather conditions (fractional cloud cover, general weather, wind speed and sea surface state).

STATION	DATE	TIME ON (GMT)	DEPTH (M)	CONDITIONS
1	29/04/05	08:32	43	$\frac{3}{10}$, high haze, clear, wind 9 knots, 2.5m swell
2	29/04/05	11:01	53	$\frac{6}{10}$, direct beam, wind 5.4 knots, 1.5m swell
3	29/04/05	12:59	58	$\frac{9}{10}$, high haze, wind 12.1 knots, 0.5m swell
4	29/04/05	14:55	73	$\frac{10}{10}$, fog, wind 11.6 knots, 1.5m swell
5	30/04/05	07:25	56	$\frac{10}{10}$, diffuse light, wind 7 knots, 0.5m swell
6	30/04/05	09:19	50	$\frac{9}{10}$, some direct beam, wind 6 knots, very small swell
7	30/04/05	11:15	44	$\frac{3}{10}$,direct beam, wind 3.5 knots, calm
8	30/04/05	12:54	36	$\frac{3}{10}$, high haze, clear overhead, direct beam, wind 4 knots, calm
9	30/04/05	14:30	36	$\frac{6}{10}$, high haze, direct beam, wind 6 knots, calm
10	30/04/05	16:09	25	$\frac{9}{10}$, diffuse light, wind 6.7 knots, calm
11	30/04/05	17:44	12	$\frac{9}{10}$, diffuse light, wind 4 knots, calm
12	01/05/05	07:23	24	$\frac{10}{10}$, raining, diffuse light, wind 2.7 knots, calm
13	01/05/05	08:39	32	$\frac{10}{10}$, diffuse light, wind 0.8 knots, calm
14	01/05/05	10:04	35	$\frac{10}{10}$, diffuse light, overcast, wind 3.6 knots, calm
15	01/05/05	11:22	38	$\frac{9}{10}$, brightening, wind 4.3 knots, calm
16	01/05/05	12:52	37	$\frac{9}{10}$, direct beam. wind 1 knot, calm
17	01/05/05	14:14	42	$\frac{8}{10}$, hazy, bright, wind 3.8 knots, calm
18	01/05/05	15:45	48	$\frac{9}{10}$, bright, direct beam, wind 3.5 knots, ripples, light swell
19	02/05/05	07:20	36	$\frac{2}{10}$, clear blue sky, direct beam, wind 5.7 knots, 1m swell
20	02/05/05	08:29	44	$\frac{2}{10}$, clear blue sky, direct beam, wind 5.5 knots, 0.5m swell
21	02/05/05	09:28	47	$\frac{10}{10}$, overcast, wind 5 knots, 0.5m swell

STATION	DATE	TIME ON (GMT)	DEPTH (M)	CONDITIONS
22	02/05/05	11:03	45	$\frac{9}{10}$, bright, wind 7.5 knots, 0.5m swell
23	02/05/05	12:07	44	$\frac{9}{10}$, bright, wind 12 knots, 0.5m swell
24	02/05/05	13:11	43	$\frac{9}{10}$, variable, wind 12 knots, 0.5m swell
25	02/05/05	14:36	29	$\frac{10}{10}$, overcast, wind 8 knots, 0.5m swell
26	02/05/05	15:57	41	$\frac{10}{10}$, overcast, wind 11 knots, 0.5m swell
27	03/05/05	07:59	35	$\frac{10}{10}$, overcast, wind 5.8 knots, 0.5m swell
28	03/05/05	09:25	41	$\frac{10}{10}$, overcast, wind 7.5 knots, 0.5m swell
29	03/05/05	11:17	41	$\frac{10}{10}$, overcast, brightening, wind 1.5 knots, 1m swell
30	03/05/05	13:00	56	$\frac{10}{10}$, overcast, brightening, wind 2.3 knots, 1m swell
31	03/05/05	14:30	51	$\frac{6}{10}$, direct beam, thin cloud, wind 7.5 knots, 1m swell
32	03/05/05	15:47	55	$\frac{6}{10}$, direct beam, wind 11.5 knots, 1m swell

Table 4.5. Cruise 5 - Bristol Channel, April/May 2005. The table contains information on the date and time at which the station was sampled, the depth of water and weather conditions (fractional cloud cover, general weather, wind speed and sea surface state).

CRUISE	INSTRUMENTATION DEPLOYED	WATER SAMPLE ANALYSIS
Oban, April 2003	AC9, AC9 Plus, CTD, HydroScat-2, HyperPro, TriOS	Filter pad and CDOM absorption, chlorophyll and SPM concentrations
Oban, April 2004	AC9 Plus, CTD, HydroScat-2, TriOS	Filter pad and CDOM absorption, chlorophyll and SPM concentrations
Sound of Jura, June 2004	AC9 Plus, CTD, HydroScat-2, SPMR, HyperPro, TriOS	Filter pad and CDOM absorption, chlorophyll and SPM concentrations
AMT 15, September/October 2004	AC9 Plus, CTD, Profiling Radiometers, HyperPro	Filter pad absorption and chlorophyll concentration
Bristol Channel, April/May 2005	AC9, CTD, HydroScat-2, SPMR, HyperPro, TriOS	Filer pad and CDOM absorption, chlorophyll and SPM concentrations

Table 4.6. Instrumentation deployed and water sample analyses performed for all cruises.

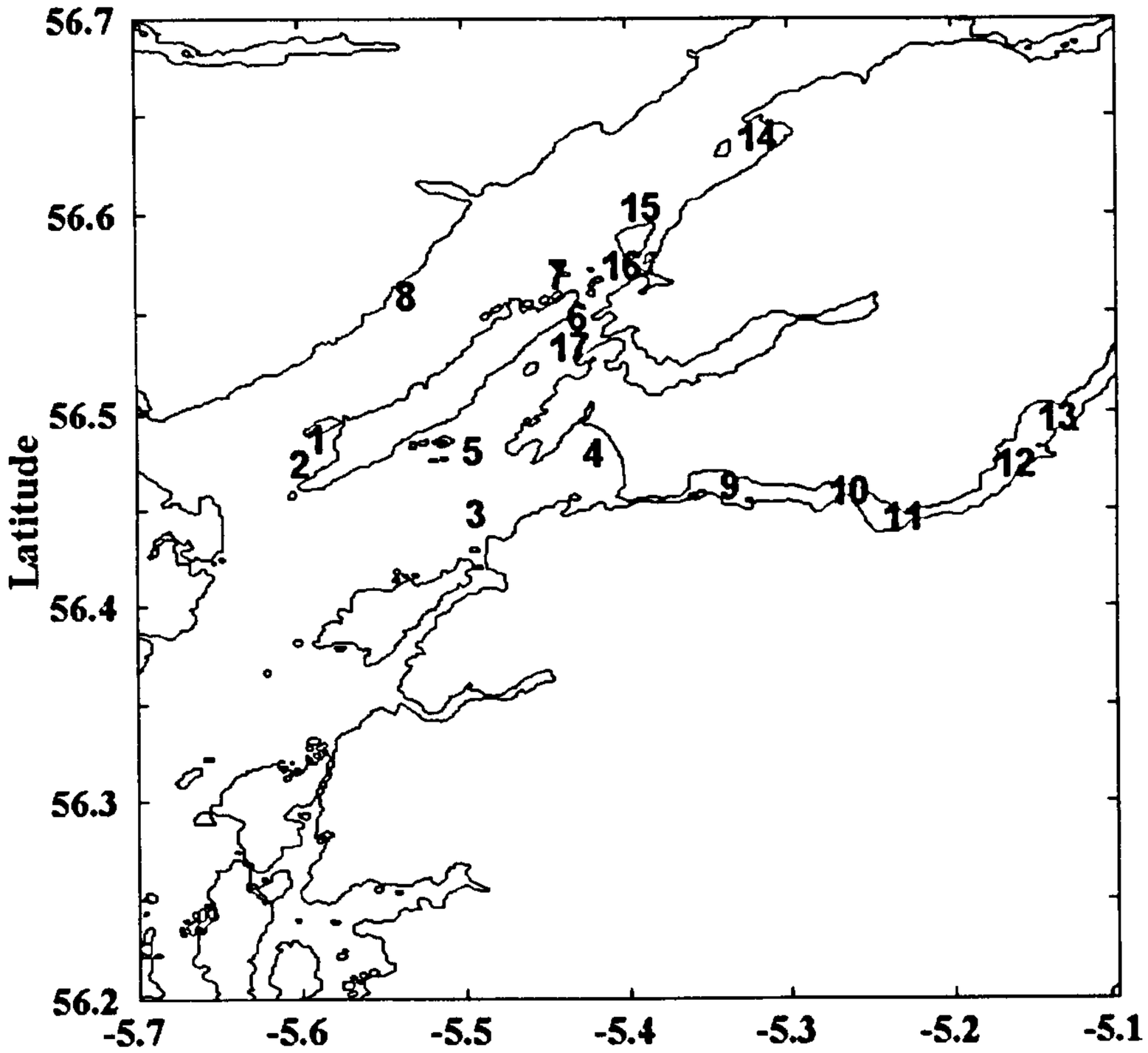

Figure 4.1. Cruise 1 – Oban, April 2003, illustrating the locations of stations sampled. Sampling was conducted between the 22nd and the 25th of April 2003 on board the *RV Calanus*.

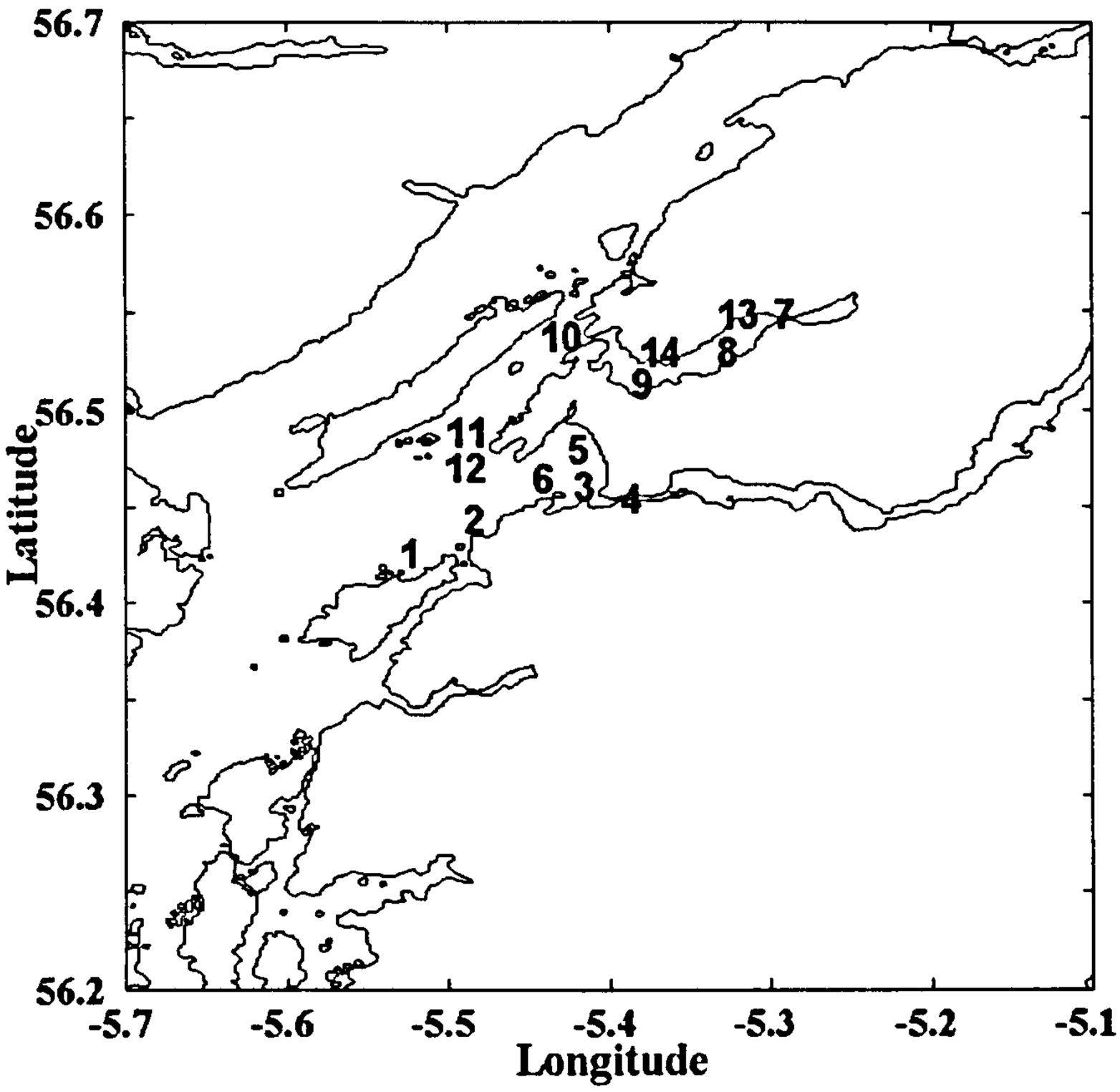

Figure 4.2. Cruise 2 - Oban, April 2004, illustrating the locations of stations sampled. Sampling was conducted between the 14th and 16th of April 2004 on board the *RV Seol Mara.*

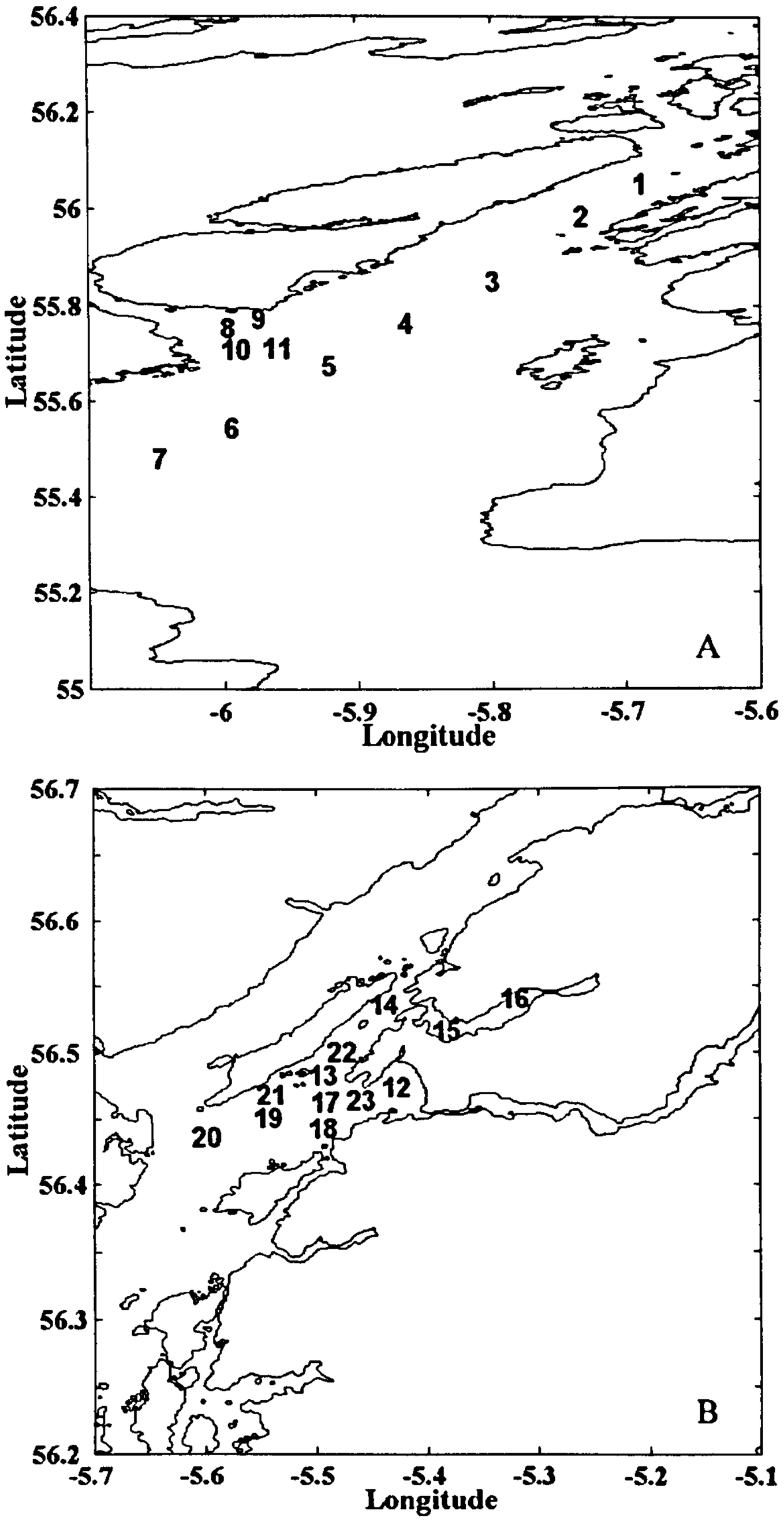

Figure 4.3. Cruise 3 – Sound of Jura, June 2004 illustrating the locations of the stations sampled. (A) The transect was conducted in the Sound of Jura from the 21st to the 23rd of June 2004. (B) The area around Oban was sampled on the 24th and 25th of June 2004. The cruise was conducted on board the *RV Calanus*.

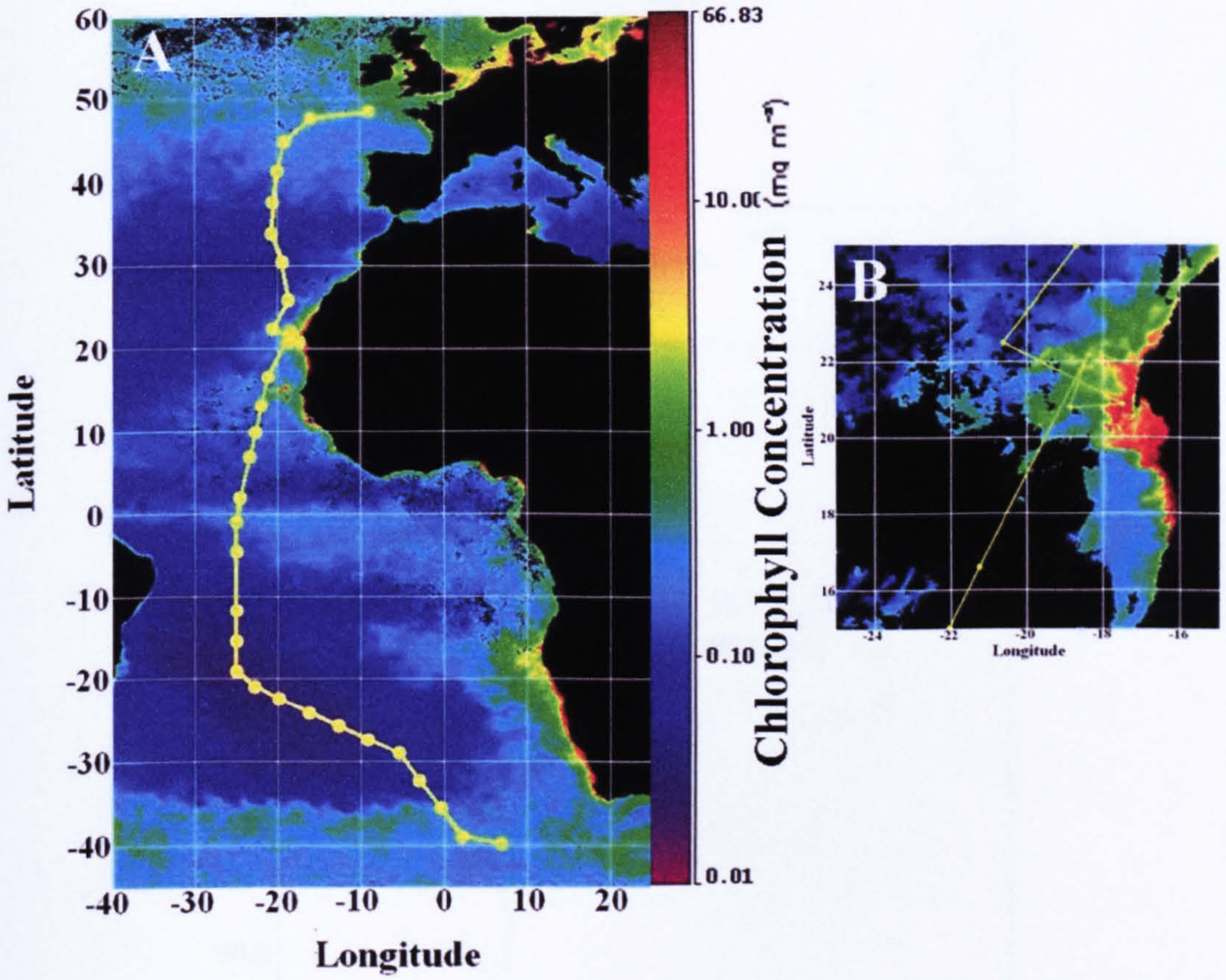

Figure 4.4. Cruise 4 - AMT 15, September/October 2004. (A) Map illustrates the cruise transect overlaid on a seasonally averaged MODIS Aqua Chlorophyll *a* image (16/09/04 to 15/12/04). (B) Illustrates the stations sampled in the North African Upwelling. This image is of the chlorophyll *a* weekly averaged data (29/09/04 to 06/10/04) from MODIS Aqua.

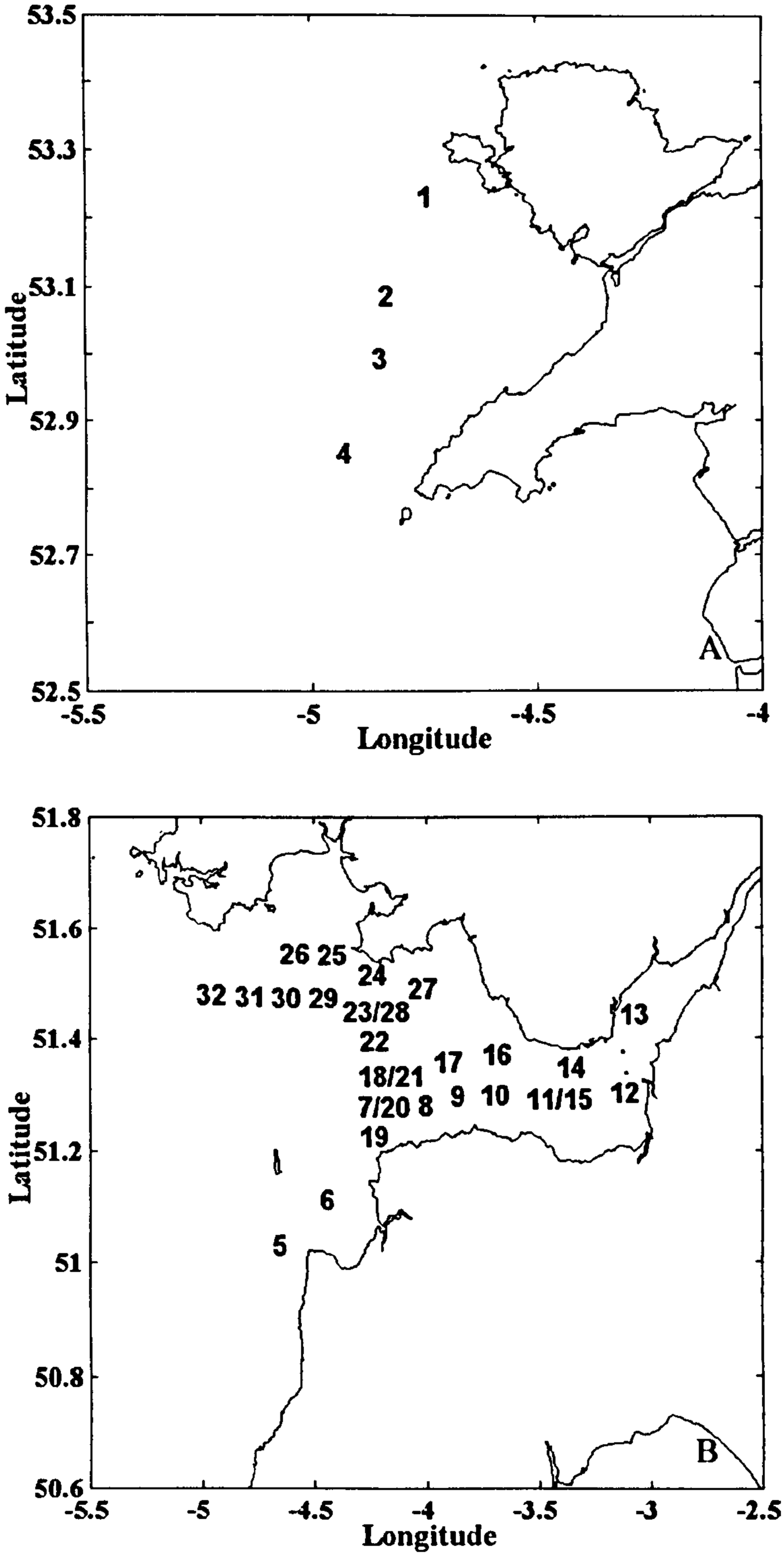

Figure 4.5. Cruise 5 – Bristol Channel, April/May 2005. (A) illustrates the location of stations sampled near Anglesey on the 29th of April 2005. (B) illustrates the locations of stations sampled in the Bristol Channel between the 30th of April and the 3rd of May 2005. Sampling was conducted on board the *RV Prince Madog*.

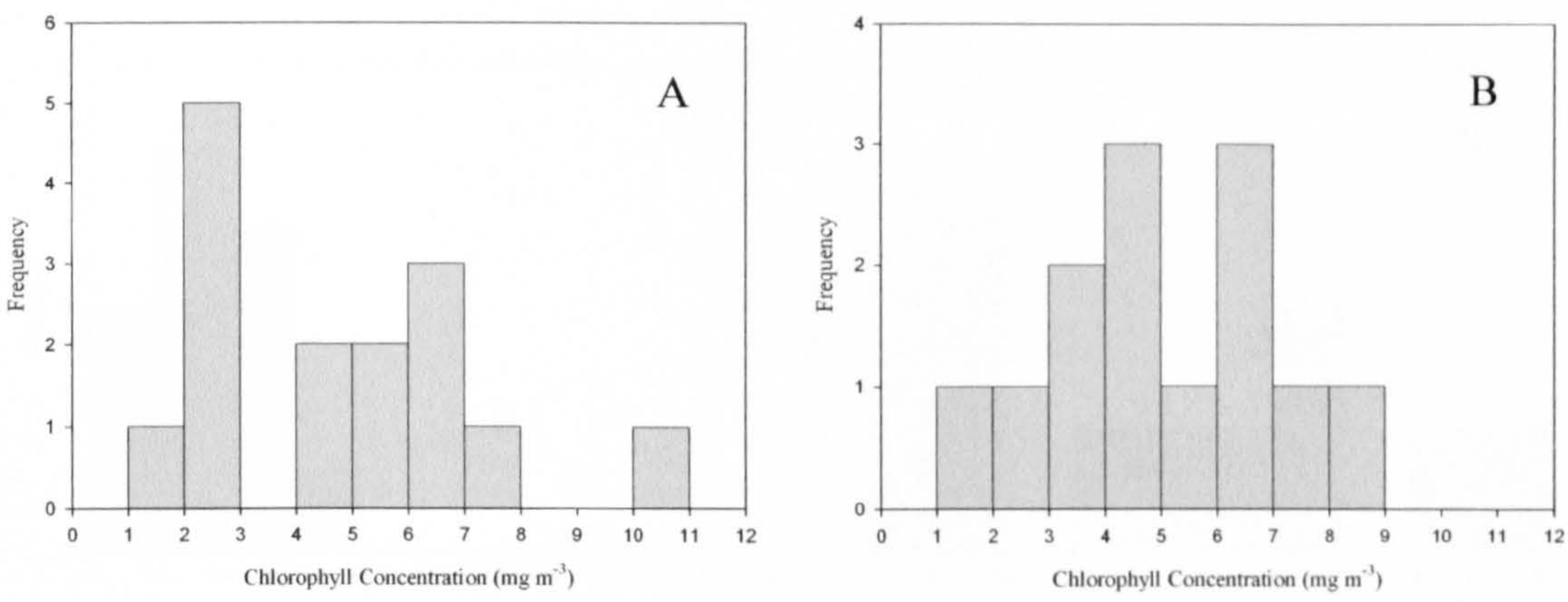

Figure 4.6. Histograms of chlorophyll concentrations. Panel (A) illustrates the distribution of chlorophyll concentrations for Oban 2003, (B) for Oban 2004, (C) for the Sound of Jura 2004 and (D) for the Bristol Channel 2005 cruise.

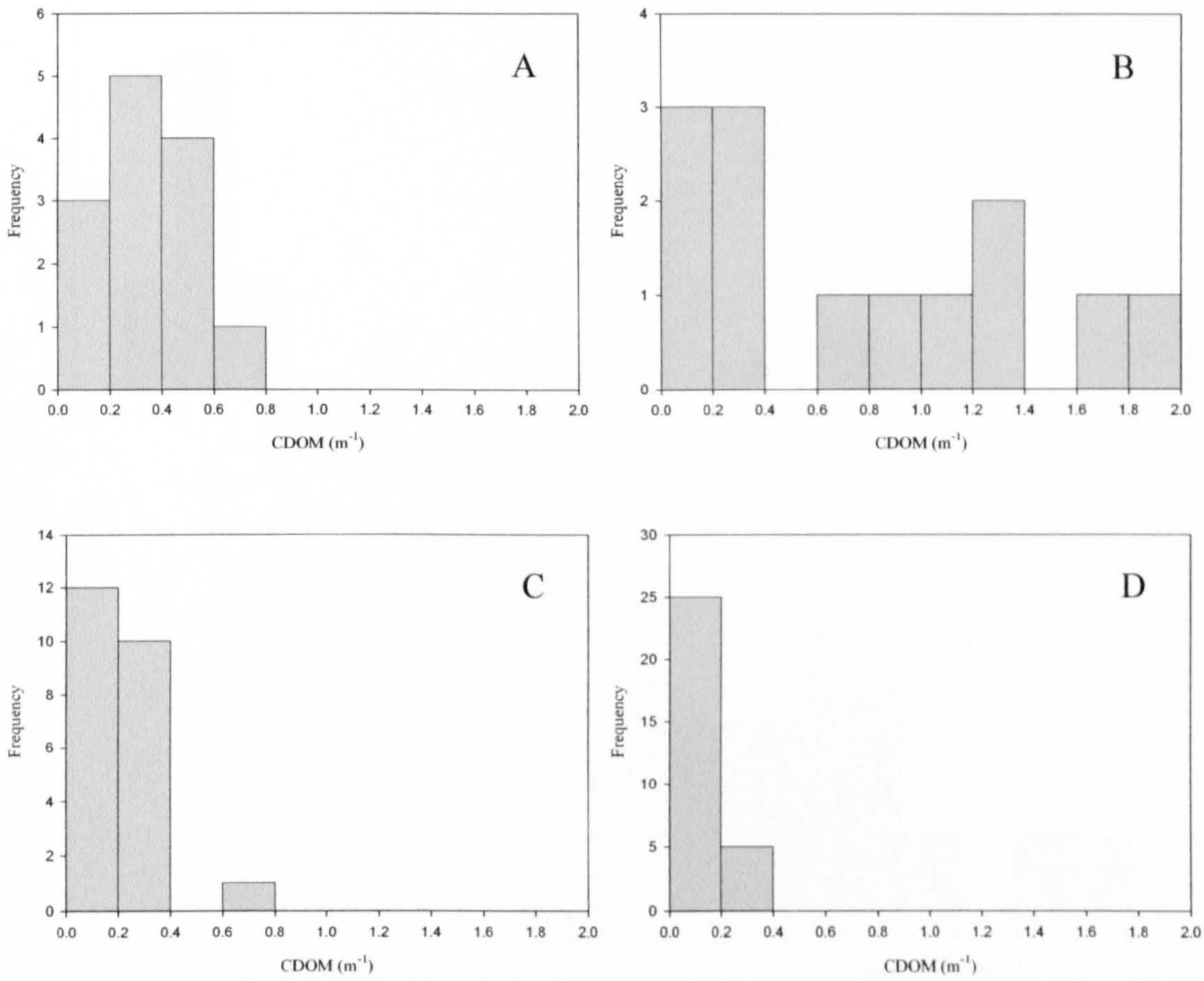

Figure 4.7. Histograms of CDOM concentration, measured as $a(440)$. Panel (A) shows the distribution of CDOM for Oban 2003, (B) Oban 2004, (C) the Sound of Jura 2004 and (D) the Bristol Channel 2005.

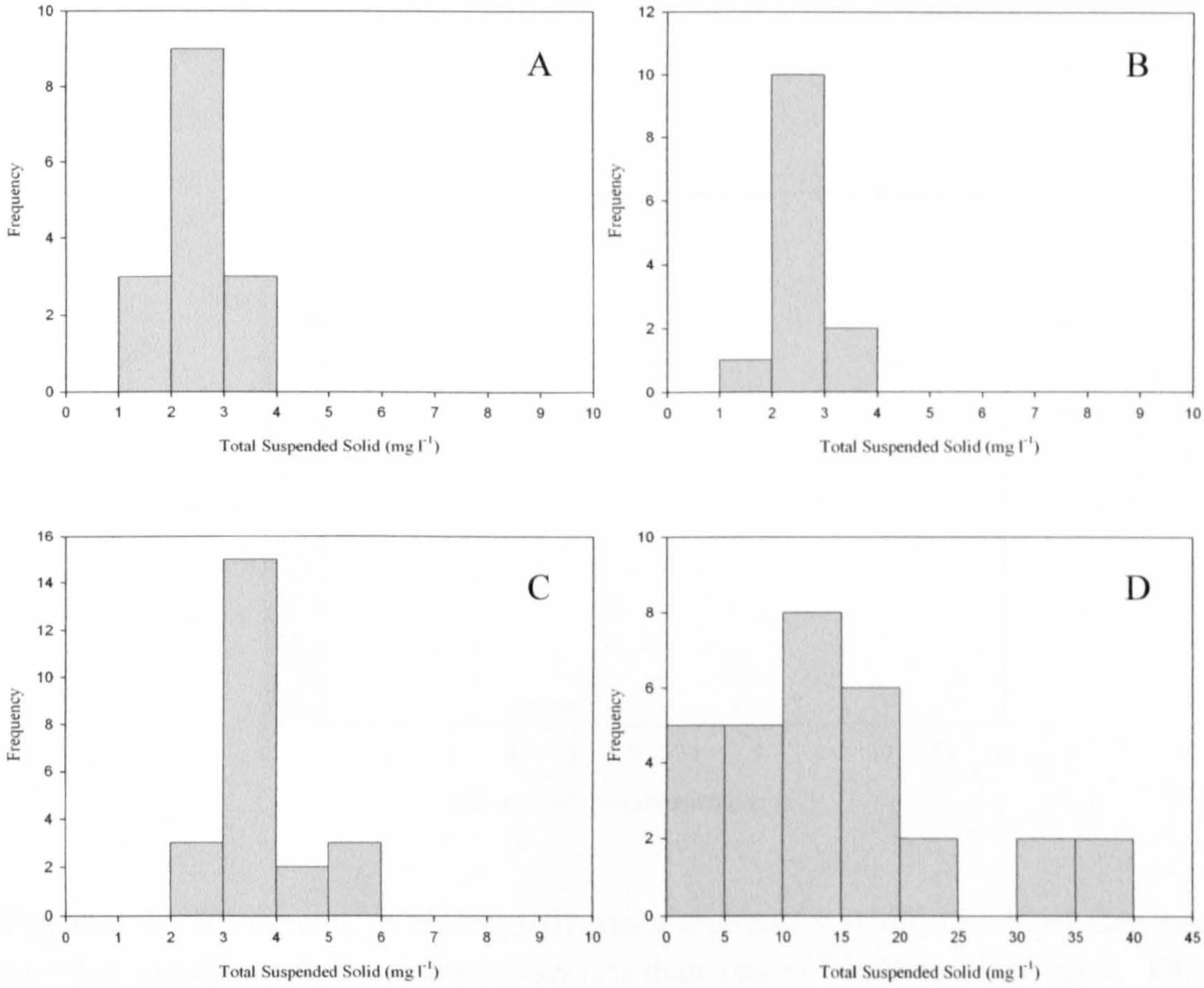

Figure 4.8. Histograms of total suspended solid concentrations. Panel (A) Oban 2003, (B) Oban 2004 and (C) the Sound of Jura 2004. Panel (D) illustrates the distribution of concentrations retrieved during the Bristol Channel 2005 cruise. Note the different concentration scale due to the high levels of TSS found during this cruise.

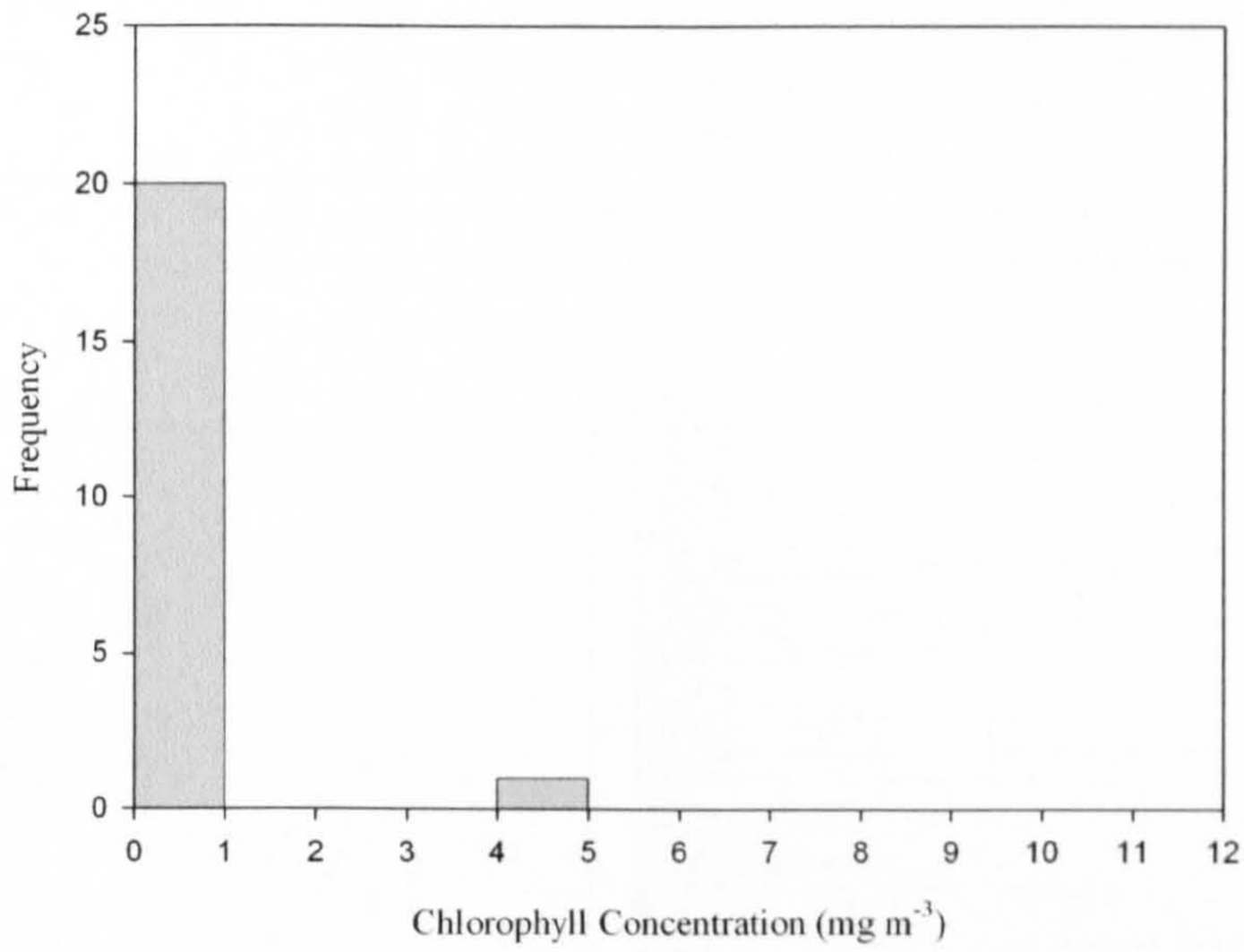

Figure 4.9. Histograms of chlorophyll concentration for AMT 15. Most stations sampled had chlorophyll concentrations less than $1 mg\,m^{-3}$ in the surface layer. The exception to this was the station sampled in the North African Upwelling which had a chlorophyll concentration of $4.5 mg\,m^{-3}$.

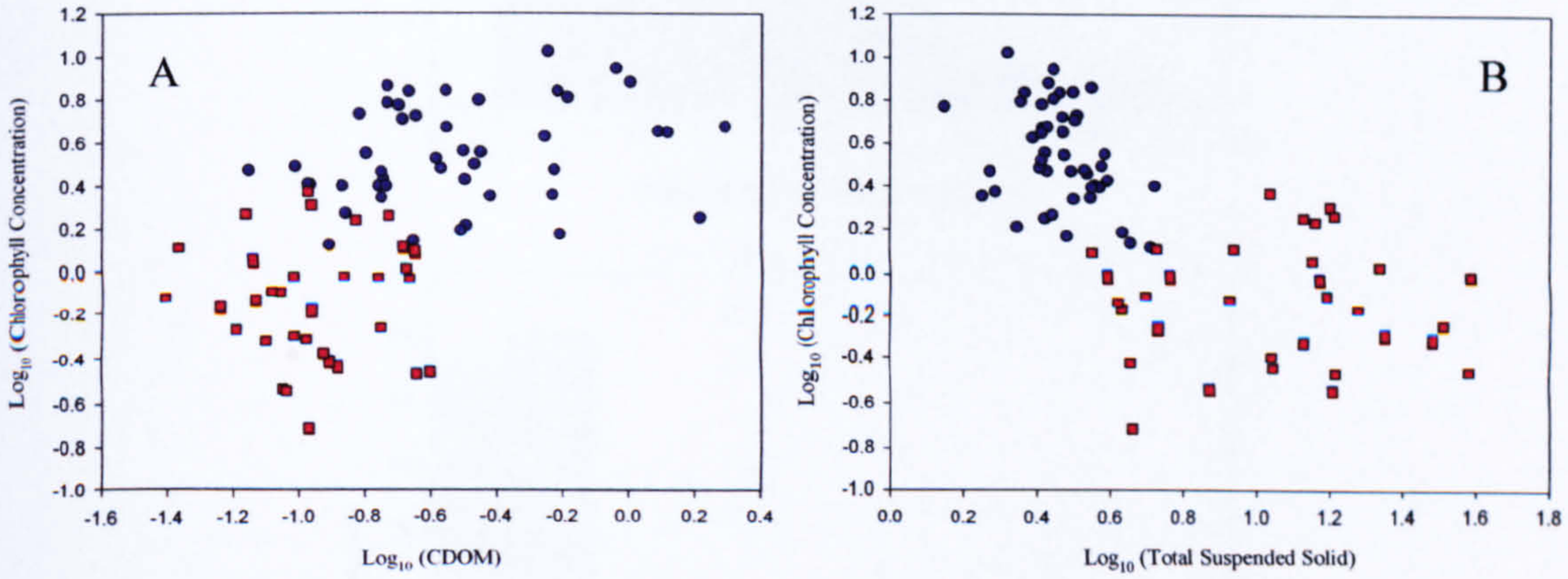

Figure 4.10. Constituent concentrations of coastal water. Panel (A) illustrates chlorophyll plotted against CDOM, (B) chlorophyll plotted against TSS and (C) TSS plotted against CDOM. All constituent concentrations have been $\log_{10}$ transformed. Panel (D) shows the tree diagram for the cluster analysis performed on the in-water constituents, revealing a high level bifurcation.

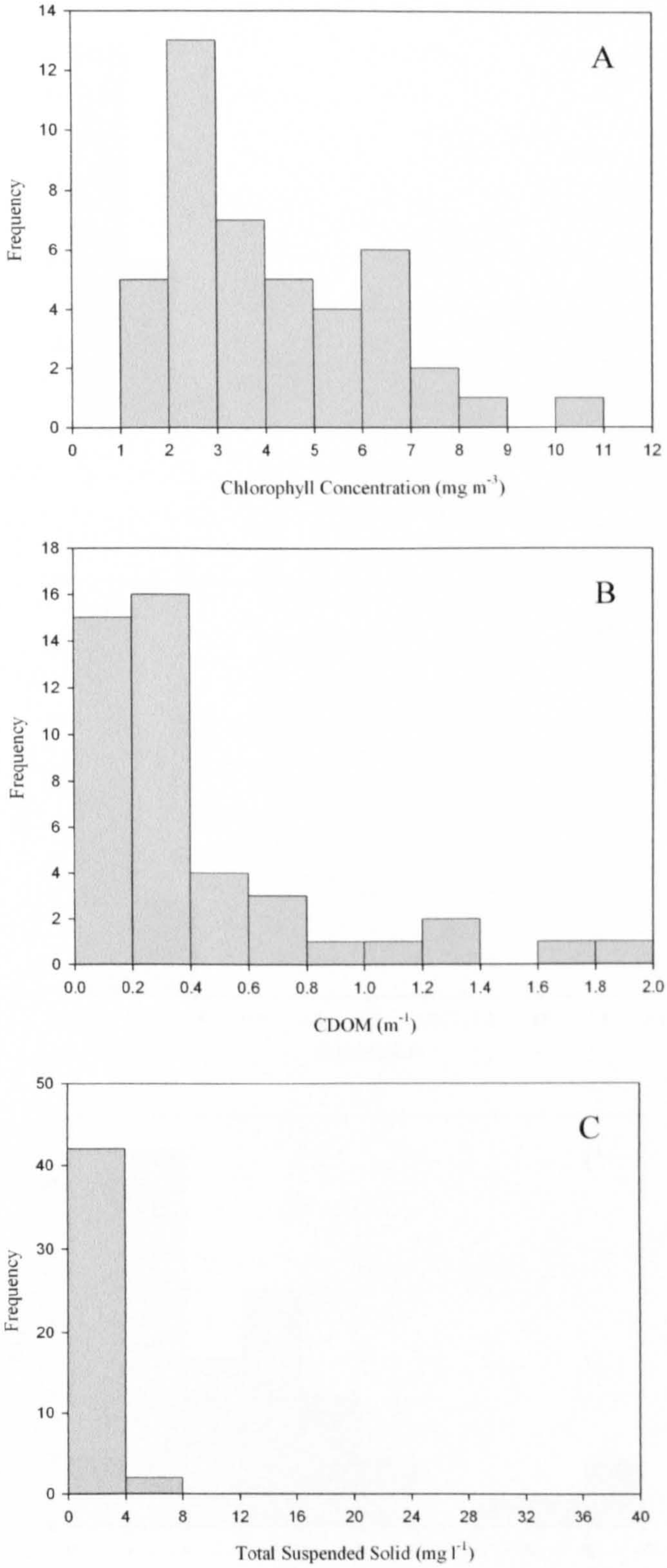

Figure 4.11. Histograms of constituent concentrations cluster coloured blue in the tree diagram of Figure 4.10. Panel (A) illustrates the chlorophyll concentration, (B) the CDOM concentration and (C) the TSS concentration.

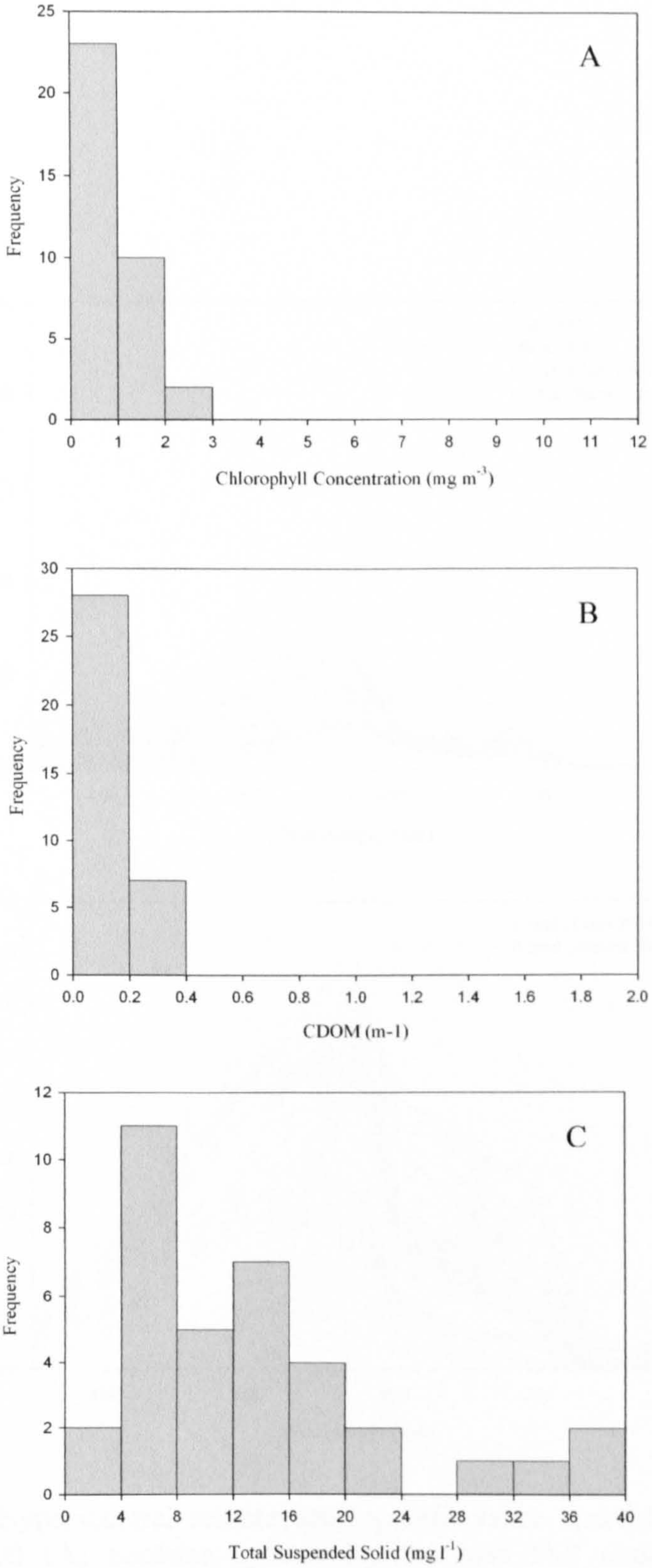

Figure 4.12. Histograms of constituent concentrations for cluster coloured red in tree diagram of Figure 4.10. Panel (A) illustrates the chlorophyll concentration, (B) the CDOM concentration and (C) the TSS concentration.

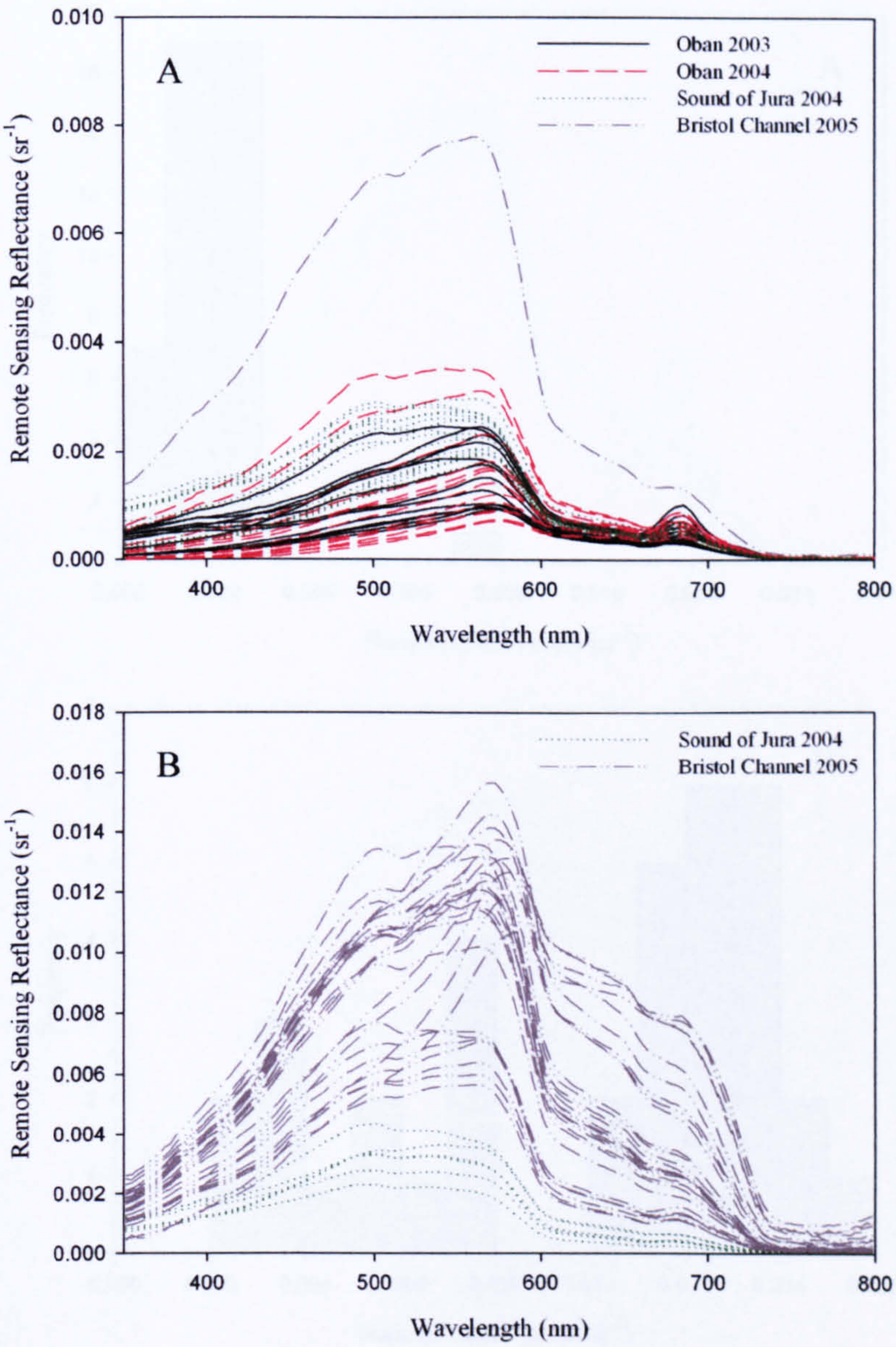

Figure 4.13. Hyperspectral remote sensing reflectance spectra for constituent clusters. Panel (A) contains spectra for the low TSS cluster with higher concentrations of chlorophyll and more varied levels of CDOM and panel (B) contains spectra for the higher concentrations of TSS with low levels of chlorophyll and CDOM.

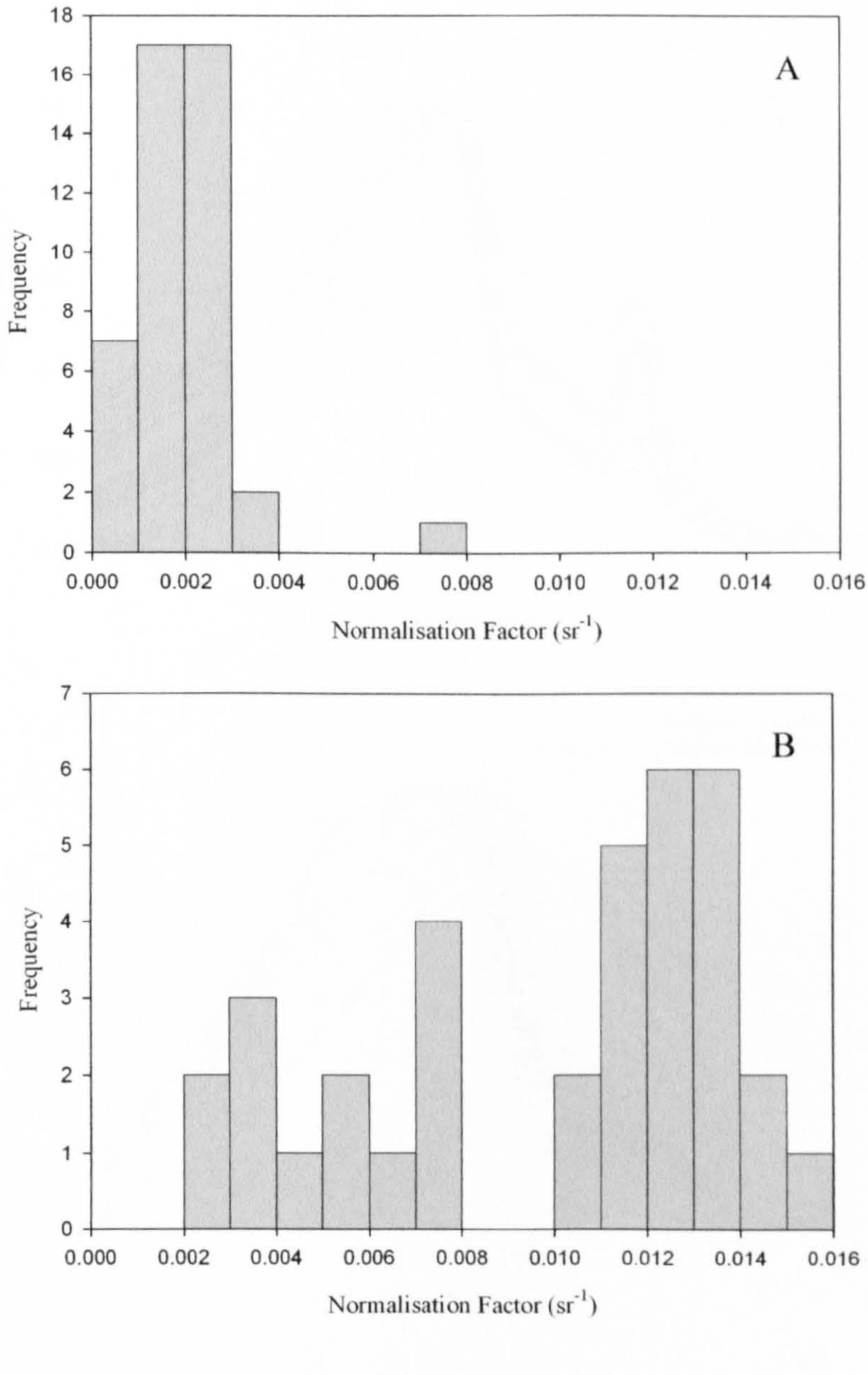

Figure 4.14. Normalisation factors for hyperspectral remote sensing reflectance spectra. Panel (A) contains the normalisation factor for the low TSS cluster with higher concentrations of chlorophyll and more varied levels of CDOM and panel (B) for the higher concentrations of TSS with low levels of chlorophyll and CDOM.

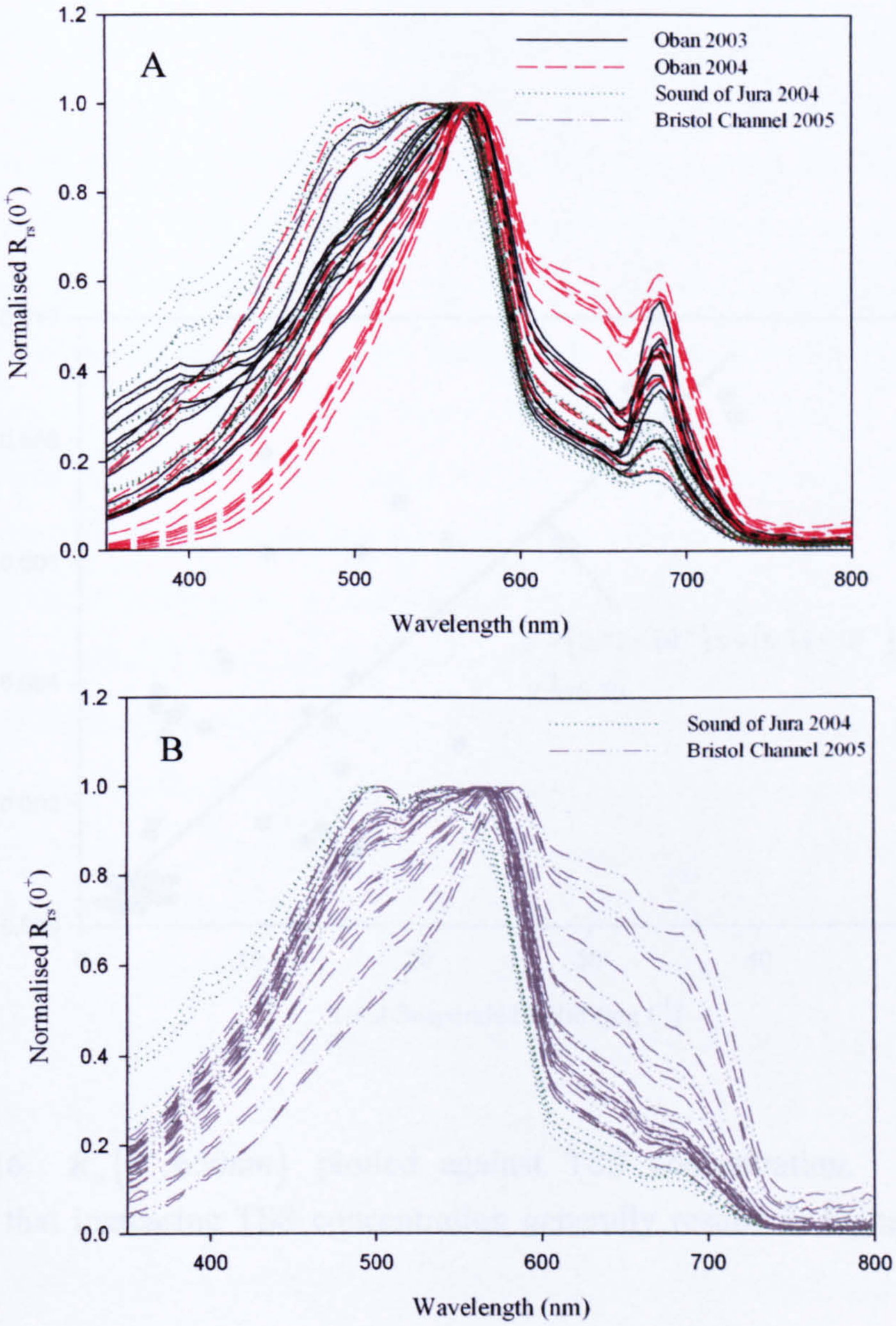

Figure 4.15. Normalised hyperspectral remote sensing reflectance spectra. Panel (A) contains normalised spectra for the low TSS cluster with higher concentrations of chlorophyll and more varied levels of CDOM and panel (B) for the higher concentrations of TSS with low levels of chlorophyll and CDOM.

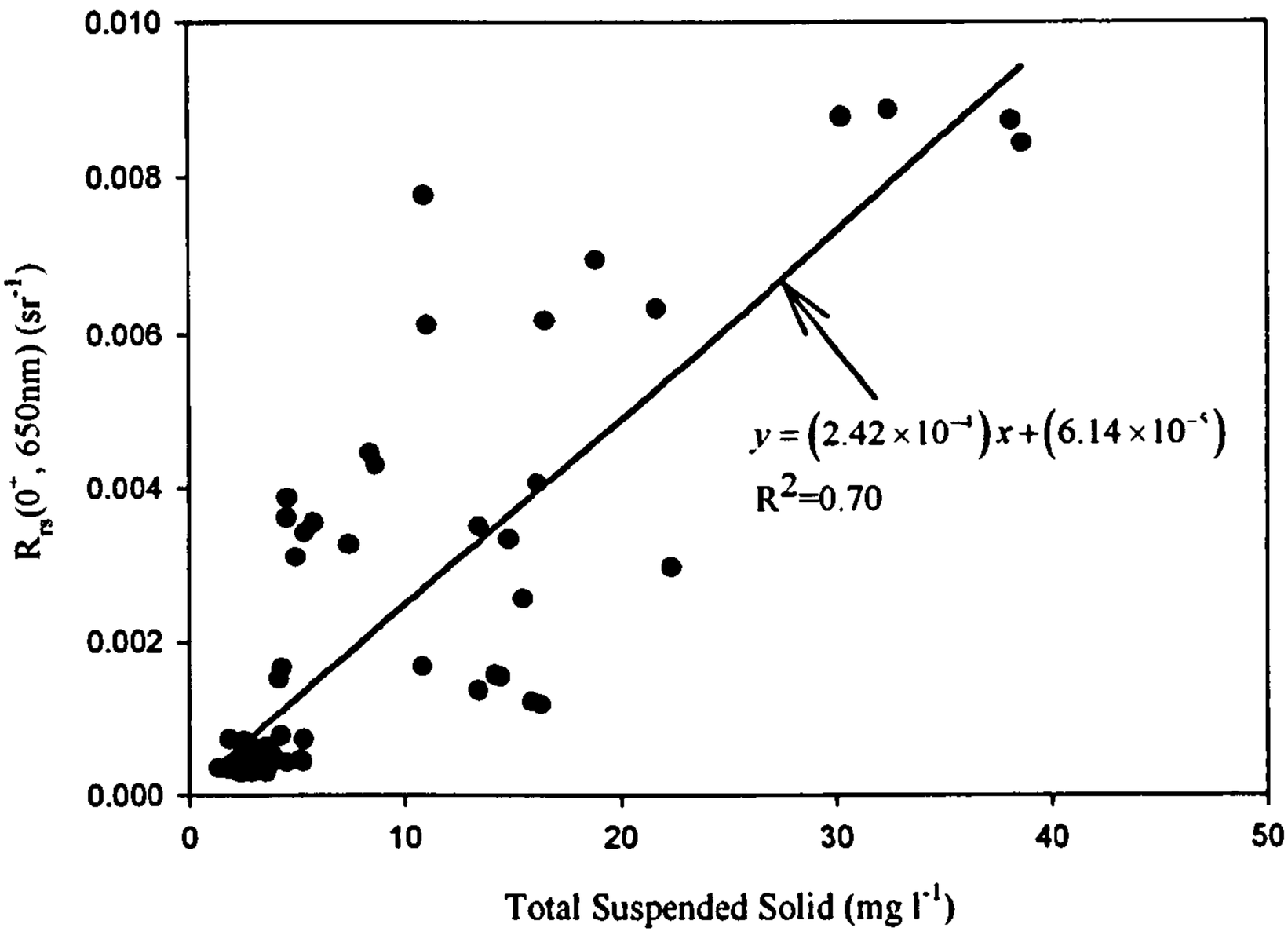

Figure 4.16. $R_{rs}(0^+, 650nm)$ plotted against TSS concentration. The figure illustrates that increasing TSS concentration generally results in higher values of $R_{rs}(0^+)$.

Chapter 5: Hyperspectral Radiance Transfer Modelling

Remote sensing reflectance, R_{rs}, signals contain information on the ability of a water body to return light to the surface. This signal varies depending upon the composition of the water (Wang and Cota, 2003; Doxaran *et al*, 2005; Stramska and Stramski, 2005). In the past discrete bandwidth sensors have been used to sample the in-water light field and water leaving signals and band ratio algorithms used to calculate information about the water body, such as the chlorophyll concentration. Remote sensing platforms such as SeaWiFS, MODIS and MERIS also measure radiance at discrete bandwidths (Tables 5.1, 5.2 and 5.3). Recently high resolution (hyperspectral) instrumentation has become more widely available. Hyperspectral instruments allow information to be gathered in intervals of a few nanometres across the spectrum, typically from 350 to 800nm, instead of in a limited number of discrete bands. An additional benefit is that the information obtained can be integrated over appropriate bandwidths to match any ocean colour sensor, for example SeaWiFS, MODIS and MERIS. The aim of this chapter is to investigate whether additional information can be obtained from hyperspectral measurements as opposed to discrete bandwidths. The effects of inelastically scattered light (e.g. Raman scattering, CDOM fluorescence and chlorophyll fluorescence) on the water leaving R_{rs} signal will also be considered.

5. 1. Radiance Transfer Model Configuration

As a preliminary step to investigate variations in the R_{rs} signal it was necessary to model a variety of water types. The models used for this work were created using the Hydrolight (version 4.2) radiance transfer computer package. Case 1 waters, where the main optically significant component besides the water is chlorophyll,

were modelled for a variety of chlorophyll concentrations. These models were constructed to investigate the spectral response of $R_{rs}(0^+)$ to increasing chlorophyll concentration.

Following this a variety of case 2 waters were modelled. In case 2 waters the main optically important components, in addition to water, are chlorophyll, CDOM (coloured dissolved organic matter) and MSS (mineral suspended solid). To investigate the effects of these components on the $R_{rs}(0^+)$ signal three batches of Hydrolight model runs were carried out with (a) chlorophyll and CDOM, (b) chlorophyll and MSS and (c) chlorophyll, CDOM and MSS. This allowed the effects of introducing CDOM and MSS into the model independently and jointly to be investigated. Inputs to the Hydrolight models were chosen to reflect the range of values observed between the upper and lower limits of chlorophyll, CDOM and MSS concentrations found in West of Scotland coastal waters. Table 5.4 shows the range and combinations of chlorophyll, CDOM and MSS concentrations used.

Inputs to the Hydrolight radiance transfer models are described below.

5.1.1. Case 1 Model

The Hydrolight model for case 1 water was set-up as follows:

1. The ABCase 1 inherent optical property model was selected.
2. The absorption and scattering properties of pure water were specified using the information contained in Pope and Fry (1997).
3. The chlorophyll concentration was set to be constant with depth. Chlorophyll concentrations for which the model was run were: $0, 0.1, 0.5, 1, 2.5, 5, 7.5$ and $10 mg\, m^{-3}$.
4. The average Petzold particle phase function was selected.
5. Inelastic scattering effects included chlorophyll fluorescence, CDOM fluorescence and Raman scattering.
6. The model was run between 400 and 750nm in 3.5nm intervals.
7. The solar zenith angle was set to 30^0 with clear sky conditions.

8. The downwelling irradiance conditions were determined using the semi-empirical RADTRAN model.
9. Infinitely deep bottom boundary conditions were selected.
10. A maximum depth of 20m was selected with calculations carried out at 1m intervals.

The ABCase1 model is based on an updated version of the Gordon-Morel Case 1 water model (Morel and Maritorena, 2001). The total absorption coefficient of this model is represented by:

$$a_{total}(\lambda)=a_w(\lambda)+a_p(\lambda)+a_{CDOM}(\lambda) \qquad (5.1)$$

where $a_{total}(\lambda)$ is the total absorption coefficient, $a_w(\lambda)$ is the absorption by pure water, $a_p(\lambda)$ is the absorption by phytoplankton cells and $a_{CDOM}(\lambda)$ is the absorption by CDOM.

The absorption by pure water is given in Pope and Fry (1997). Absorption by phytoplankton cells is represented by:

$$a_p(\lambda)=0.06\times A_{chl}(\lambda)\times\left[Chl(z)\right]^{0.65} \qquad (5.2)$$

where $A_{chl}(\lambda)$ is the chlorophyll specific absorption coefficient given in Prieur and Sathyendranath (1981) and $Chl(z)$ is the chlorophyll concentration specified by the user. Absorption by CDOM covaries with particulate absorption according to:

$$a_{CDOM}(z,\lambda)=0.2\times a_p(z,440nm)\times\exp\left(-0.014(\lambda-440)\right) \qquad (5.3)$$

The scattering coefficient, $b(z,\lambda)$, for particulate material is as follows:

$$b(z,\lambda)=0.3\times\left[Chl(z)\right]^{0.62}\times\left(\frac{550}{\lambda}\right) \qquad (5.4)$$

Scattering by CDOM is assumed to be zero.

The incident irradiation conditions in the model are generated using the RADTRAN model (Gregg and Carder, 1990) which calculates the direct (solar) and diffuse (background sky) irradiances. The default settings of solar zenith angle of 30^0 and clear sky conditions were used and RADTRAN generated irradiances at 1nm intervals which were then averaged into the required wavebands.

5. 1. 2. Case 2 Model

To investigate case 2 water three batches of model runs were set-up. The first batch included the effects of chlorophyll and CDOM, the second the effects of chlorophyll and MSS and the third the effects of chlorophyll, CDOM and MSS. The Hydrolight set-up for the chlorophyll, CDOM and MSS batch is described below:

1. The ABCase2, a four component inherent optical property model, was selected.
2. The absorption and scattering properties of pure water were specified using the information contained in Pope and Fry (1997).
3. Chlorophyll concentration was set to be constant with depth.
4. The default Hydrolight chlorophyll specific absorption file was selected.
5. Scattering by chlorophyll was described by a power law.
6. The average Petzold phase function was selected.
7. CDOM concentration was specified at 440nm and set to be constant with depth.
8. CDOM absorption was described by an exponential function.
9. The mineral concentration was set to be constant with depth.
10. The mineral specific absorption was set to the Hydrolight default.
11. The mineral specific absorption was described by a power law.
12. Inelastic scattering effects included chlorophyll fluorescence, CDOM fluorescence and Raman scattering.
13. The model was run between 400 and 750nm in 3.5nm intervals.
14. The solar zenith angle was set equal to 30^0 with clear sky conditions.
15. The downwelling irradiance conditions were determined using the semi-empirical RADTRAN model.

16. Infinitely deep bottom boundary conditions were selected.
17. A maximum depth of 20m was selected with calculations carried out at 1m intervals.

For the batch of models dealing with the chlorophyll and CDOM components, the MSS concentration was set equal to zero. Similarly, for the batch of models dealing with the chlorophyll and MSS combination, the CDOM concentration was set equal to zero.

The default chlorophyll specific absorption is given in Prieur and Sathyendranath (1981). The CDOM absorption coefficient, $a_{CDOM}(\lambda)$, is represented by the following exponential function:

$$a_{CDOM}(\lambda)=a_{CDOM}(440)\times\exp\left(-0.014(\lambda-440)\right) \qquad (5.5)$$

The default mineral specific absorption file in Hydrolight is a composite of values from Bukata (1995) and Gallie and Murtha (1992).

Scattering by particulate material, for example chlorophyll and minerals, is represented by the following power law (Loisel and Morel, 1998):

$$b(\lambda)=0.407\times[X]^{0.795}\times\left(\frac{660}{\lambda}\right) \qquad (5.6)$$

where $b(\lambda)$ is the scattering coefficient at wavelength λ and X is the concentration of either chlorophyll or minerals.

Figure 2.1 illustrates the absorption spectra of the default Hydrolight settings for water, chlorophyll and MSS. Included in this figure is the absorption profile for CDOM obtained using equation (5.5). Table 5.4 (A) to (C) lists the chlorophyll, CDOM and MSS concentrations for which these case models were carried out.

5. 2. Inelastic Processes

The Hydrolight models included the effects of inelastic processes, namely Raman scattering, CDOM fluorescence and chlorophyll fluorescence. Inelastic scattering

events redistributed the photons in the water body between wavelengths. In this section the impact of these scattering processes on the $R_{rs}(0^+)$ spectra will be investigated.

5. 2. 1. Raman Scattering

The effect of Raman scattering on the $R_{rs}(0^+)$ spectra was modelled using the Hydrolight ABCase1 model. As the main source of Raman scattering is water molecules, the model was run with the chlorophyll concentration set to $0 mg\,m^{-3}$ to maximize the influence of the Raman scattering on the spectra. The effects of CDOM and chlorophyll fluorescence were excluded. The model was set up following the procedure laid out in section 5. 1. 1. Two separate runs were conducted, one which included Raman scattering and the other excluding Raman scattering. Figure 5.1 (A) illustrates the difference observed in the two $R_{rs}(0^+)$ spectra and panel (B) shows the percentage difference in the $R_{rs}(0^+)$ values between the two spectra. Figure 5.1 (B) shows that the effect of Raman scattering was to increase the reflectance signal by 5 to 10% between 450 and 500nm. Above 500nm the percentage difference increases to between 10 and 20%. The percentage difference is accentuated by the low reflectance signals in this spectral region. Therefore, any deviation from the original value would show up as a higher percentage difference even though the absolute magnitude of the deviation is small. Looking again at Figure 5.1 (A) it can be seen that above 550nm it is difficult to separate the two spectra due to the magnitude of the R_{rs} values. The effects of Raman scattering deeper in the water column can be more significant (Hu and Voss, 1997; Bartlett *et al* 1998; Schroeder *et al*, 2003). However, in this investigation the concern is only with the effects at the surface, where the Raman scattering is found not to have a strong influence on the $R_{rs}(0^+)$ signal. In fact the inclusion of chlorophyll would decrease Raman scattering at short wavelengths as the signal can be attenuated by the presence of the chlorophyll.

5. 2. 2. CDOM Fluorescence

CDOM fluorescence is a broad band fluorescent feature. To investigate its impact on the $R_{rs}(0^+)$ spectra a set of Hydrolight ABCase 2 models were carried out with the chlorophyll and MSS concentration set to zero while the concentration of CDOM at $a(440)$ was varied. All other inelastic scattering processes were excluded. Figure 5.2 illustrates the $R_{rs}(0^+)$ spectra calculated for various CDOM concentrations including and excluding CDOM fluorescence. Panel (A) illustrates the spectra for $CDOM = 0.2m^{-1}$, (B) for $CDOM = 0.5m^{-1}$, (C) for $CDOM = 1m^{-1}$ and (D) for $CDOM = 2m^{-1}$. As the CDOM concentration increases the fluorescence feature becomes more prominent in the blue spectral region, peaking around 490nm. For waters which have low chlorophyll and MSS concentrations, CDOM fluorescence may be an important feature in the $R_{rs}(0^+)$ spectra. The above calculations were carried out in the absence of chlorophyll and MSS to maximise the impact of CDOM fluorescence on the $R_{rs}(0^+)$ spectra. However, due to the location of the CDOM fluorescence in the blue region of the spectrum it will be susceptible to absorption by chlorophyll and MSS if these components are present. Generally the effects of CDOM fluorescence for concentrations typical of shelf sea and open ocean conditions (i.e. $\leq 0.5m^{-1}$ at $a(440)$) on the $R_{rs}(0^+)$ spectra are small. However, at higher concentrations of CDOM (i.e. $\geq 1m^{-1}$ at $a(440)$), in this data found to occur only in Scottish sea lochs heavily influenced by fresh water runoff from the surrounding hills, the fluorescence can be clearly observed in the $R_{rs}(0^+)$ spectra.

5. 2. 3. Chlorophyll Fluorescence

Figure 5.3 illustrates the effect of chlorophyll fluorescence, which appears in the red region of the spectrum with a peak centred on 685nm (Gordon, 1979). Hydrolight assumes that the fluorescence emission is Gaussian in nature with a peak centred at 685nm with a full width half maximum (FWHM) of 25nm and that the quantum yield of fluorescence is constant with time and depth. A set of Hydrolight runs were

conducted using the ABCase1 model and the procedure set out in section 5. 1. 1. As the chlorophyll concentration was increased the peak in the red, attributed to chlorophyll fluorescence, also increased. The model runs contained only chlorophyll, but the presence of other optically important materials such as CDOM and MSS can attenuate the chlorophyll fluorescence signal. This will be investigated further in Chapter 8.

5. 2. 4. Assessment of the Impact of Inelastic Scattering on the $R_{rs}(0^+)$ Spectra

It was found that the effect of Raman scattering on the $R_{rs}(0^+)$ spectra was small, though it may be important deeper down the water column. CDOM fluorescence can be an important feature of the $R_{rs}(0^+)$ spectra in the presence of low chlorophyll and MSS concentrations and high CDOM levels (sea loch concentrations). However, due to the location of the CDOM fluorescence in the blue region of the spectrum it will be susceptible to attenuation by other optically important components, namely chlorophyll and MSS. It was also apparent that chlorophyll fluorescence can strongly influence the $R_{rs}(0^+)$ spectra in the red and that the fluorescence signal increases with chlorophyll concentration. Chlorophyll fluorescence may be attenuated by the presence of CDOM and MSS, and this will be investigated further in a later chapter.

5. 3. Variations in the Shape of Hyperspectral Remote Sensing Reflectance Spectra

The magnitude of the $R_{rs}(0^+)$ spectra varies according to (Morel and Prieur, 1977; Morel and Gentili, 1996):

$$R_{rs} \propto \frac{b_b}{a + b_b} \tag{5.7}$$

Consequently the spectral shape of the $R_{rs}(0^+)$ signal may provide information on the content of the water body. To investigate the response of the $R_{rs}(0^+)$ spectra to water body content, several batches of Hydrolight radiance transfer models were run.

5. 3. 1. Normalisation of Modelled Hyperspectral $R_{rs}(0^+)$ Spectra

It was decided that to compare spectral shapes the modelled $R_{rs}(0^+)$ spectra would be normalised by their maximum value. This also makes application of the results less sensitive to errors in the measurement of absolute water leaving radiances. Comparison between the high resolution, hyperspectral, spectra and discrete bandwidth spectra are also discussed. Figure 5.4, 5.6, 5.11 and 5.16 illustrate the normalised $R_{rs}(0^+)$ spectra obtained from the Hydrolight models. Figure 5.4 is for case 1 water with varying chlorophyll concentration, Figure 5.6 is for case 2 water containing chlorophyll and CDOM, Figure 5.11 is for case 2 water containing chlorophyll and MSS and Figure 5.16 is for case 2 water containing chlorophyll, CDOM and MSS.

i. Normalised Spectra for Case 1 Water

In Figure 5.4 as the chlorophyll concentration increases the relative reflectance in the blue is reduced and peaks appear in the green and red. The reduction in the blue is due to an increase in absorption by the chlorophyll. The emergence of a peak in the red is associated with chlorophyll fluorescence.

ii. Normalised Spectra for Case 2 Water: Chlorophyll and CDOM

Figure 5.6 (A) to (D) illustrate the normalised $R_{rs}(0^+)$ spectra obtained for varying CDOM concentrations with chlorophyll concentrations of (A)$0\,mg\,m^{-3}$, (B)$0.1\,mg\,m^{-3}$, (C) $1\,mg\,m^{-3}$ and (D)$10\,mg\,m^{-3}$. As the CDOM concentration increases, the reflectance in the blue decreases due to increased absorption by CDOM. The presence of a peak around 490nm in panel (A) is associated with CDOM fluorescence. However, as the chlorophyll level increases the CDOM

fluorescence is reduced. In panel (C) ($Chl = 1 mg\,m^{-3}$) a shoulder is observed around 490nm due to the CDOM fluorescence but in panel (D) ($Chl = 10 mg\,m^{-3}$) the CDOM fluorescence signature is missing. This is due to the increase in absorption in the blue by chlorophyll. As CDOM concentrations increase changes in the peak wavelength position, structure between 490 and 590nm and in the gradient between 400nm and the peak value are observed in panels (A), (B) and (C) of Figure 5.6 ($Chl = 0.1, 1$ and $10 mg\,m^{-3}$). The emergence of a peak around 570nm as the chlorophyll concentration increases is due to the increase in absorption in the blue and low absorption in the green. The chlorophyll fluorescence feature becomes more prominent as the chlorophyll concentration is increased.

iii. Normalised Spectra for Case 2 Water: Chlorophyll and MSS

Figure 5.11 (A) to (D) illustrate the peak normalised $R_{rs}\left(0^{+}\right)$ spectra for case 2 water containing chlorophyll and MSS. In panel (A) $Chl = 0 mg\,m^{-3}$, (B) $Chl = 0.1 mg\,m^{-3}$, (C) $Chl = 1 mg\,m^{-3}$ and (D) $Chl = 10 mg\,m^{-3}$: in all three cases the MSS concentration was varied between $1 mg\,l^{-1}$ and $10 mg\,l^{-1}$. Figure 5.11 (A) shows that as the MSS concentration is increased there is a reduction in the relative reflectance in the blue due to the increased absorption. However, due to the effects of increased backscattering with increasing MSS concentration the reduction is not as dramatic as when dealing with CDOM (Figure 5.6). A shift in the peak position occurs as the MSS concentration is increased, this is not obvious in the case where $Chl = 10 mg\,m^{-3}$ (Figure 5.11 (D)). Variation in the red region of the spectrum (after 600nm) due to the increase in backscattering with MSS concentration is also observed. As the chlorophyll concentration increased a clear peak around 570nm was observed. The chlorophyll fluorescence peak is not as prominent as in Figures 5.4 and 5.6, which suggests that the chlorophyll fluorescence signal is affected by the composition of the water body.

iv. Normalised Spectra for Case 2 Water: Chlorophyll, CDOM and MSS

Figure 5.16 illustrates the normalised spectra for the last batch of Hydrolight case 2 models which include the affects of chlorophyll, CDOM and MSS on the $R_{rs}(0^+)$ signal. Panel (A), where $Chl = 0.1 mg\,m^{-3}$, shows that for combinations that included $CDOM = 0.1 m^{-1}$ or $1 m^{-1}$ and $MSS \leq 10 mg\,l^{-1}$, the CDOM fluorescence feature could be detected. This can be observed to a lesser extent in panel (B) where $Chl = 1 mg\,m^{-3}$. Again shifts in the position of the peak as the concentration of the components, CDOM and MSS, increases occurred. In the red section of the spectrum for all combinations of CDOM and MSS with $MSS = 10 mg\,l^{-1}$ a higher relative reflectance signal is found, presumably associated with the increase in backscattering. The lowest values in the red this is found to occur where $CDOM = 0.1 m^{-1}$ and $MSS = 0.1 mg\,l^{-1}$, which is most likely due to low backscattering associated with the low level of MSS. The magnitude of the chlorophyll fluorescence peak varies with the combinations of CDOM and MSS.

5. 3. 2. Comparison of Hyperspectral and Discrete Bandwidth Spectra

i. Case 1 Water

For case 1 water Figure 5.5 illustrates the spectra obtained by binning the normalised hyperspectral data into SeaWiFS, MODIS and MERIS wavebands (see Tables 5.1 to 5.3). Comparing Figure 5.4 (the hyperspectral data) to Figure 5.5 (the multispectral data) it was found that the hyperspectral data detected more subtle changes in the $R_{rs}(0^+)$ spectra and that the multispectral data under-sampled some regions. The SeaWiFS, MODIS and MERIS wavebands do not resolve the fine structure in the spectral regions between 400 to 450nm and 500 to 560nm. This is especially clear between 500 to 560nm. The hyperspectral data shows a change in gradient occurring at 600nm which is not displayed in the multispectral data for SeaWiFS and MODIS, MERIS being the only sensor to illustrate this. The SeaWiFS wavebands do not sample the chlorophyll fluorescence feature but the MODIS and

MERIS wavebands do. MODIS and MERIS both measure chlorophyll fluorescence at wavelengths offset from the peak emission and a correction (Gower, 2004) has to be applied.

ii. Case 2 Water: Chlorophyll and CDOM

Figures 5.7 to 5.10 illustrate the multispectral spectra obtained by binning the high resolution data for case 2 water containing chlorophyll and CDOM. The structure of the gradient between 400 and 490nm was poorly reflected in the multispectral figures and the presence of a secondary peak around 580nm was missed. Variations in the gradient after 580nm were not shown in the multispectral figures. For $Chl = 0.1 mg\,m^{-3}$ and varying CDOM concentrations (Figures 5.6 (B) and 5.8) the multispectral sensors miss the detail and fine structure contained between 490 and 590nm. After 590nm the SeaWiFS spectra contain no real information about the spectral shape apart from the negative gradient. In Figure 5.6 (B) there are three distinct steps in the spectra after 590nm. This area is under-sampled by all the multispectral sensors, though MERIS samples this area better that the others. A similar situation is observed in the multispectral data for $Chl = 1$ and $10 mg\,m^{-3}$ (Figure 5.6 (C) and (D) and Figures 5.9 and 5.10). In the case of $Chl = 1 mg\,m^{-3}$ (Figure 5.9) the structure of the CDOM fluorescence shoulder is not fully resolved. Similarly, the structure and fine detail between 490 and 590nm is not shown in the case where $Chl = 0.1 mg\,m^{-3}$. Variations in the peak wavelength of the reflectance signal are missed due to the fixed position of the bands in the spectra obtained for all values of chlorophyll for which the modelling was conducted.

iii. Case 2 Water: Chlorophyll and MSS

Comparing Figure 5.11 for the hyperspectral data and Figures 5.12 to 5.15 for the multispectral data for water containing chlorophyll and MSS, similar problems with the multispectral figures that were observed previously occur. For chlorophyll concentrations, $Chl = 0$ and $0.1 mg\,m^{-3}$ (Figure 5.11 A and B and Figures 5.12 and 5.13) the multispectral sensors fail to reveal the fine structure contained between 400 and 570nm. They also fail to capture the position of the peak signal and the

variations in this position. The spectral area between 560 and 670nm, depending upon the position of the bands, is badly under-sampled, with changes in the gradient after 570nm being poorly reflected. A similar situation is observed in Figure 5.14 and Figure 5.15 for the higher chlorophyll concentrations. Again the lack of any real detail in the spectra between 570 and 750nm in the multispectral figures is noted.

iv. Case 2 Water: Chlorophyll, CDOM and MSS

Comparing the hyperspectral (Figure 5.16) and multispectral figures (Figure 5.17, 5.18 and 5.19) for case 2 water containing chlorophyll, CDOM and MSS the same problems are observed as described previously. In the case where $Chl = 0.1 mg\,m^{-3}$ the structure in the signal between 450 and 570nm is missed by the multispectral sensors. After 570nm there is a lack of detail in the multispectral figures and a large area of under sampling between 570 and 670nm, depending upon the positions of the bandwidths.

5. 4. Summary

a. A programme of Hydrolight radiance transfer modelling was carried out to investigate the potential of using high resolution, hyperspectral, $R_{rs}\left(0^{+}\right)$ spectra as a tool for retrieving information on the water body. Raman scattering from the water molecules was found to have only a small effect on the $R_{rs}\left(0^{+}\right)$ spectra. CDOM fluorescence is an important feature of the spectrum only in water with high CDOM levels $\left(\geq 1 m^{-1}\right)$ and low chlorophyll and MSS concentrations. Chlorophyll fluorescence produced a peak in the red which appeared to increase as the chlorophyll concentration increased. However, the peak was attenuated by the presence of CDOM and MSS. This effect will be examined further in Chapter 8.

b. The modelled hyperspectral $R_{rs}\left(0^{+}\right)$ spectra were scaled by their peak values in order to compare spectral shapes. Changes in spectral shape occurred due to

variations in the content of the water body. Increasing the chlorophyll concentration decreased the relative reflectance in the blue and a fluorescence peak emerged in the red. CDOM and MSS reduced the relative reflectance in the blue and green. At high levels of CDOM $\left(\geq 1m^{-1}\right)$, CDOM fluorescence can be a significant feature of the $R_{rs}\left(0^{+}\right)$ spectrum. MSS increased the relative reflectance in the red due to backscattering.

c. Comparing the high resolution data with discrete bandwidth multispectral data, obtained by binning into SeaWiFS, MODIS and MERIS wavebands, revealed several limitations in the multispectral data. These were loss of detail and fine structure in the spectrum due to the binning process and linear interpolation between wavebands, areas of spectral under sampling and loss of peak positions. The main area of spectral under sampling occurred between 560 and 670nm, depending upon the position of the wavebands. Variations in the peak position were missed due to the fixed nature of the wavebands.

The question of whether the higher resolution data can offer any useful information on the content of the water body is posed in the next chapter.

BAND	CENTRAL WAVELENGTH (NM)	BANDWIDTH (NM)
1	412	402-412
2	443	433-453
3	490	480-500
4	510	500-520
5	555	545-565
6	670	660-680

Table 5.1. SeaWiFS wavebands used to transform hyperspectral data into multispectral spectra.

BAND	CENTRAL WAVELENGTH (NM)	BANDWIDTH (NM)
8	411.3	405-420
9	442.0	438-448
10	486.9	483-493
11	529.6	526-536
12	546.8	546-556
13	665.5	662-672
14	676.8	673-683
15	746.4	743-753

Table 5.2. MODIS wavebands used to transform hyperspectral data into multispectral spectra.

BAND	CENTRAL WAVELENGTH (NM)	BANDWIDTH (NM)
1	412.5	407.5-417.5
2	442.5	437.5-447.5
3	490	485-495
4	510	505-515
5	560	555-565
6	620	615-625
7	665	660-670
8	681.25	677.5-685
9	705	695-710

Table 5.3. MERIS wavebands used to transform hyperspectral data into multispectral spectra.

(A)

CASE 2: CHL AND CDOM	
Chlorophyll $\left(mg\,m^{-3}\right)$	0, 0.1, 1, 10
CDOM $\left(m^{-1}\right)$	0.1, 0.25, 0.5, 0.75, 1, 1.25, 1.5, 2

(B)

CASE 2: CHL AND MSS	
Chlorophyll $\left(mg\,m^{-3}\right)$	0, 0.1, 1, 10
MSS $\left(mg\,l^{-1}\right)$	1, 2, 5, 7, 10

(C)

CASE2: CHL, CDOM AND MSS	
Chlorophyll $\left(mg\,m^{-3}\right)$	0, 0.1, 1, 10
CDOM $\left(m^{-1}\right)$	0.1, 0.5, 1
MSS $\left(mg\,l^{-1}\right)$	0.1, 1, 10

Table 5.4. Chlorophyll, CDOM and MSS concentrations used in Hydrolight case 2 models. (A) shows the values of chlorophyll and CDOM used in this batch of models. (B) shows the values of chlorophyll and MSS used in this batch of models. (C) shows the values of chlorophyll, CDOM and MSS used in this batch of models. For batches of models ran using the values in (A) and (B) the chlorophyll concentration was held constant while the CDOM/MSS was varied. For the batch of runs carried out using the information in (C) the chlorophyll concentration was held constant for all possible combinations of CDOM and MSS.

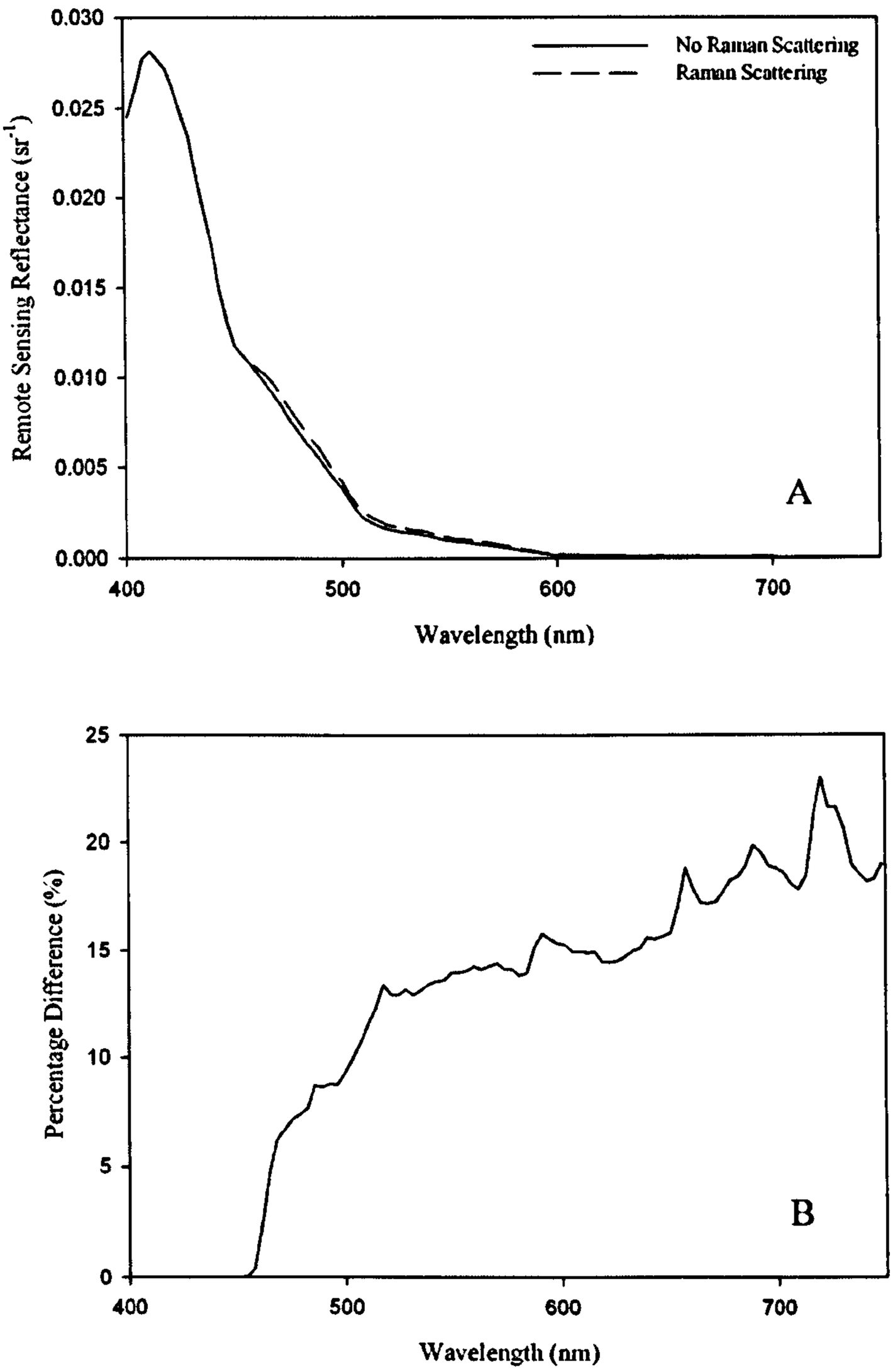

Figure 5.1. Raman scattering. Panel (A) illustrates modelled $R_{rs}\left(0^{+}\right)$ with and without Raman scattering included. Panel (B) illustrates the percentage difference in $R_{rs}\left(0^{+}\right)$ between the spectra in which Raman scattering has been included and excluded. The models used the Hydrolight ABCase1 model with the chlorophyll concentration set equal to $0 mg\, m^{-3}$.

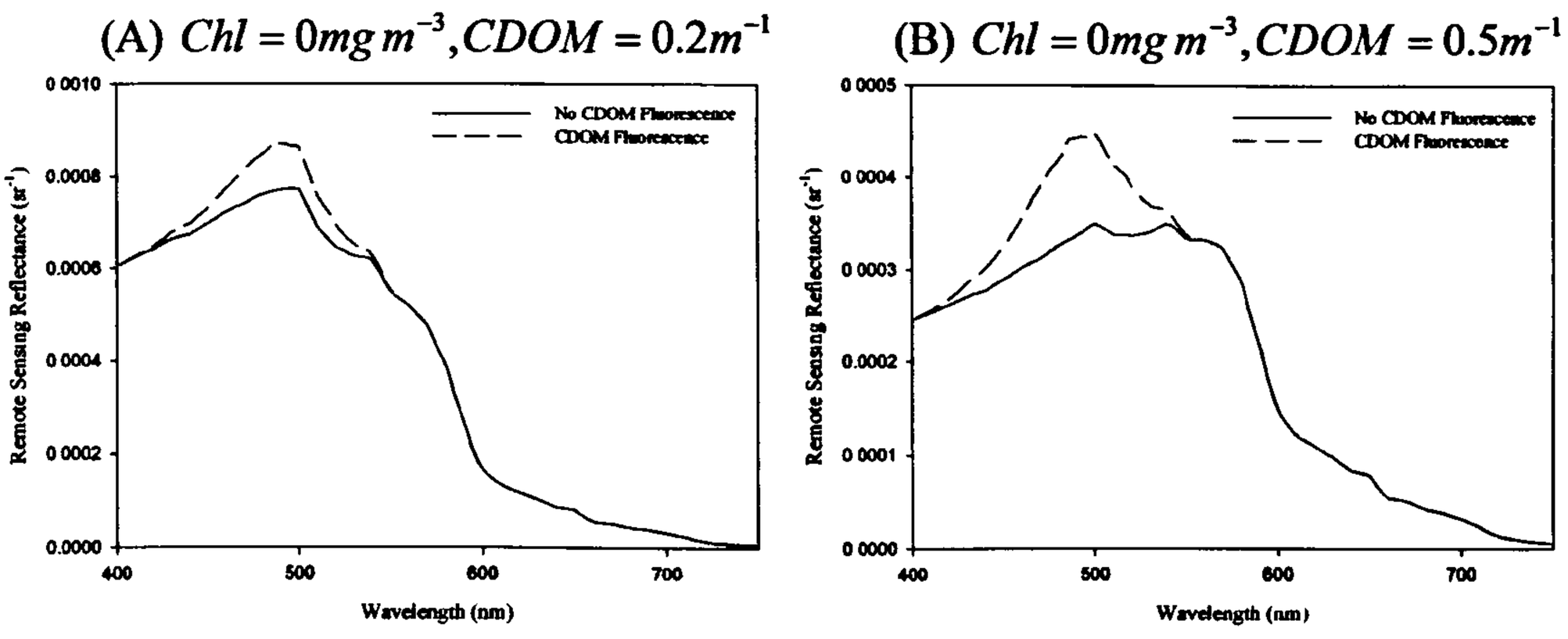

Figure 5.2. CDOM fluorescence: Hydrolight ABCase2 model. The chlorophyll concentration was set to $0mg\,m^{-3}$ and the CDOM value was (A) $0.2m^{-1}$, (B) $0.5m^{-1}$, (C) $1m^{-1}$ and (D) $2m^{-1}$. In all cases two runs were carried out, one in which CDOM fluorescence was included and the other in which it was excluded.

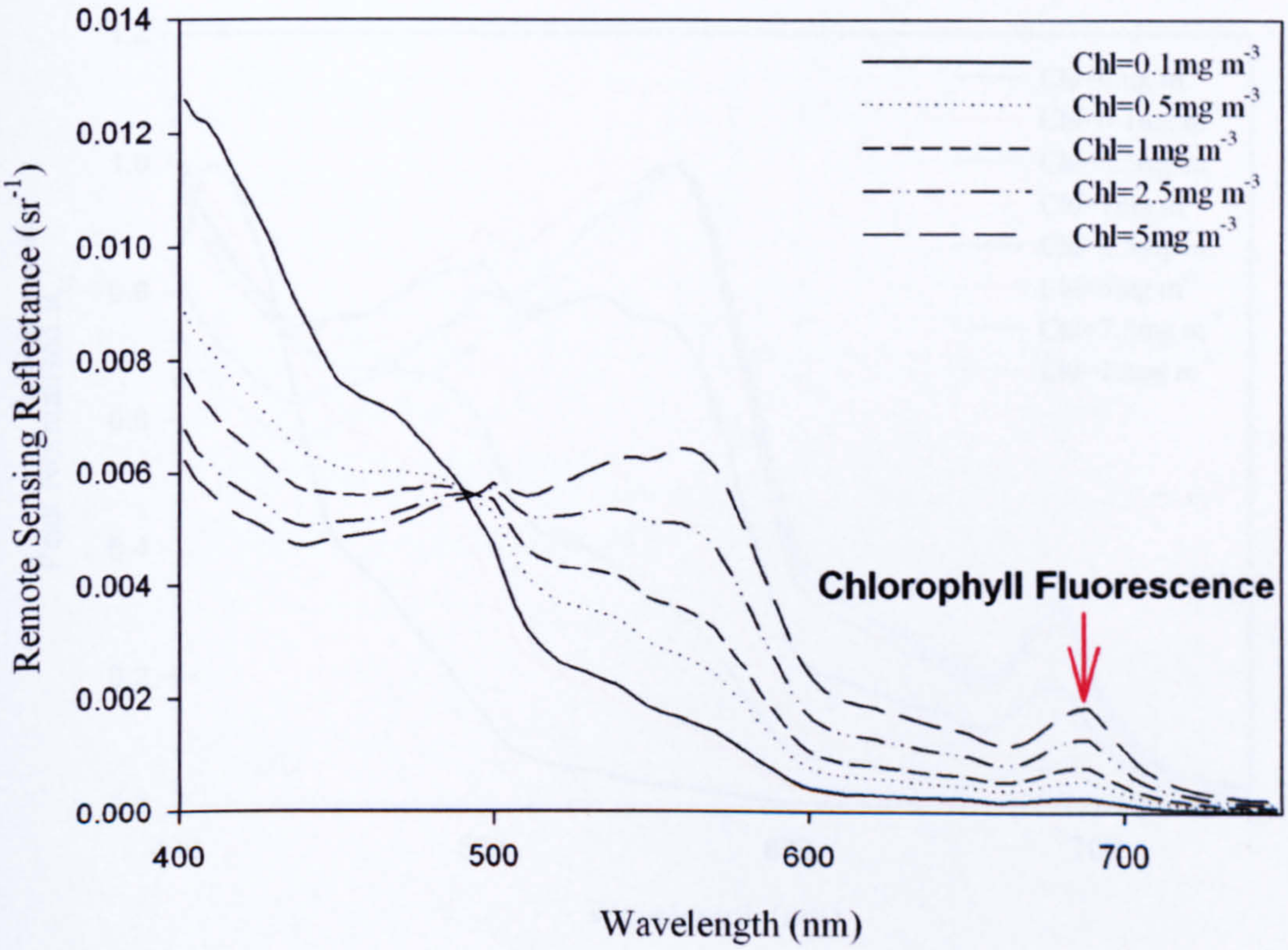

Figure 5.3. Effects of including the inelastic process of chlorophyll fluorescence on the $R_{rs}\left(0^{+}\right)$ spectra, modelled using the Hydrolight ABCase1 model for a variety of chlorophyll concentrations with Raman scattering and CDOM fluorescence included.

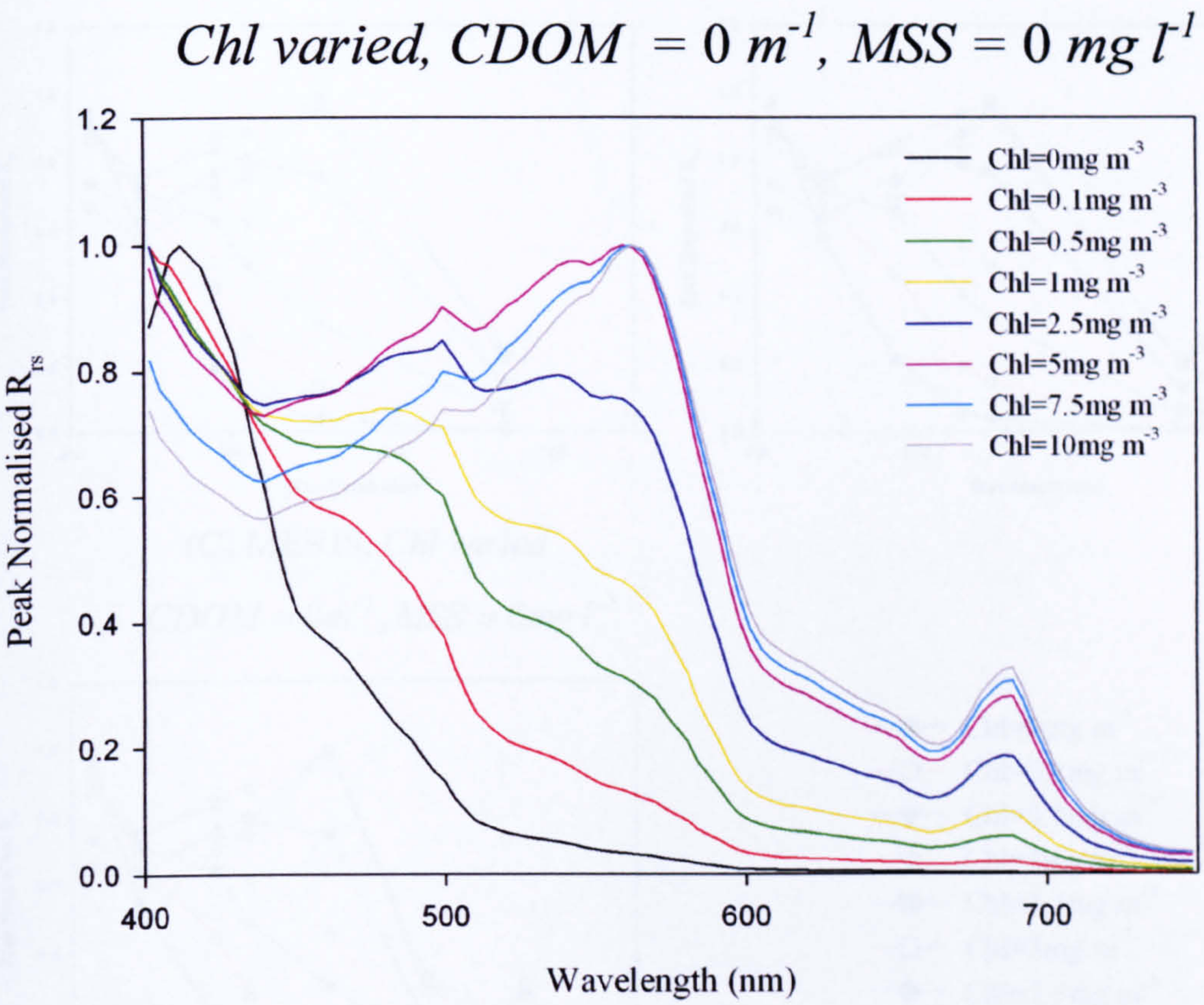

Figure 5.4. Hyperspectral normalised remote sensing reflectance spectra for case 1 waters modelled with Hydrolight using the ABCase1 model for various chlorophyll concentrations. The curves were normalised using the maximum R_{rs} value for each spectrum.

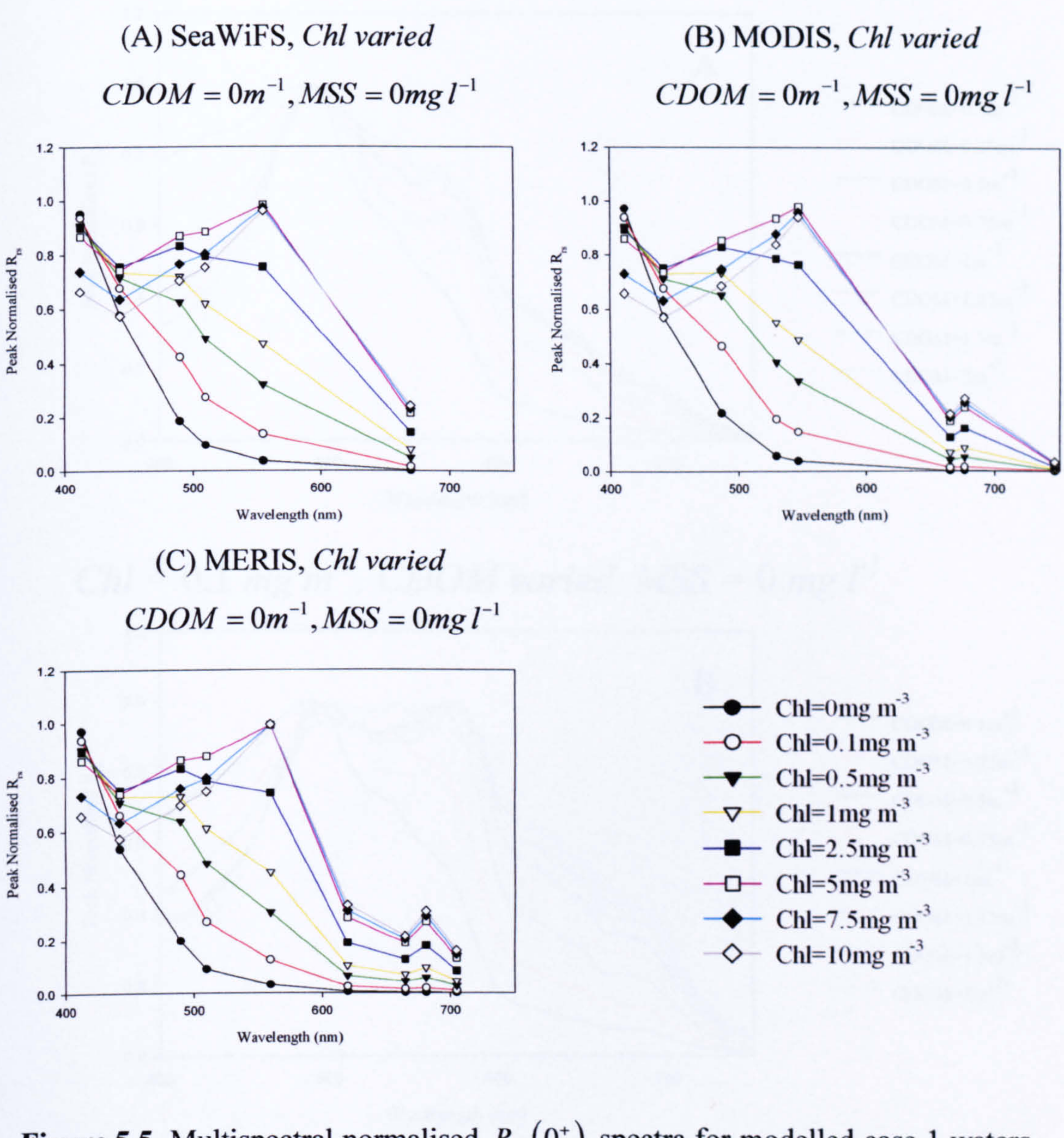

Figure 5.5. Multispectral normalised $R_{rs}\left(0^{+}\right)$ spectra for modelled case 1 waters. Panels (A) to (C) illustrate the spectra obtained by binning Hydrolight hyperspectral outputs into (A) SeaWiFS, (B) MODIS and (C) MERIS wavebands.

Chl = 0 *mg* m^{-3}, *CDOM varied, MSS* = 0 *mg* l^{-1}

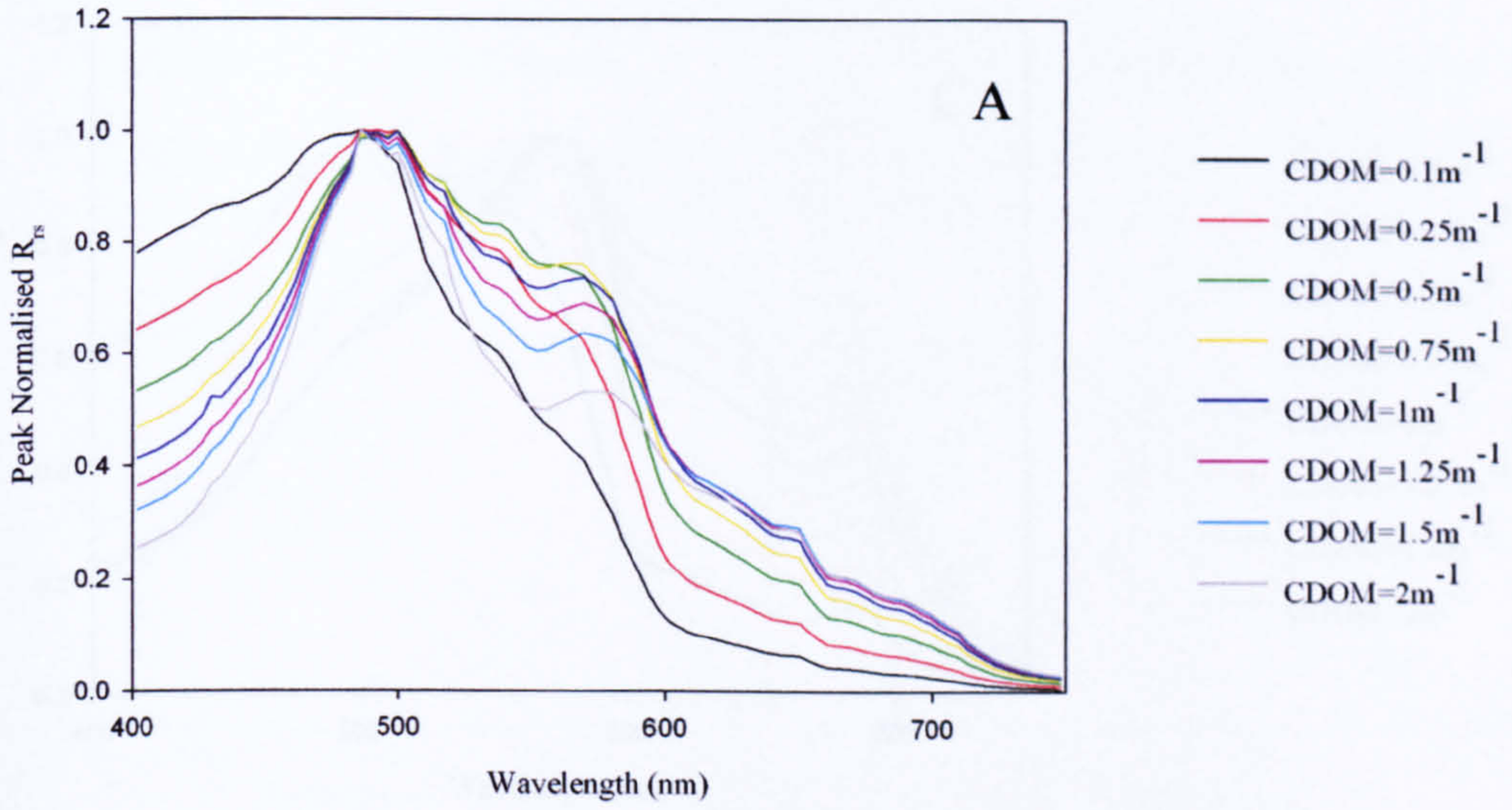

Chl = 0.1 *mg* m^{-3}, *CDOM varied, MSS* = 0 *mg* l^{-1}

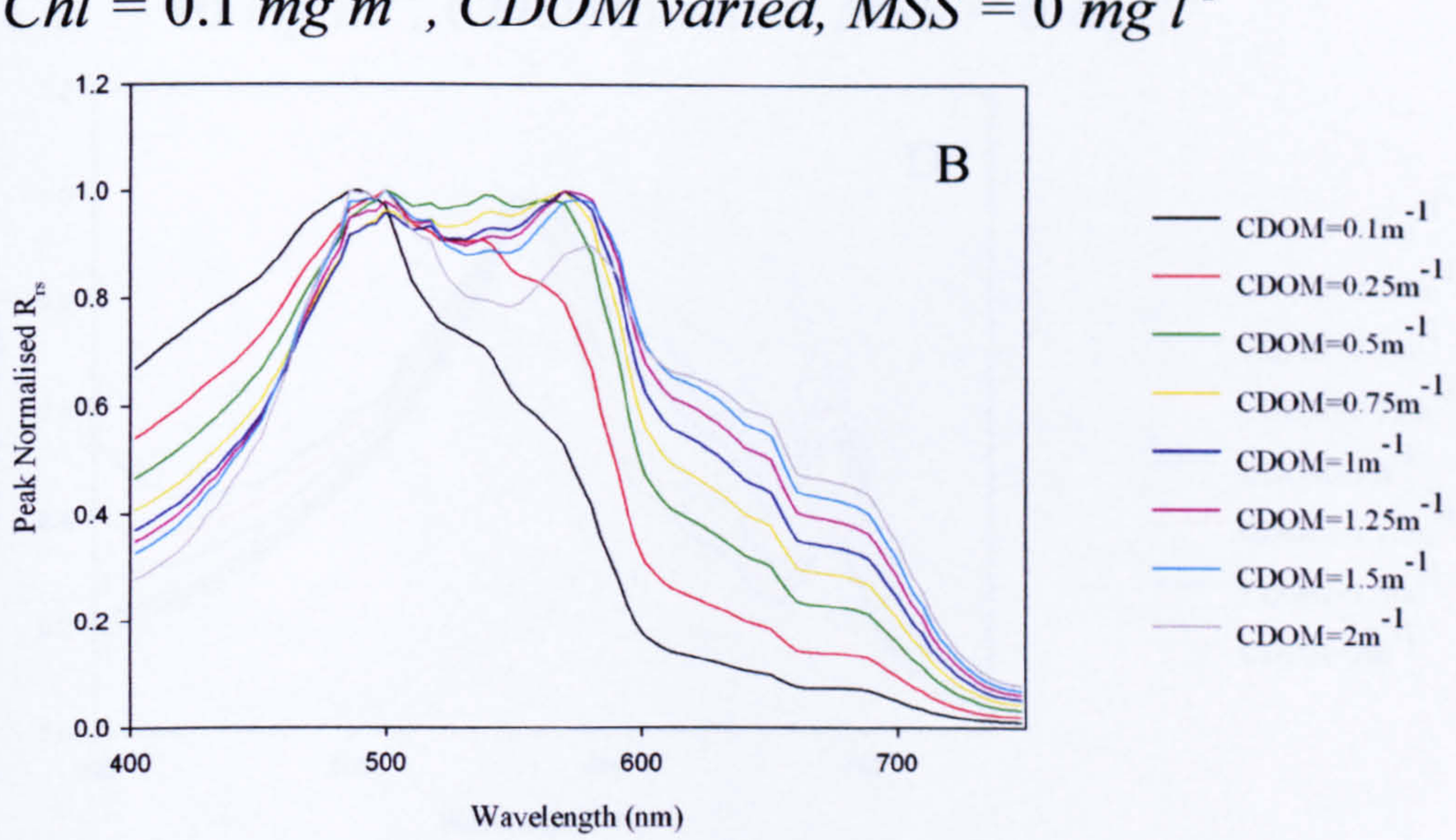

Figure 5.6. (i) Normalised $R_{rs}\left(0^{+}\right)$ spectra for case 2 waters containing chlorophyll and CDOM. In panels (A) to (D) the chlorophyll concentration was held constant while the CDOM concentration was varied. In (A) $Chl = 0\,mg\,m^{-3}$ and (B) $Chl = 0.1\,mg\,m^{-3}$.

$Chl = 1\ mg\ m^{-3}$, $CDOM$ varied, $MSS = 0\ mg\ l^{-1}$

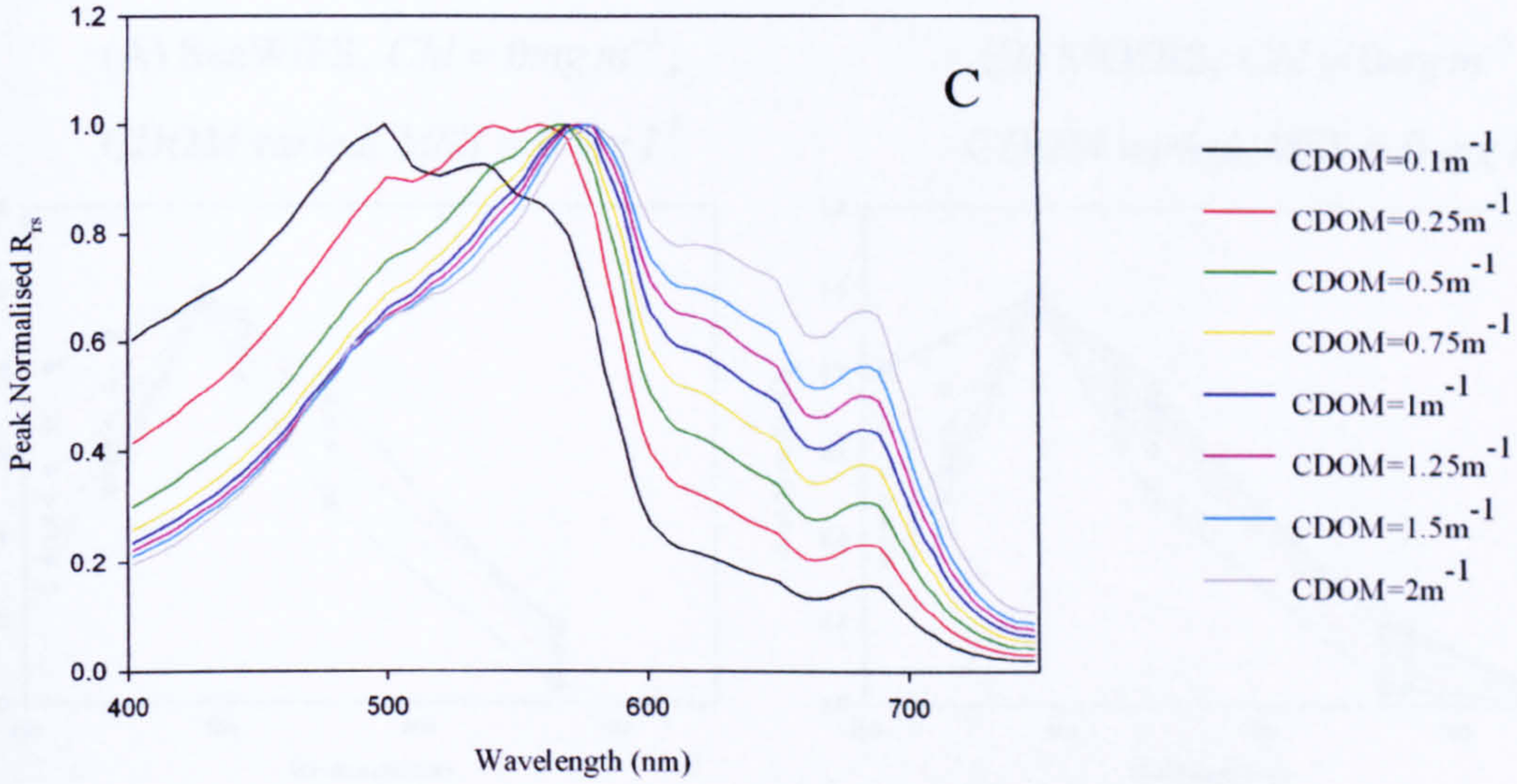

$Chl = 10\ mg\ m^{-3}$, $CDOM$ varied, $MSS = 0\ mg\ l^{-1}$

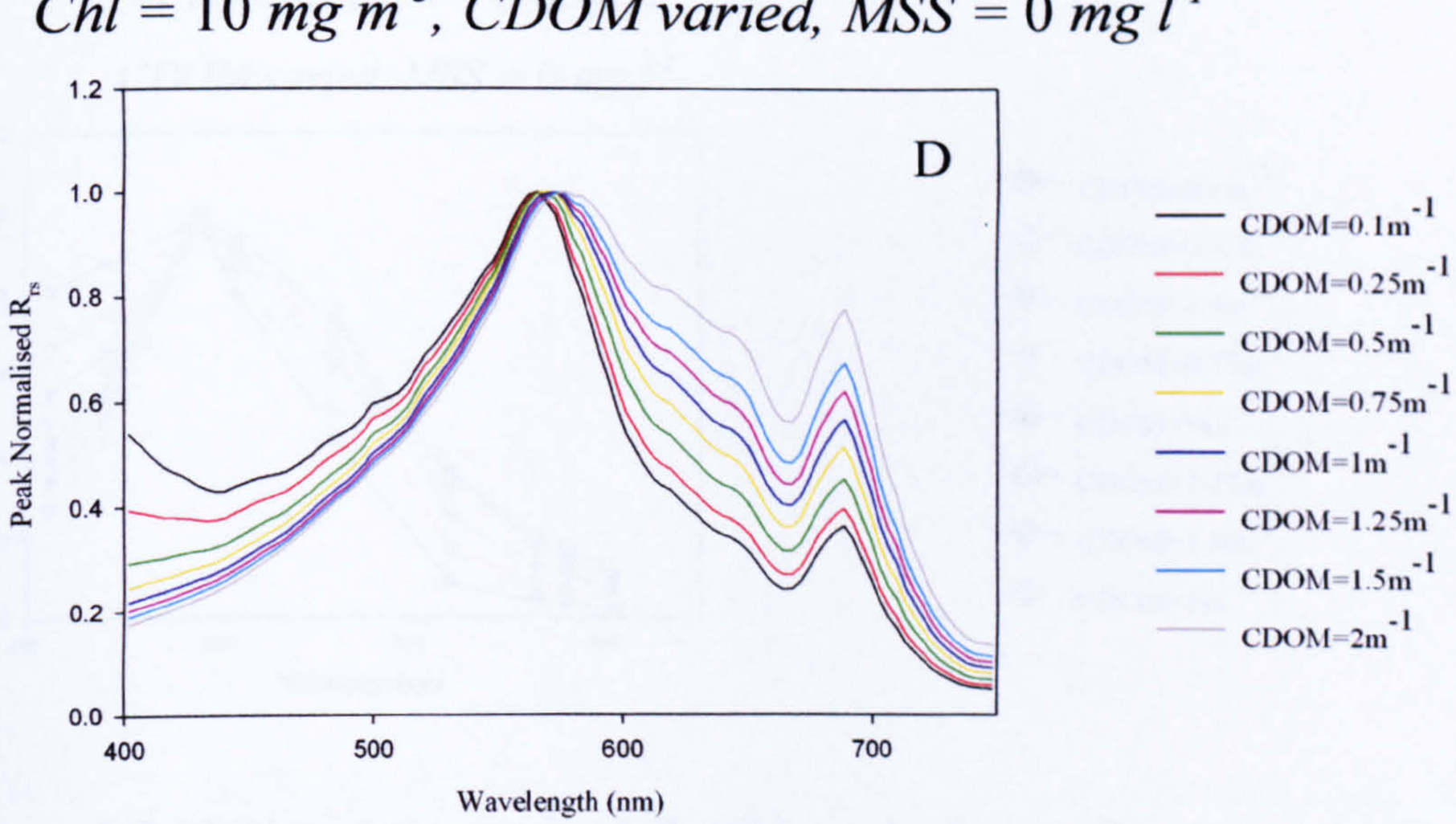

Figure 5.6. (ii) Normalised $R_{rs}\left(0^{+}\right)$ spectra for case 2 waters containing chlorophyll and CDOM. In (C) $Chl = 1 mg\, m^{-3}$ and (D) $Chl = 10 mg\, m^{-3}$.

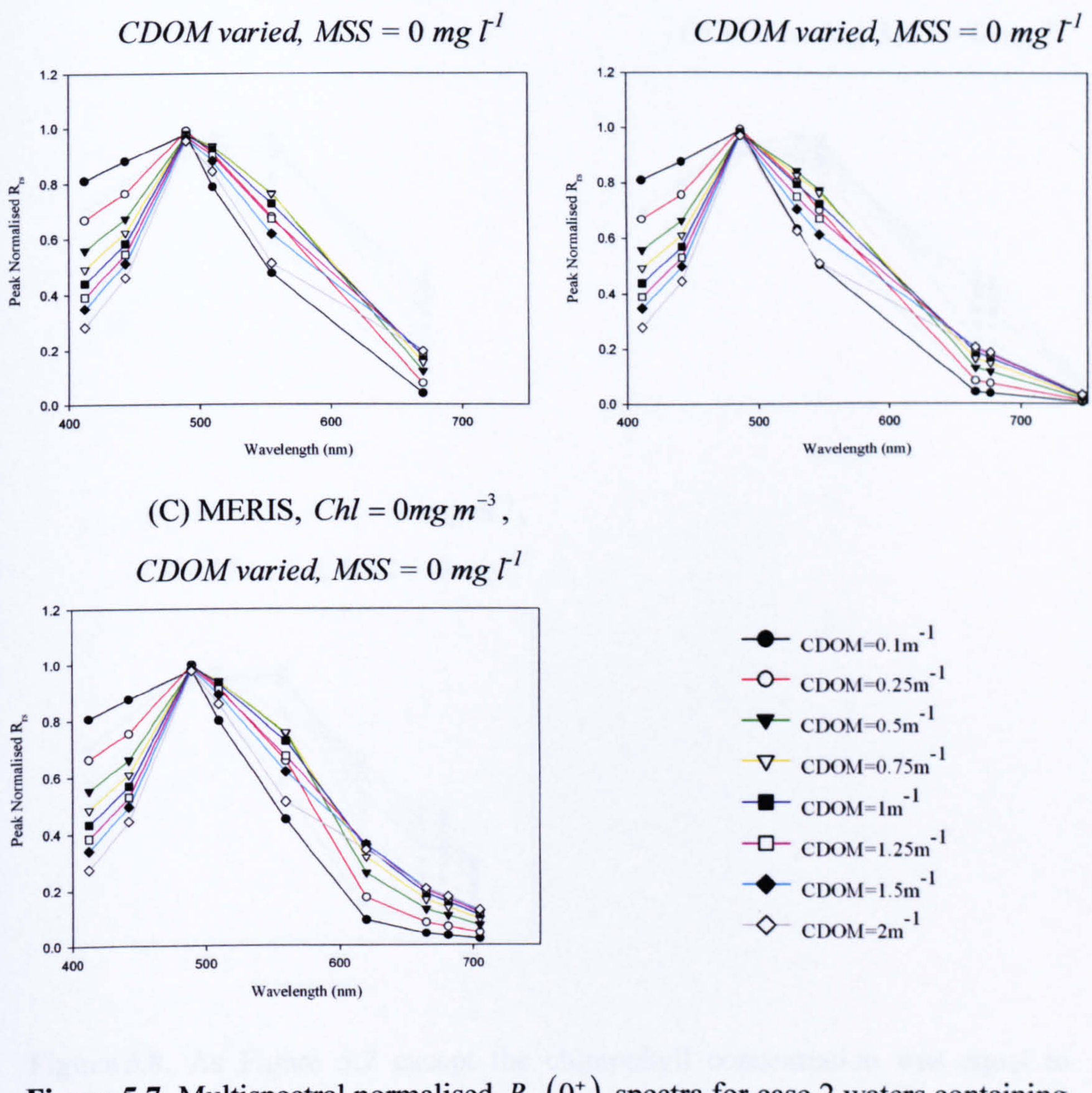

Figure 5.7. Multispectral normalised $R_{rs}\left(0^{+}\right)$ spectra for case 2 waters containing chlorophyll and CDOM. Panels (A) to (C) illustrate the spectra obtained by binning Hydrolight hyperspectral outputs into (A) SeaWiFS, (B) MODIS and (C) MERIS wavebands. For the spectra shown above the chlorophyll concentration was equal to $0 mg\,m^{-3}$ and the CDOM concentration was varied.

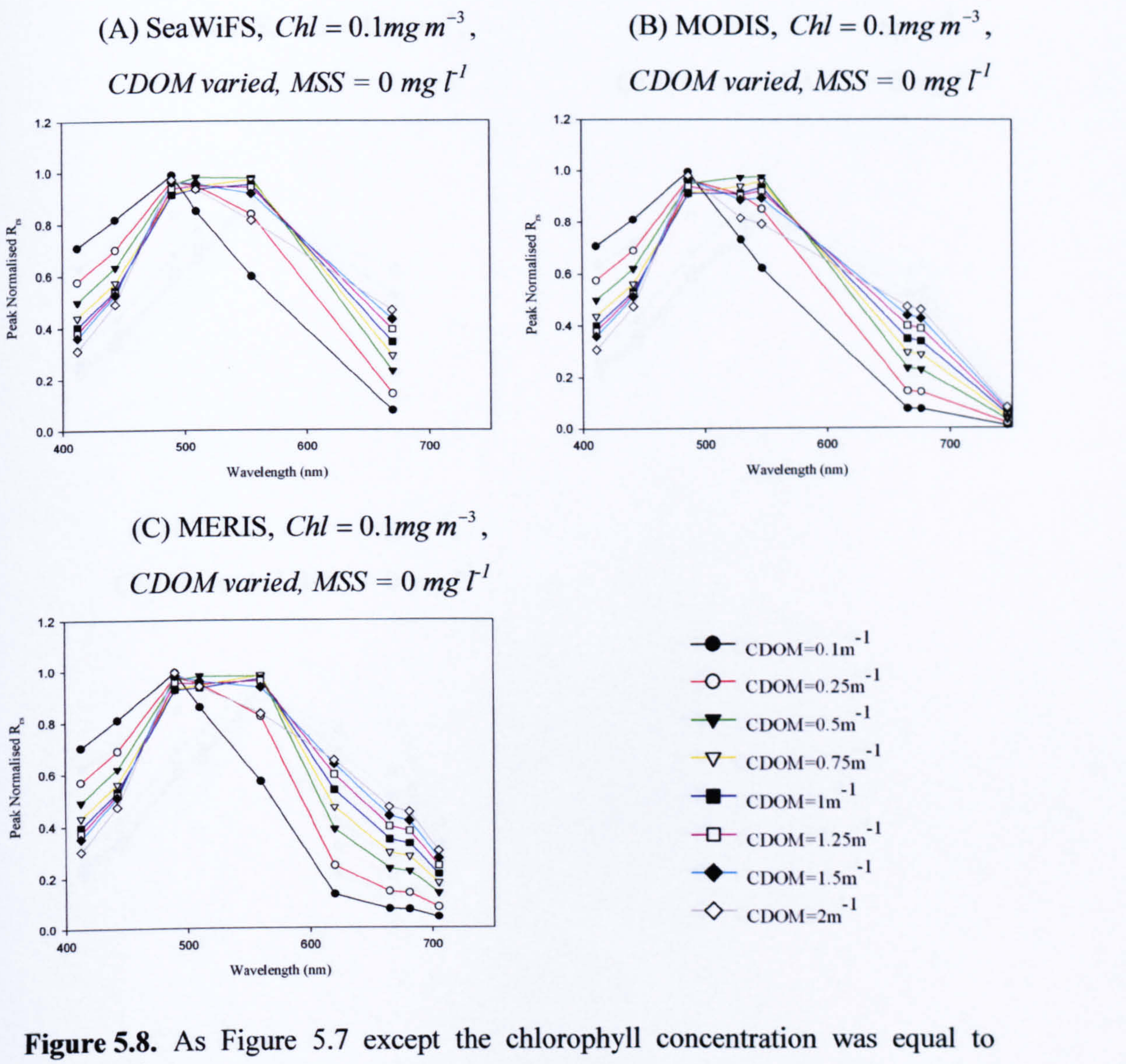

Figure 5.8. As Figure 5.7 except the chlorophyll concentration was equal to $0.1mg\,m^{-3}$.

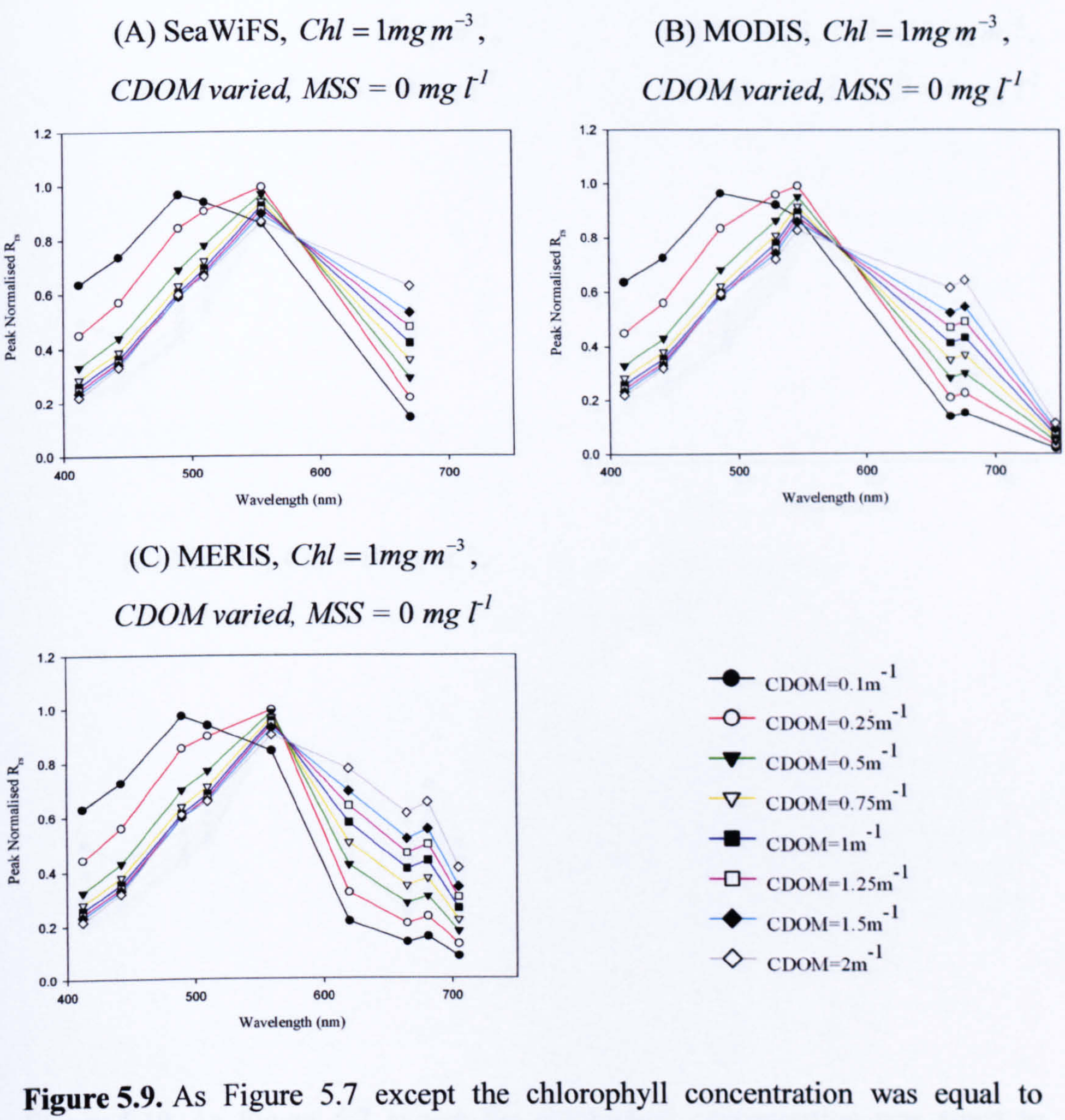

Figure 5.9. As Figure 5.7 except the chlorophyll concentration was equal to $1mg\,m^{-3}$.

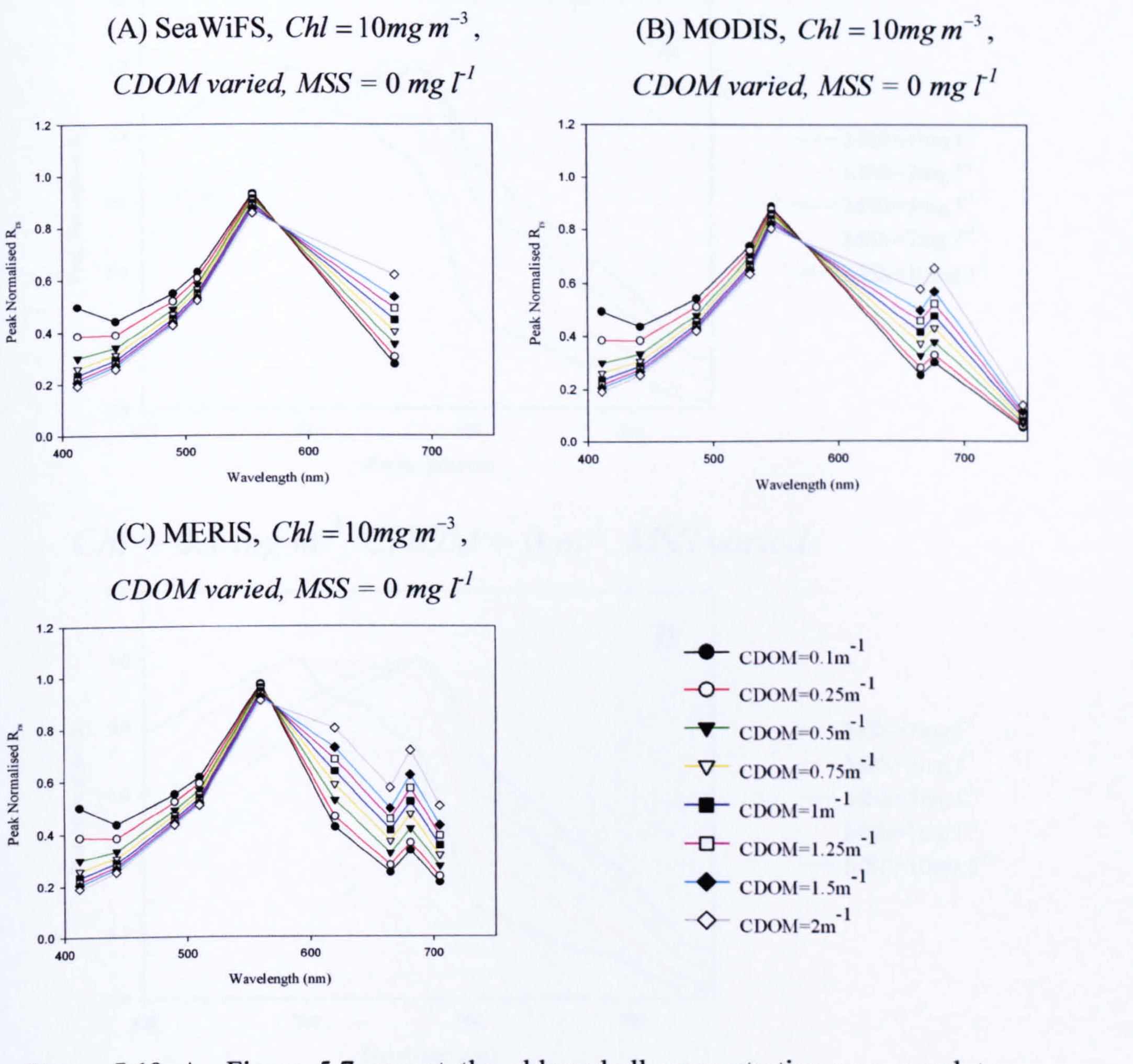

Figure 5.10. As Figure 5.7 except the chlorophyll concentration was equal to $10\,mg\,m^{-3}$.

Chl = 0 *mg* m^{-3}, *CDOM* = 0 m^{-1}, *MSS varied*

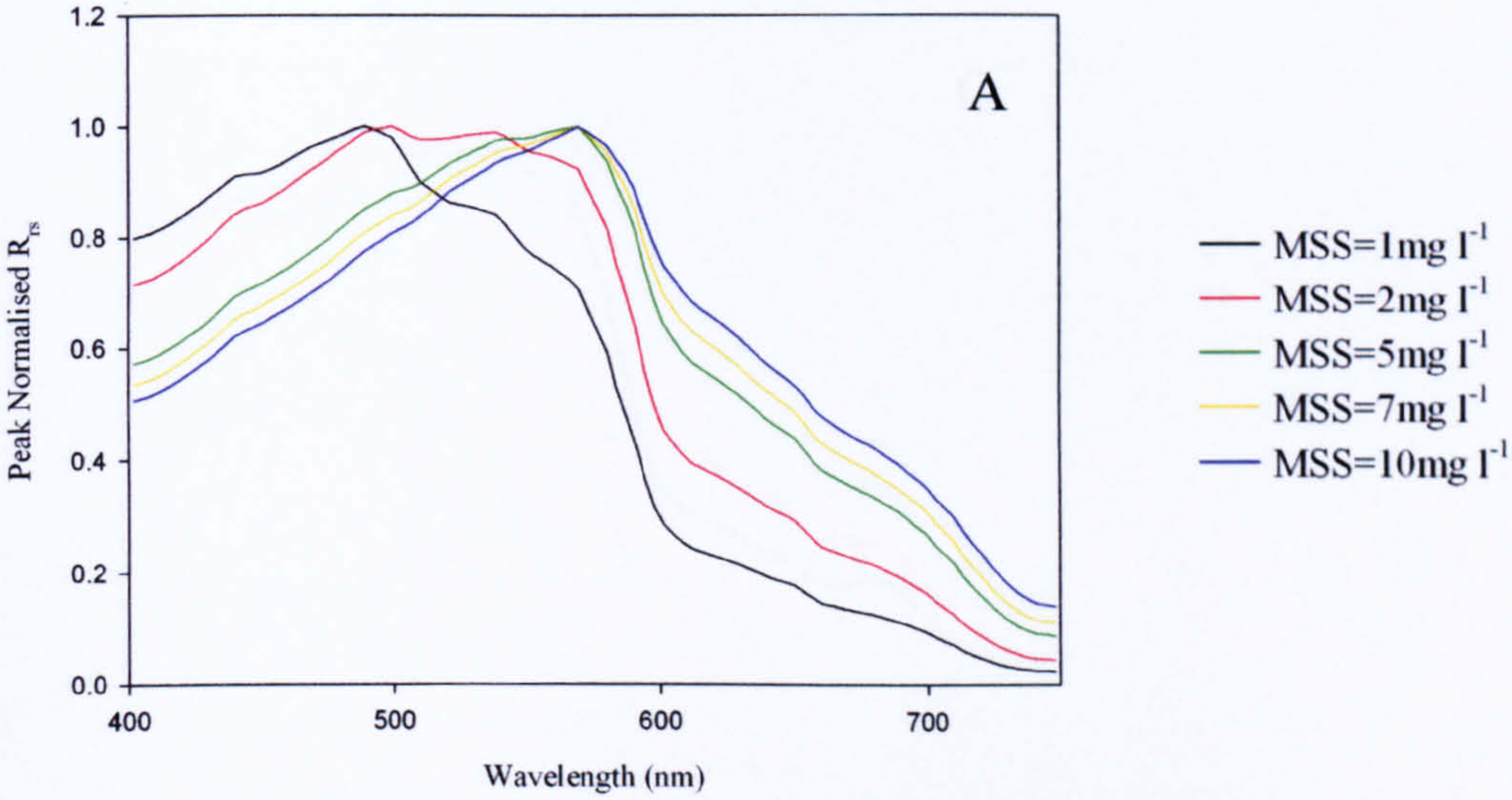

Chl = 0.1 *mg* m^{-3}, *CDOM* = 0 m^{-1}, *MSS varied*

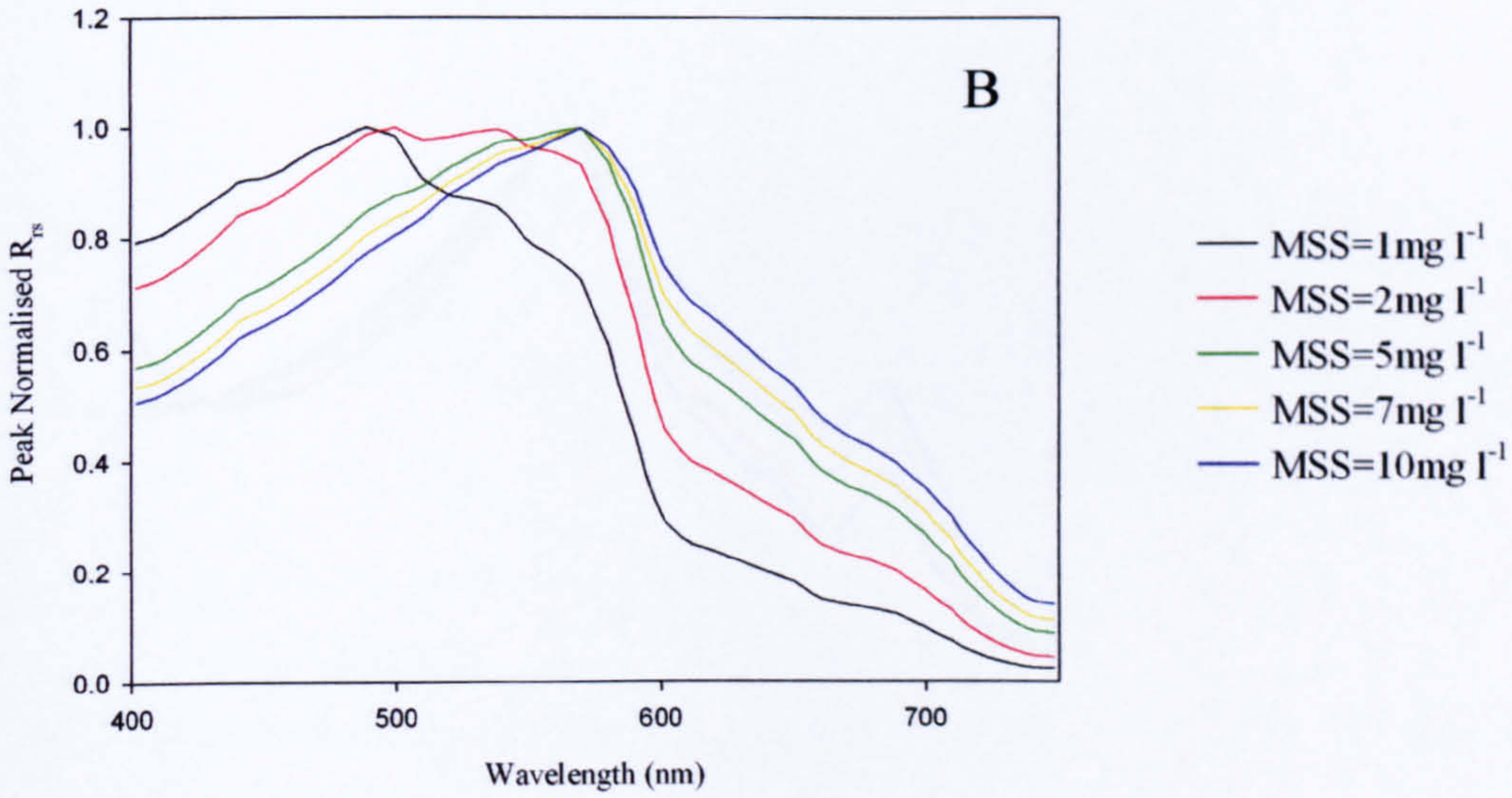

Figure 5.11. (i) Hyperspectral normalised $R_{rs}\left(0^{+}\right)$ spectra for case 2 waters containing chlorophyll and MSS. In panels (A) to (D) the chlorophyll concentration was held constant while the MSS concentration was varied. . In (A) $Chl = 0\,mg\,m^{-3}$, and (B) $Chl = 0.1\,mg\,m^{-3}$.

$Chl = 1\ mg\ m^{-3}$, $CDOM = 0\ m^{-1}$, *MSS varied*

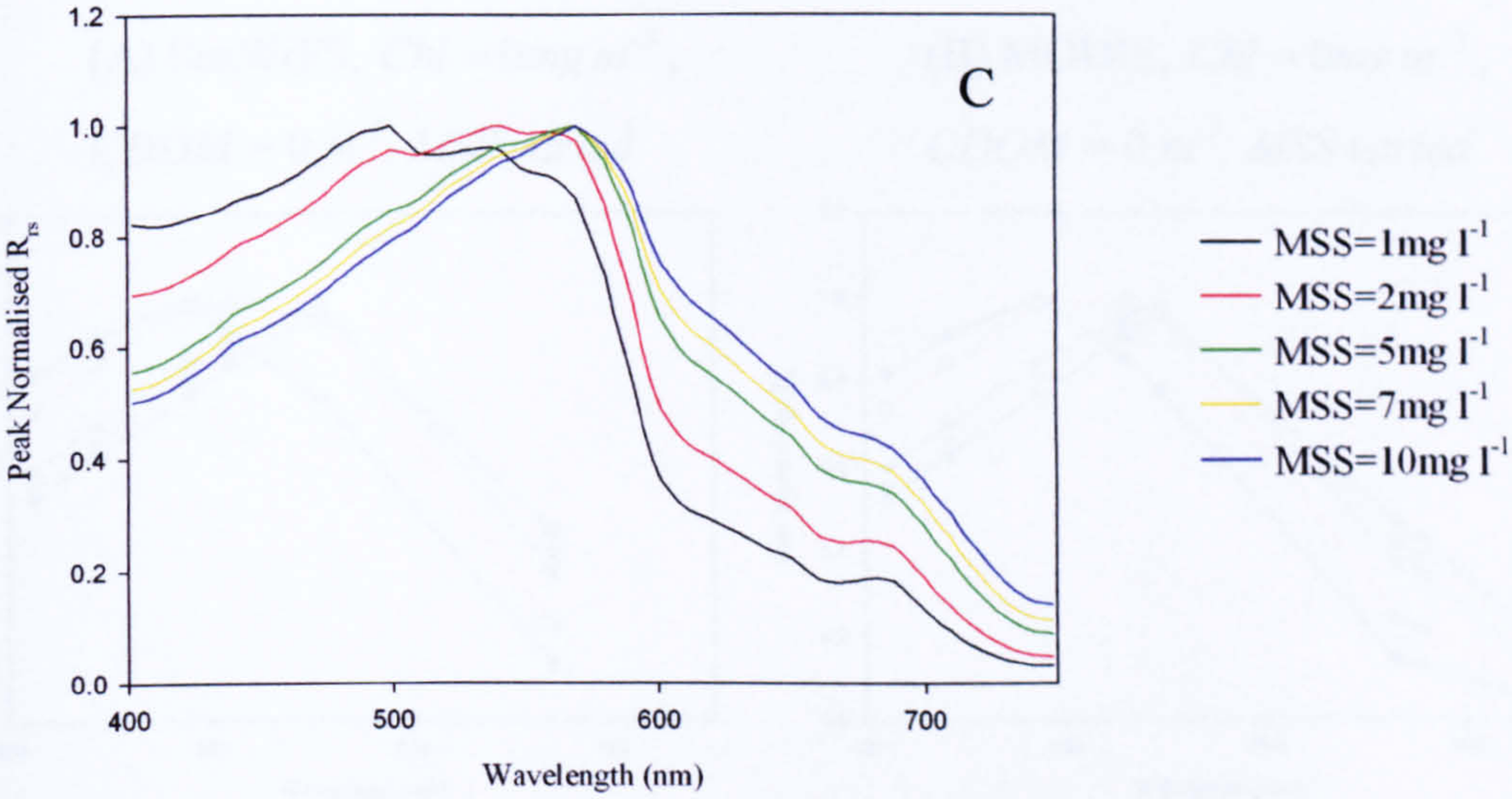

$Chl = 10\ mg\ m^{-3}$, $CDOM = 0\ m^{-1}$, *MSS varied*

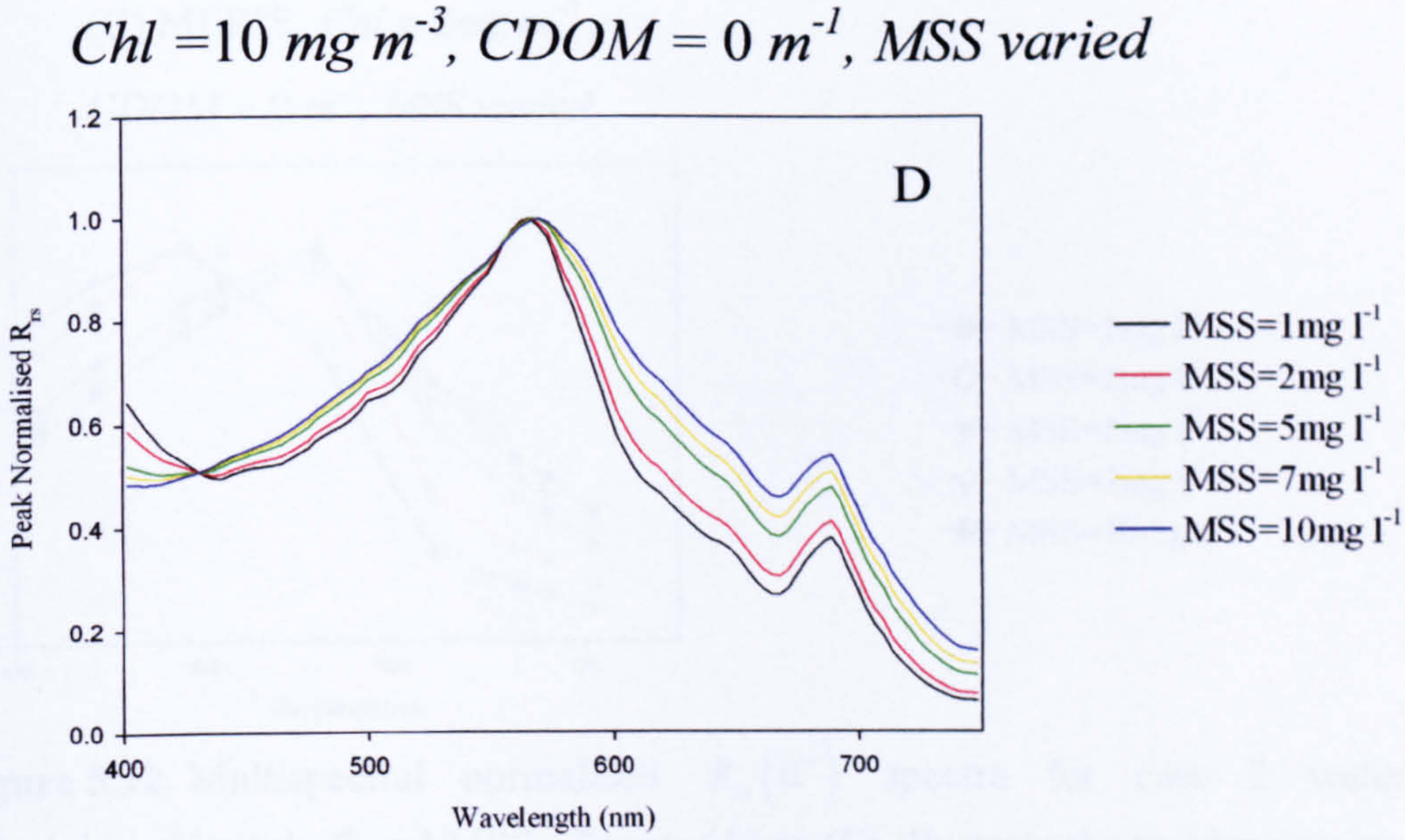

Figure 5.11. (ii) Hyperspectral normalised $R_{rs}\left(0^{+}\right)$ spectra for case 2 waters containing chlorophyll and MSS. In (C) $Chl = 1\,mg\,m^{-3}$ and (D) $Chl = 10\,mg\,m^{-3}$.

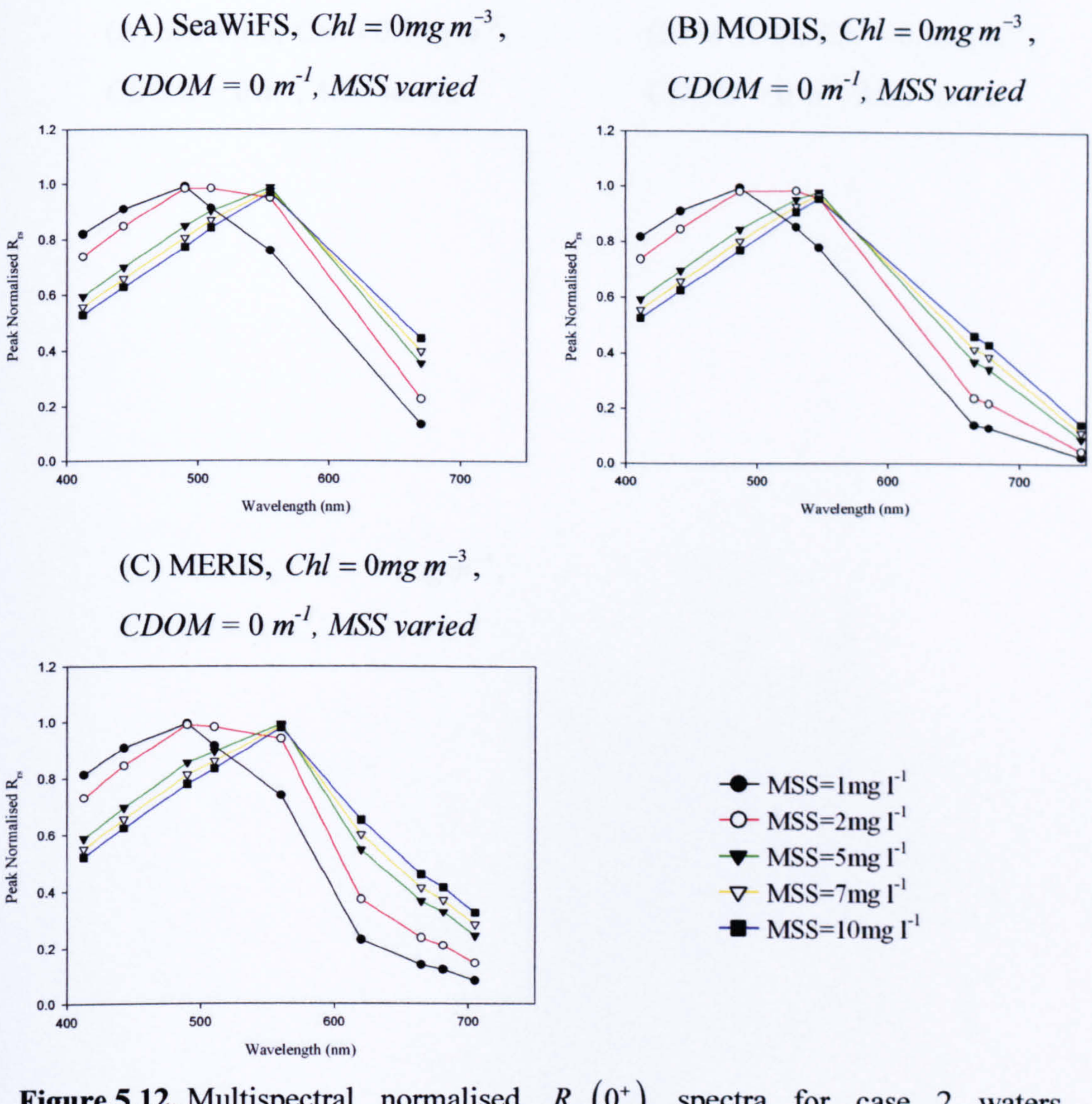

Figure 5.12. Multispectral normalised $R_{rs}\left(0^{+}\right)$ spectra for case 2 waters containing chlorophyll and MSS. Panels (A) to (C) illustrate the spectra obtained by binning Hydrolight hyperspectral outputs into (A) SeaWiFS, (B) MODIS and (C) MERIS wavebands. For the spectra shown above the chlorophyll concentration was equal to $0\,mg\,m^{-3}$ and the MSS concentration was varied.

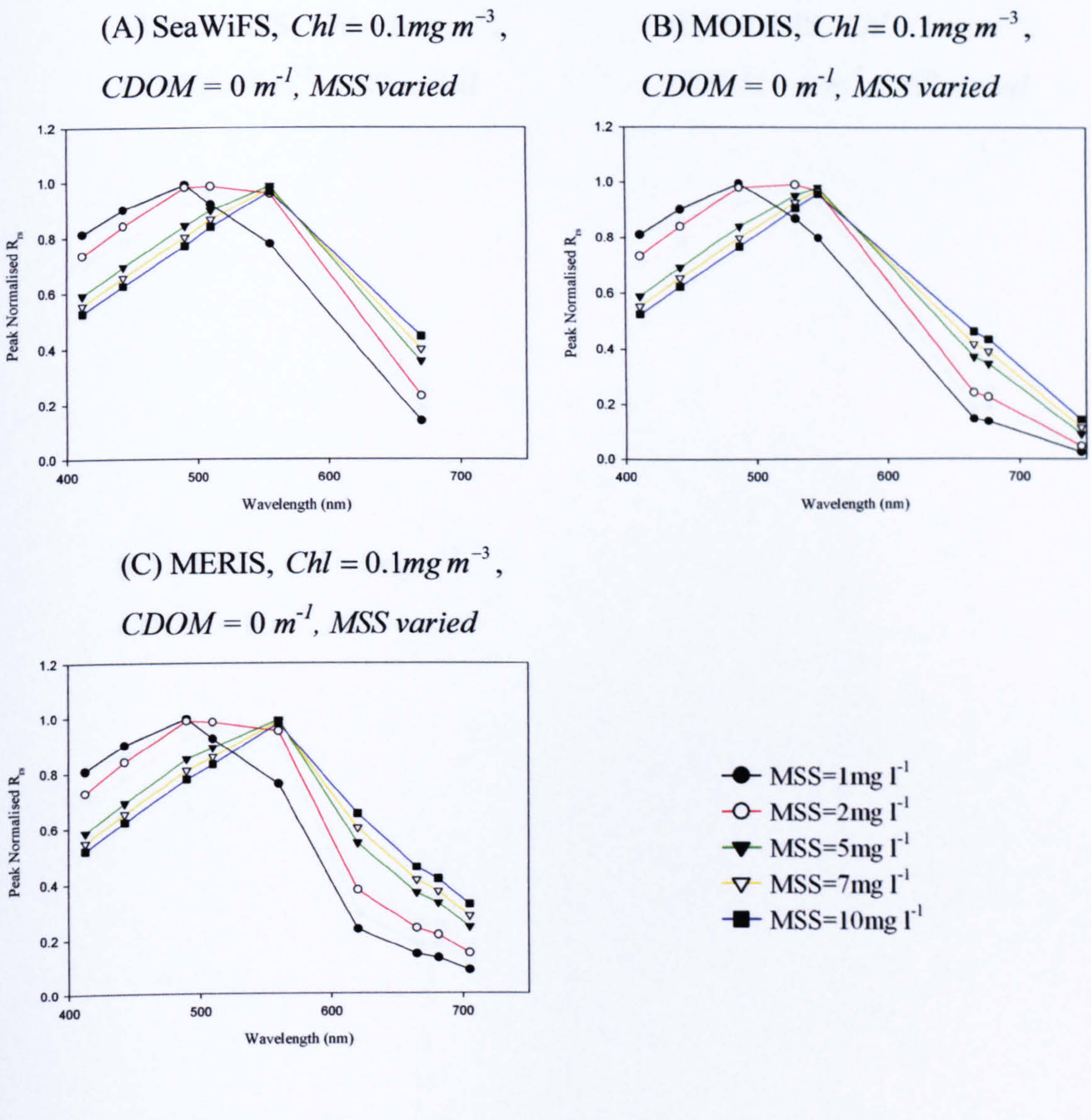

Figure 5.13. As Figure 5.12 except the chlorophyll concentration was equal to $0.1mg\,m^{-3}$.

(A) SeaWiFS, $Chl = 1 mg\, m^{-3}$,
$CDOM = 0\ m^{-1}$, *MSS varied*

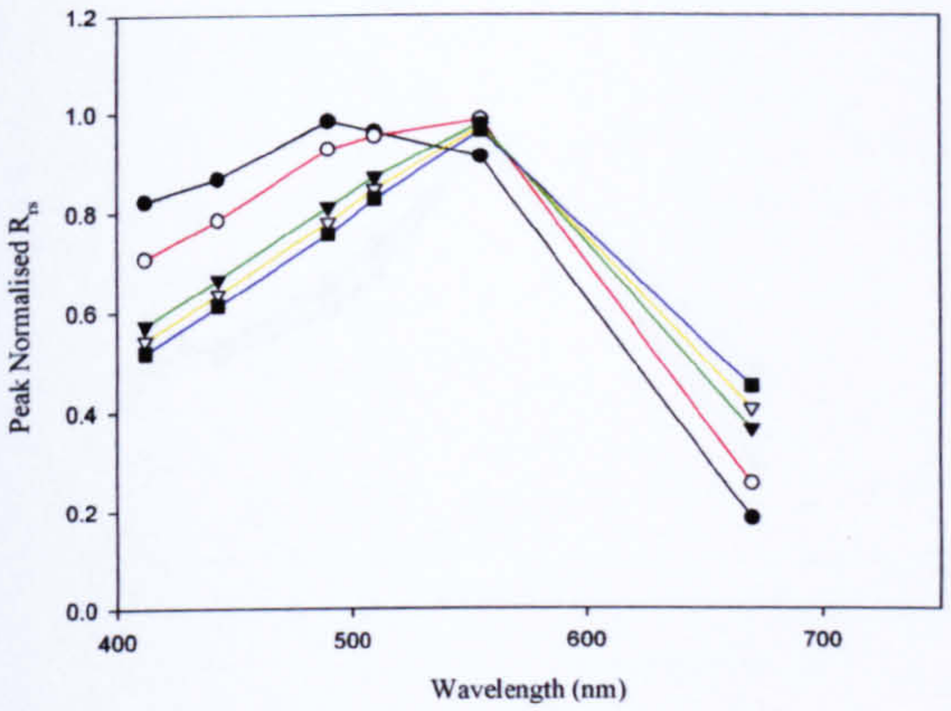

(B) MODIS, $Chl = 1 mg\, m^{-3}$,
$CDOM = 0\ m^{-1}$, *MSS varied*

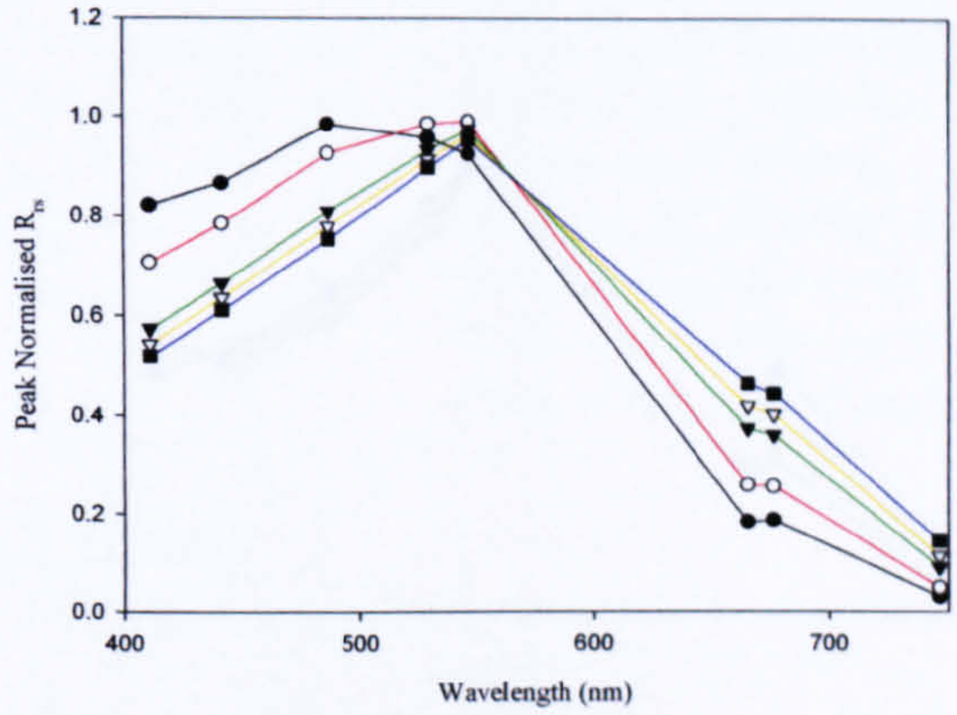

(C) MERIS, $Chl = 1 mg\, m^{-3}$,
$CDOM = 0\ m^{-1}$, *MSS varied*

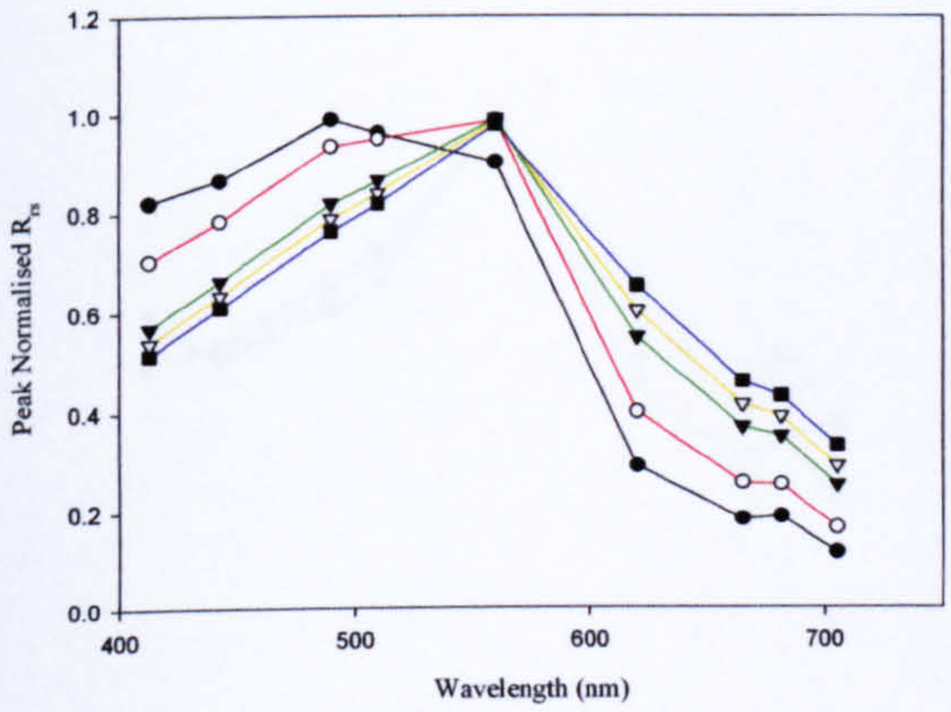

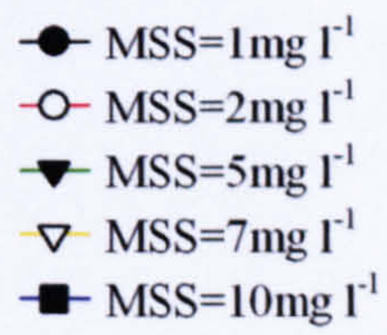

Figure 5.14. As Figure 5.12 except the chlorophyll concentration was equal to $1 mg\, m^{-3}$.

(A) SeaWiFS, $Chl = 10 mg\, m^{-3}$,

CDOM = 0 m^{-1}, MSS varied

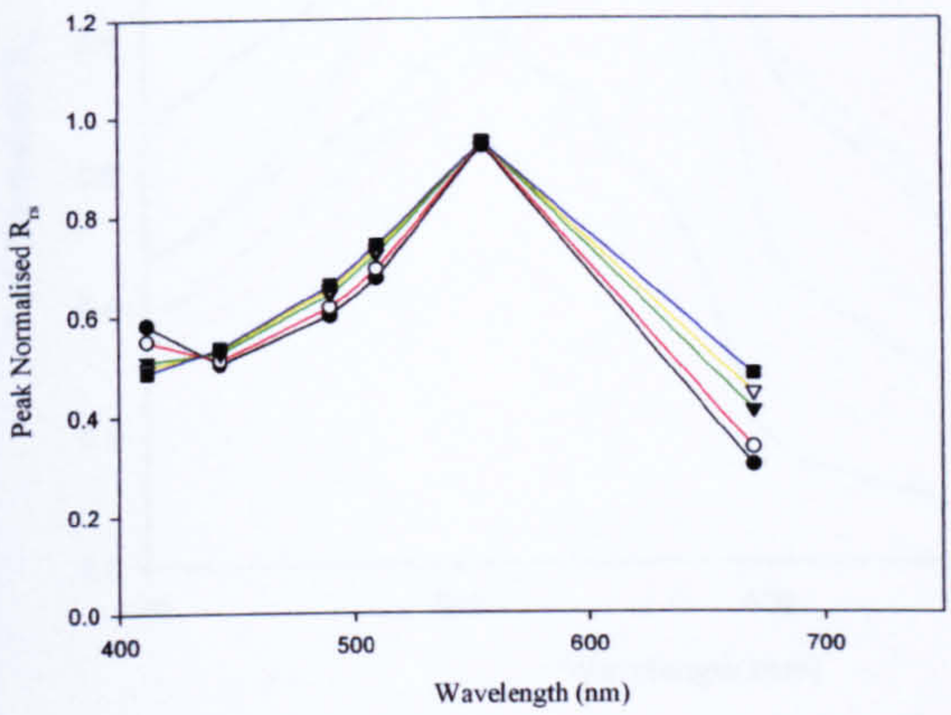

(B) MODIS, $Chl = 10 mg\, m^{-3}$,

CDOM = 0 m^{-1}, MSS varied

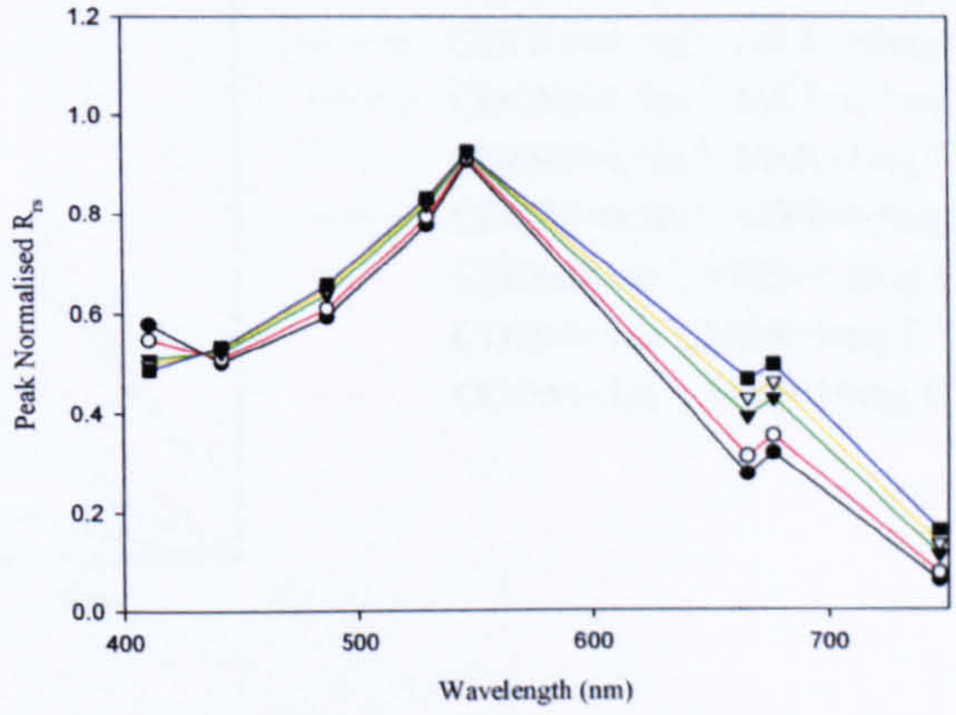

(C) MERIS, $Chl = 10 mg\, m^{-3}$,

CDOM = 0 m^{-1}, MSS varied

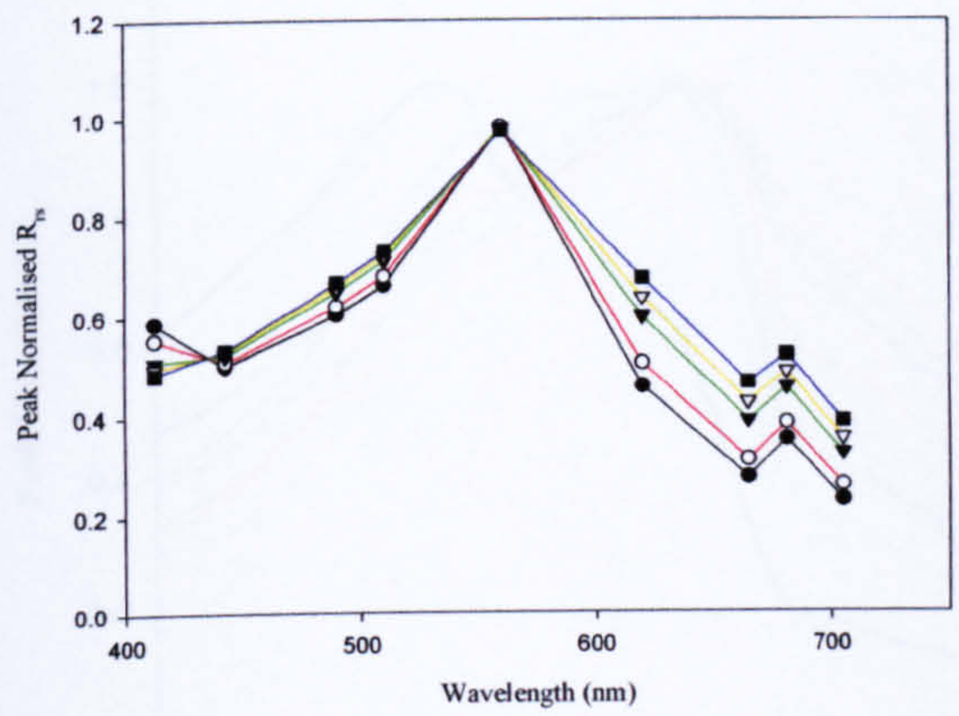

Figure 5.15. As Figure 5.12 except the chlorophyll concentration was equal to $10 mg\, m^{-3}$.

Chl = 0 *mg* m^{-3}, *CDOM and MSS varied*

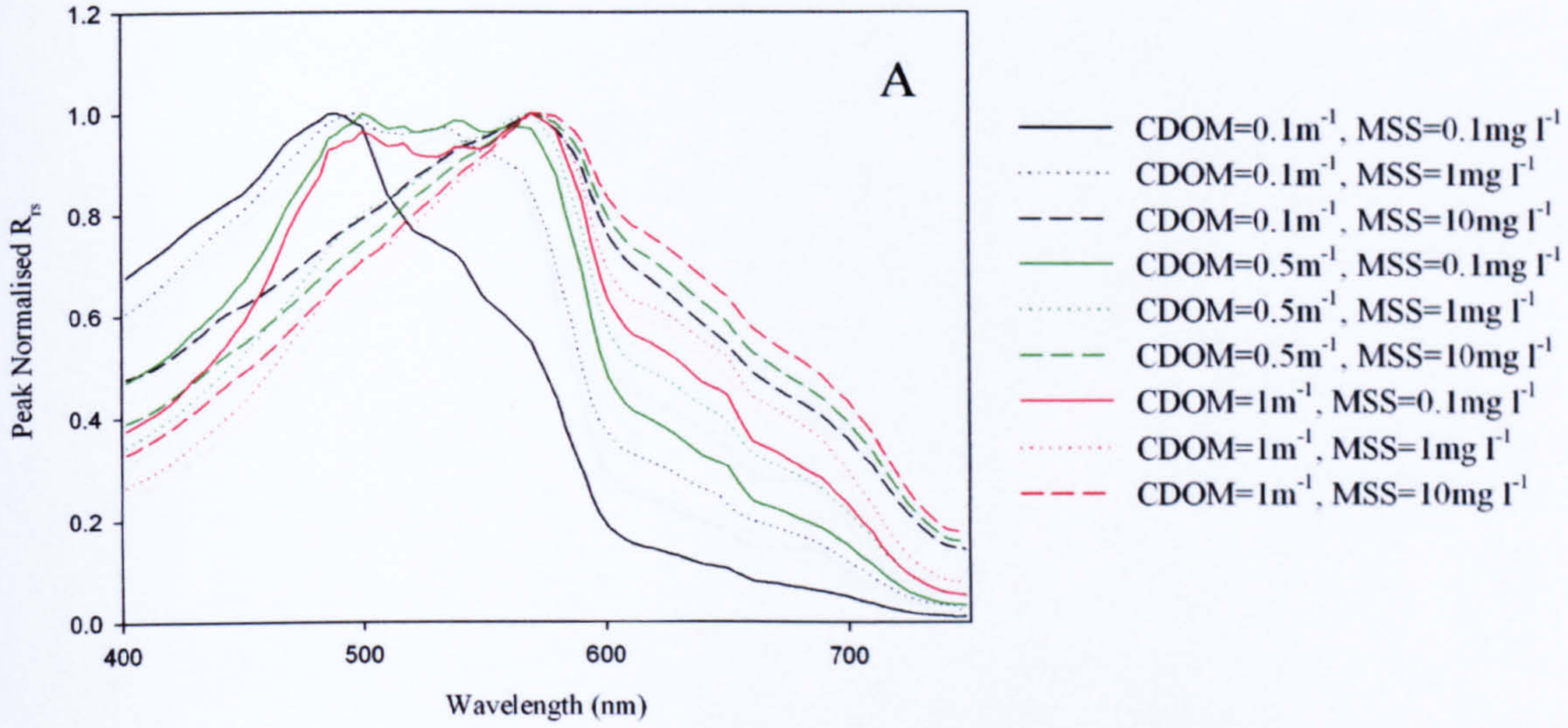

Chl = 0.1 *mg* m^{-3}, *CDOM and MSS varied*

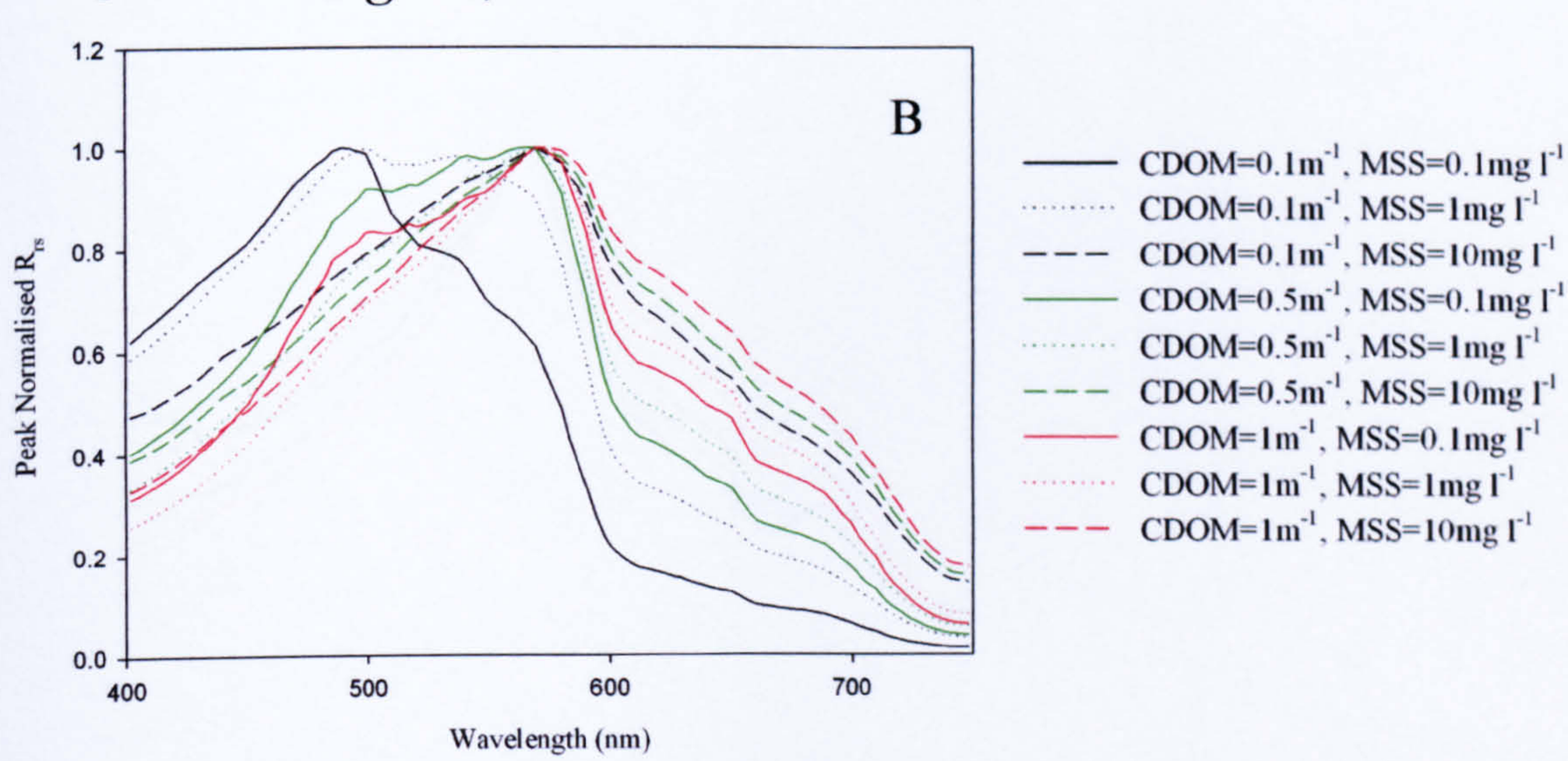

Figure 5.16. (i) Hyperspectral normalised $R_{rs}\left(0^{+}\right)$ spectra for case 2 waters containing chlorophyll, CDOM and MSS. In panels (A) to (D) the chlorophyll concentration was held constant while the CDOM and MSS combination was varied. . In (A) $Chl = 0\,mg\,m^{-3}$, and (B) $Chl = 0.1\,mg\,m^{-3}$.

Chl = 1 *mg* m^{-3}, *CDOM and MSS varied*

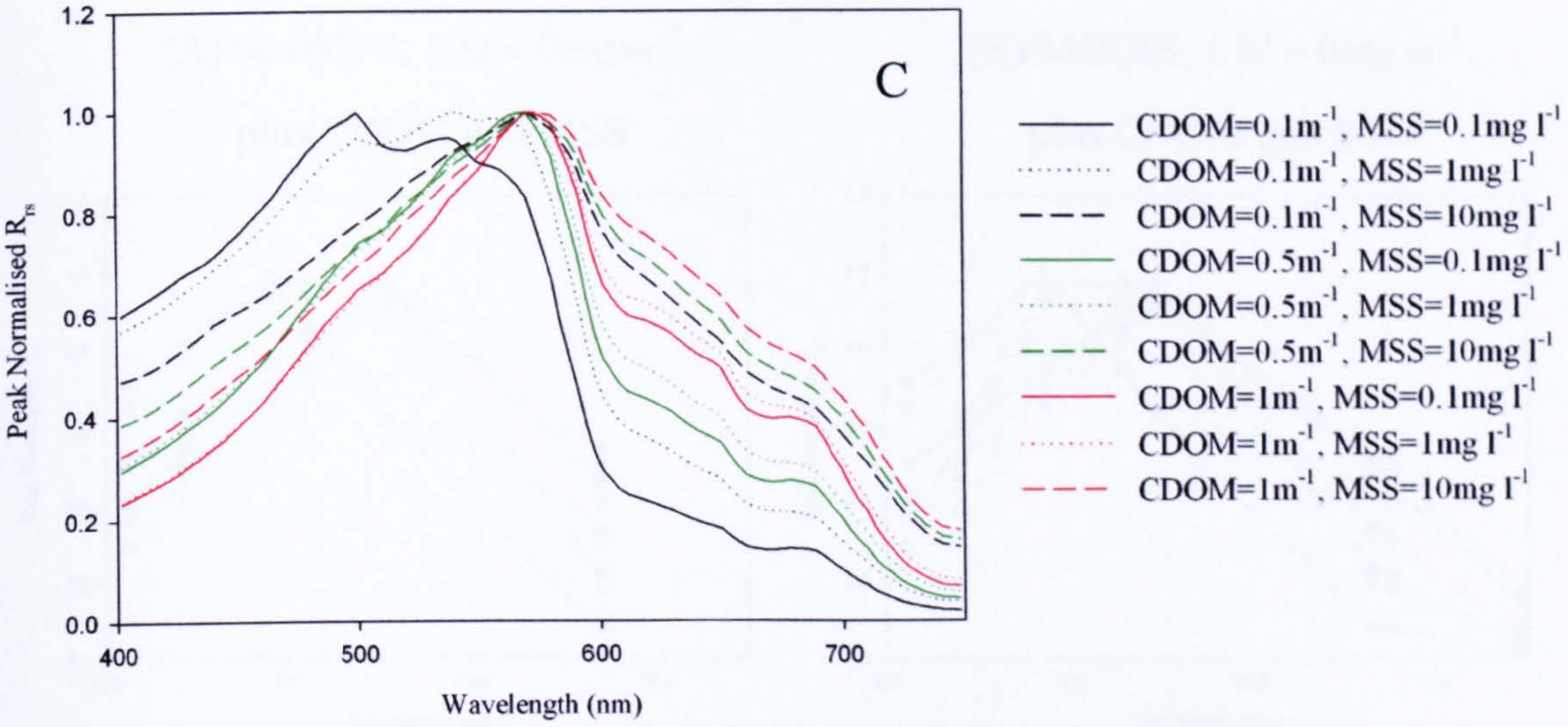

Chl = 10 *mg* m^{-3}, *CDOM and MSS varied*

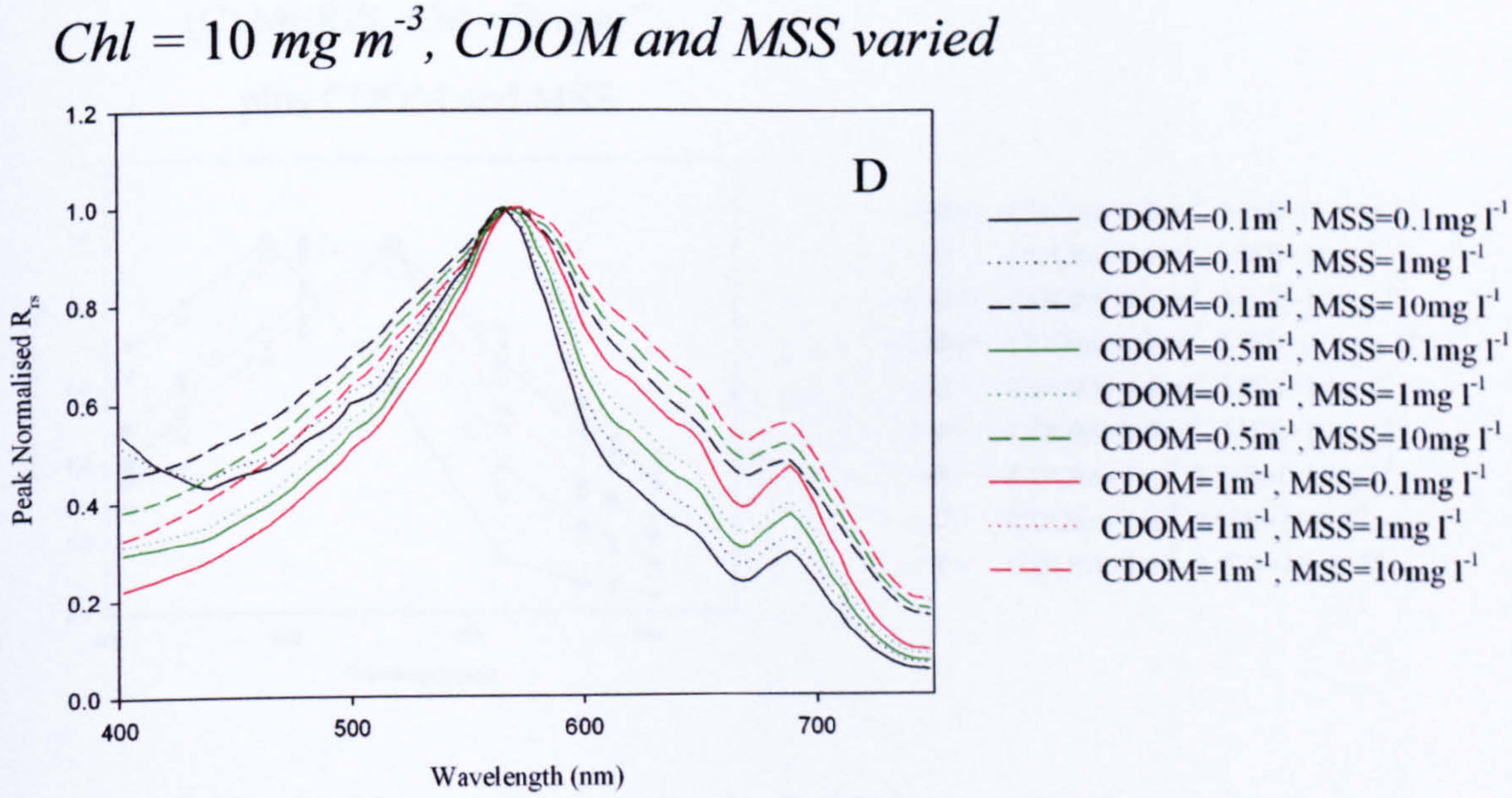

Figure 5.16. (ii) Hyperspectral normalised $R_{rs}\left(0^{+}\right)$ spectra for case 2 waters containing chlorophyll, CDOM and MSS. In (C) $Chl = 1 mg\, m^{-3}$, and (D) $Chl = 10 mg\, m^{-3}$.

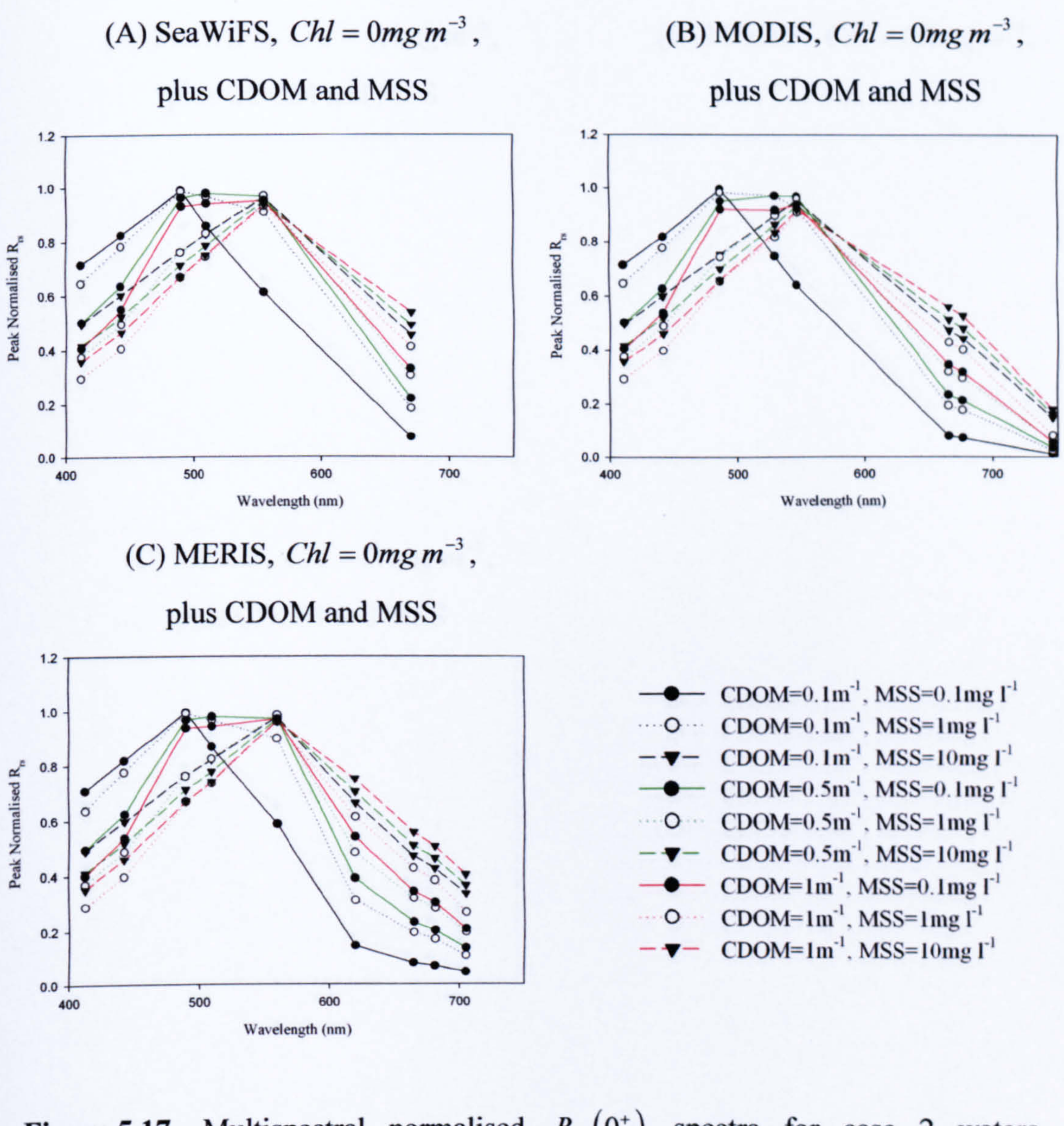

Figure 5.17. Multispectral normalised $R_{rs}\left(0^{+}\right)$ spectra for case 2 waters containing chlorophyll, CDOM and MSS. Panels (A) to (C) illustrate the spectra obtained by binning Hydrolight hyperspectral outputs into (A) SeaWiFS, (B) MODIS and (C) MERIS wavebands. For the spectra shown above the chlorophyll concentration was equal to $0\,mg\,m^{-3}$ and the CDOM and MSS combination was varied.

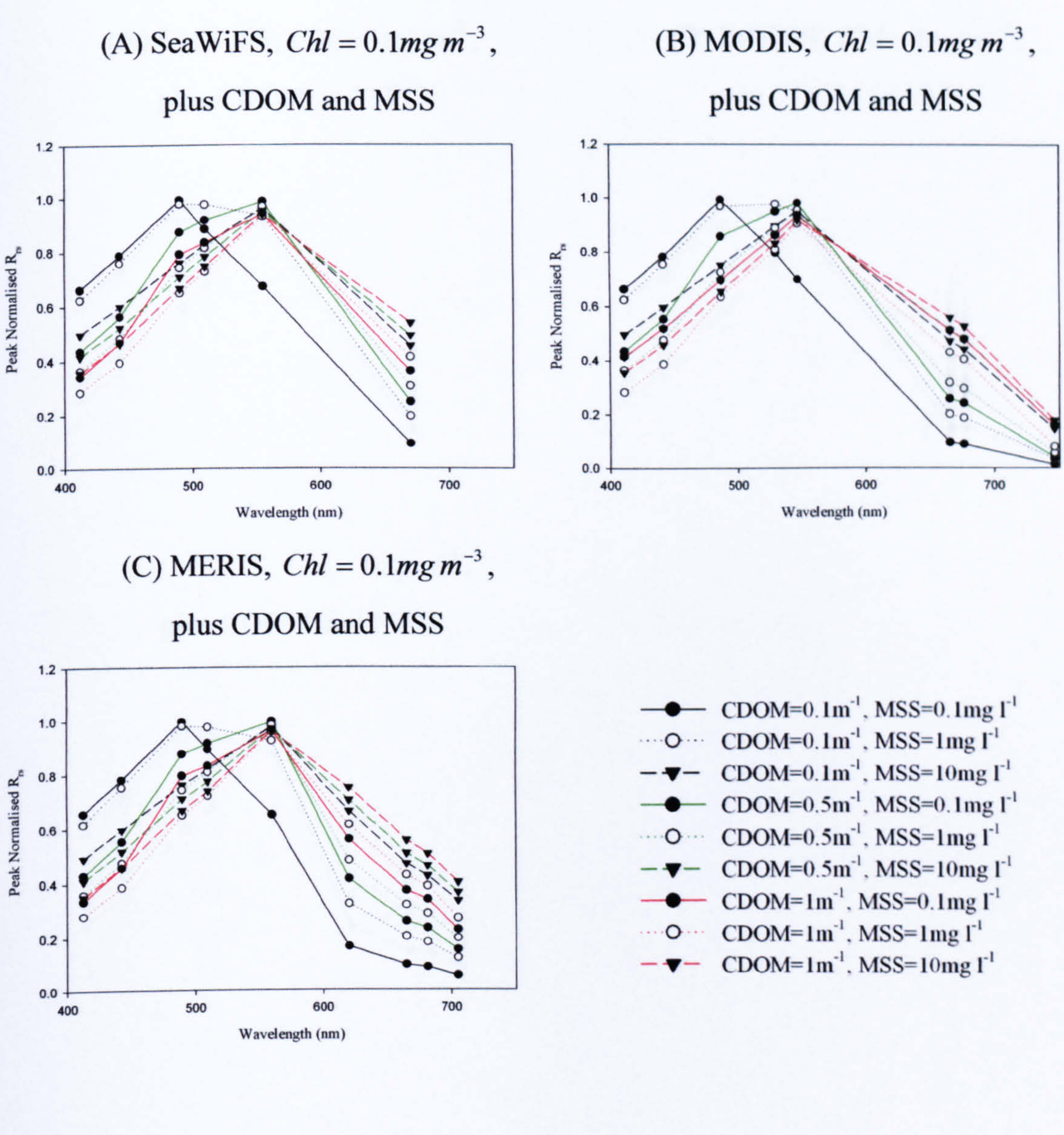

Figure 5.18. As Figure 5.17 excpet the chlorophyll concentration was equal to $0.1mg\,m^{-3}$.

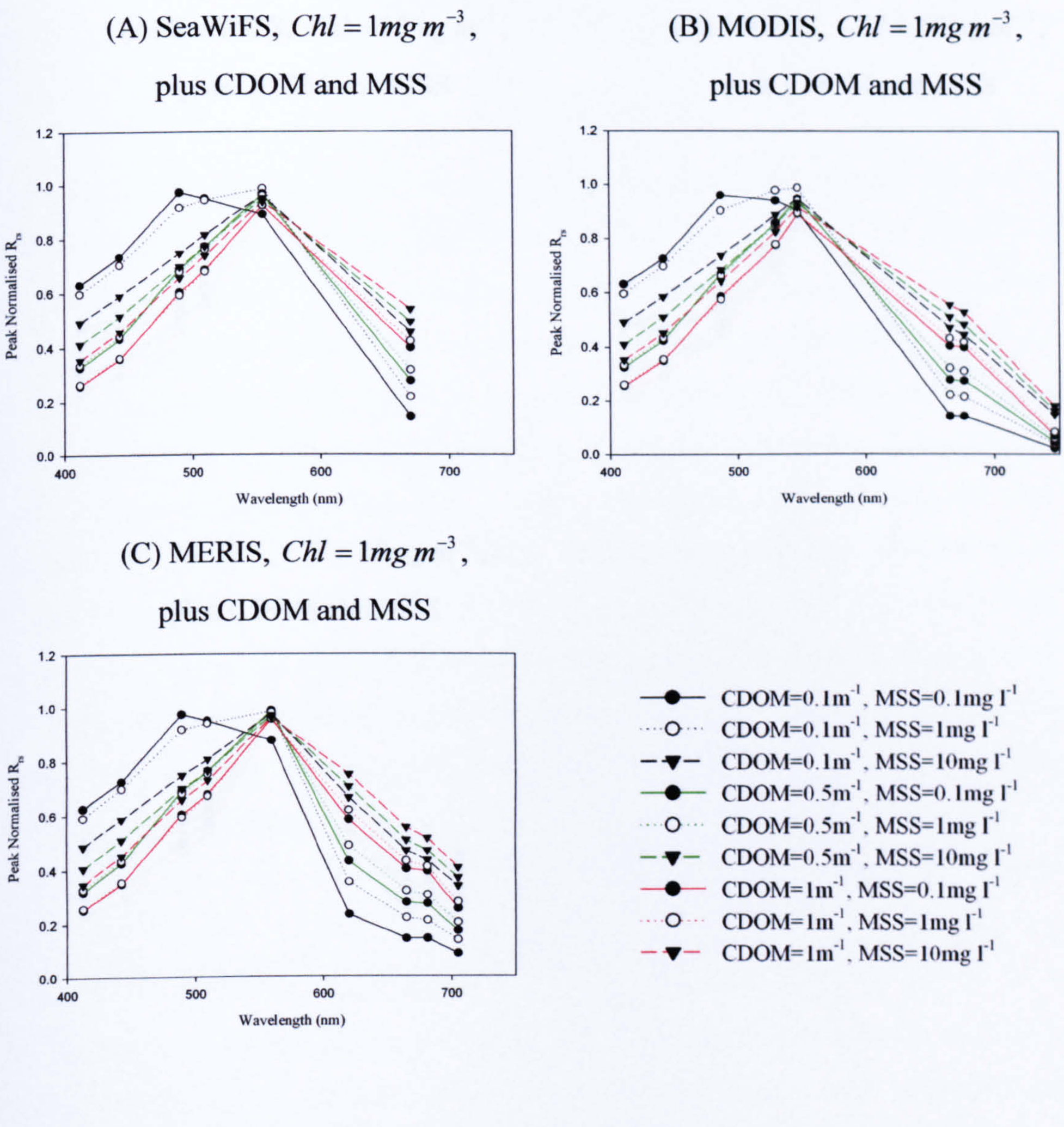

Figure 5.19. As Figure 5.17 excpet the chlorophyll concentration was equal to $1mg\,m^{-3}$.

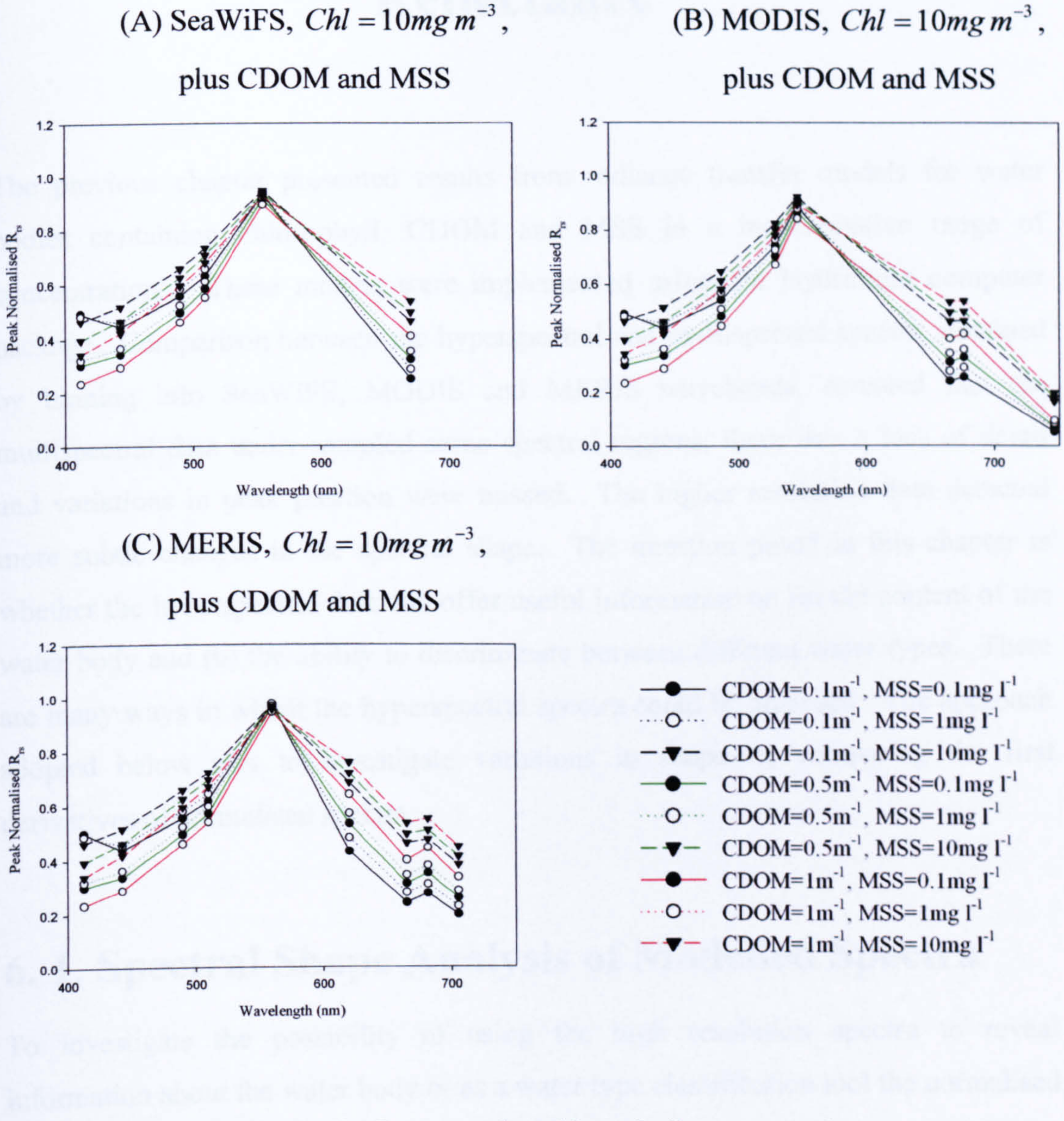

Figure 5.20. As Figure 5.17 except the chlorophyll concentration was equal to $10\,mg\,m^{-3}$.

Chapter 6: Exploratory Water Type Discrimination Using Modelled and Measured Hyperspectral Remote Sensing Reflectance

The previous chapter presented results from radiance transfer models for water bodies containing chlorophyll, CDOM and MSS in a representative range of concentrations. These models were implemented using the Hydrolight computer package. Comparison between the hyperspectral and multispectral spectra, obtained by binning into SeaWiFS, MODIS and MERIS wavebands, revealed that the multispectral data under-sampled some spectral regions, there was a loss of detail and variations in peak position were missed. The higher resolution data detected more subtle changes in the spectral shape. The question posed in this chapter is whether the hyperspectral data can offer useful information on (a) the content of the water body and (b) the ability to discriminate between different water types. There are many ways in which the hyperspectral spectra could be analysed. The approach adopted below was to investigate variations in shape by comparing the first derivatives of normalised spectra.

6. 1. Spectral Shape Analysis of Modelled Spectra

To investigate the possibility of using the high resolution spectra to reveal information about the water body or as a water type classification tool the normalised spectra obtained from the Hydrolight models (Chapter 5 section 5.1) were differentiated with respect to wavelength. Prior to the spectra being differentiated a smoothing function was applied (a three point centred moving average). Factors considered included peak positions, zero crossings, and curvature of the first order

differentiated spectra. Higher order derivatives proved difficult to interpret due to noise in the spectra.

6. 1. 1. First Order Derivatives of Modelled Spectra

The differentiated spectra are shown in Figure 6.1 to Figure 6.4. Figure 6.1 shows spectra for waters containing chlorophyll only, Figure 6.2 for chlorophyll and CDOM, Figure 6.3 for chlorophyll and MSS and Figure 6.4 for chlorophyll, CDOM and MSS. Inspection of these figures indicated that the following features, which are labelled in Figure 6.1, might be of interest:

Feature A. Integral between 400 and 455nm.
Feature B. Spectral region between 455 and 560nm.
Feature C. Trough between 560 and 615nm.
Feature D. Spectral region between 615 and 660nm.
Feature E. Peak to trough system between 660 and 750nm.

i. Feature A

When only chlorophyll was included in the model (Figure 6.1) this feature was negative and a trough was observed. As the chlorophyll concentration increased the trough was filled but still remained negative. In Figures 6.2, 6.3 and 6.4 the spectra were positive with the exception of high chlorophyll and low concentrations of CDOM and MSS. **Error! Reference source not found.** illustrates the results of integrating the spectra between 400 and 455nm. The integral was generally positive when CDOM, MSS or both components together were present in the water. The integral was generally negative when only chlorophyll was present or for clear oceanic water. Exceptions occurred when the chlorophyll concentration was high $\left(\geq 5 mg\, m^{-3}\right)$, CDOM was low $\left(\leq 0.1 m^{-1}\right)$ and/or MSS was low $\left(\leq 2 mg\, l^{-1}\right)$. For typical oceanic and shelf sea conditions, the sign of the integral of this feature, either positive or negative, could therefore be used as an indicator of either case 1 (negative) or case 2 (positive) water.

ii. Feature B

Inspection of this region of the spectrum suggested that it would be difficult to obtain useful information due to its complex nature. It was therefore decided to concentrate on other areas.

iii. Feature C

In clear water the trough of Feature C, located between 560 and 615nm, was absent. In the presence of chlorophyll the trough appeared to deepen but its shape was retained. In the presence of either CDOM or MSS the trough was filled and the width narrowed. The full width half maximum (FWHM) values of the trough observed in Feature C were calculated for the spectra illustrated in Figures 6.1 to 6.4. Figure 6.6 contains the results of this analysis. In the presence of chlorophyll only the FWHM of the trough did not vary greatly, remaining between 30 and 40nm. The introduction of MSS into the model reduced the FWHM, with values ranging from 20 to 40nm. CDOM also had a narrowing effect on the trough. For values of CDOM $\leq 1m^{-1}$ the FWHM values ranged between 20 and 40 nm. However, for higher concentrations of CDOM $\left(\geq 1m^{-1}\right)$ the FWHM varied between 10 and 20nm. Therefore, if the value of the FWHM varied between 10 and 20nm then CDOM dominated water could be expected. A FWHM between 30 and 40nm may indicate waters influenced by chlorophyll. In the absence of a trough or in the presence of a very shallow trough then it was more likely that the water had low concentrations of constituents.

iv. Feature D

The range from 615 to 660nm was a relatively featureless region of the spectrum. A small peak and trough occurred in this region but analysis of this feature yielded no useful information.

v. Feature E

The last feature considered was the peak and trough of Feature E which was generated by differentiation of the chlorophyll fluorescence peak. Analysis of the variation in the peak to trough height showed that for water containing only

chlorophyll an exponential function could be fitted to the data which was correlated with the chlorophyll concentration $\left(R^2 = 0.98\right)$.

$$y = 0.2437 \exp^{(268.9005x)} \tag{6.1}$$

where y is the chlorophyll concentration $\left(mg\,m^{-3}\right)$ and x is the peak to trough height. This is illustrated in Figure 6.7. For values of $CDOM \leq 0.5\,m^{-1}$, typical of shelf seas, a variation in the peak to trough height which would influence the chlorophyll concentration retrieved using equation (6.1) was observed. The introduction of MSS into the water column had little effect on this feature. It should be noted, however, that the model assumed that the quantum yield of fluorescence was constant.

6. 1. 2. Dependency of Spectral Derivative Features on Seawater Composition

To investigate the dependency of the three main hyperspectral features (the integral, FWHM and peak to trough height) on the constituent concentrations Pearson's Product Moment, which measures the linear association between two parameters was calculated. The possible correlation values range from 1, indicating a strong positive correlation, to -1, indicating a strong negative correlation. A value of 0 would indicate that there was no linear relationship between the variables. Table 6.1 contains the correlation values for the modelled data. The integral was strongly negatively correlated with chlorophyll and slightly positively correlated with CDOM. The FWHM was reasonably well positively correlated with chlorophyll but negatively correlated with CDOM and MSS, with CDOM having a slightly stronger correlation. The peak to trough height had a strong positive correlation with chlorophyll, and was positively correlated with CDOM but to a lesser extent. MSS was found to have no correlation with the integral and peak to trough height, with a correlation coefficient close to 0 in both cases.

Table 6.1 indicates that none of the hyperspectral features were solely correlated with any of the in-water constituents, and suggests that neither the CDOM nor the MSS concentration could be retrieved from the hyperspectral features using simple

linear relationships. Chlorophyll was the in-water constituent most strongly related with the hyperspectral features but any relationship that existed could be perturbed by the presence of other in-water constituents.

6. 1. 3. Review of Spectral Shape Analysis for Modelled Spectra

a. The normalised spectra were differentiated with respect to wavelength and three regions of the differentiated spectrum were identified as being of interest.

A. Integral between 400 and 455nm

C. FWHM between 560 and 615nm

E. Peak to trough height between 660 and 750nm

Feature A

The sign of the integral between 400 and 455nm could be used to discriminate between case 1 and case 2 water: negative indicated case 1 water and positive indicated case 2 water.

Feature C

The FWHM of the trough located between 560 and 615nm yielded information on the content of the water body. It was found that in the absence of a trough clear water was present and if the FWHM ranged between 30 and 40nm the water was dominated by chlorophyll. A FWHM ranging between 20 and 40nm suggested water that contained CDOM and/or MSS, as both of these components had a narrowing effect on the trough. FWHM between 10 and 20nm indicated the presence of high concentrations of CDOM or MSS.

Feature E

The peak/trough system between 660 and 750nm was only present if chlorophyll was included in the model. Analysis of the peak to trough height revealed that a relationship may exist between the height and the chlorophyll concentration though

this is affected by the presence of CDOM which had a deepening impact on the trough.

b. Calculation of Pearson's Product Moment showed that none of the hyperspectral features were solely related to any of the constituents (Table 6.1). It was found that chlorophyll was most strongly correlated with the hyperspectral features but the presence of other optically important constituents could perturb any relationship that existed between the chlorophyll concentration and hyperspectral feature in question. Neither the CDOM nor the MSS concentration could be retrieved from the hyperspectral features using simple linear relationships.

The next stage of the investigation was to apply the features discussed above, observed in the theoretical models, to actual field measurements of hyperspectral $R_{rs}\left(0^{+}\right)$.

6. 2. Spectral Shape Analysis of Field Measurements

In this section field measurements were assessed to investigate whether they contained the same features as the Hydrolight modelled spectra.

6. 2. 1. First Order Derivative Spectra of Field Measurements

Field measurements of hyperspectral $E_d\left(0^{+}\right)$ and $L_u\left(0^{-}\right)$ were averaged over a time interval in which there was a steady signal (typically 300 seconds) and $L_u\left(0^{-}\right)$ measurements were extrapolated through the air-water interface using the equations set out in Chapter 3, section 3.1.6. Values of $E_d\left(0^{+}\right)$ and $L_u\left(0^{+}\right)$ were put into equation (6.2) to calculate $R_{rs}\left(0^{+},\lambda\right)$:

$$R_{rs}\left(0^{+}\right)=\frac{L_u\left(0^{+}\right)}{E_d\left(0^{+}\right)} \tag{6.2}$$

where $R_{rs}\left(0^{+}\right)$ is the above-surface remote sensing reflectance measured in steradians $\left(sr^{-1}\right)$. The hyperspectral $R_{rs}\left(0^{+}\right)$ spectra were normalised by the maximum value occurring in each spectrum, smoothed using a three point centred moving average and differentiated with respect to wavelength. Figure 6.8 illustrates the results for selected stations with high concentrations of chlorophyll (OB03-13), CDOM (OB04-08) and TSS (BC05-14), along with an oceanic station (AM15-51) close to the centre of the South Atlantic gyre and a typical shelf sea station (SJ04-22) with average concentrations of chlorophyll, CDOM and TSS. Table 6.2 contains information on the concentration of the constituents found at these stations. The spectra measured at sea showed similar features to the modelled spectra in the previous section (6.1.1). For coastal and shelf sea waters, the first derivative spectrum between 400 and 455nm was positive but for the oceanic water the spectrum was negative. The trough between 560 and 615nm was present for most stations, but absent in the clear oceanic water as predicted by the models. Variation in the peak to trough height, located between 660 to 750nm, was also evident in the examples shown. The measured spectra all showed the features predicted by the theoretical models, the next stage was to examine the relationship between hyperspectral features and in-water constituents.

6.2.2. Dependency of Spectral Features on Seawater Composition

The dependency of the three hyperspectral features (the integral, FWHM and peak to trough), observed in the differentiated field measurements, upon seawater composition was investigated by calculating Pearson's Product Moment. Table 6.3 contains the results of the correlation test. For the field data the integral was strongly negatively correlated with chlorophyll and was also negatively correlated with CDOM. It showed a small positive correlation with TSS. The FWHM did not show a strong correlation with any of the constituents but was found to be most strongly negatively correlated with TSS. The FWHM was also negatively correlated with

CDOM and showed no correlation with chlorophyll. The peak to trough height was shown to be strongly positively correlated with chlorophyll, and positively correlated with CDOM but to a lesser extent. TSS showed a small negative correlation with the peak to trough height.

Pearson's Product Moment again shows that the hyperspectral features were not solely related to any individual in-water constituent. Chlorophyll was the constituent most strongly correlated with the hyperspectral features, the integral and peak to trough height, but any relationship that existed would be perturbed by the presence of CDOM or TSS.

6. 3. Water Type Discrimination Using Hyperspectral $R_{rs}\left(0^{+}\right)$ Field Measurements

The three most prominent hyperspectral features that occur in the differentiated spectra (the integral, FWHM and peak to trough height) were assessed as possible keys to water type classification.

6. 3. 1. Discrimination between Open Ocean and Coastal Water

Plots of the integral value between 400 and 455nm against the constituent concentrations revealed some interesting features, illustrated in Figure 6.9. In panel (A) the sign of the integral was negative for AMT 15 stations except three which have been identified as occurring on the European shelf and in the North African Upwelling. For all the stations in the open ocean the sign of the integral was negative. For the Oban 2003, Oban 2004, Sound of Jura 2004 and Bristol Channel 2005 cruises the sign of the integral remained positive, in agreement with the prediction of the models in section 6.1.1. Plotting the integral against CDOM and TSS (with AMT 15 omitted) confirmed that where these constituents were present the integral remained positive. This was confirmed by plotting histograms of the integral value for each cruise (Figure 6.10). For cruises Oban 2003, Oban 2004, the Sound of Jura 2004 and the Bristol Channel 2005 the integral was always positive.

For the AMT cruise, Figure 6.10 panel (E), the majority of stations sampled had a negative integral. The three exceptions occurred on the European shelf and in the North African Upwelling. It was therefore possible to use the sign of the integral between 400 and 455nm to discriminate between open ocean and other waters.

6.3.2. Cluster Analysis of Hyperspectral Derivative Features Occurring in Coastal Water

For the Oban 2003, Oban 2004, the Sound of Jura 2004 and the Bristol Channel 2005 cruises the possibility of differentiating between water dominated by different constituents (e.g. CDOM or TSS) was investigated. The optical properties of coastal waters are extremely dynamic and large variability exists in temporal and spatial scales. Estuaries and areas affected by strong tidal movement tend to have high TSS values due to re-suspension of sediments, whereas sea lochs can have high CDOM concentrations due to fresh water run-off from the surrounding land. As the composition of the water body varies, changing the values of the absorption and backscattering coefficients, the observed $R_{rs}(0^+)$ spectrum also varies, due to equation (5.7). The presence of optically important material can have a negative impact on algorithms designed to retrieve information about the water body. As a result of the complex nature of coastal waters, sub-classification is potentially important for targeting algorithms to specific water types.

Pearson's Product Moment showed that no simple relationships existed between the hyperspectral features and the in-water constituents. However, performing a cluster analysis on the hyperspectral features using the Data Desk software package revealed four high level clusters which may be of use in discriminating between water types. Figure 6.11 illustrates the $\log_{10}$ transforms of the hyperspectral features plotted against one another. Panel (A) illustrates the integral plotted against the FWHM, (B) the integral plotted against the peak to trough height and (C) the peak to trough height plotted against the FWHM. Panel (D) of this figure illustrates the results of the cluster analysis performed on the hyperspectral features. The histograms contained in Figure 6.12 to Figure 6.15 illustrate the constituent

concentrations for each cluster of the hyperspectral feature identified in the cluster analysis.

Cluster 1

The first cluster, the points marked blue in the Figure 6.11, consisted of West of Scotland coastal waters sampled during the Oban 2003, Oban 2004 and the Sound of Jura 2004 cruises. Figure 6.12 contains histograms of the constituent concentration for this cluster. Stations found in this cluster typically had a wide range of chlorophyll and CDOM concentrations with lower TSS values. 96% of stations had a chlorophyll concentration $\geq 3 mg\, m^{-3}$ and 96% had TSS $\leq 4 mg\, l^{-1}$.

Cluster 2

The second cluster, the points marked red, have been identified as a mixture of West of Scotland and Bristol Channel stations. These Bristol Channel stations were sampled at the seaward end of the channel. Figure 6.13 illustrates the histograms of constituent concentration for this cluster. These stations tended to have low levels of chlorophyll, with the concentration being $\leq 3.0 mg\, m^{-3}$. The CDOM concentration was also low $\left(\leq 0.6 m^{-1}\right)$ with 81% of stations having a CDOM concentration $\leq 0.2 m^{-1}$. The TSS concentration was varied but generally high with 78% of station having a TSS $\geq 4 mg\, l^{-1}$.

Cluster 3

In the third cluster, points coloured green, the majority of stations were found further up the Bristol Channel in muddier water. One of these stations was located off the coast of Anglesey in an area of the Irish Sea known for its high TSS levels (Bowers *et al*, 2002). Histograms of the constituent concentrations for this cluster are illustrated in Figure 6.14. This cluster contained stations with high TSS values, with 78% having a TSS $\geq 16 mg\, l^{-1}$. The cluster also had low chlorophyll $\left(\leq 2 mg\, m^{-3}\right)$ and CDOM $\left(\leq 0.4 m^{-1}\right)$ concentrations.

Cluster 4

The fourth and last cluster, coloured cyan in Figure 6.11, comprised of stations from the Loch Creran area. Figure 6.15 contains histograms of constituent concentrations for this cluster. The chlorophyll concentration tended to be high, with 89% of stations having a concentration $\geq 4 mg\, m^{-3}$. The CDOM concentration was varied but 56% of stations had high CDOM values, $\geq 0.8 m^{-1}$. The concentration of TSS for stations in this cluster was low, with all stations having a TSS $\leq 4 mg\, l^{-1}$.

Analysis of the four clusters occurring within the hyperspectral feature dataset revealed that the clusters were logically associated with the composition of the water body. However, there was no direct mapping between the constituent clusters identified in Chapter 4 and the hyperspectral feature clusters. This is due to the fact that no individual constituent was solely responsible for the variation in the hyperspectral features, as illustrated by the Pearson's Product Tests. Clusters 1 and 4 were comprised of low TSS waters with generally higher and more varied concentrations of chlorophyll. Clusters 2 and 3 were generally comprised of stations with higher and more varied concentrations of TSS and with low levels of both chlorophyll and CDOM. The hyperspectral feature clustering did not show any obvious relationship with geography, though the Bristol Channel stations did get apportioned to the more turbid clusters (clusters 2 and 3).

6. 4. Examination of Normalised $R_{rs}(0^+)$ Spectra for Clusters Derived From Hyperspectral Features

By inspecting the hyperspectral $R_{rs}(0^+)$ spectra obtained on the research cruises according to the hyperspectral feature classification schemes used in 6.3.2 it was possible to investigate whether the spectral shape observed was consistent with knowledge of the stations derived from other measurements.

6. 4. 1. Open Ocean Cluster

Figure 6.16 illustrates the peak normalised hyperspectral $R_{rs}(0^+)$ spectra for the open ocean stations sampled during the course of AMT 15. The spectral shapes illustrated in the figure were in keeping with the spectral shape that one would expect to observe for open ocean water, given the low concentration of constituents in the surface layer. However, examination of the hyperspectral derivative features and chlorophyll concentration revealed no simple relationships existed. This may be in part due to the low levels of chlorophyll present in the surface layer.

6. 4. 2. Coastal Water Clusters

Using the clusters obtained by analysis of the hyperspectral features of the derivative spectra the peak normalised field $R_{rs}(0^+)$ spectra were plotted together on a single plot for each cluster. Figure 6.17 allowed the similarity in the spectral shape and any variations that occurred in and between each cluster to be assessed.

Cluster 1

Panel (A) illustrates the spectra for the first cluster, coloured blue on the tree diagram (Figure 6.5 panel (D)). This cluster was identified as water with a range of chlorophyll and CDOM concentrations but with low TSS. All the spectra in this panel show the solar stimulated chlorophyll fluorescence peak which indicates the presence of chlorophyll in the water.

Cluster 2

In panel (B), the second cluster which is marked red on the cluster analysis diagram, the stations were identified as low chlorophyll and CDOM water with a wider range of TSS concentrations. The absence of a clear chlorophyll fluorescence peak is consistent with this identification.

Cluster 3

Panel (C) shows normalised spectra for the highly turbid stations of the third cluster, points marked green in Figure 6.9 (D). The absence of the chlorophyll fluorescence peak again indicates low chlorophyll content while the raised section at wavelengths longer than 600nm indicate more turbid water.

Cluster 4

Cluster 4, the points coloured cyan in the tree diagram, was more complicated. These stations generally had high concentrations of chlorophyll and/or CDOM and low TSS levels. The presence of a well established chlorophyll fluorescence peak was consistent with the high chlorophyll levels, though the fluorescence peak was less evident in the Oban 2004 stations. This could be due to suppression of the fluorescence peak by CDOM. For the Oban 2003 stations there was a bump in the spectra located around 430nm. This bump could be due to strong absorption by chlorophyll as chlorophyll has its main absorption band located in this spectral region. In the case of the Oban 2004 stations the spectral area between 350 and 550nm appears to have been influenced by the strong absorption of CDOM.

The spectral shape observed for each of the four clusters was generally representative of the content of the water body. It has already been established that the hyperspectral features of the derivative spectra were not uniquely related to the concentrations of the in-water components. Nevertheless, splitting the spectra up according to clusters derived from the hyperspectral features may prove useful for targeting remote sensing algorithms to optically complex water.

6. 5. Summary of Hyperspectral Feature Identification and Cluster Analysis

a. Variations in the shape of hyperspectral spectra were investigated by normalising and differentiating the spectra. Differentiation was limited to the first order as higher order derivative spectra were too noisy to interpret.

b. Applying the normalisation and differentiation process revealed that similar hyperspectral features appeared in the field measurements and in the Hydrolight models.

c. Pearson's Product Moment revealed that none of the hyperspectral features of the derivative field measurements were solely related to the in-water constituents.

d. The extent to which the three hyperspectral features (the integral, the FWHM and the peak to trough height) could be used as a water type classifier was investigated. Results of this investigation revealed that the integral could be used to differentiate between open ocean and other waters.

e. Analysis of the shelf sea stations was more complicated. Cluster analysis of the hyperspectral features did reveal four clusters which were linked to the composition of the water body. The spectral shape of these clusters was generally representative of the composition of the water body.

The next objective was to investigate the possibility of retrieving quantitative information on the water body using standard remote sensing algorithms and to assess whether the hyperspectral clusters were useful for targeting remote sensing algorithms to different water types.

	CHLOROPHYLL	CDOM	MSS
Integral between 400 and 455nm	-0.83	0.18	-0.05
FWHM between 560 and 615nm	0.66	-0.57	-0.32
Peak to trough height between 660 and 750nm	0.90	0.31	0.06

Table 6.1. Pearson's Product Moment correlation coefficients calculated for Hydrolight runs conducted for Case 2 waters containing chlorophyll, CDOM and MSS.

STATION ID	CHLOROPHYLL $\left(mg\,m^{-3}\right)$	CDOM $\left(m^{-1}\right)$	TSS $\left(mg\,l^{-1}\right)$
OB03-13	10.5	0.6	2.1
OB04-08	4.7	1.9	2.7
SJ04-22	2.2	0.4	3.5
AM15-51	0.2	N/A	N/A
BC05-14	0.9	0.2	38.6

Table 6.2. Near-surface concentrations of optically active constituents for the stations illustrated in Figure 6.8.

	CHLOROPHYLL	CDOM	TSS
Integral between 400 and 455nm	-0.71	-0.49	0.22
FWHM between 560 and 615nm	0.06	-0.27	-0.55
Peak to trough height between 660 and 750nm	0.78	0.39	-0.21

Table 6.3. Pearson's Product Moment correlation coefficients calculated for coastal water dataset containing information on the Oban 2003, Oban 2004, Sound of Jura 2004 and Bristol Channel 2005 research cruises.

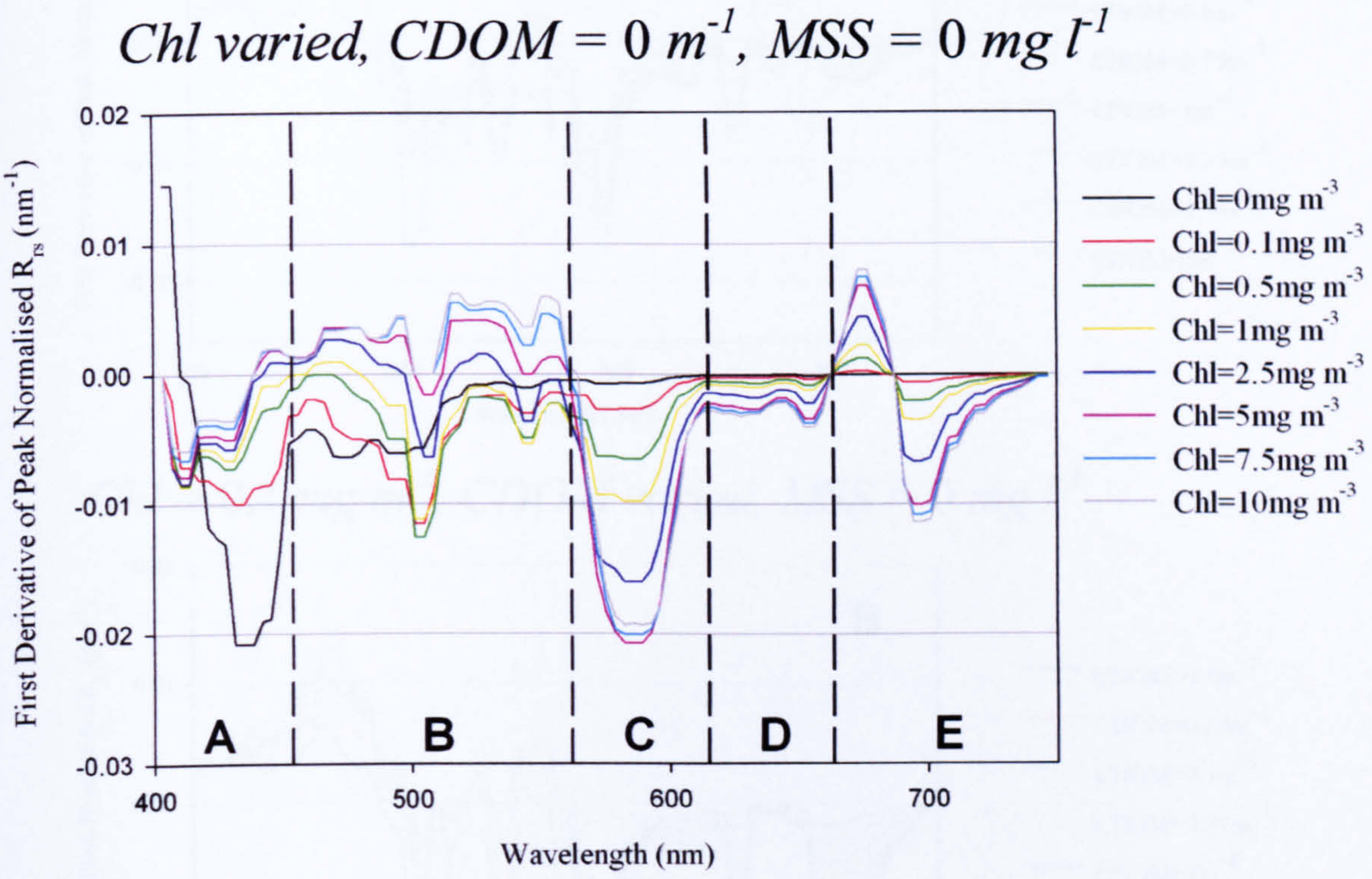

Figure 6.1. First derivative of the normalised hyperspectral case 1 waters modelled in Hydrolight. Prior to differentiation the spectra had a smoothing function applied to reduce the noise in the differentiated spectra.

Chl = 0 *mg* m^{-3}, *CDOM varied, MSS* = 0 *mg* l^{-1}

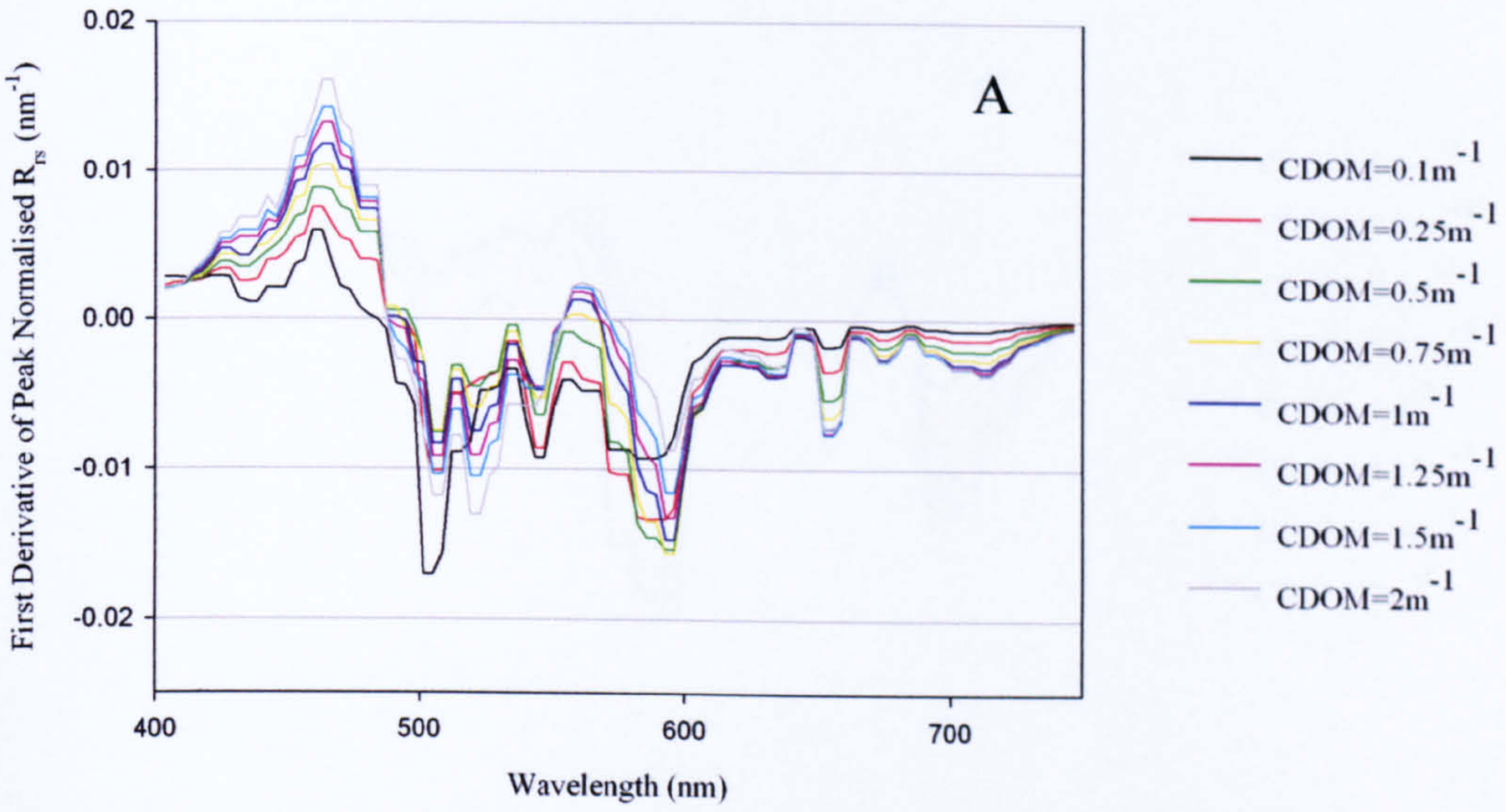

Chl = 0.1 *mg* m^{-3}, *CDOM varied, MSS* = 0 *mg* l^{-1}

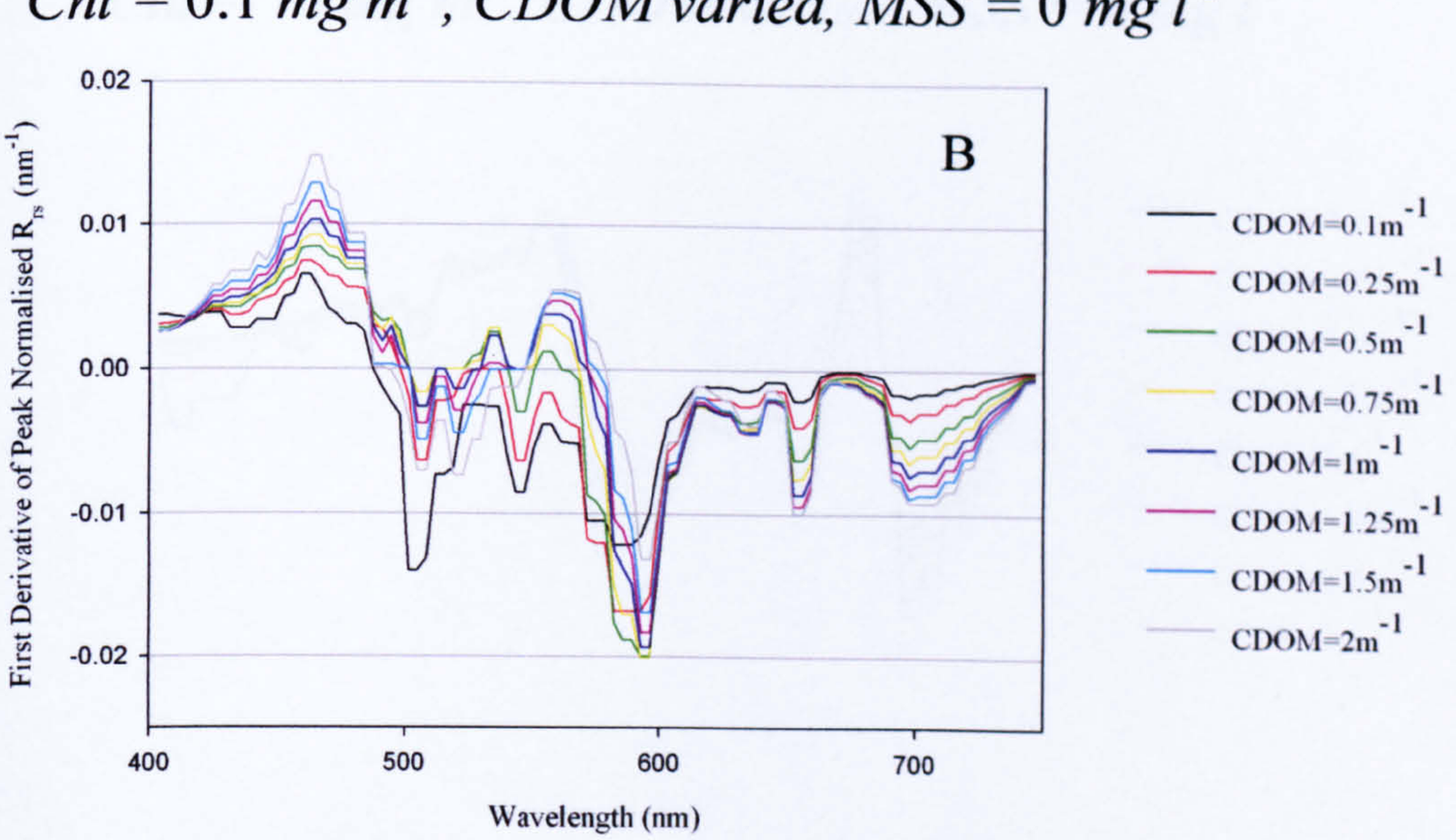

Figure 6.2. (i) First derivative of normalised hyperspectral $R_{rs}\left(0^{+}\right)$ spectra for case 2 waters containing chlorophyll and CDOM. In panel (A) $Chl = 0\,mg\,m^{-3}$, (B) $Chl = 0.1\,mg\,m^{-3}$, (C) $Chl = 1\,mg\,m^{-3}$ and (D) $Chl = 10\,mg\,m^{-3}$ and the CDOM concentration in each case was varied.

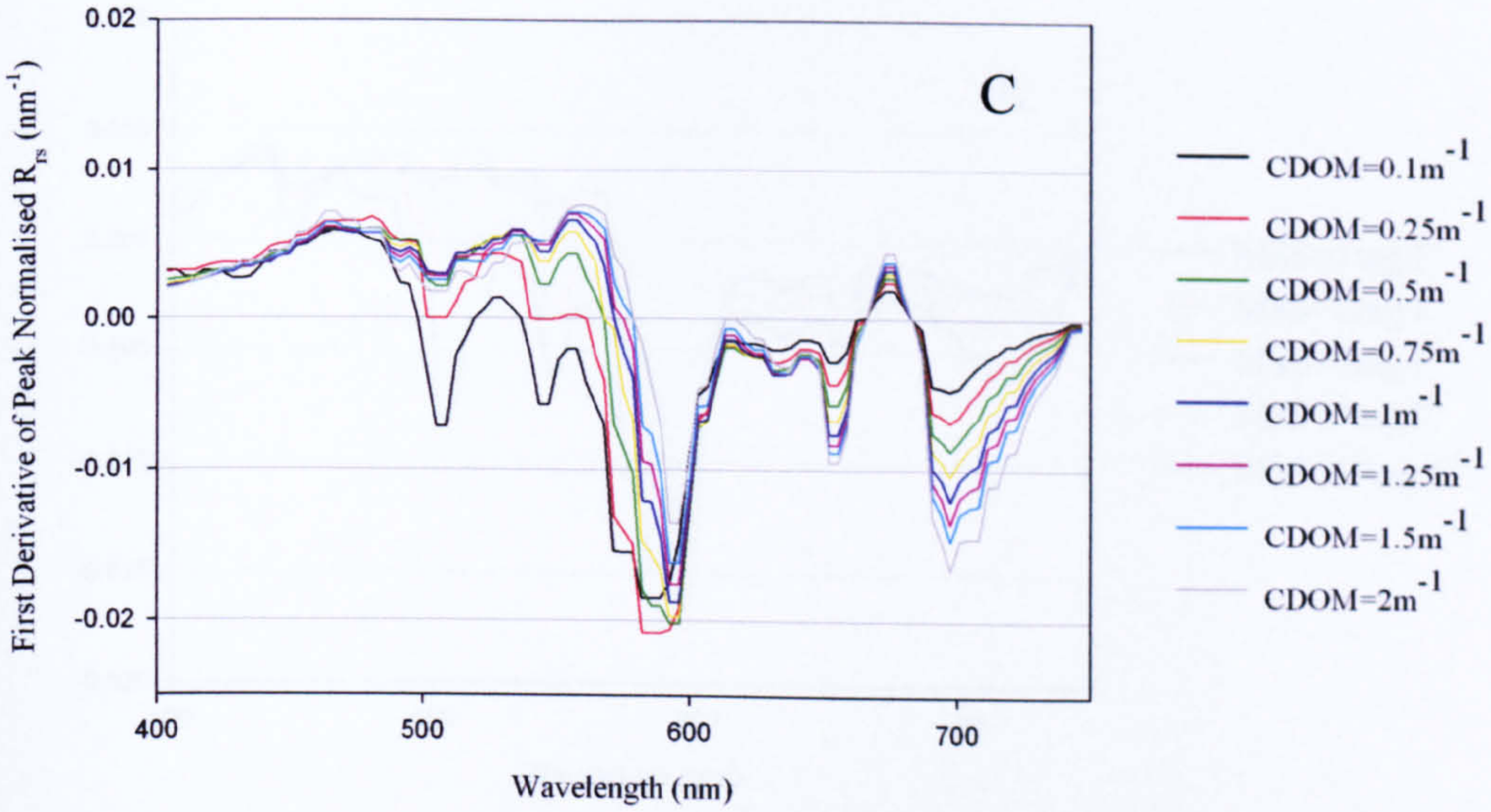

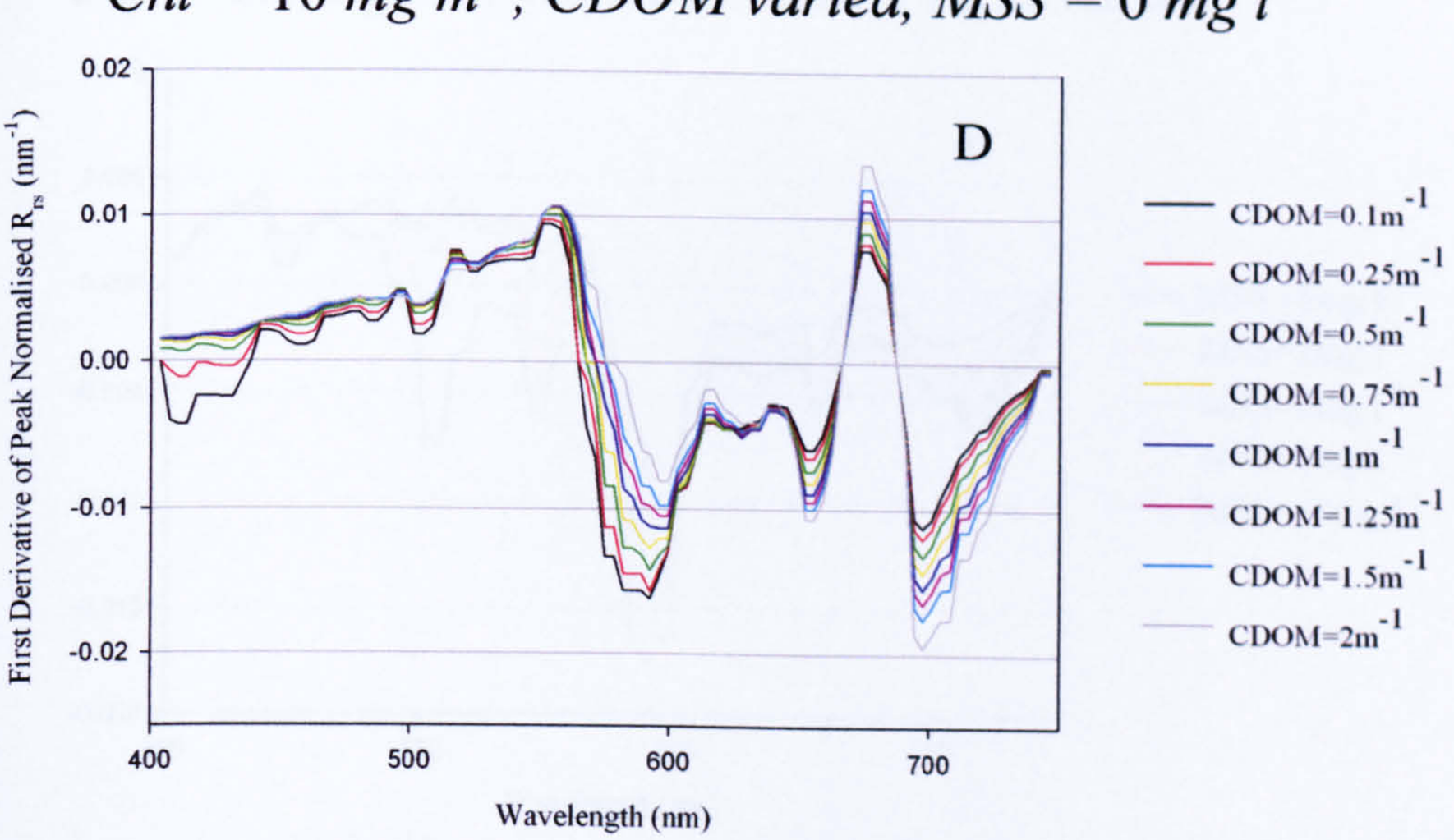

Figure 6.2. (ii) First derivative of normalised hyperspectral $R_{rs}\left(0^{+}\right)$ spectra for case 2 waters containing chlorophyll and CDOM. In panel (A) $Chl = 0\,mg\,m^{-3}$, (B) $Chl = 0.1\,mg\,m^{-3}$, (C) $Chl = 1\,mg\,m^{-3}$ and (D) $Chl = 10\,mg\,m^{-3}$ and the CDOM concentration in each case was varied.

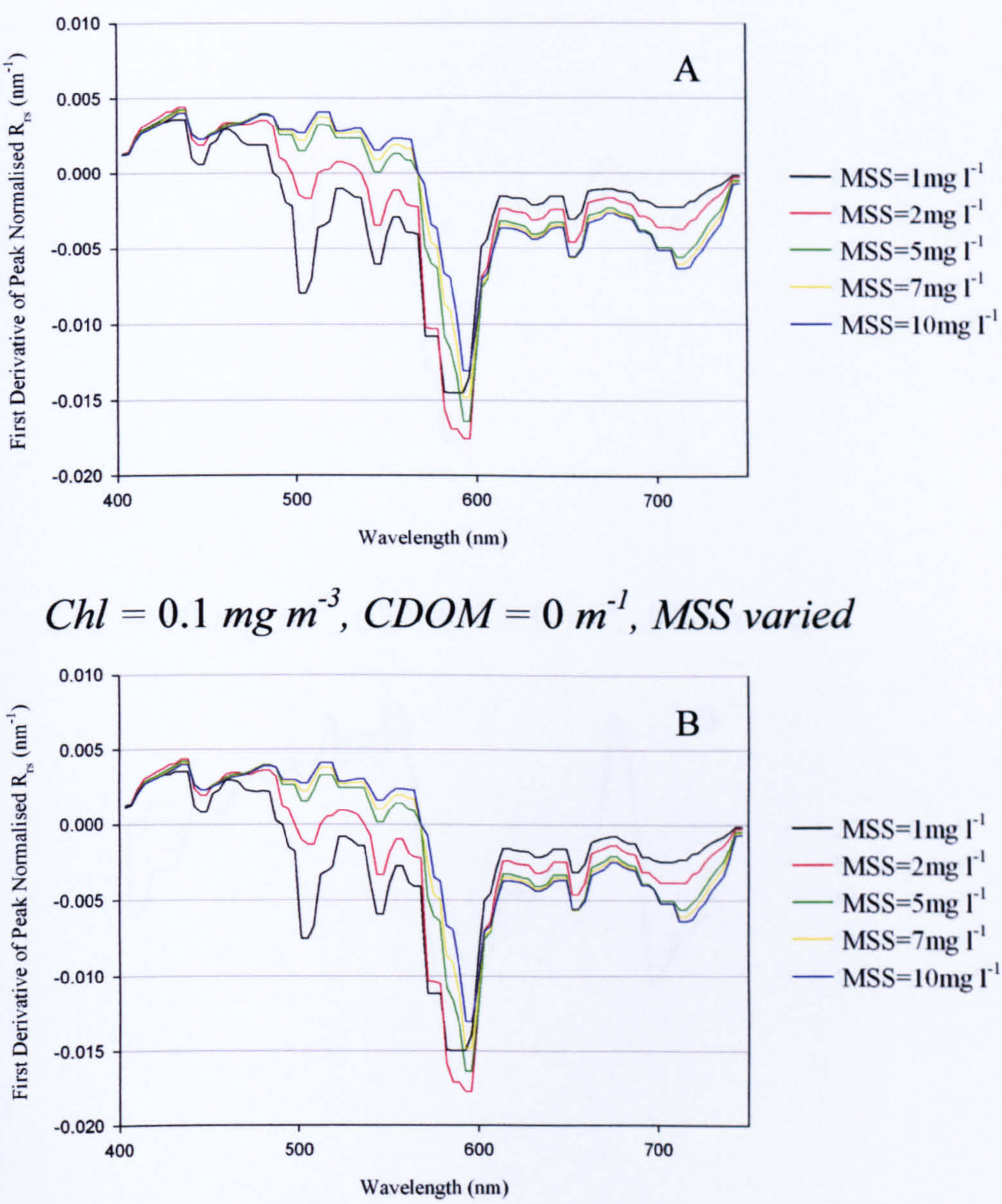

Figure 6.3. (i) First derivative of normalised hyperspectral $R_{rs}\left(0^{+}\right)$ spectra for case 2 waters containing chlorophyll and MSS. In panel (A) $Chl = 0\,mg\,m^{-3}$, (B) $Chl = 0.1\,mg\,m^{-3}$, (C) $Chl = 1\,mg\,m^{-3}$ and (D) $Chl = 10\,mg\,m^{-3}$ and the MSS concentration in each case was varied.

$Chl = 1\ mg\ m^{-3}$, $CDOM = 0\ m^{-1}$, *MSS varied*

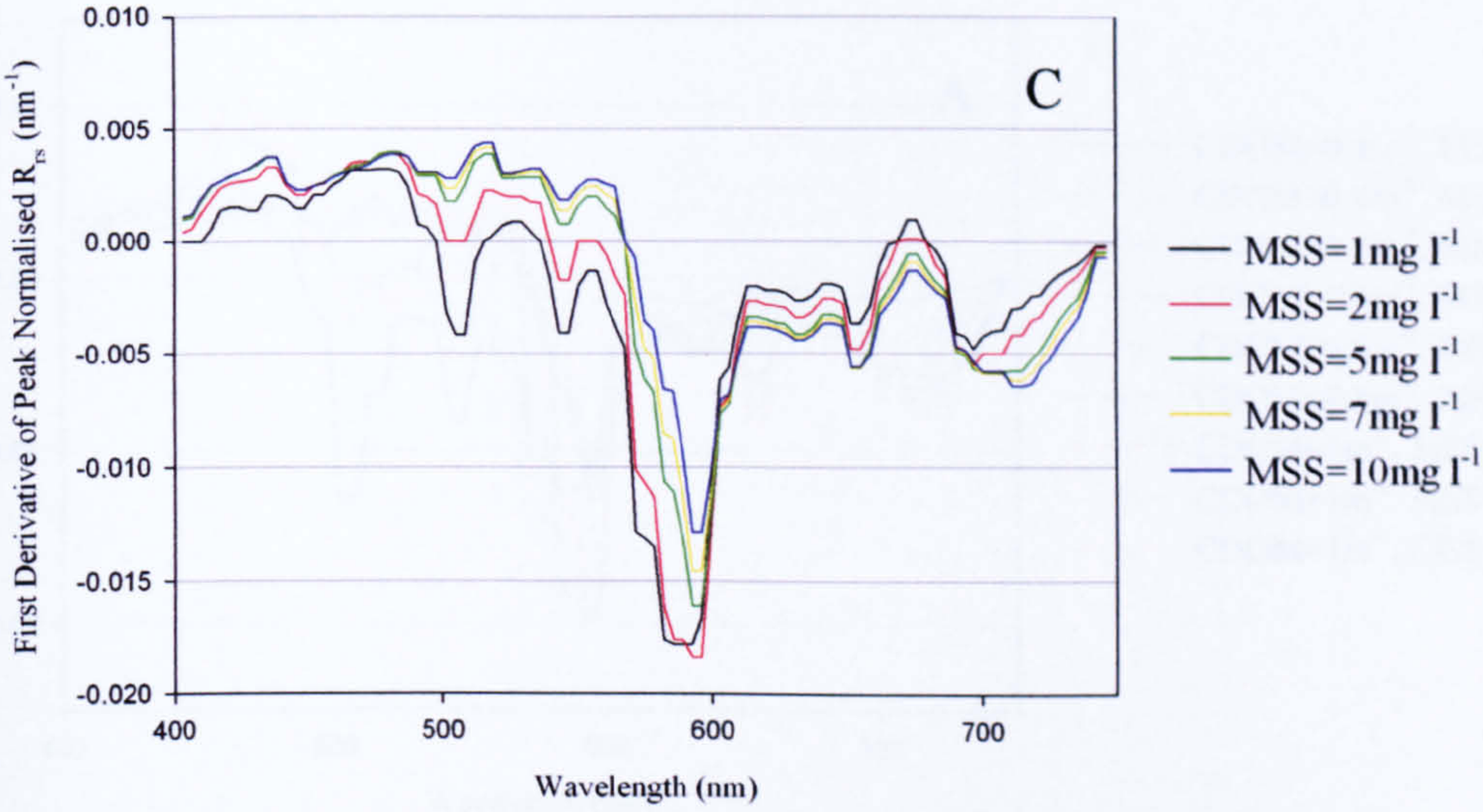

$Chl = 10\ mg\ m^{-3}$, $CDOM = 0\ m^{-1}$, *MSS varied*

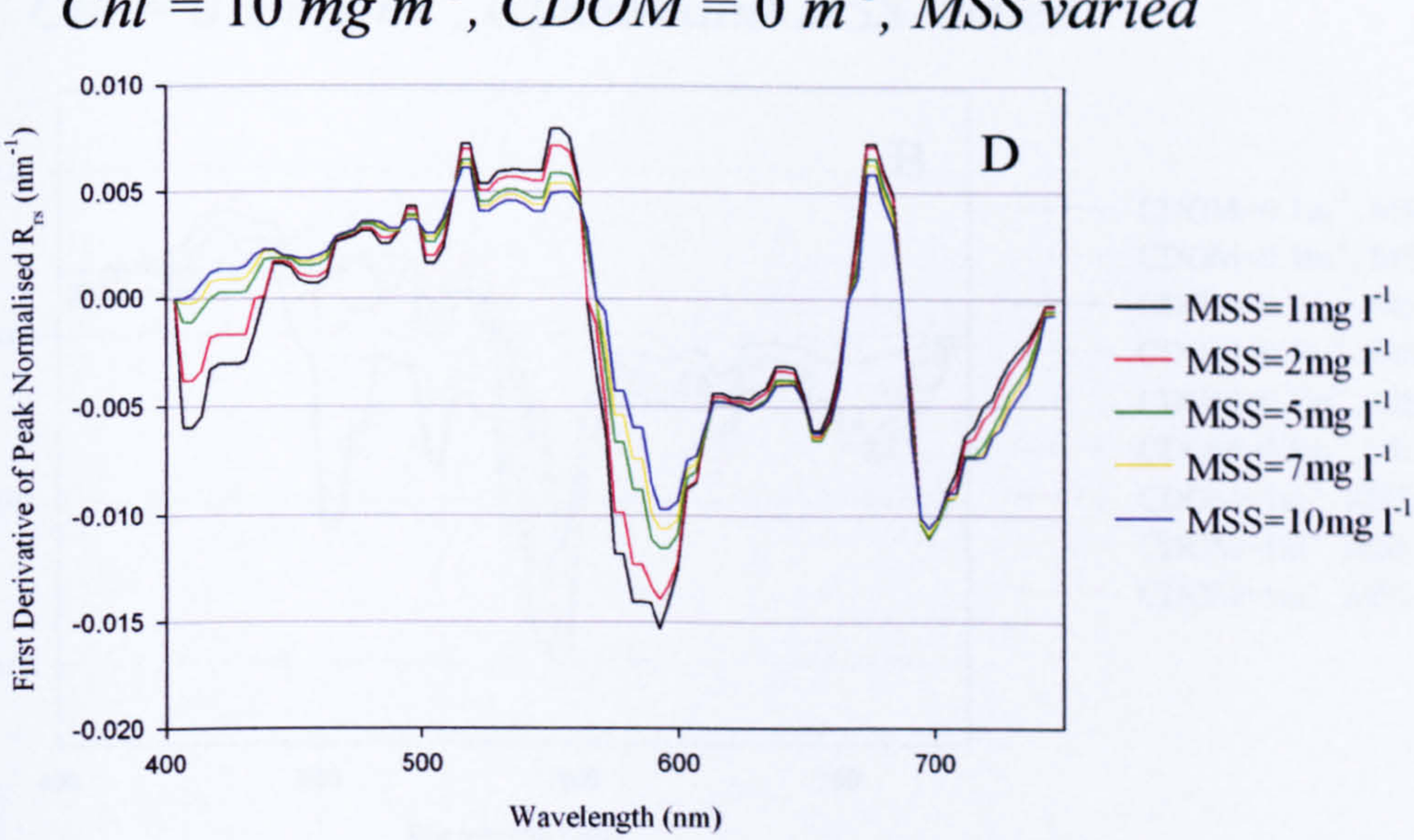

Figure 6.3. (ii) First derivative of normalised hyperspectral $R_{rs}\left(0^{+}\right)$ spectra for case 2 waters containing chlorophyll and MSS. In panel (A) $Chl = 0\,mg\,m^{-3}$, (B) $Chl = 0.1\,mg\,m^{-3}$, (C) $Chl = 1\,mg\,m^{-3}$ and (D) $Chl = 10\,mg\,m^{-3}$ and the MSS concentration in each case was varied.

Chl = 0 *mg* m^{-3}, *CDOM and MSS varied*

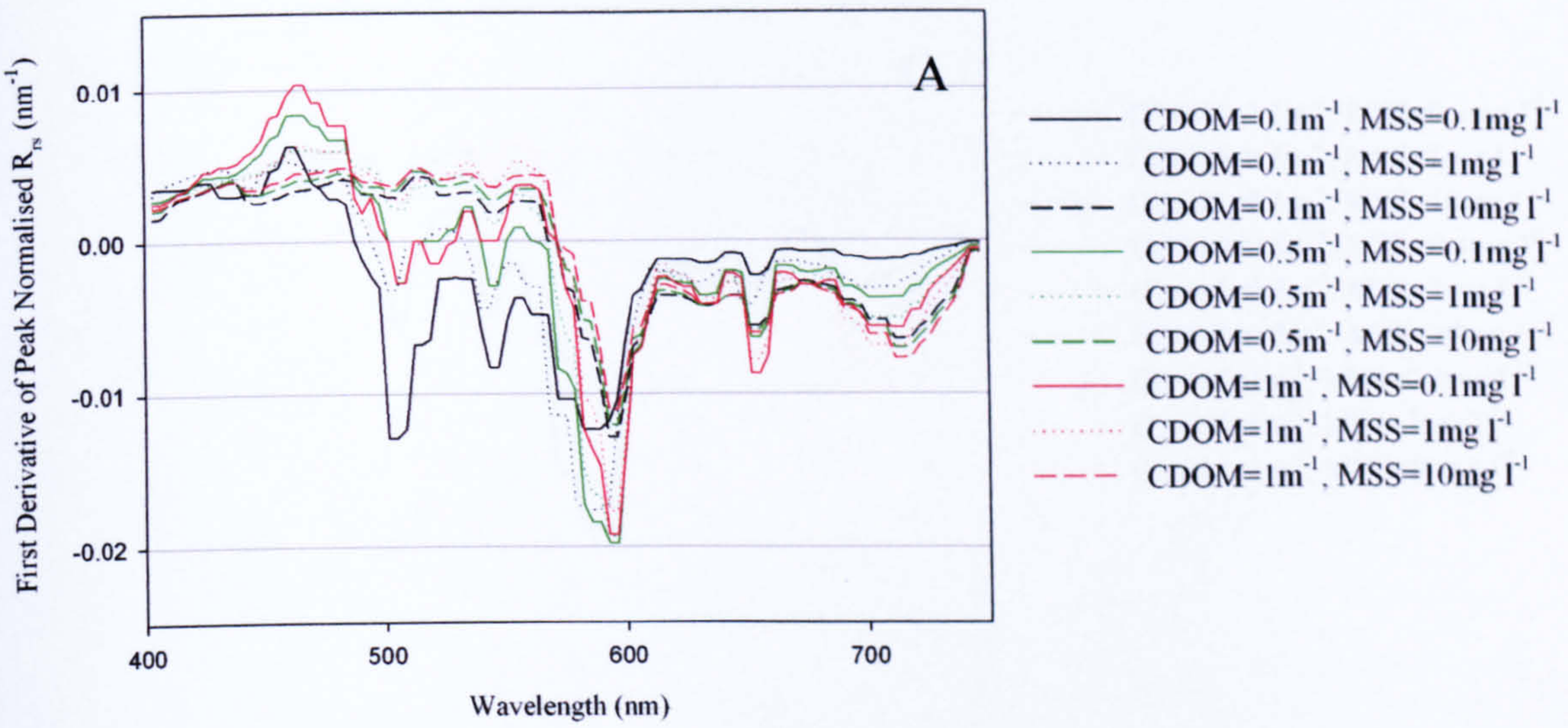

Chl = 0.1 *mg* m^{-3}, *CDOM and MSS varied*

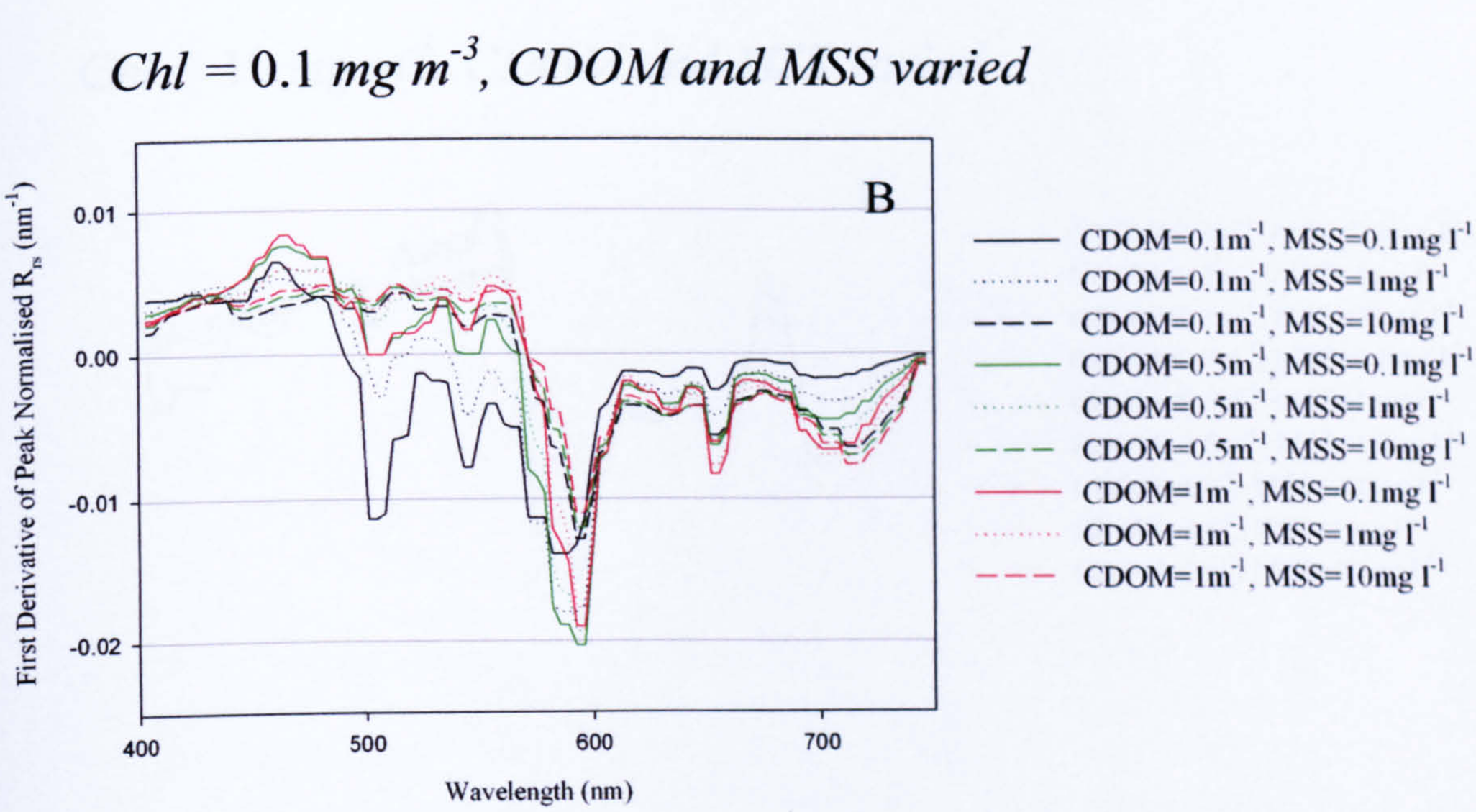

Figure 6.4. (i) First derivative of normalised hyperspectral $R_{rs}\left(0^{+}\right)$ spectra for case 2 waters containing chlorophyll, CDOM and MSS. In (A) $Chl = 0\,mg\,m^{-3}$, (B) $Chl = 0.1\,mg\,m^{-3}$, (C) $Chl = 1\,mg\,m^{-3}$ and (D) $Chl = 10\,mg\,m^{-3}$ and the CDOM and MSS combination was varied accordingly.

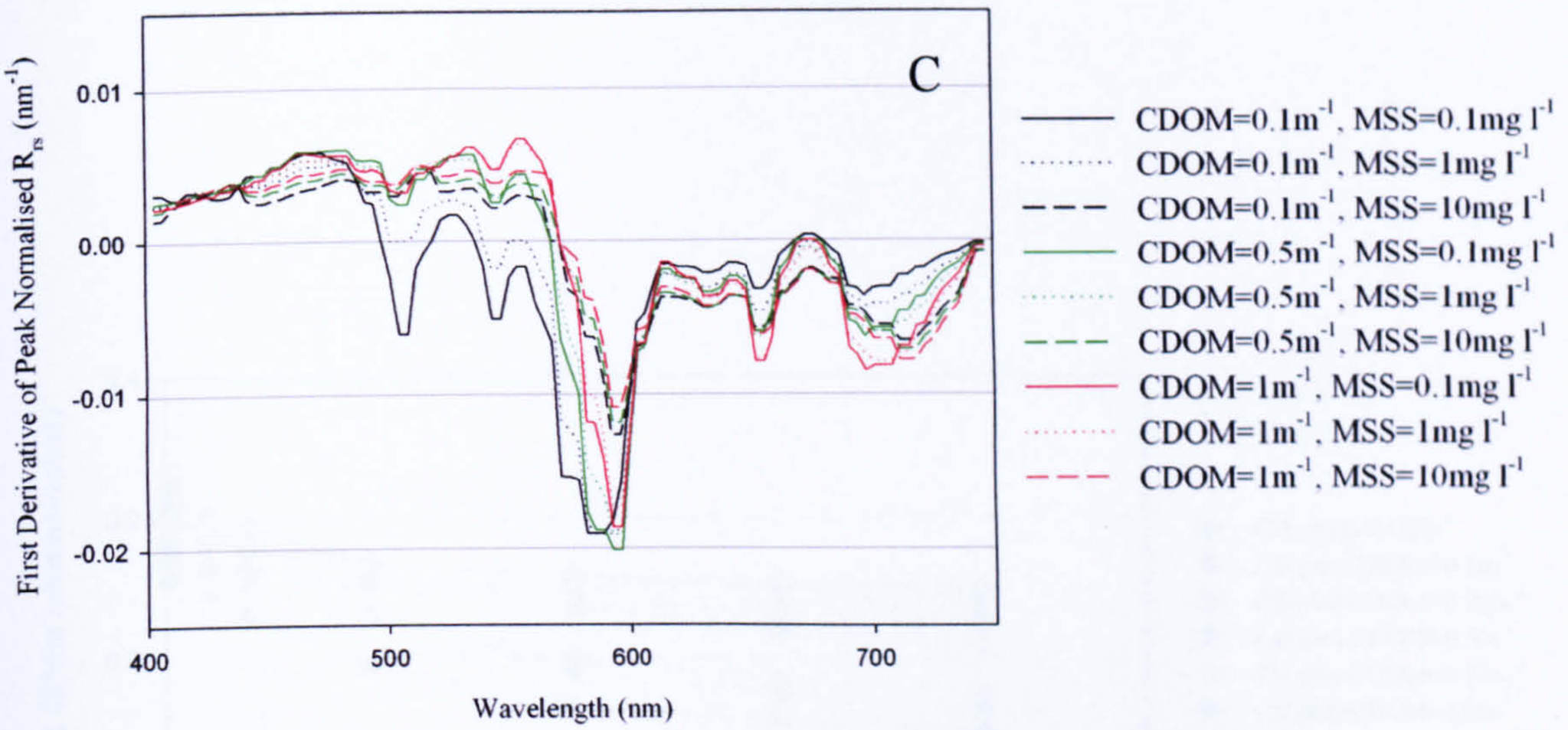

Figure 6.4. (ii) First derivative of normalised hyperspectral $R_{rs}\left(0^{+}\right)$ spectra for case 2 waters containing chlorophyll, CDOM and MSS. In panel (A) $Chl = 0\,mg\,m^{-3}$, (B) $Chl = 0.1\,mg\,m^{-3}$, (C) $Chl = 1\,mg\,m^{-3}$ and (D) $Chl = 10\,mg\,m^{-3}$ and the CDOM and MSS combination was varied accordingly.

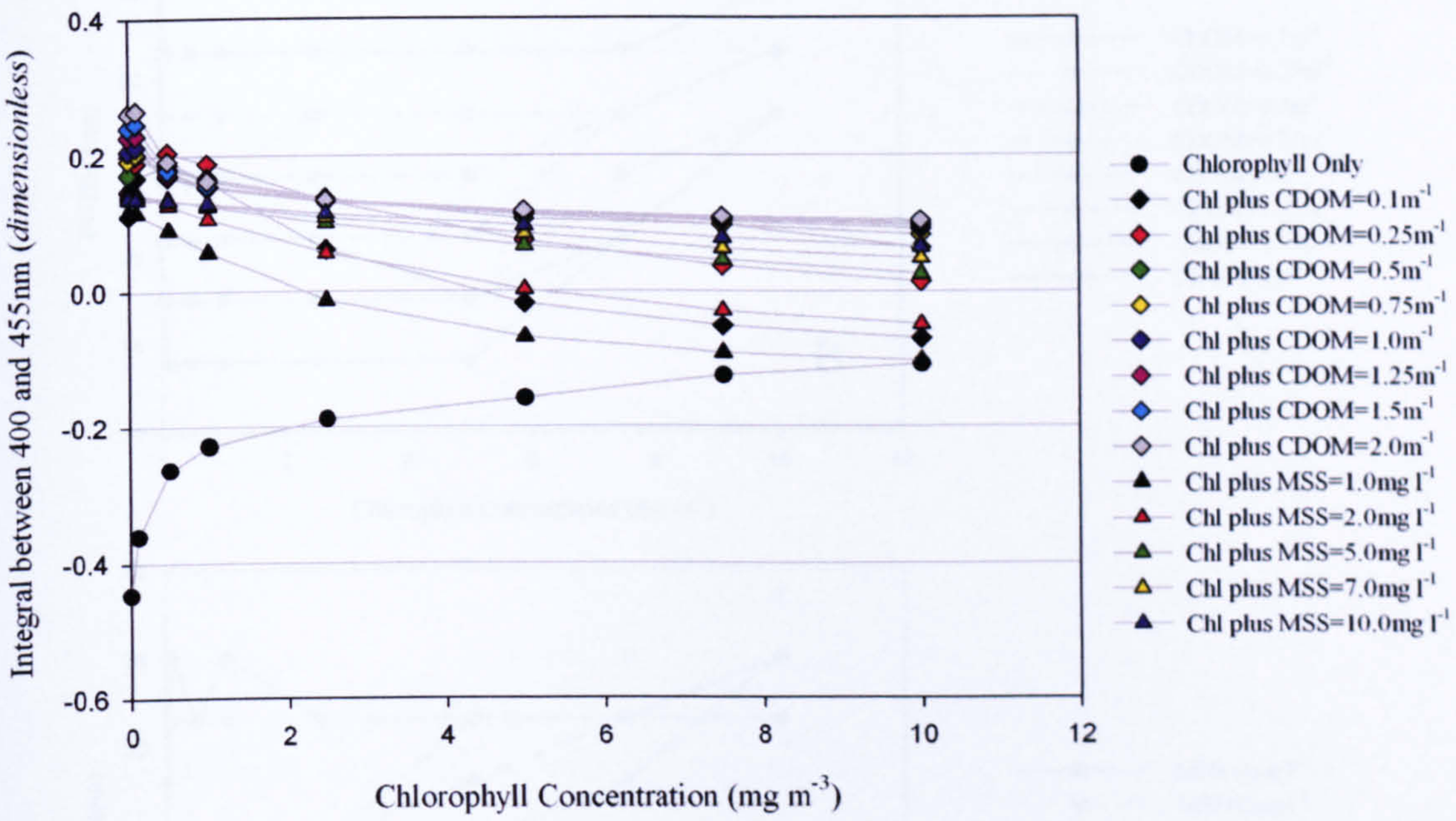

Figure 6.5. Integral, Feature A, between 400 and 455nm. For waters containing only chlorophyll the sign of the integral was negative. For waters containing significant concentrations of CDOM or MSS the sign of the integral became positive. However, at $Chl \geq 5 mg\, m^{-3}$ and low concentrations of CDOM $\left(\leq 0.1 m^{-1}\right)$ and MSS $\left(\leq 2 mg\, l^{-1}\right)$ the sign of the integral remained negative.

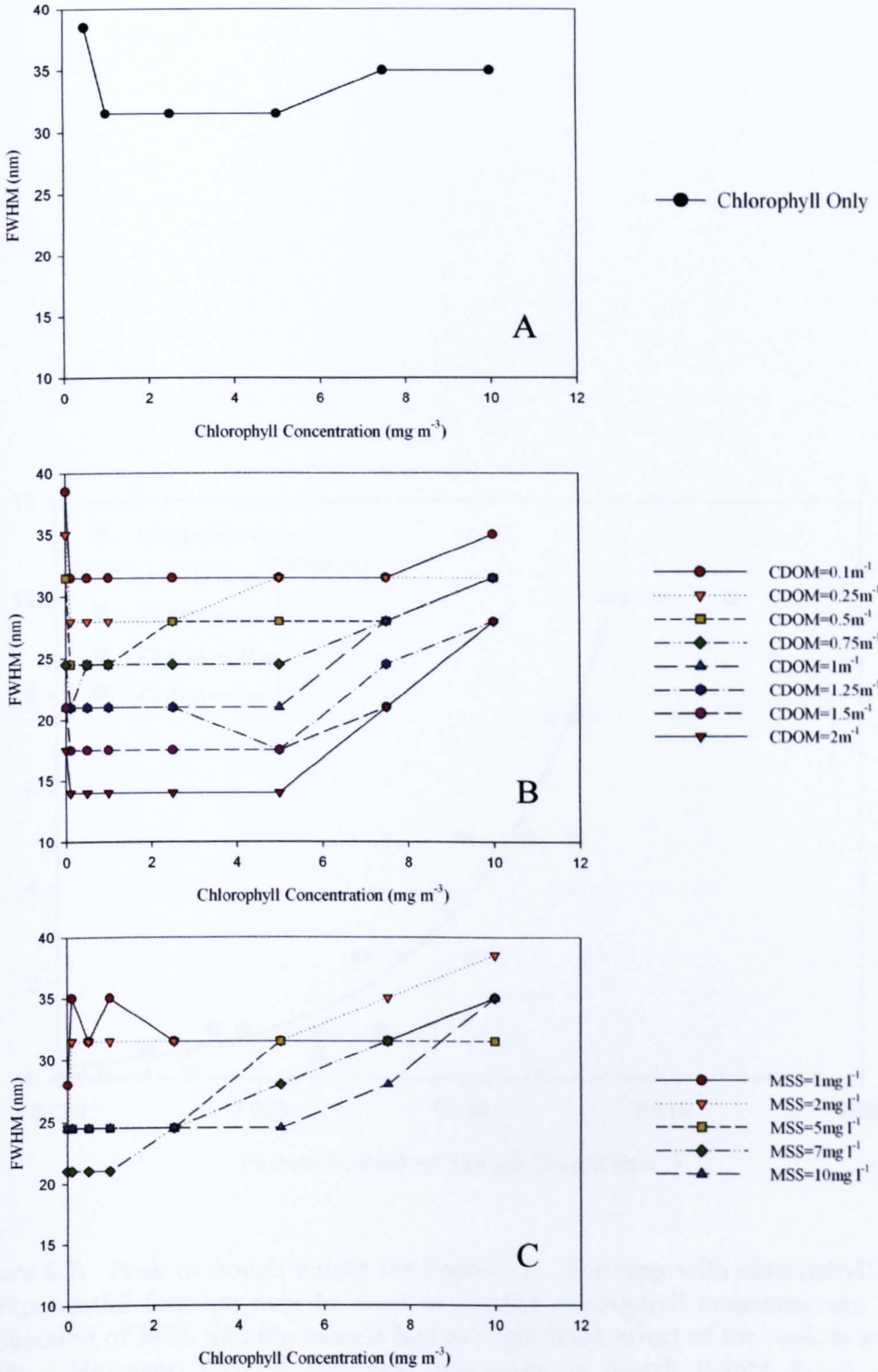

Figure 6.6. Full width half maximum (FWHM) for the trough located between 560 and 615nm, Feature C in the differentiated spectra. Panel (A) illustrates the FWHM when chlorophyll is included, (B) for chlorophyll and CDOM and (C) for chlorophyll and MSS.

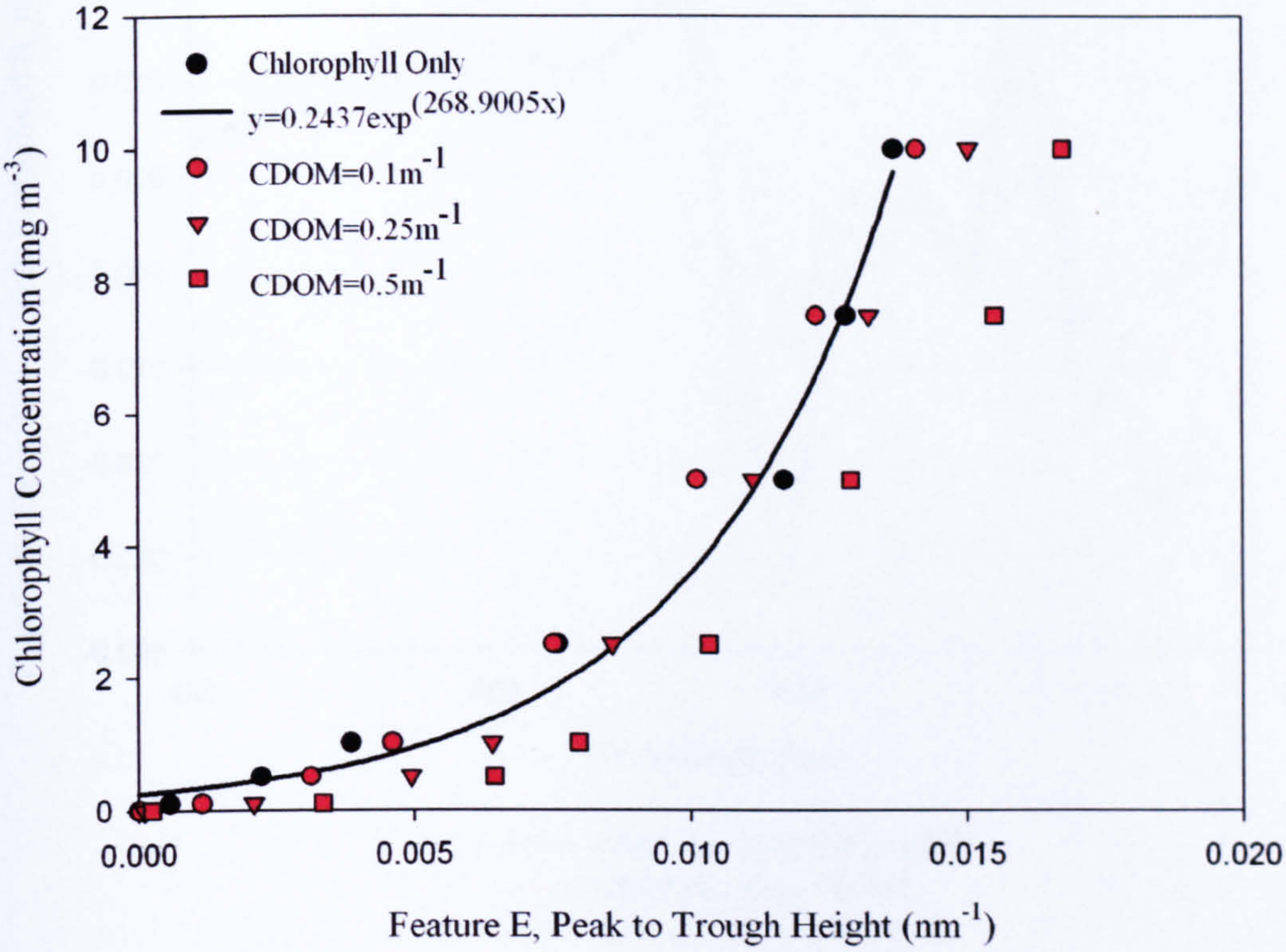

Figure 6.7. Peak to trough height for Feature E. For runs with chlorophyll only an exponential function may be used to predict chlorophyll concentration. The introduction of MSS into the models had no significant effect of the peak to trough height. However, CDOM increased the peak to trough height for a given chlorophyll concentration.

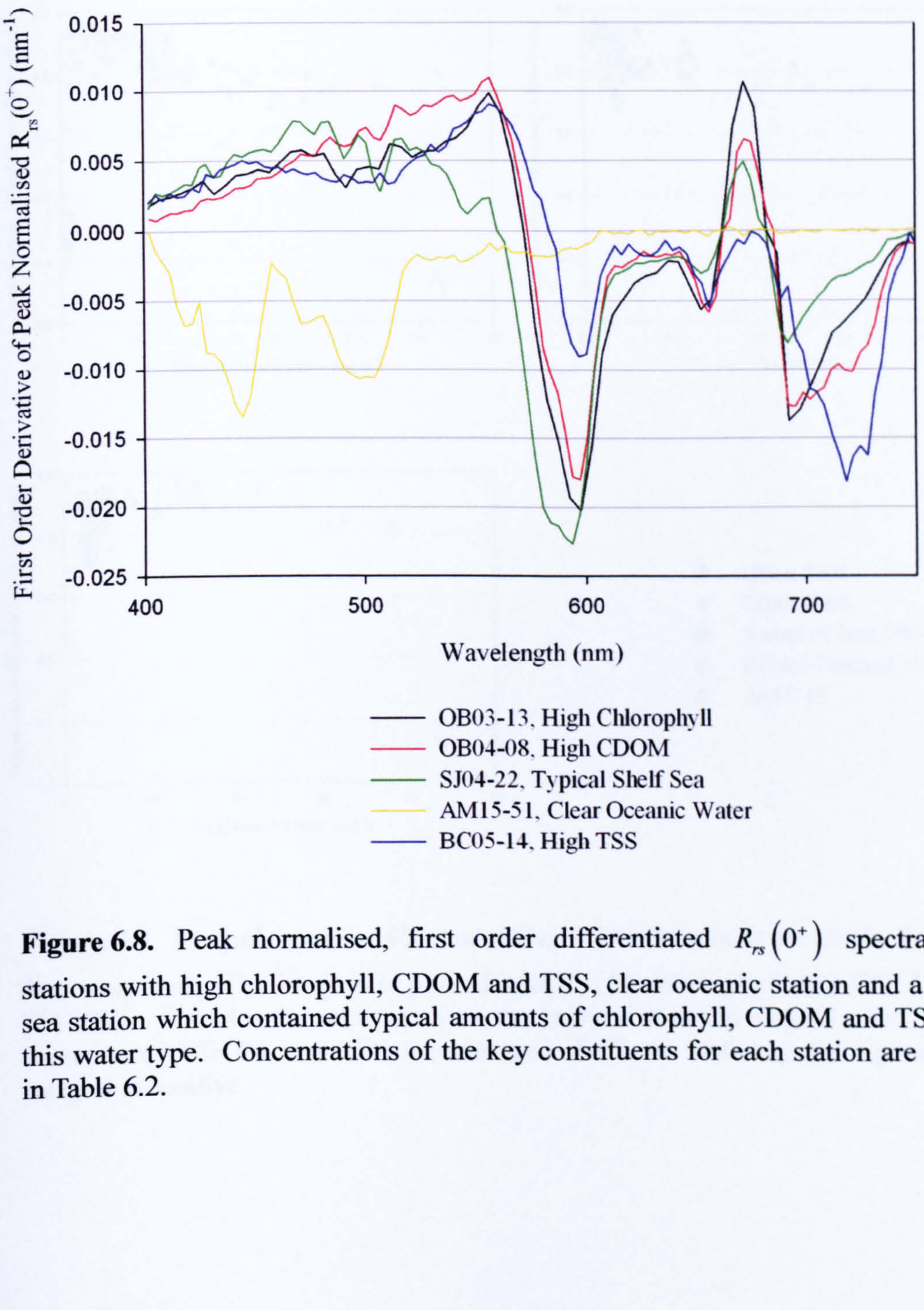

Figure 6.8. Peak normalised, first order differentiated $R_{rs}\left(0^+\right)$ spectra, for stations with high chlorophyll, CDOM and TSS, clear oceanic station and a shelf sea station which contained typical amounts of chlorophyll, CDOM and TSS for this water type. Concentrations of the key constituents for each station are listed in Table 6.2.

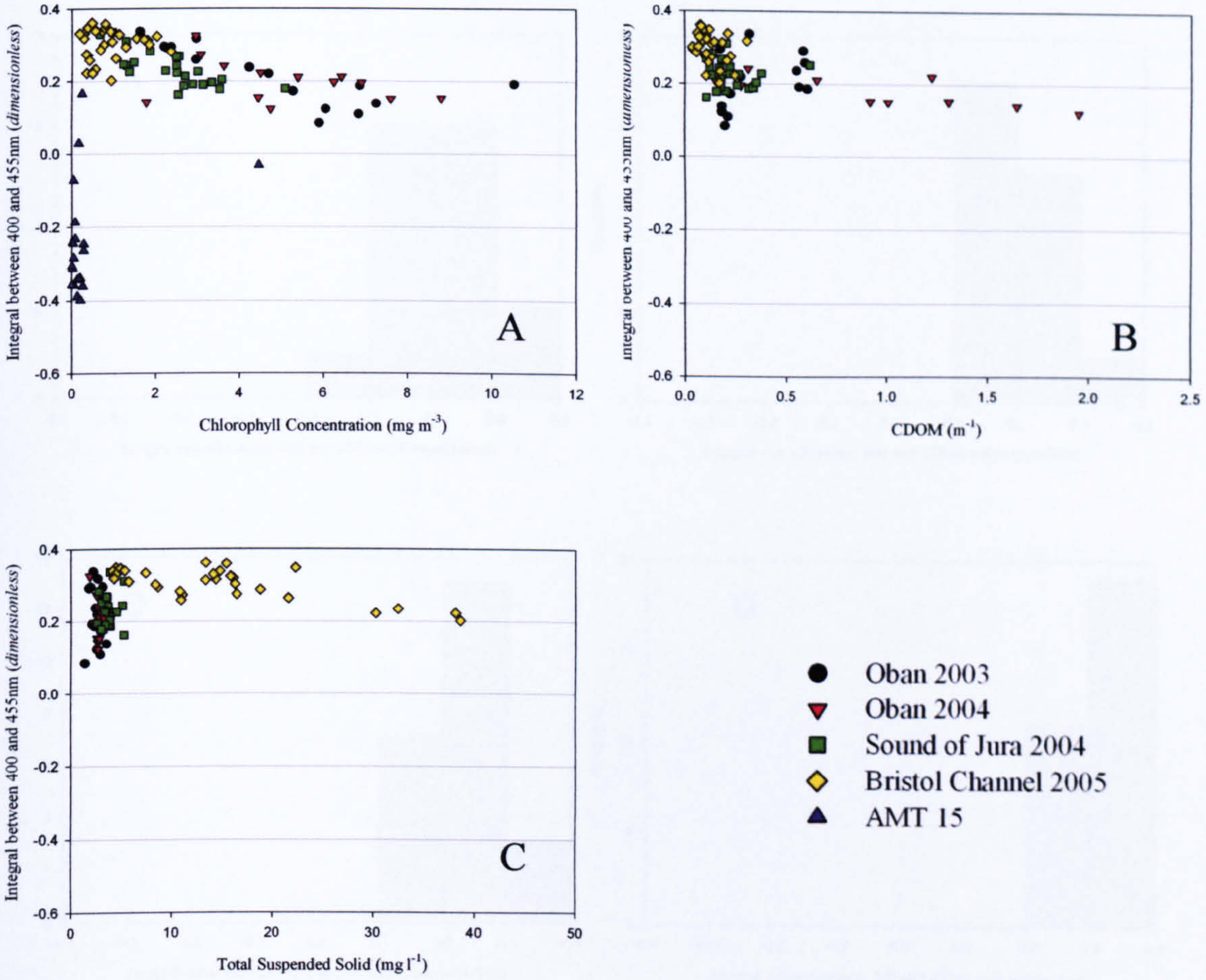

Figure 6.9. Integral between 400 and 455nm for all stations at which $R_{rs}(0^+)$ was measured. The integral is plotted against (A) chlorophyll, (B) CDOM and (C) TSS. For clear oceanic stations the integral remains negative but in the presence of CDOM and TSS (coastal and shelf sea stations) the sign of the integral is positive.

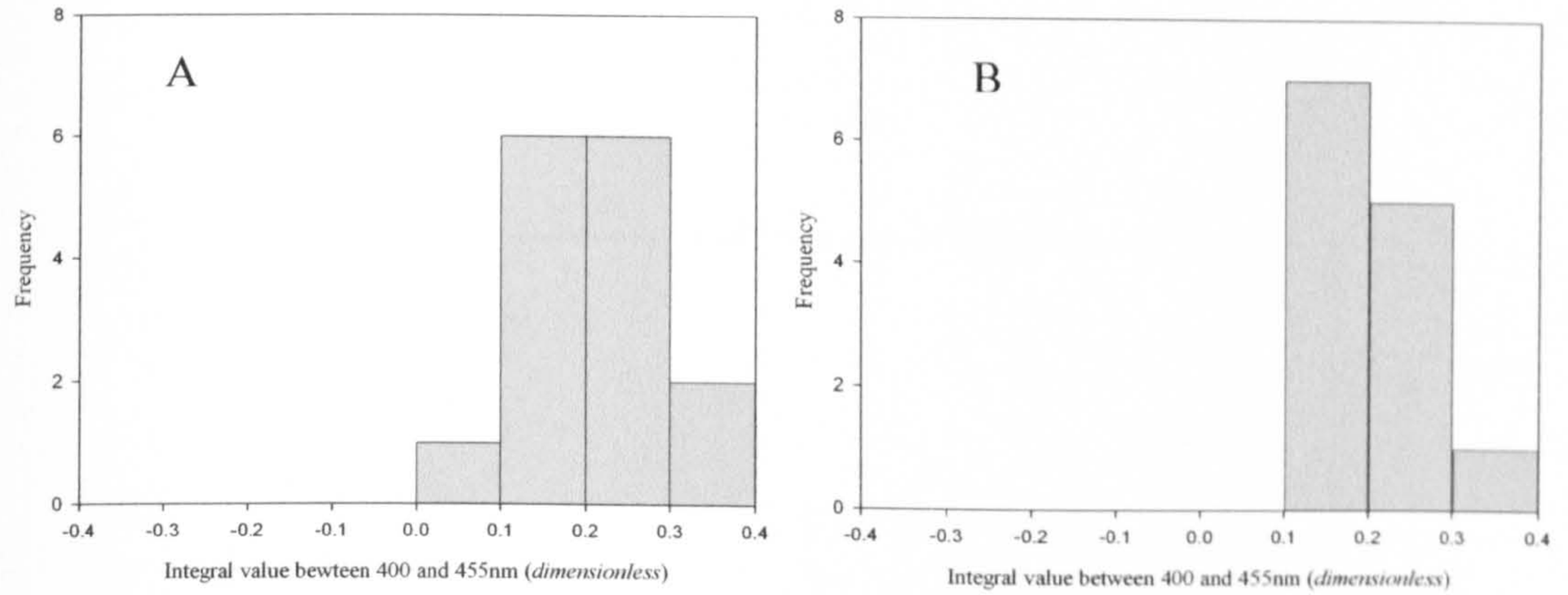

Figure 6.10. (i) Histograms of integral value between 400 and 455nm. Panel (A) illustrates the integral values for the Oban 2003, (B) for the Oban 2004, (C) for the Sound of Jura 2004, (D) the Bristol Channel 2005 and (E) AMT 15 cruises.

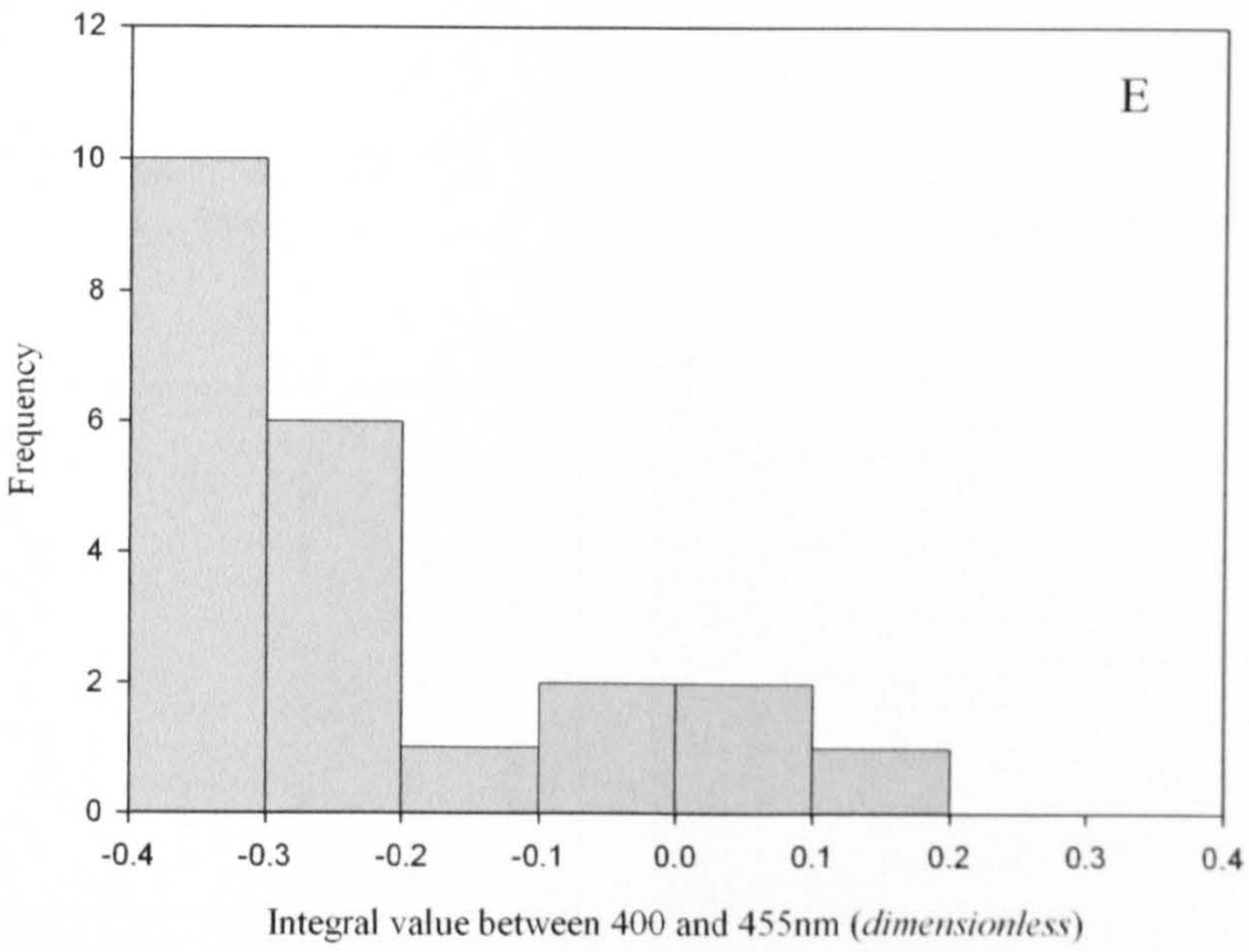

Figure 6.10. (ii) Histograms of integral value between 400 and 455nm. Panel (A) illustrates the integral values for the Oban 2003, (B) for the Oban 2004, (C) for the Sound of Jura 2004, (D) AMT 15 and (E) the Bristol Channel 2005 cruises.

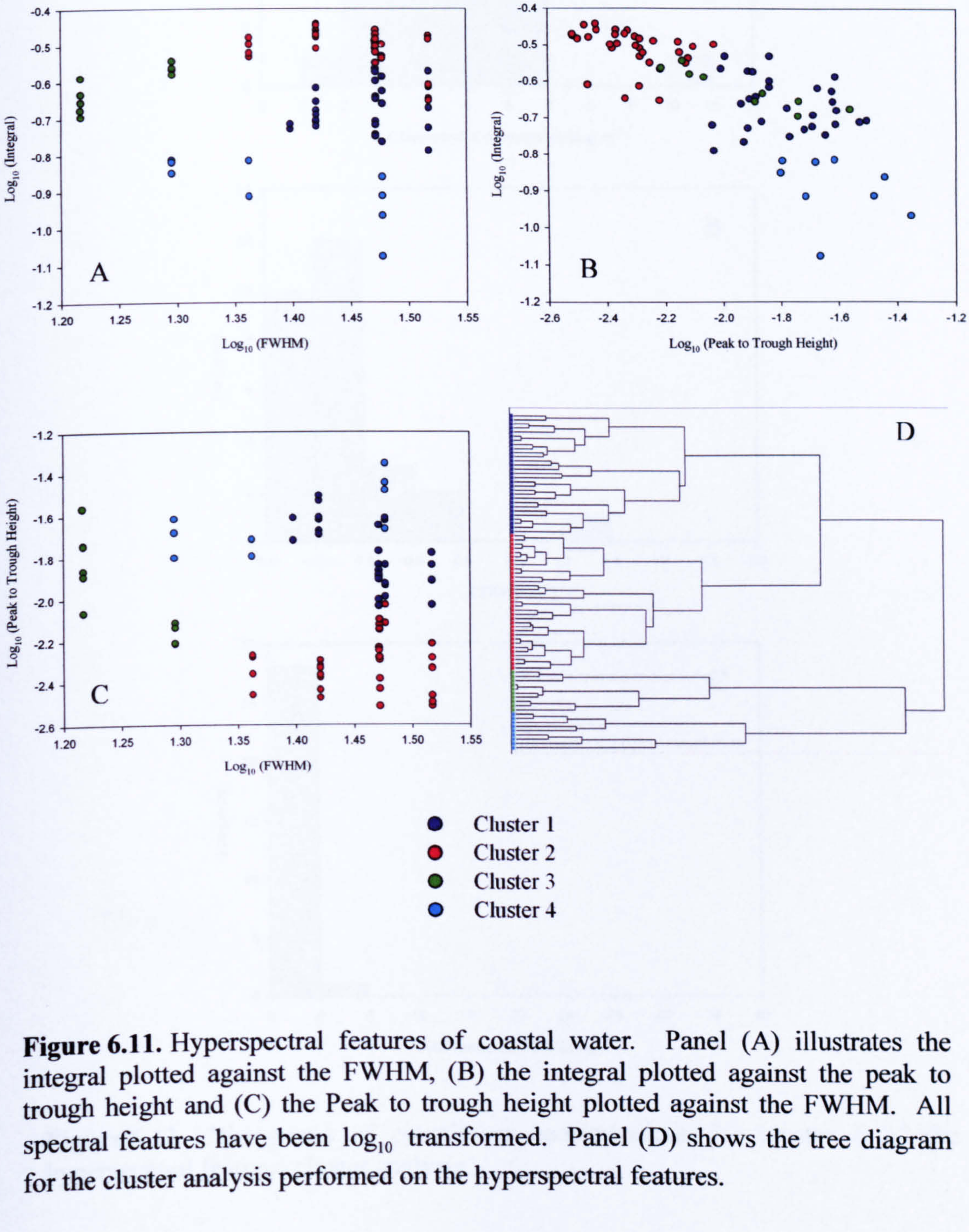

Figure 6.11. Hyperspectral features of coastal water. Panel (A) illustrates the integral plotted against the FWHM, (B) the integral plotted against the peak to trough height and (C) the Peak to trough height plotted against the FWHM. All spectral features have been $\log_{10}$ transformed. Panel (D) shows the tree diagram for the cluster analysis performed on the hyperspectral features.

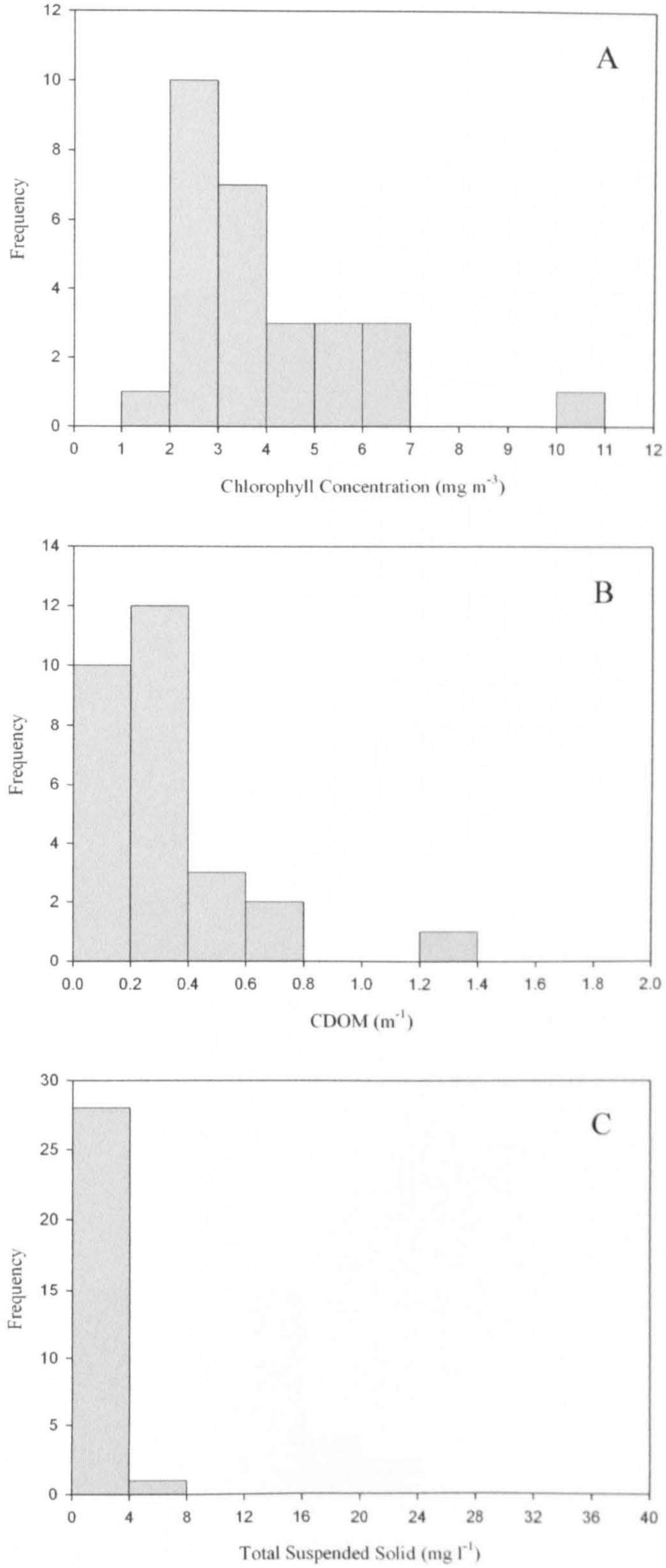

Figure 6.12. Histograms of constituent concentrations for cluster 1 of the hyperspectral features cluster analysis.

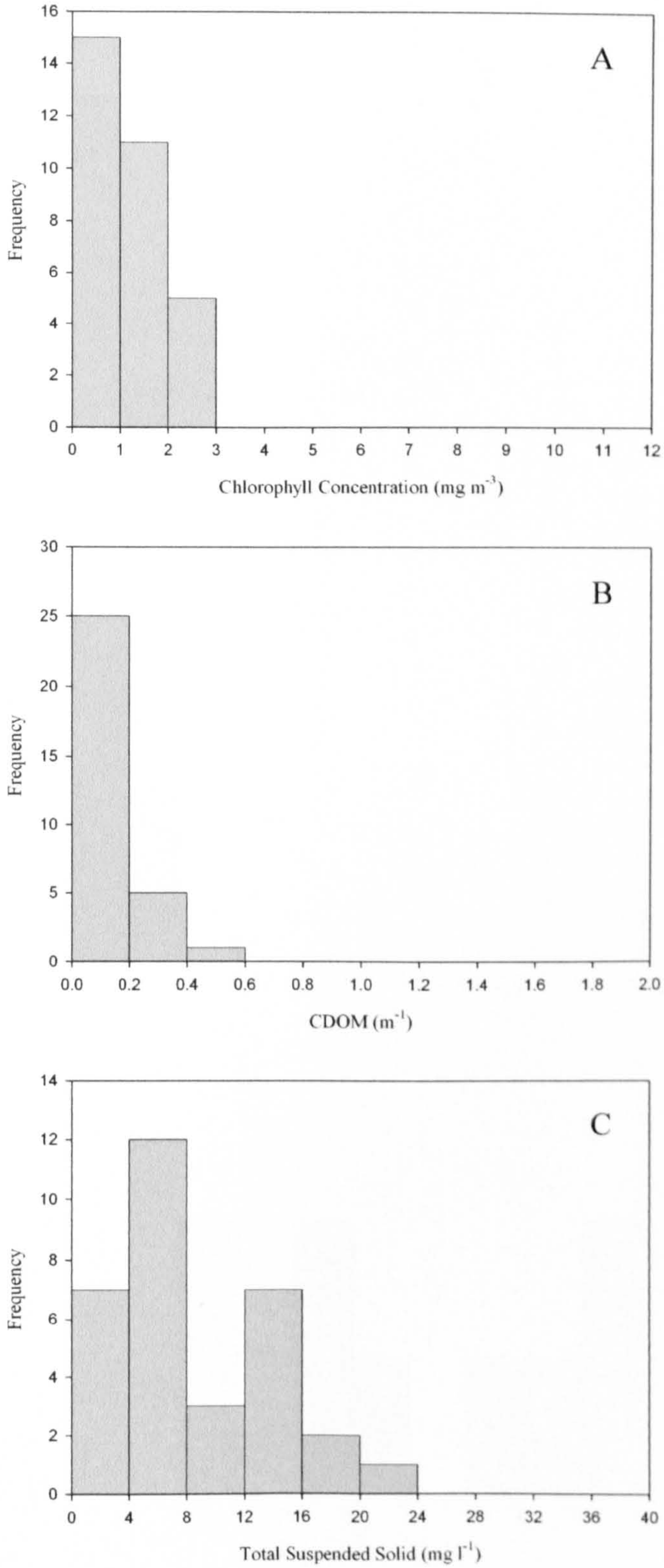

Figure 6.13. Histograms of constituent concentrations for cluster 2 of the hyperspectral features cluster analysis.

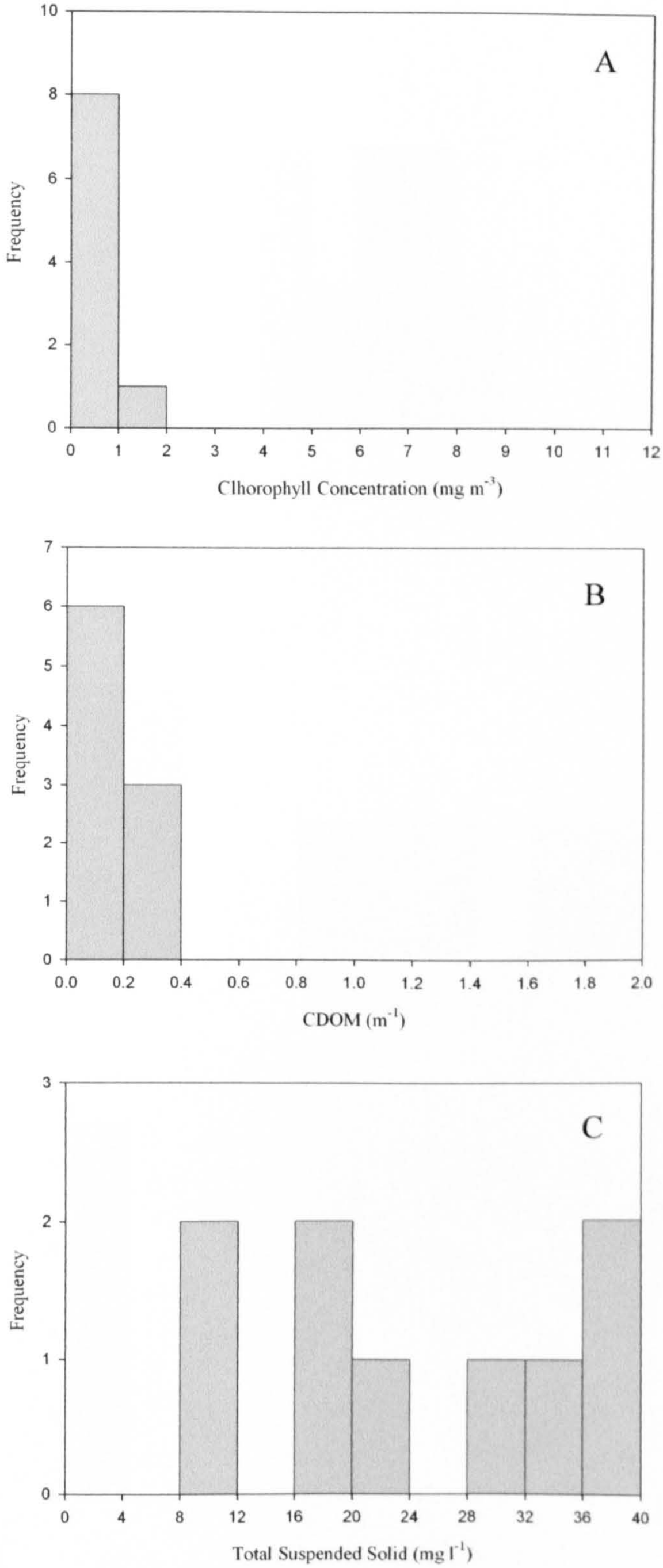

Figure 6.14. Histograms of constituent concentrations for cluster 3 of the hyperspectral features cluster analysis.

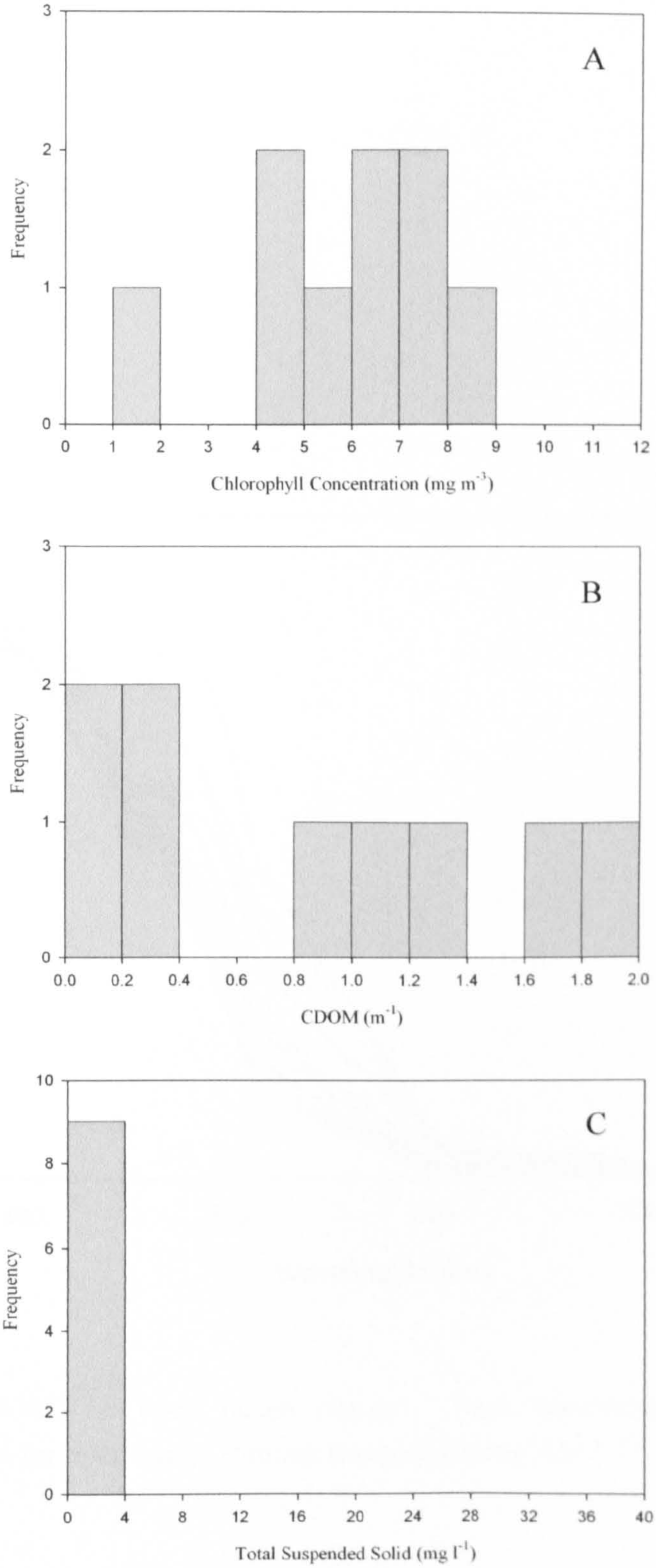

Figure 6.15. Histograms of constituent concentrations for cluster 4 of the hyperspectral features cluster analysis.

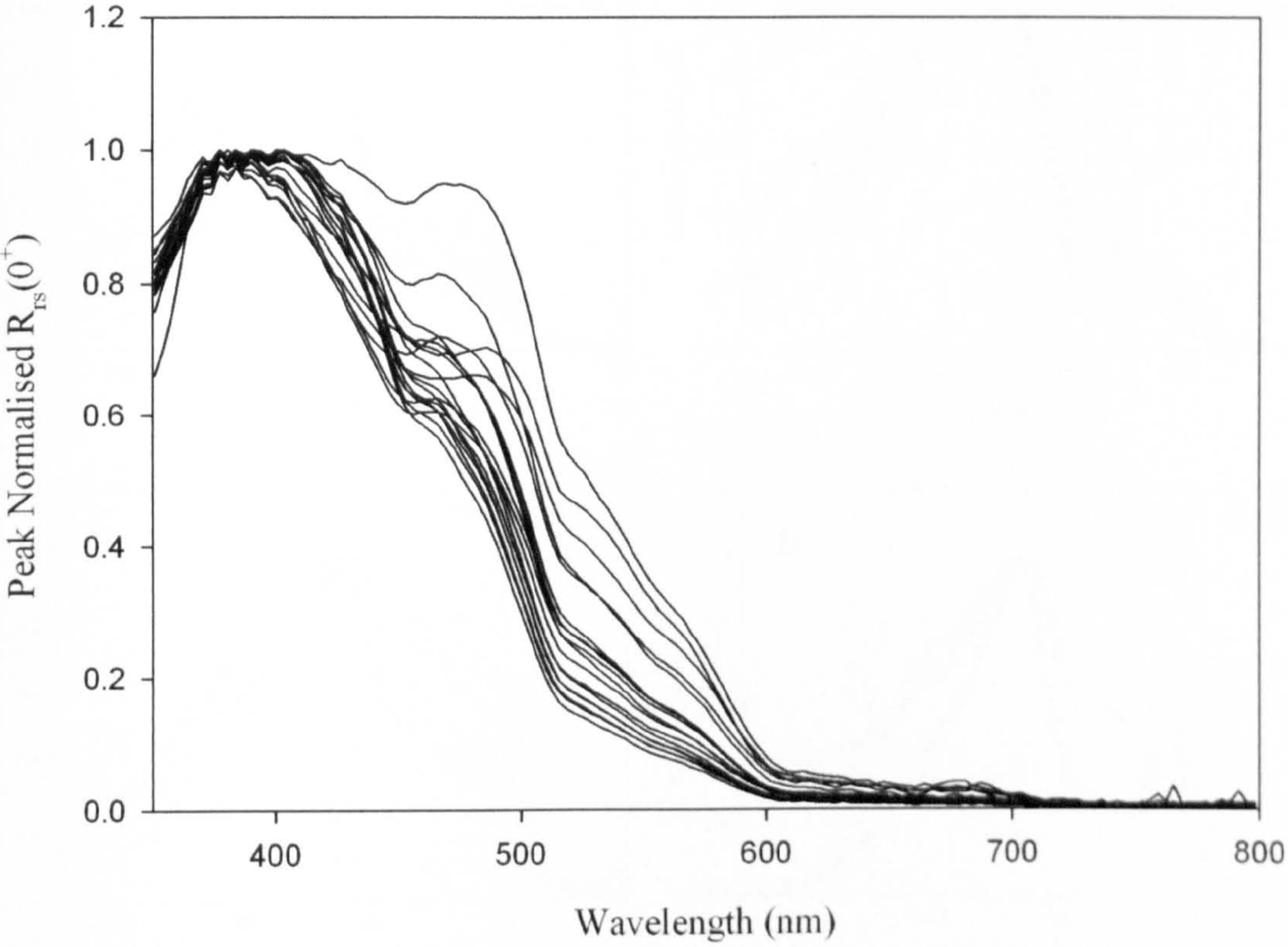

Figure 6.16. AMT 15 open ocean cluster. Peak normalised hyperspectral $R_{rs}\left(0^{+}\right)$ spectra for open ocean stations sampled during AMT 15.

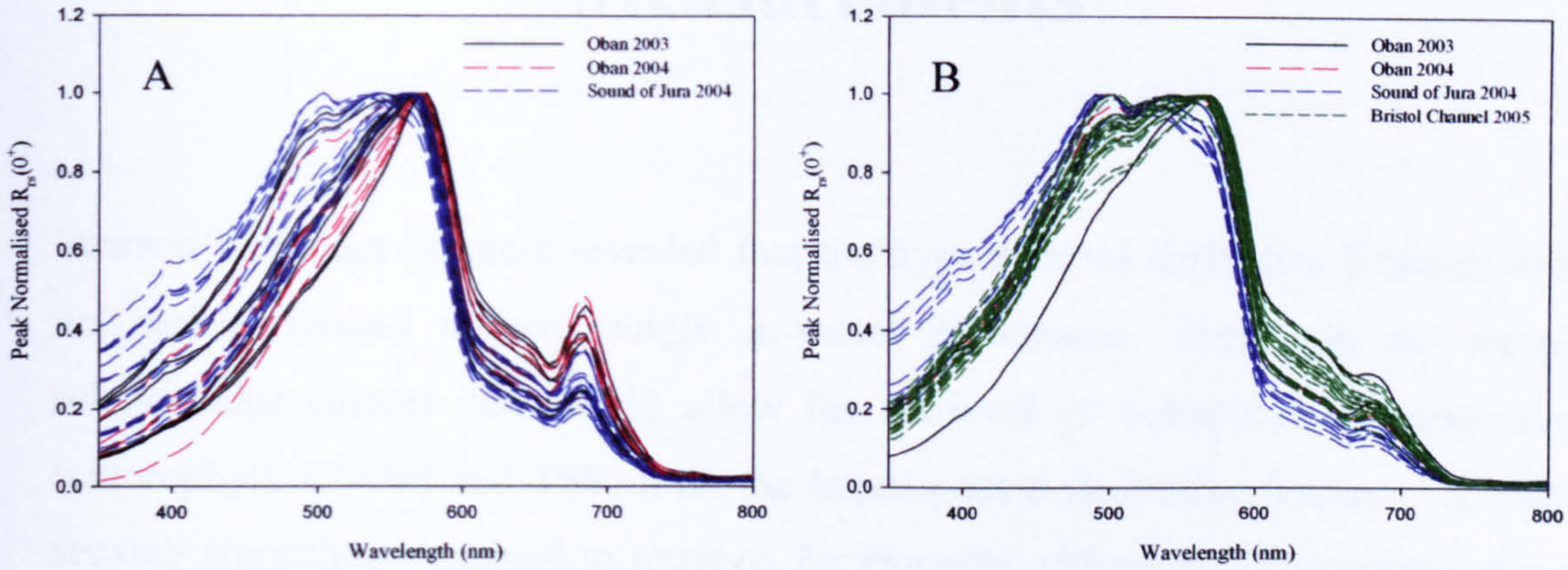

Figure 6.17. Peak normalised hyperspectral $R_{rs}\left(0^+\right)$ spectra allocated according to the results of the cluster analysis of hyperspectral features in first order differentiated spectra. Panel (A) contains the spectra for cluster 1, (B) for cluster 2, (C) for cluster 3 and (D) for cluster 4.

Chapter 7: Assessment of the Performance of Multispectral Remote Sensing Algorithms in Coastal Waters Using Data Derived From Hyperspectral Reflectance Measurements

Pearson's Product Moment revealed that the hyperspectral derivative features were not solely related to any single in-water constituent. Therefore, no simple relationships existed that would allow the retrieval of constituent concentration (chlorophyll, CDOM and TSS) form the hyperspectral derivative features. Remote sensing algorithms designed to retrieve, for example, chlorophyll concentration can be perturbed by the presence of other material in the water body. In this chapter examples of current remote sensing algorithms are applied to the coastal water dataset to assess the extent to which accurate information about the water body can be retrieved. The extent to which improved information on constituent concentrations can be retrieved from hyperspectral remote sensing reflectance signals using hyperspectral features is also investigated in this chapter.

Shelf seas and coastal water contain a mixture of optically important components which influence ocean colour and water leaving radiance. Algorithm development for such areas is difficult due to the wide variety of water types that can exist. Therefore, targeting algorithms to specific water types is potentially important in such optically complex water. A number of remote sensing algorithms were tested on data from shelf sea and coastal waters to assess the extent to which quantitative information about the in-water constituents could be gained. The four clusters identified in the analysis of the hyperspectral derivative features made it possible to investigate how well the algorithms worked in the different water types identified.

7. 1. Chlorophyll *a* Algorithms

Four chlorophyll *a* algorithms were tested, SeaWiFS OC4V4, MODIS Chlor_a_2, MODIS Chlor_a_3 and MERIS OC4E. For each of these algorithms hyperspectral data was binned into the necessary wavebands and substituted into the appropriate equation. The calculated values (algorithm) were then plotted against *in situ* measurements of chlorophyll *a*, together with a 1:1 line and linear regression line.

7. 1. 1. SeaWiFS OC4V4

The SeaWiFS OC4V4 algorithm (O'Reilly *et al*, 1998; O'Reilly *et al*, 2000) is a four band reflectance ratio algorithm which takes the form:

$$Chl\,a_{OC4V4} = 10^{0.366-3.067R+1.930R^2+0.649R^3-1.532R^4} \tag{7.1}$$

where R is the $\log_{10}$ of the maximum band ratio:

$$R = \log_{10}\left[\max\left(\frac{R_{rs}(443)}{R_{rs}(555)}, \frac{R_{rs}(490)}{R_{rs}(555)}, \frac{R_{rs}(510)}{R_{rs}(555)}\right)\right] \tag{7.2}$$

and $R_{rs}(\lambda)$ is the remote sensing reflectance at wavelength λ.

Figure 7.1 panel (A) illustrates the results of the comparison between OC4V4 and measured values of chlorophyll *a*. Clusters 3 and 4, water with high values of TSS or CDOM and chlorophyll, produce badly overestimated values of chlorophyll using OC4V4. This is a problem known to occur in highly turbid water (Wozniak and Stramski, 2004; Doxaran *et al*, 2004; Dall'Olmo *et al*, 2005). Removal of these clusters from the analysis produced an improved agreement between the calculated and measured values with a $R^2 = 0.64$. The 1:1 line shows that the OC4V4 algorithm tends to overestimate the chlorophyll concentration in the shelf sea stations sampled.

7.1.2. MODIS Chlor_a_2

The next chlorophyll algorithm tested was the MODIS Chlor_a_2 (MOD-21, parameter 26) from Carder *et al*, 1999. This is a three band reflectance ratio algorithm which takes the form:

$$Chl\,a_{Chlo\_a\_2} = 10^{0.283-2.753R+1.457R^2+0.659R^3-1.403R^4} \tag{7.3}$$

where R is the $\log_{10}$ of the maximum band ratio:

$$R = \log_{10}\left[\max\left(\frac{R_{rs}(443)}{R_{rs}(551)}, \frac{R_{rs}(488)}{R_{rs}(551)}\right)\right] \tag{7.4}$$

and $R_{rs}(\lambda)$ is the remote sensing reflectance at wavelength λ.

Figure 7.2 panel (A) illustrates the results of plotting the calculated values against the measured *in situ* values. For water heavily influenced by TSS or CDOM and chlorophyll (clusters 3 and 4 respectively) the algorithm produced very high estimates of the chlorophyll *a* concentration. Removing clusters 3 and 4 and performing a simple linear regression gave a R^2 of 0.58 with a gradient of 0.85. The MODIS Chlor_a_2 algorithm, like OC4V4, overestimates the chlorophyll *a* concentration in these waters.

7.1.3. MODIS Chlor_a_3

The second MODIS algorithm tested was Chlor_a_3 (MOD-21, parameter 27, Carder *et al*, 1999) which takes the form:

$$Chl\,a_{Chlor\_a\_3} = 10^{0.289-3.20R+1.2R^2} \tag{7.5}$$

where R is given by:

$$R = \log_{10}\frac{R_{rs}(488)}{R_{rs}(551)} \tag{7.6}$$

and $R_{rs}(\lambda)$ is the remote sensing reflectance at wavelength λ.

Figure 7.3 shows the calculated chlorophyll *a* values regressed against the measured *in situ* values for this algorithm. Panel (A) contains information with all the clusters included. Panel (B) shows the results of performing a linear regression using only clusters 1 and 2. This revealed a R^2 of 0.59 and a gradient of 1.13. The algorithm overestimates chlorophyll *a* concentrations even with clusters 3 and 4 removed.

7. 1. 4. MERIS OC4E

The four band reflectance ratio used by MERIS, OC4E, takes the form:

$$Chl\,a_{OC4E} = 10^{0.368-2.814R+1.456R^2+0.768R^3-1.292R^4} \tag{7.7}$$

where R is the $\log_{10}$ of the maximum band ratio:

$$R = \log_{10}\left[\max\left(\frac{R_{rs}(443)}{R_{rs}(560)}, \frac{R_{rs}(490)}{R_{rs}(560)}, \frac{R_{rs}(510)}{R_{rs}(560)}\right)\right] \tag{7.8}$$

and $R_{rs}(\lambda)$ is the remote sensing reflectance at wavelength λ.

Figure 7.4 illustrates the algorithm chlorophyll values plotted against the measured values. As with the previous algorithms, clusters 3 and 4 give overestimations of the chlorophyll *a* concentration. Removing these clusters results in improved agreement between the calculated and measured values (Figure 7.4 panel (B)), with a R^2 of 0.64 and gradient of 0.83. This is the best R^2 value observed for any of the four chlorophyll algorithms tested. As with previous algorithms, the calculated values of chlorophyll tend to be an overestimation of the measured values.

7. 1. 5. Chlorophyll *a* Algorithm Review

None of the remote sensing algorithms tested were successful at retrieving accurate estimates of the chlorophyll *a* concentration. Clusters 3 and 4, the highly turbid

waters dominated by TSS or CDOM and chlorophyll, produced large overestimates of the chlorophyll *a* concentration when the remote sensing reflectance band ratio algorithms were applied. In all cases removing these clusters improved the agreement observed between the calculated and measured chlorophyll *a* values. Table 7.1 contains information on the gradient and R^2 values obtained for each algorithm. The MERIS OC4E algorithm gave the best R^2 value (0.64) with a gradient that was reasonably close to one (0.83). The algorithms tested here all overestimated the *in situ* chlorophyll *a* concentration even with clusters 3 and 4 removed, and the MODIS Chlor_a_3 algorithm performed particularly poorly in this respect.

7. 2. MODIS Absorption Algorithms

MODIS documentation also provides algorithms for the retrieval of the absorption coefficient at 675nm for phytoplankton and at 400nm for CDOM. The algorithms provided for the absorption coefficient estimations are tested in this section by comparing the values calculated to the measured *in situ* data.

7. 2. 1. Phytoplankton Absorption Coefficient

According to Carder *et al* (2003) the phytoplankton absorption coefficient at 675nm can be estimated using the following equation:

$$a_{phyto}(675) = 0.328 \times \left(10^{-0.919+1.037\rho_{25}-\left(0.407\times(\rho_{25})^2\right)-3.531\rho_{35}+\left(1.702\times(\rho_{35})^2\right)} - 0.08 \right) \quad (7.9)$$

where ρ_{ij} are $\log_{10}$ of the ratio of the remote sensing reflectance of MODIS channel i to channel j.

Substituting the necessary values into equation (7.9), it was possible to calculate values of $a_{phyto}(675)$. These values were then plotted against measurements of $a_{phyto}(675)$ obtained using the filter pad absorption technique (Chapter 3 section 3.2.2) and corrected for the effects of pathlength amplification (Chapter 3 section

3.2.3). Figure 7.5 (A) illustrates this. From the figure it can be seen that, with the exception of cluster 3, the MODIS algorithm (equation (7.9)) tends to underestimate the value of $a_{phyto}(675)$. In panel (B) cluster 3 (high TSS stations in the Bristol Channel) has been removed and a linear regression conducted. The linear regression yielded a gradient of 0.34 and R^2 of 0.51. The low gradient and R^2 values showed that the MODIS $a_{phyto}(675)$ algorithm did not provide accurate estimates of the absorption by phytoplankton at 657nm.

It should be noted that the Oban 2004 stations were not included in this analysis due to the poor quality of filter pad absorption data.

7. 2. 2. CDOM Absorption Coefficient

An algorithm for the estimation of the absorption by CDOM at 400nm (MOD-21, parameter 30) is set out in Carder *et al* (2003) and takes the form:

$$a_{CDOM}(400) = 1.5 \times \left(10^{-1.147 - 1.963\rho_{15} - \left(1.01 \times (\rho_{15})^2\right) + 0.856\rho_{25} + \left(1.702 \times (\rho_{25})^2\right)} \right) \qquad (7.10)$$

where ρ_{ij} are $\log_{10}$ of the ratio of the remote sensing reflectance of MODIS channel i to channel j.

The calculated values were plotted against the measured values of $a_{CDOM}(400)$ in Figure 7.6. Panel (A), with all clusters included, shows relatively good agreement between the calculated and measured values. In panel (B) a linear regression on all the clusters produced a good R^2 value of 0.91 and gradient of 0.70. Performing individual linear regressions on each cluster (data not shown) revealed that cluster 2 had the poorest agreement between the calculated and measured values of $a_{CDOM}(400)$. Panel (B) also revealed that at higher CDOM concentrations the calculated values tend to be underestimated. In panel (C) cluster 2 has been removed and regression repeated. Removing cluster 2 only slightly improved the agreement between the calculated and measured values, with a R^2 value of 0.91 and gradient of 0.71. The good R^2 value and reasonably good gradient showed that the algorithm

provided reasonable estimates of $a_{CDOM}(400)$, inspection of Figure 7.6 panel (C) revealed that higher CDOM concentrations $(\geq 1 m^{-1})$ tended to be underestimated.

7.2.3. Absorption Coefficient Review

The MODIS algorithm for $a_{phyto}(675)$ underestimated these values when compared with the *in situ* filter pad data. The exception to this was cluster 3. Cluster 3 was identified as turbid water with high TSS concentrations and low levels of chlorophyll. However, the CDOM algorithm worked well. It appears that retrieval of $a_{CDOM}(400)$ is possible in shelf sea waters using remote sensing algorithms.

7.3. SeaWiFS $K_d(490)$ Algorithm

7.3.1. SeaWiFS $K_d(490)$ Algorithm Performance

An algorithm for $K_d(490)$, the diffuse attenuation coefficient for downwelling irradiance at 490nm, was first developed by Austin and Petzold (1981) for use with CZCS (Coastal Zone Colour Scanner) data. Mueller and Trees (1997) adapted the algorithm for use with SeaWiFS wavebands and the current algorithm (Mueller, 2000) takes the form:

$$K_d(490) = 0.016 + a\left[\frac{nL_w(490)}{nL_w(555)}\right]^b \qquad (7.11)$$

where 0.016 is the diffuse attenuation coefficient at 490nm for pure water, $nL_w(\lambda)$ is the normalised water leaving radiance at wavelength λ, a and b are derived constants which take the value of 1.5645 and -1.5401 respectively.

In order to calculate $K_d(490)$ using equation (7.11) it was first necessary to calculate values of the normalised water leaving radiance, $nL_w(\lambda)$, at the appropriate wavelengths. $nL_w(\lambda)$ was calculated using the following equation:

$$nL_w(\lambda) = L_w(\lambda) \times \frac{F_0(\lambda)}{E_s(\lambda)} \qquad (7.12)$$

where $L_w(\lambda)$ is the water leaving radiance at wavelength λ, $E_s(\lambda)$ is the surface irradiance value at wavelength λ and $F_0(\lambda)$ is the mean extraterrestrial solar irradiance at wavelength λ. $F_0(\lambda)$ values were found to be equal to 2.009 and 1.899 $W\,m^{-2}\,nm^{-1}$ for 490 and 555nm respectively (Werhli, 1985).

Measured values of $L_w(\lambda)$ and $E_s(\lambda)$ (taken here as the value of $E_d(0^+,\lambda)$, the downwelling irradiance just above the sea surface) were binned into the SeaWiFS 490 and 555nm wavebands. The appropriate values of $nL_w(\lambda)$ were calculated using equation (7.12), and substituted into equation (7.11) to calculate $K_d(490)$. Calculated values of $K_d(490)$ were then compared with *in situ* measurements of $K_d(490)$ made using either the Satlantic HyperPro (Oban 2003) or the Satlantic SPMR (Sound of Jura 2004 and Bristol Channel 2005). No profiling radiometric data was available for the Oban 2004 cruise, which was omitted from this analysis. *In situ* measurements of $K_d(490)$ were made at a depth of either 2 or 3m. Figure 7.7 illustrates the relationship between the SeaWiFS algorithm $K_d(490)$ values and the *in situ* measurements of $K_d(490)$. Overall there is no good relationship between the calculated and measured values, but two distinct branches can be seen. These branches correspond to (A) clusters 1 and 4 (low TSS and a range of chlorophyll and CDOM), and (B) clusters 2 and 3 (waters with high values of TSS with low concentrations of chlorophyll and CDOM). For the branch consisting of clusters 2 and 3 the algorithm grossly underestimated the values of $K_d(490)$. Mueller (2000) states that SeaWiFS $K_d(490)$ algorithm values greater than $0.25m^{-1}$ should be regarded with caution.

7.3.2. $K_d(490)$ Tuned Dual Algorithm

In situ measurements of $K_d(490)$ were plotted against the nL_w waveband ratio used in equation (7.11) in Figure 7.8. Two branches were again observed to occur composed of (A) clusters 1 and 4 for the lower branch and (B) clusters 2 and 3 for the higher branch. Curves were fitted through the set of branches (Figure 7.9) and the a and b coefficients of the $K_d(490)$ algorithm (equation (7.11)) were tuned to better suit the two branches, thus providing us with a dual algorithm enabling the retrieval of $K_d(490)$. For waters with low TSS and a wide range of chlorophyll and CDOM values (clusters 1 and 4) the curve fitting procedure produced the following coefficients:

$$a = 0.138113$$
$$b = -2.57586$$
$$R^2 = 0.69$$

For clusters 2 and 3, the high and varied concentrations of TSS with low values of chlorophyll and CDOM, the following coefficients were found:

$$a = 0.189054$$
$$b = -6.22841$$
$$R^2 = 0.94$$

Figure 7.9 shows the results of the curve fitting procedure and Table 7.2 contains information on the a and b coefficients of equation (7.11) for the standard SeaWiFS $K_d(490)$ algorithm and for the tuned dual algorithm for our dataset. The tuned dual $K_d(490)$ algorithms for the data can be written as:

Clusters 1 and 4: Low TSS with varied chlorophyll and CDOM.

$$K_d(490)_{C14} = 0.016 + 0.138113\left[\frac{nL_w(490)}{nL_w(555)}\right]^{-2.57586} \qquad (7.13)$$

Clusters 2 and 3: High and varied TSS with low chlorophyll and CDOM.

$$K_d(490)_{C23} = 0.016 + 0.189054\left[\frac{nL_w(490)}{nL_w(555)}\right]^{-6.22841} \qquad (7.14)$$

In order to check the performance of the dual $K_d(490)$ algorithm the calculated values were plotted against the *in situ* measurements of $K_d(490)$ (Figure 7.10). This is a marked improvement on the standard SeaWiFS $K_d(490)$ algorithm performance with the dual algorithms producing gradients very close to one, 0.96 in both cases, with R^2 values of 0.62 in panel (A) for clusters 1 and 4 and 0.94 in panel (B) for clusters 2 and 3.

7. 4. Summary

a. The four clusters identified from the hyperspectral measurements enabled the operation of standard remote sensing algorithms in optically complex water to be assessed.

b. The chlorophyll algorithms tested (SeaWiFS OC4V4, MODIS Chlor_a_2, MODIS Chlor_a_3 and MERIS OC4E) produced substantial overestimates in the chlorophyll *a* concentration when applied to clusters 3 and 4. Removing these clusters improved the relationship observed between the algorithm and measured values of chlorophyll *a*, but the algorithms tested still tended to overestimate the chlorophyll *a* concentration. The MERIS OC4E algorithm performed the best on this dataset with a gradient of 0.83 and R^2 of 0.64.

c. The MODIS $a_{phyto}(675)$ algorithm underestimated $a_{phyto}(675)$ for each of the hyperspectral clusters except cluster 3. However, the MODIS $a_{CDOM}(400)$ algorithm was successful at retrieving accurate values of the absorption coefficient of CDOM at 400nm in coastal water.

d. The SeaWiFS $K_d(490)$ algorithm (Mueller, 2000) underestimated $K_d(490)$ values. Two branches were observed in Figure 7.7 which were identified as (A) clusters 1 and 4, and (B) clusters 2 and 3. Considering these two branches independently new a and b coefficients were obtained, thus providing a tuned dual $K_d(490)$ algorithm to apply to the dataset.

e. From the work carried out in this chapter it appears that the majority of standard remote sensing algorithms fail when applied to the coastal water dataset. The exception to this was the MODIS $a_{CDOM}(400)$ algorithm. The hyperspectral derivative feature classification of water types can help show why remote sensing algorithms break down in certain water types (e.g. due to high turbidity) and can be useful in the targeting of algorithms to different water types in coastal and shelf sea waters.

ALGORITHM	GRADIENT	OFFSET	R^2
SeaWiFS OC4V4	0.75	1.96	0.64
Terra MODIS Chlor_a_2	0.85	1.81	0.58
Terra MODIS Chlor_a_3	1.13	1.66	0.59
MERIS OC4E	0.83	1.81	0.64

Table 7.1. Linear regression parameters for reflectance band ratio algorithm calculations of chlorophyll *a* plotted against measured *in situ* chlorophyll *a* concentration. Linear regressions were carried out using data from clusters 1 and 2 only.

ALGORITHM	A	B
SeaWiFS $K_d(490)$	0.15645	-1.5401
Tuned $K_d(490)$ for Clusters 1 and 4	0.138113	-2.57586
Tuned $K_d(490)$ for Clusters 2 and 3	0.189054	-6.22841

Table 7.2. a and b coefficients for the $K_d(490)$ algorithm (equation (7.11)). The coefficients listed in the table above are for the current SeaWiFS $K_d(490)$ algorithm provided by Mueller (2000) and for the tuned dual algorithm for the dataset investigated in this chapter.

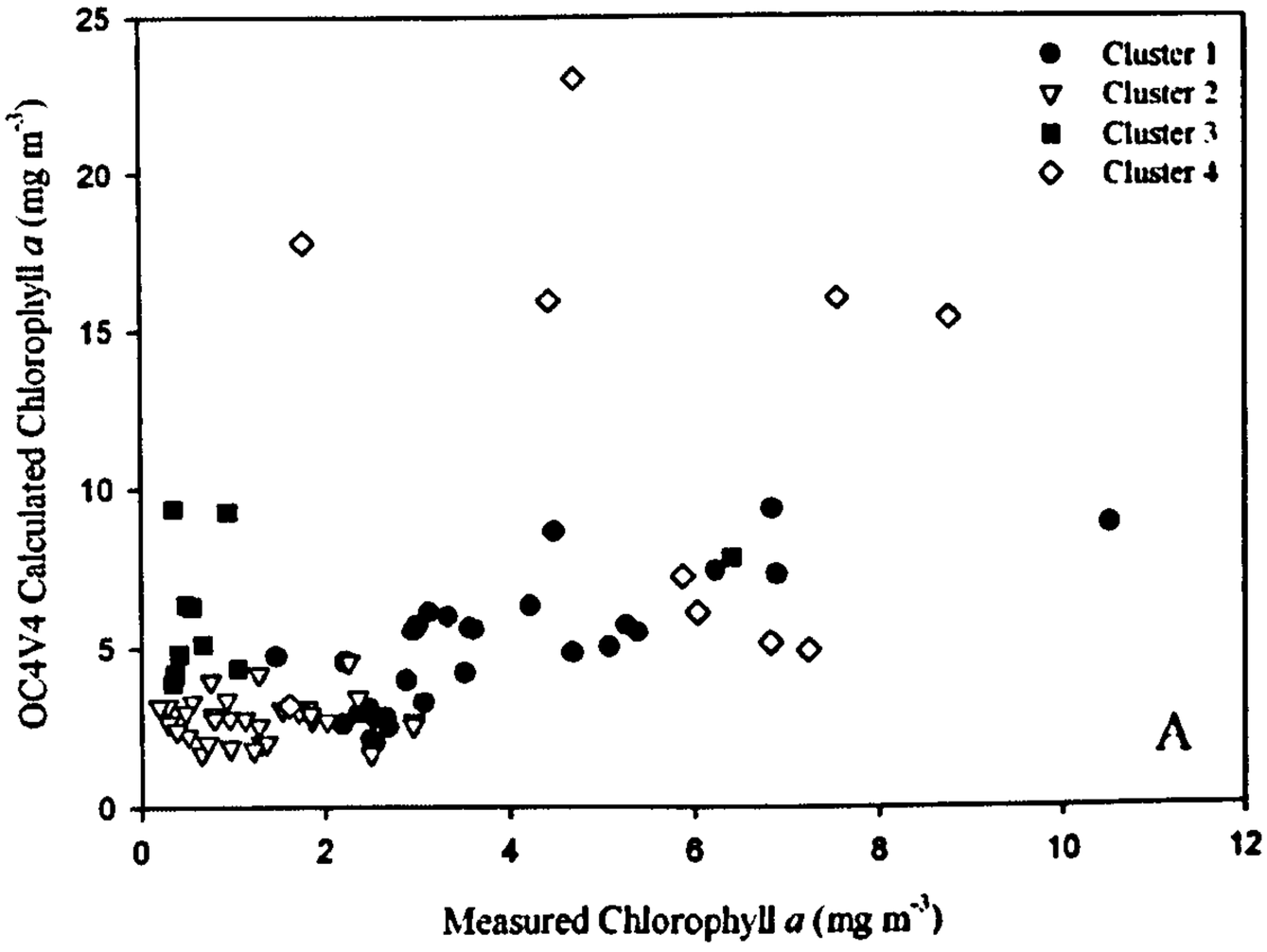

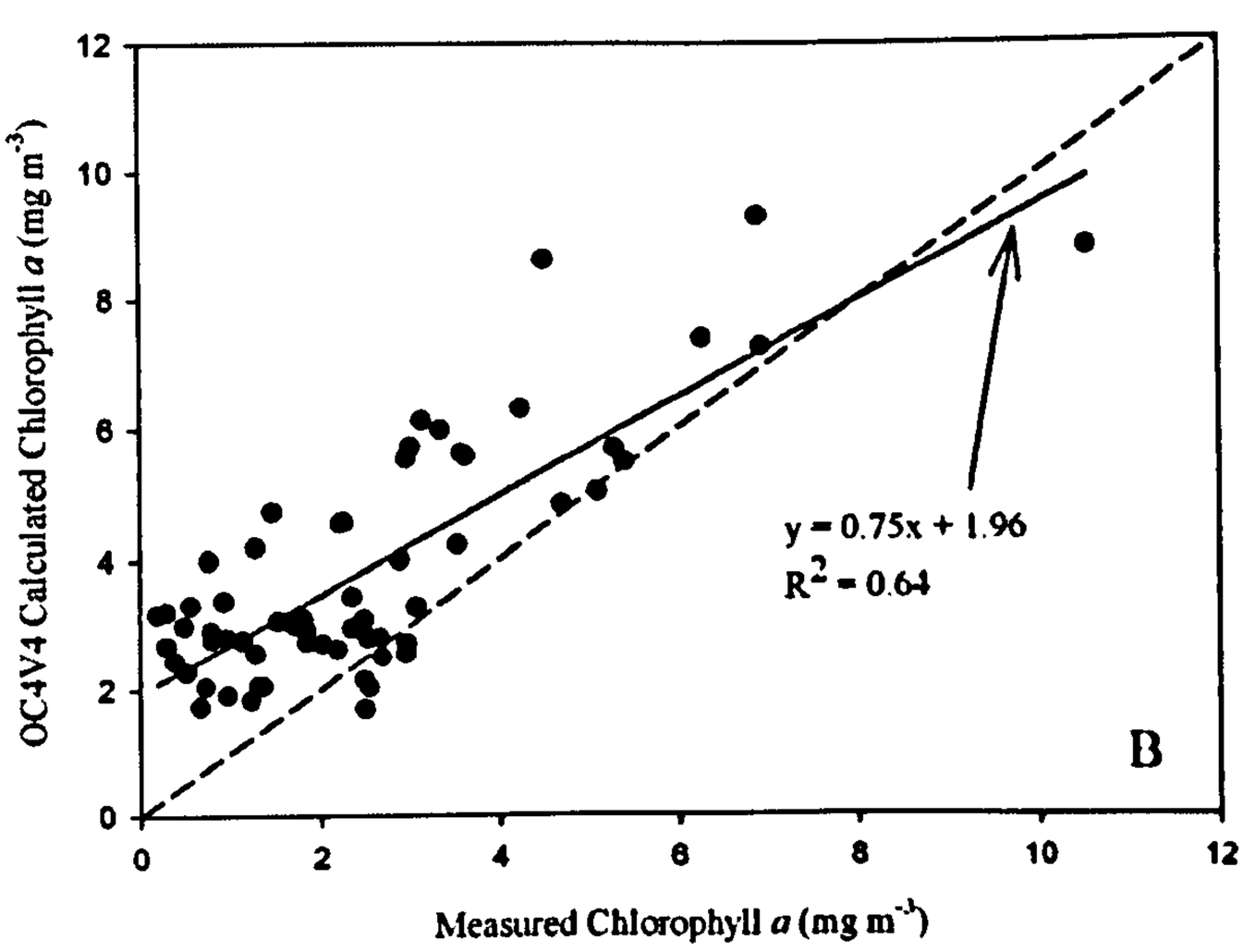

Figure 7.1. SeaWiFS OC4V4 algorithm applied to shelf sea data. Panel (A) shows the comparison between the calculated (algorithm) values and all four hyperspectral clusters. Panel (B) contains information on clusters 1 and 2 only.

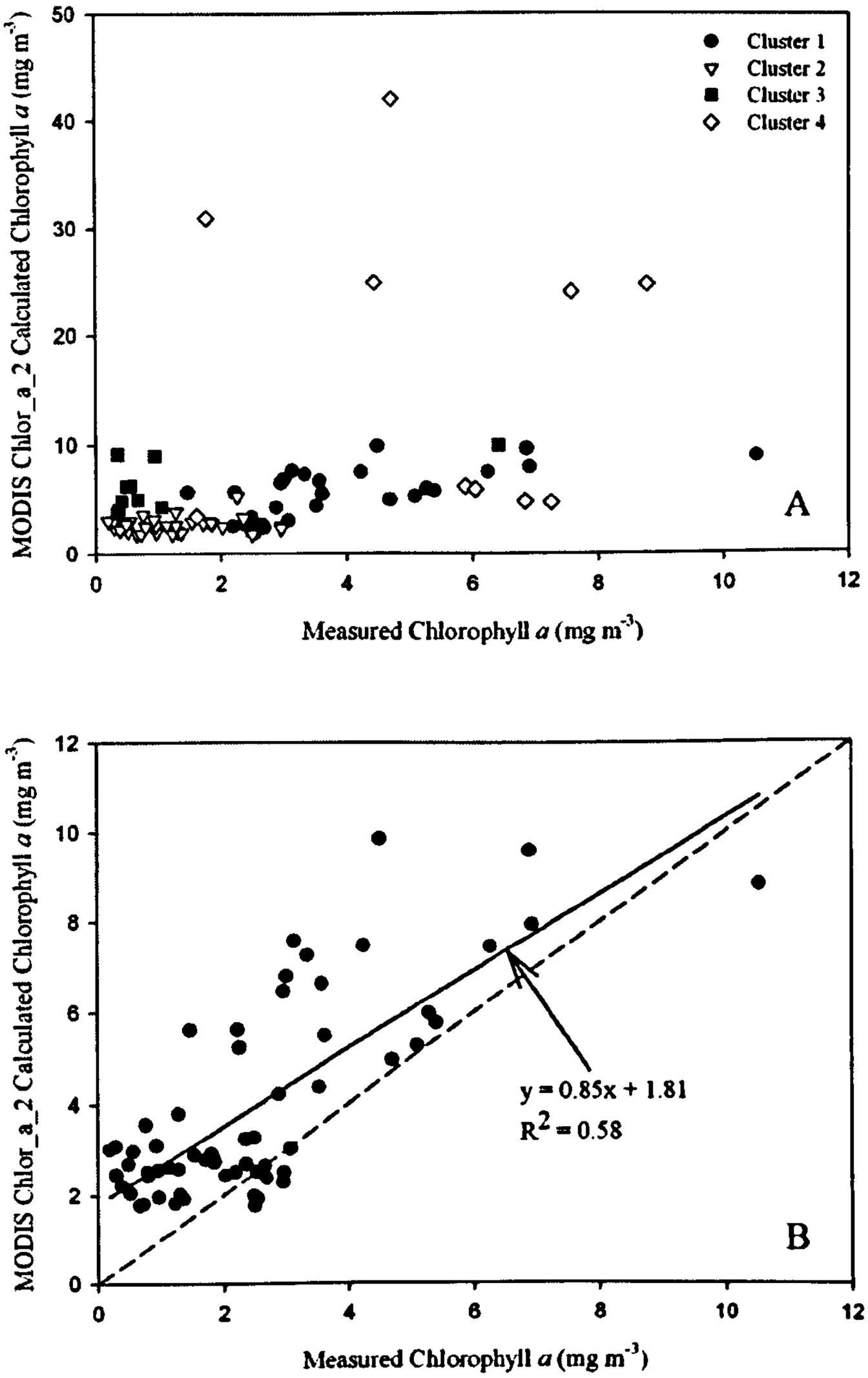

Figure 7.2. MODIS Chlor_a_2 algorithm applied to shelf sea data. Panel (A) shows the comparison between the calculated (algorithm) values and all four hyperspectral clusters. Panel (B) contains information on clusters 1 and 2 only.

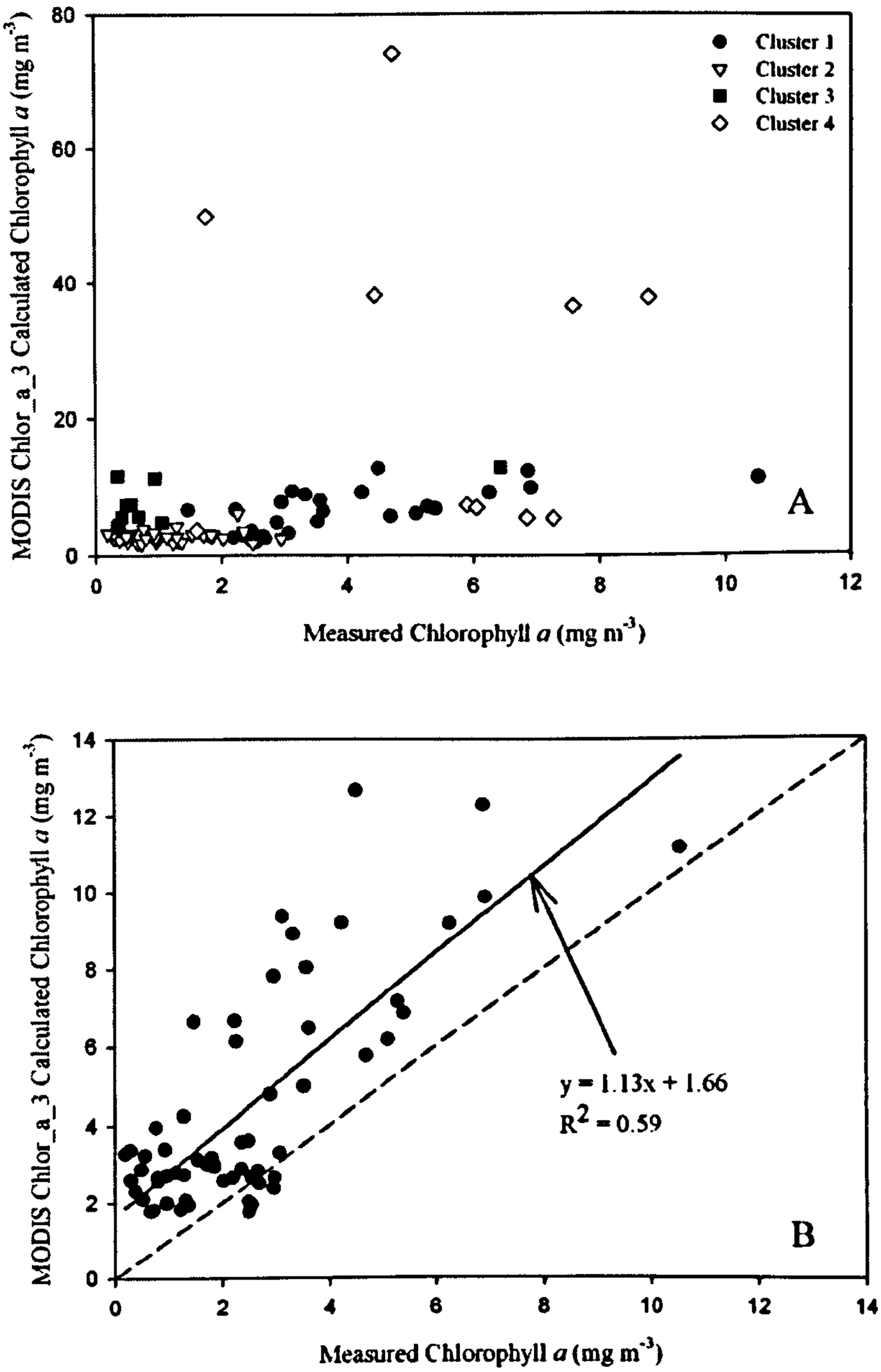

Figure 7.3. MODIS Chlor_a_3 algorithm applied to shelf sea data. Panel (A) shows the comparison between the calculated (algorithm) values and all four hyperspectral clusters. Panel (B) contains information on clusters 1 and 2 only.

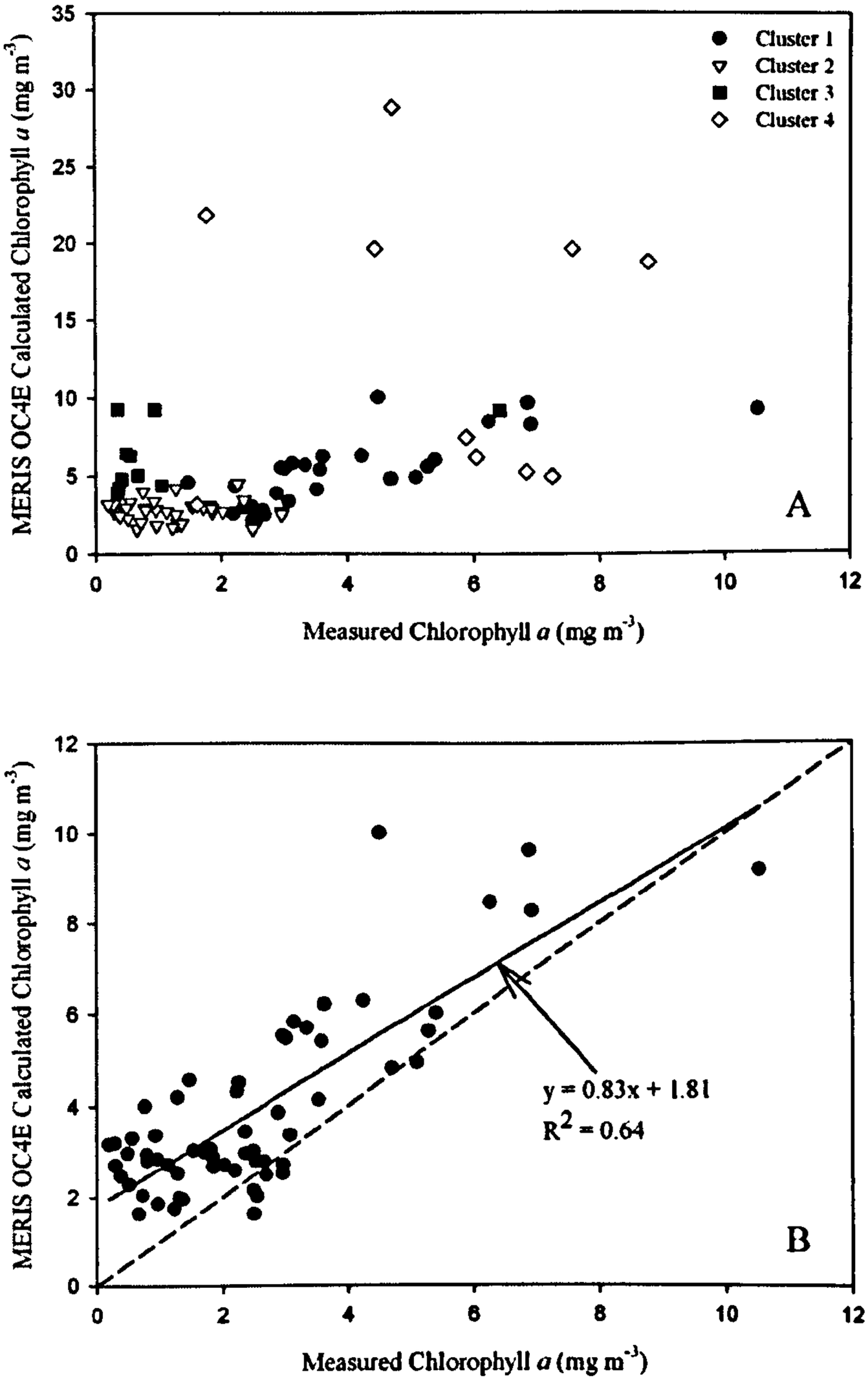

Figure 7.4. MERIS OC4E algorithm applied to shelf sea data. Panel (A) shows the comparison between the calculated (algorithm) values and all four hyperspectral clusters. Panel (B) contains information on clusters 1 and 2 only.

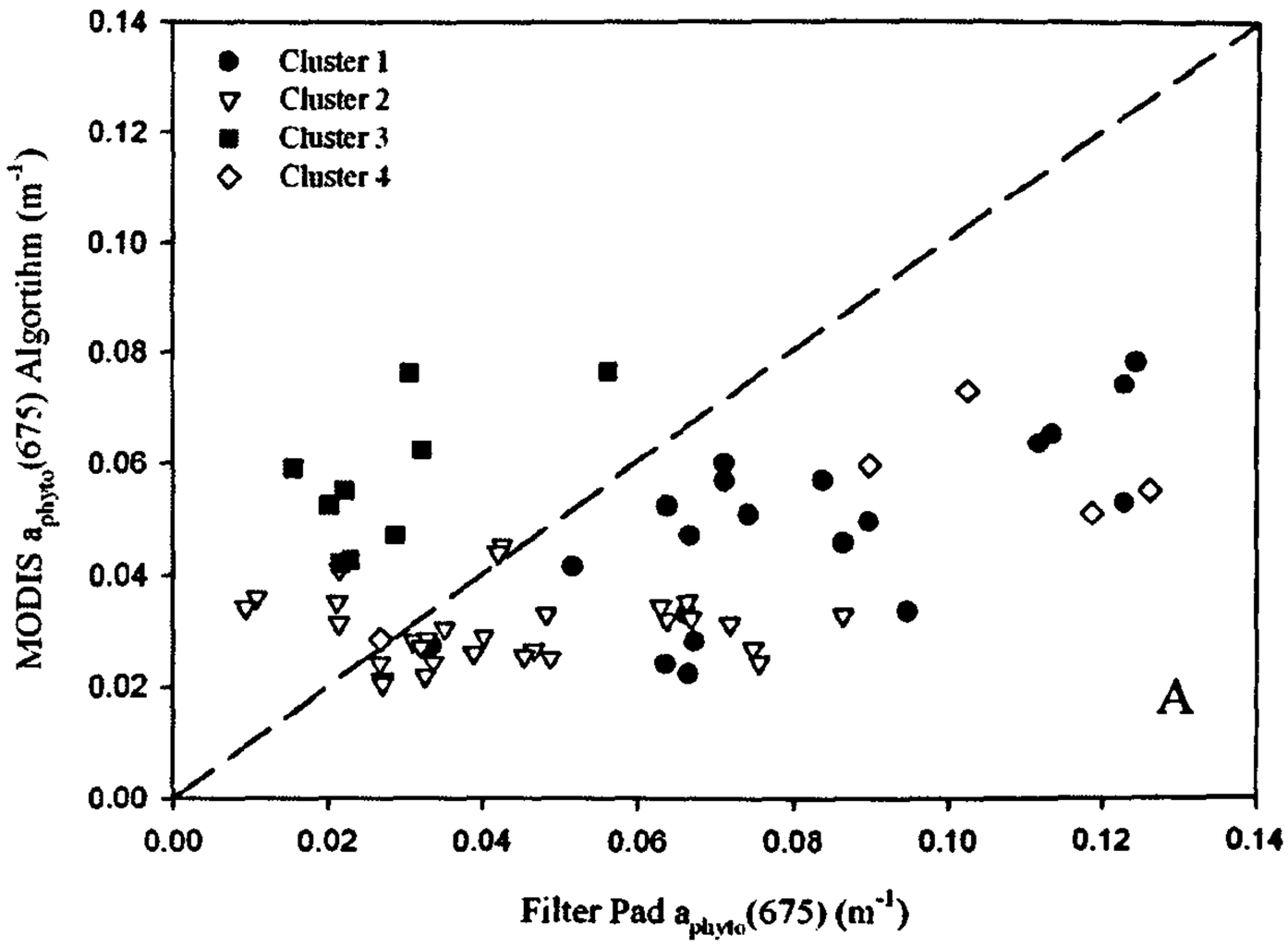

Figure 7.5. MODIS $a_{phyto}(675)$ algorithm applied to shelf sea dataset. The figure illustrates the comparison between calculated (algorithm) values of $a_{phyto}(675)$ and measured *in situ* values of $a_{phyto}(675)$, determined using the filter pad absorption technique. In panel (A) all of the clusters have been used, in panel (B) cluster 3 has been removed.

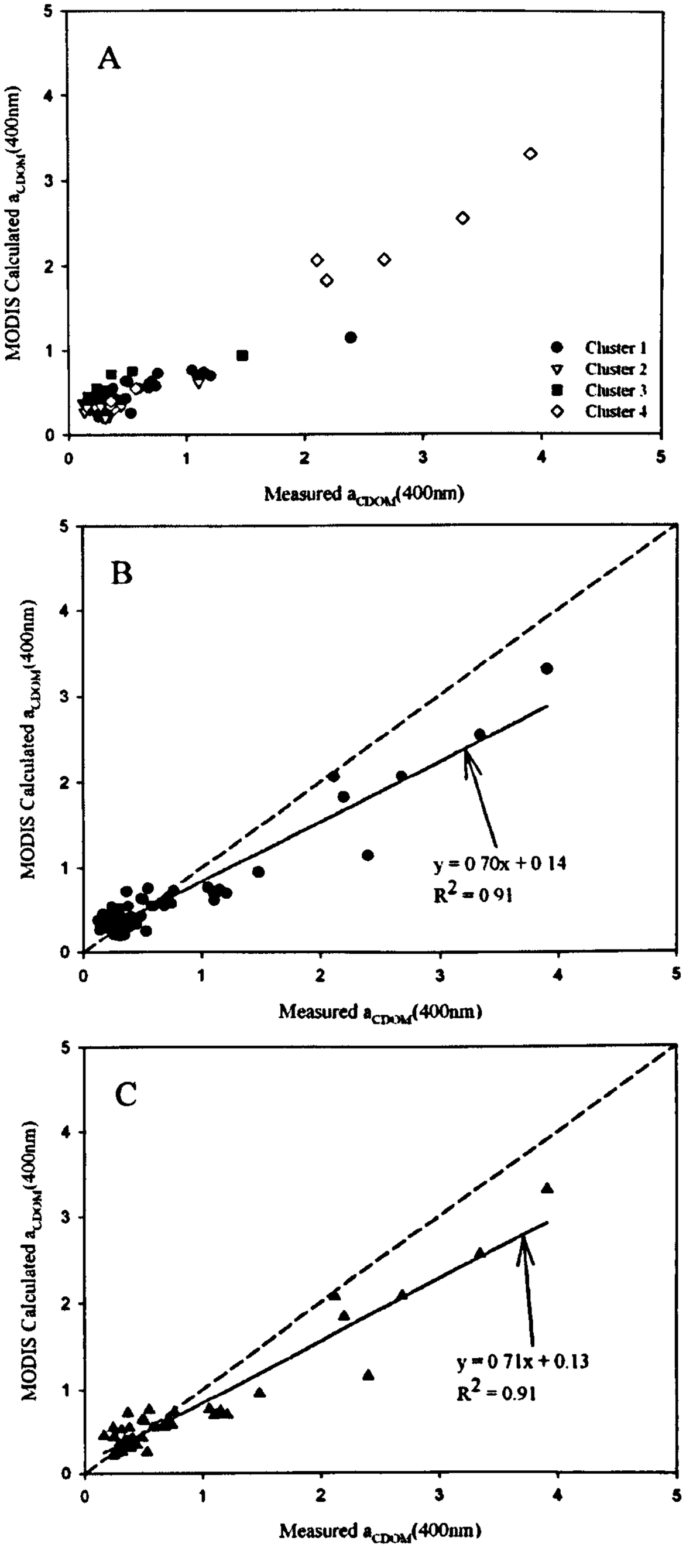

Figure 7.6. MODIS $a_{CDOM}(400)$ algorithm applied to shelf sea dataset. Panel (A) illustrates the comparison between calculated (algorithm) and measured $a_{CDOM}(400)$ values plotted in terms of the four clusters. In Panel (B) a linear regression has been applied to all the data (i.e. all four clusters have been included) and in panel (C) cluster 2 has been removed.

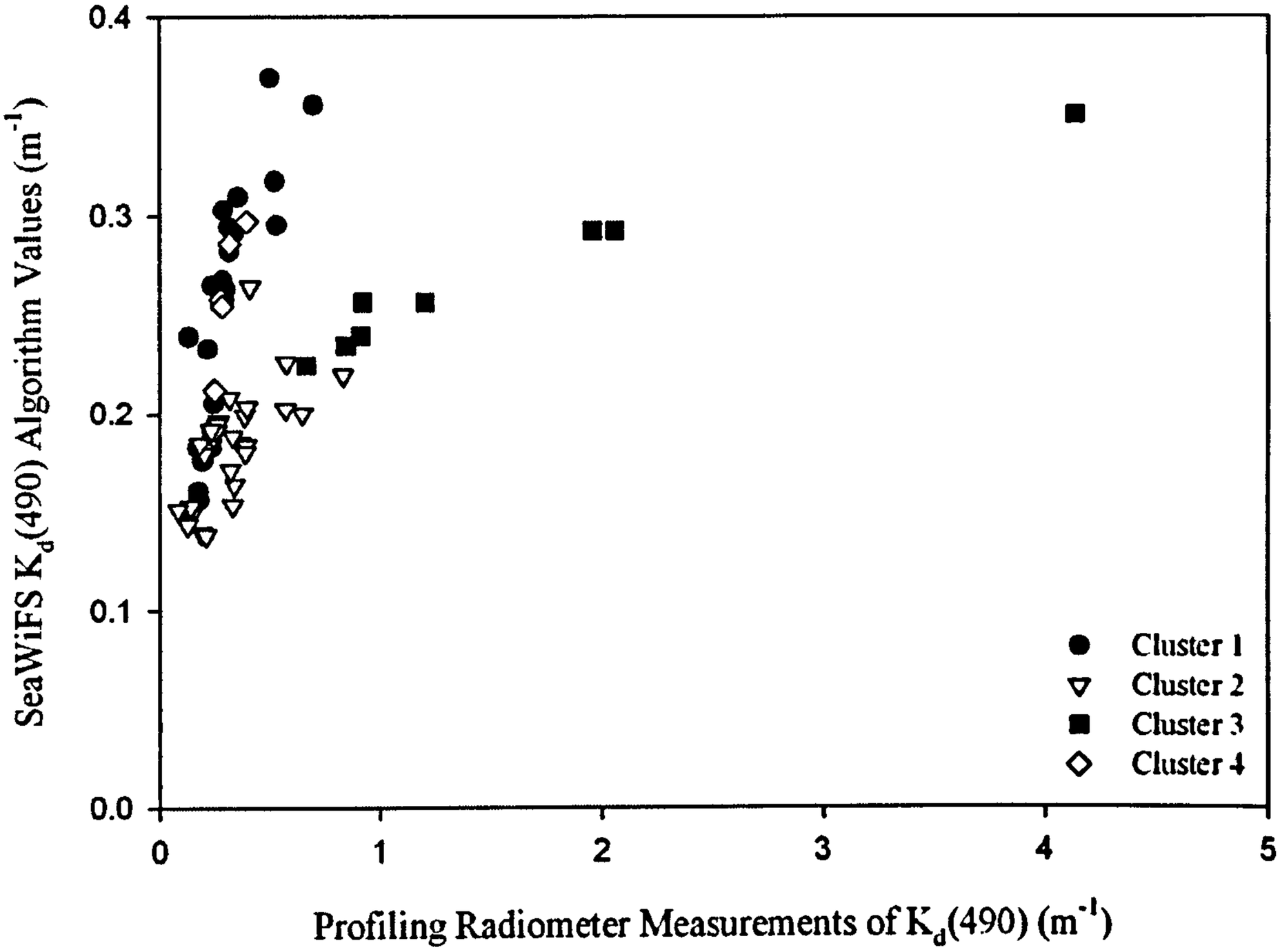

Figure 7.7. SeaWiFS $K_d(490)$ algorithm values plotted against *in situ* measurements of $K_d(490)$. Data points are identified according to the cluster analysis of the hyperspectral features (see Chapter 6 section 6.3.2). In this figure two branches can be observed. The first branch is composed of stations from clusters 1 and 4 and the second of stations from clusters 2 and 3.

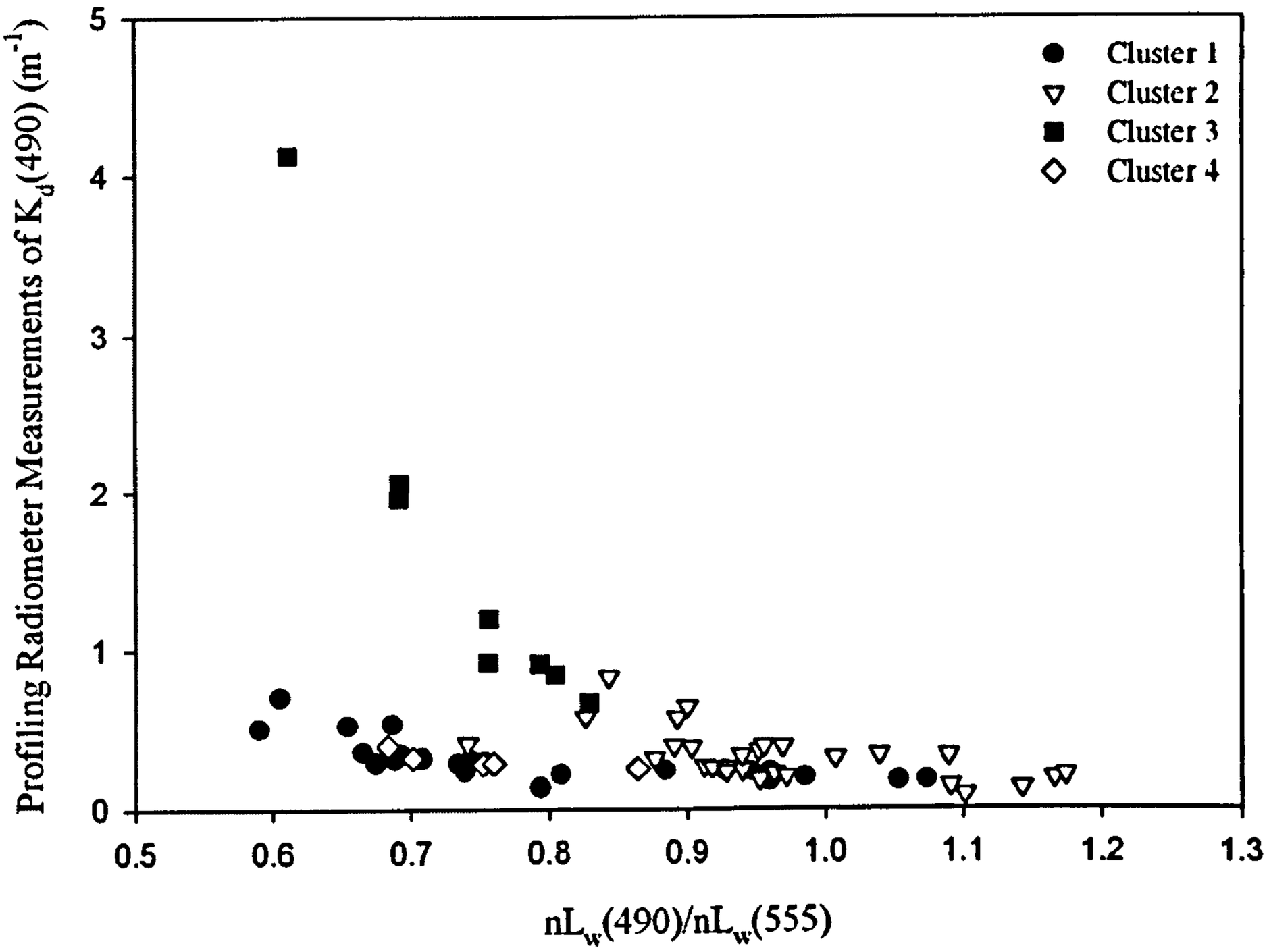

Figure 7.8. *In situ* $K_d(490)$ measurements plotted against the normalised water leaving radiance ratio of equation (7.11), $nL_w(490)/nL_w(555)$. Data points are identified according to the cluster analysis of the hyperspectral features (see Chapter 6 section 6.3.2). In this figure two branches can be observed one branch is composed of stations from clusters 1 and 4 and the other from clusters 2 and 3.

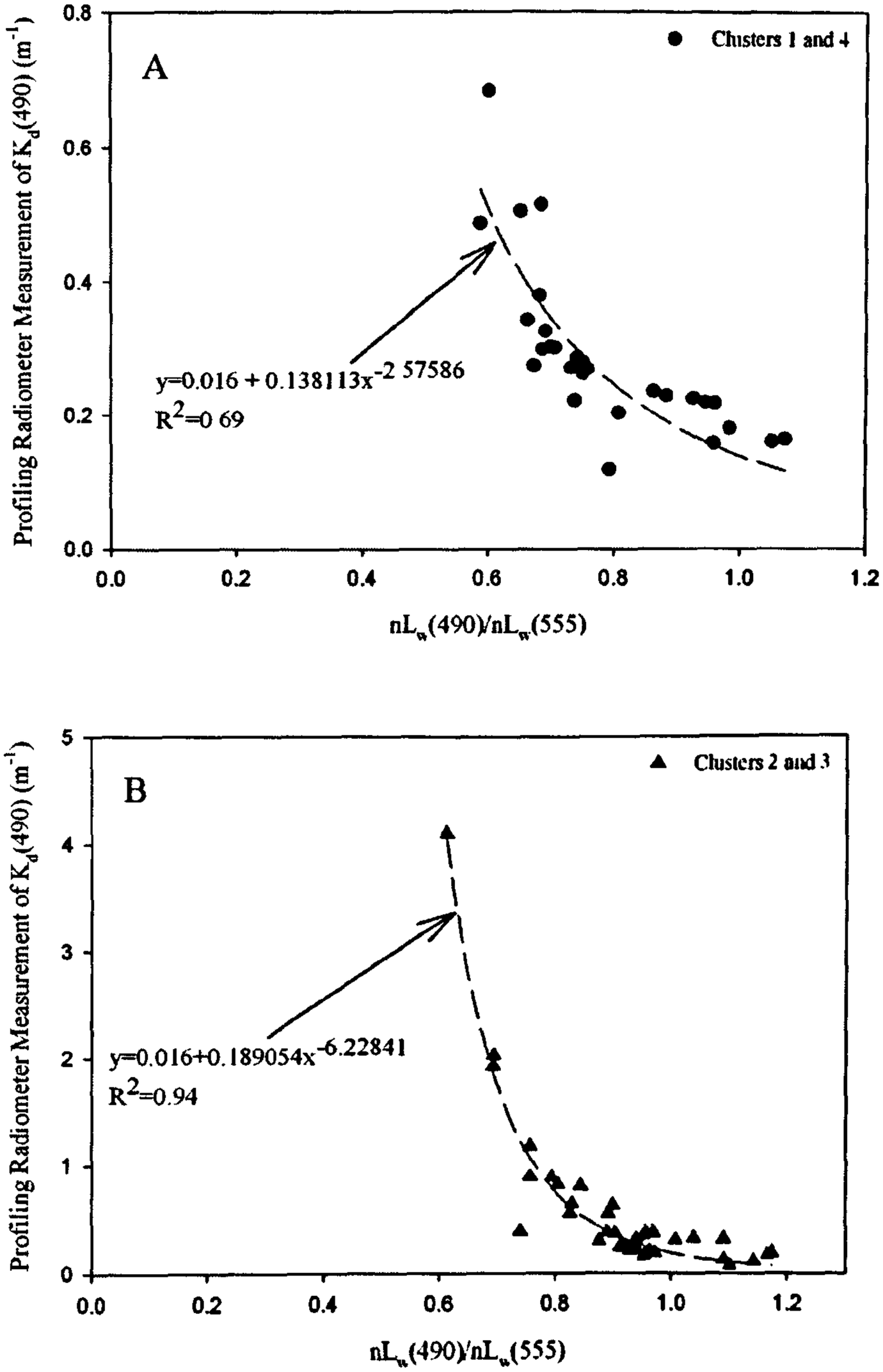

Figure 7.9. *In situ* $K_d(490)$ measurements plotted against the normalised water leaving radiance ratio of equation (7.11) $nL_w(490)/nL_w(555)$. Both panels illustrate the result of performing curve fitting on the dataset in order to determine new a and b coefficients and tune the standard SeaWiFS $K_d(490)$ algorithm to improve its performance in these water types. Panel (A) is for clusters 1 and 4, low TSS water with variable concentrations of chlorophyll and CDOM. Panel (B) is for clusters 2 and 3, high and varied TSS water with low concentrations of chlorophyll and CDOM.

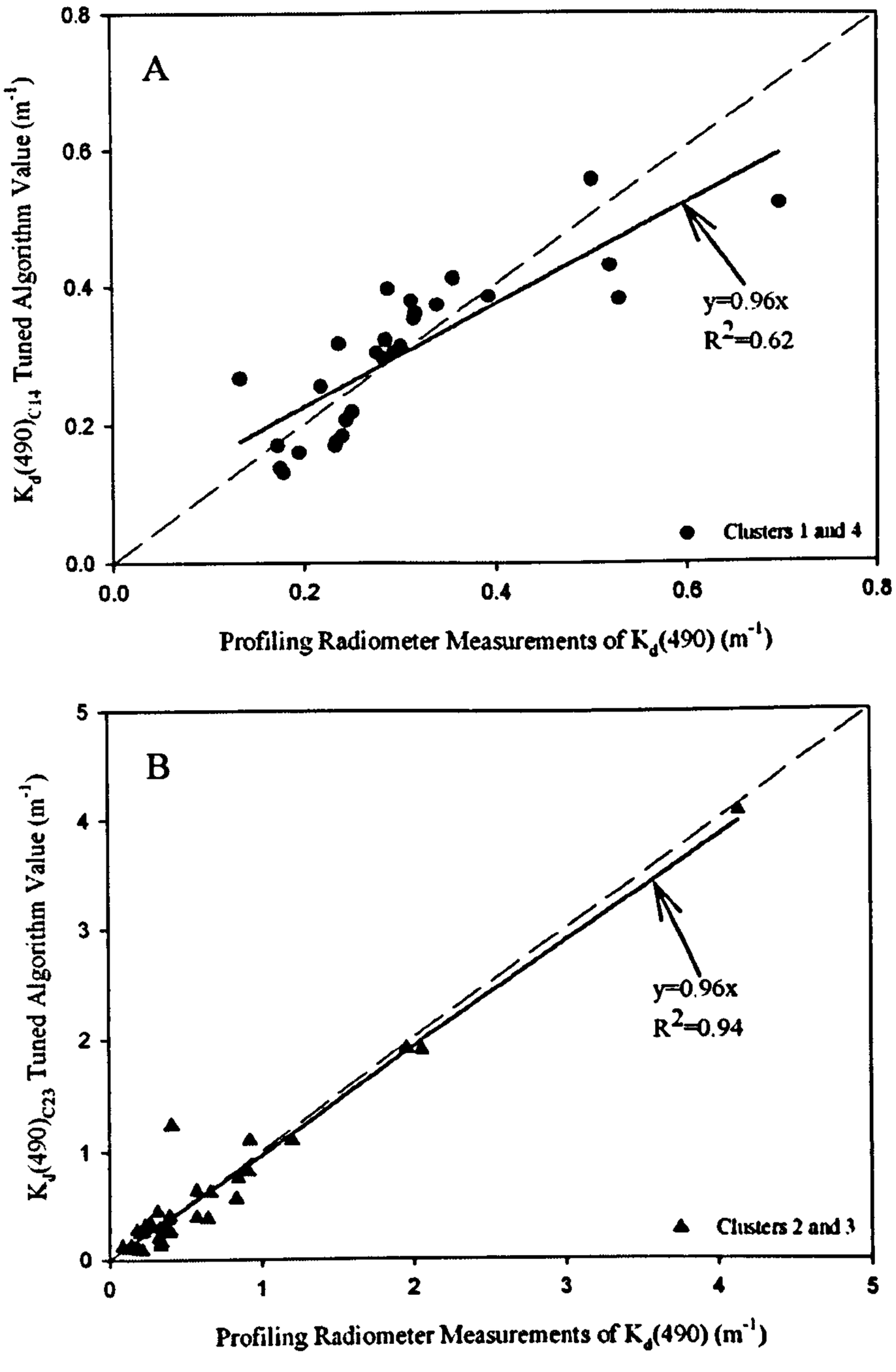

Figure 7.10. Tuned dual algorithms for $K_d(490)$ regressed against *in situ* measurements of $K_d(490)$. Panel (A) illustrates the results of the regression for clusters 1 and 4 and panel (B) for clusters 2 and 3. The tuned dual algorithm shows an improved performance over the standard SeaWiFS $K_d(490)$ algorithm.

Chapter 8: Factors Influencing the Magnitude of Solar Stimulated Fluorescence Line Height in Coastal Waters

In previous chapters it was noted that the presence of chlorophyll in the water body could produce a red peak in the water leaving radiance and remote sensing reflectance spectra. This red peak is caused by chlorophyll fluorescence (Neville and Gower, 1977; Gordon, 1979). Recently it has become possible to measure chlorophyll fluorescence on a global scale using satellites such as MODIS and MERIS (Abbott and Letelier, 1999; Bricaud *et al*, 1999; Huot *et al*, 2005). It has been suggested that chlorophyll fluorescence line height (FLH) may be of particular use in case 2 waters where CDOM and SPM can interfere with standard chlorophyll band ratio algorithms (Gower *et al*, 1999). In this chapter FLH measurements in coastal and shelf sea water will be investigated and the effects of other optically important components, such as CDOM and SPM, on FLH will be considered.

8. 1. Fluorescence Line Height

It has been suggested (Kishino *et al*, 1984; Culver and Perry, 1997; Gower *et a*l, 1999; Gower *et al*, 2004) that the magnitude of the fluorescence signal can be related to the pigment concentration (chlorophyll *a*) of the water body. In this section the relationship between chlorophyll FLH and the chlorophyll *a* concentration is examined.

8. 1. 1. Definition of Fluorescence Line Height

Chlorophyll fluorescence occurs in the red with its peak centred at 685nm (Gordon, 1979), but FLH is not simply the value of the water leaving radiance or remote sensing reflectance signal at this wavelength. It is first necessary to define a baseline for the signal present in the absence of chlorophyll fluorescence. The value of the radiance or reflectance at the baseline must then be subtracted from the fluorescence peak in order to calculate FLH. A linear baseline is generally used, calculated by choosing two wavelengths on either side of the fluorescence band and extrapolating between them. Different remote sensing satellites, such as MODIS and MERIS, use different wavebands for the linear baseline extrapolation. They also require a weighting factor to be applied to the FLH as the fluorescence is measured in a waveband which is off the centre of the actual peak (Gower *et al*, 2004). In this study the baseline wavelengths chosen were 650nm and 740nm and the fluorescence peak was found to occur at 685nm. Figure 8.1 illustrates the position of the wavelengths, baseline and FLH. The baseline and FLH were calculated as follows:

$$Baseline\ L_w(\lambda_f) = L_w(\lambda_1) - \left[\frac{(L_w(\lambda_1) - L_w(\lambda_2))}{(\lambda_2 - \lambda_1)} \times (\lambda_f - \lambda_1)\right] \qquad (8.1)$$

and

$$FLH\ L_w(\lambda_f) = L_w(\lambda_f) - Baseline\ L_w(\lambda_f) \qquad (8.2)$$

where L_w is the water leaving radiance (this can be replaced by the remote sensing reflectance), λ_1 is 650nm, λ_2 is 740nm and λ_f is 685nm .

8. 1. 2. Relationship between FLH and Chlorophyll Concentration

Figure 8.2 shows FLH, calculated from the water leaving radiance spectra, plotted against *in situ* measurements of the chlorophyll *a* concentration. The figure indicates that no simple linear relationship exists in coastal water that would enable the chlorophyll *a* concentration to be estimated from the FLH measurement. There

remains the possibility, however, that FLH measurements may provide information on the physiological status of phytoplankton populations.

Letelier *et al* (1997) (see also Abbott and Letelier, 1999) suggested that plotting the fluorescence per unit chlorophyll against the photosynthetically available radiation (PAR) could produce a relationship whose initial slope is proportional to the quantum yield of fluorescence. This procedure is illustrated in Figure 8.3 panel (A). In this figure two groups of outliers were identified, originating in the Bristol Channel and in West of Scotland fjords (upper Loch Etive and Loch Creran). Ignoring these outliers, it is possible to plot a function of the form suggested by Smith (1936) through the data:

$$y = \frac{y_{\max} \times \phi_f x}{\sqrt{(y_{\max})^2 + (\phi_f x)^2}} \tag{8.3}$$

In equation (8.3) y is the FLH per unit chlorophyll (FLH/Chl), x is the PAR at the surface and ϕ_f is the quantum yield of fluorescence. For Figure 8.3 panel (A) $y_{\max}$ was set to $5.5\times10^{-5}\ W\,m\,mg^{-1}\,nm^{-1}\,sr^{-1}$ and the value of ϕ_f, found here to be 4.6%, was calculated from the initial linear slope. The function fitted was broadly similar to that obtained by Letelier *et al* (1997) and Abbott and Letelier (1999) but the observations were spread widely around the fitted curve.

As an alternative FLH was plotted against the product of PAR and chlorophyll *a* concentration and a linear relationship with a $R^2 = 0.78$ was obtained (Figure 8.3 panel (B)). This graph shows that FLH is strongly linearly correlated with PAR and chlorophyll, with the magnitude of the FLH signal depending upon both properties. It is noted that the Scottish fjord group of outliers do not conform to this relationship, though the Bristol Channel group do, showing that another factor is influencing this relationship in these waters.

The above relationships and regressions do not help with the retrieval of the chlorophyll *a* concentration as this parameter is included in the calculations. However, the spread of the data points in Figure 8.2 and Figure 8.3 helps demonstrate that chlorophyll and PAR are not the only parameters that influence the magnitude of the FLH signal.

8. 2. Optical Parameters Affecting FLH

From Figure 8.2 it was clear that no simple relationship existed between FLH and chlorophyll *a* concentration in the coastal waters sampled. The influence of other optically important parameters on FLH was therefore investigated.

8. 2. 1. Water Transparency

i. Influence of Non-algal Material on FLH from Radiance Transfer Modelling

In order to investigate the effect of CDOM and MSS on FLH in the absence of complicating factors such as varying solar angle or PAR levels, a batch of Hydrolight runs were conducted in which only the CDOM or MSS concentration were varied. The Hydrolight runs followed the procedure laid out in section 5.1.2. To investigate the effect of CDOM, the chlorophyll concentration was set equal to $10 mg\,m^{-3}$, the MSS concentration to $0 mg\,l^{-1}$ and the CDOM $a(440)$ value was varied between 0.1 and $2 m^{-1}$. For the MSS investigation the chlorophyll concentration was held constant at $10 mg\,m^{-3}$, the CDOM at $0 m^{-1}$ and the MSS concentration was varied between 1 and $10 mg\,l^{-1}$. Table 8.1 contains information on the concentrations of CDOM and MSS used. Figure 8.4 shows (FLH/Chl) plotted against CDOM in panel (A) and against MSS in panel (B). In both cases as the CDOM or MSS concentration increases the (FLH/Chl) decreases. This is probably because CDOM and MSS absorb blue photons which would otherwise be absorbed by phytoplankton and contribute to chlorophyll fluorescence.

From these Hydrolight runs it can be concluded that both CDOM and MSS reduce (FLH/Chl) and that this effect increases with the concentration of both substances.

ii. Optical Clarity of the Water Body

Using $K_d(490)$ as an indicator of the optical clarity of the water body it was possible to investigate how the FLH varied as the water became more turbid. A plot of (FLH/Chl) against $K_d(490)$ was made from the Hydrolight runs (Figure 8.5). As expected (FLH/Chl) decreased as the water body became more turbid. For a given $K_d(490)$ value MSS had a greater attenuating effect on the FLH than CDOM due to the fact that it both absorbs and scatters light and therefore has a greater diminishing effect on FLH. Included in this plot are the *in situ* measurements of (FLH/Chl) plotted against $K_d(490)$. The *in situ* measurements had a much smaller (FLH/Chl) than the modelled values even though the *in situ* values of $K_d(490)$ were generally smaller. This is probably due to factors such as varying solar angle and PAR values which influenced FLH in the field measurements but were held constant in the Hydrolight models.

iii. Exposure to Incident Irradiation

During the Oban 2004 cruise, which was focussed on measuring the solar stimulated chlorophyll fluorescence leaving the surface of the water body, two data series were obtained which captured (a) a transition between dull overcast skies to clear bright skies as a step function and (b) an episodic mixture of cloudy and clear skies. These measurements allowed variations in chlorophyll fluorescence with light history to be investigated. The location of these stations (13 and 12) is illustrated in Figure 4.2. The measurements of E_d and L_u were recorded at slightly different times due to the differing integration time of the instruments. A linear interpolation was carried out to ensure that the radiometric measurements were coincident in time, and a 3 point moving average was applied to smooth out some of the noise. The chlorophyll concentration was assumed to be constant during the period when the time series measurements were acquired.

Oban 2004 Station 13

The simpler case of a single sharp transition between dull and bright sky conditions was investigated first. Data were recorded at Station 13 (Loch Creran), Oban 2004. Figure 8.6 contains plots of (1) PAR, (2) (FLH/Chl) and (3) (FLH/Chl) divided by PAR (indicated here as κ) as a function of time. Looking at panels (1) and (2) it can be seen that when the PAR levels are low (section A), the (FLH/Chl) is also low. Between 11:25:28 and 11:26:48 there is a transitional stage when the cloud clears. Once the skies have cleared there is a substantial increase in the PAR levels, with values averaging around $1400\,\mu mol\ photons\,m^{-2}\,s^{-1}$. When the PAR values increase the (FLH/Chl) also increases (sections C and D) confirming that the (FLH/Chl) depends upon the incident PAR level. One interesting feature is that just after the skies have cleared there is a short period of time, labelled as section C on the figures, where (FLH/Chl) is slightly higher than that illustrated in section D, which shows a relatively constant (FLH/Chl). It is hypothesized that the decrease from the elevated level to the stable level is due to non-photochemical quenching as the phytoplankton cells adapt to the increased PAR levels. Panel (3) shows that the κ value ((FLH/Chl) divided by PAR) is fairly constant with time, with the exception of the transitional stage (section B), and only slightly higher under the clear sky conditions (section D) than under cloudy conditions (section A). Again it should be noted that there is an elevated area which occurs in conjunction with the increase in (FLH/Chl) just after the skies have cleared (section C).

Oban 2004 Station 12

Data at this station (Creagh Islands, near the southern tip of Lismore) were recorded under fluctuating light conditions. Figure 8.7 illustrates plots of (1) PAR, (2) (FLH/Chl) and (3) κ as a function of time. By choosing a threshold value of PAR to indicate the beginning and end of a bright phase it is possible to divide the record into bright sunlight conditions and darker sky conditions. The value of PAR chosen was $600\,\mu mol\ photons\,m^{-2}\,s^{-1}$. In panel (1) of Figure 8.7 the periods of bright light

are marked B_1, B_2 and B_3, and the dark periods are marked D_1 and D_2. Panel (2) illustrates the response of the (FLH/Chl) as function of time to the changing PAR conditions. From this panel it can be seen that as the PAR values increase so does the (FLH/Chl), as was found in the previous section. On the second and third bright (B_2 and B_3) episodes there is an initial increase in the (FLH/Chl), followed by a reduction with time. This reduction may be due to the photo-adaptive response of the phytoplankton cells (i.e. non-photochemical quenching mechanisms). Panel (3) of Figure 8.7 again illustrates the photo-adaptation of the phytoplankton cells to the variation in incident irradiation condition. In the bright phases (B_1, B_2 and B_3) κ initially starts high and decreases as the bright conditions persist, i.e. the fluorescence decreases. In the dark stages (D_1 and D_2) the κ value begins low and gradually increases due to a recovery in the fluorescence. This is not as clear in the second dark phase (D_2) as it is a more noisy period, i.e. intermittent light conditions. Again it is noted that the κ varies with the alternating light conditions but not to the same extent as the (FLH/Chl).

These data show that the relationship between PAR and (FLH/Chl) is not fixed, but varies according to the history of light exposure of the phytoplankton cells.

8. 3. Summary

a. For the coastal waters sampled during this research project FLH was not correlated with chlorophyll *a* concentration.

b. For the data gathered in this project a relationship similar to that of Letelier *et al* (1997) was obtained. These authors found that a plot of fluorescence against PAR could be fitted by a function with an initial slope proportional to the quantum yield of fluorescence. However, regressing (FLH/Chl) against PAR did not explain all of the variation observed in the FLH measurements.

c. Simulations using the Hydrolight computer package showed that the presence of CDOM or MSS had a diminishing effect on (FLH/Chl), and as $K_d(490)$ increased the (FLH/Chl) decreased. Inclusion of the *in situ* data in this plot suggested that under natural conditions this relationship is complicated by factors such as varying solar angle and PAR conditions.

d. Time series measurements of (FLH/Chl) under different incident irradiation showed that changes in the (FLH/Chl) mapped reasonably well onto changes in PAR. However, at the onset of bright light conditions the (FLH/Chl) decreased as the phytoplankton cells photo-adapted to the brighter irradiance conditions. This is probably due to non-photochemical quenching. During periods of darkness the (FLH/Chl) was shown to recover.

e. The relationship between PAR and FLH in a given body of water was found to vary according to the history of recent light exposure of the phytoplankton population.

COMPONENT	CONCENTRATION
CDOM	0.1, 0.25, 0.5, 0.75, 1, 1.25, 1.5 and 2 m^{-1}
MSS	1, 2.5, 5, 7.5 and 10 $mg\,l^{-1}$

Table 8.1. Hydrolight investigations into the impact of non-algal material on FLH. Concentration of CDOM and MSS used in Hydrolight runs to conduct the investigation into the impact of non-algal material on (FLH/Chl).

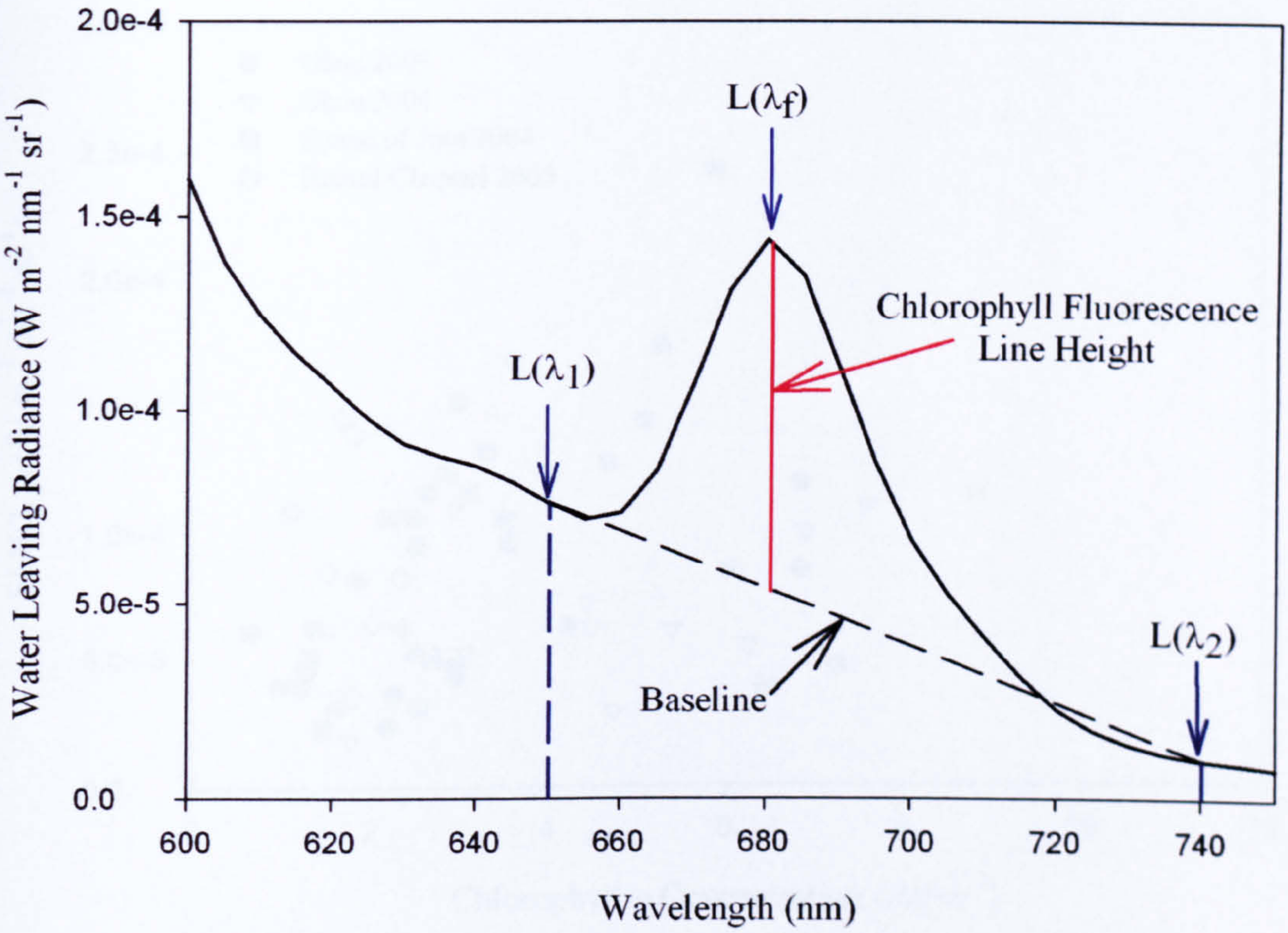

Figure 8.1. Fluorescence Line Height Definition. FLH was calculated using equations 8.1 and 8.2. The figure illustrates that the FLH is equal to the difference between the fluorescence peak height and baseline present in the absence of chlorophyll fluorescence.

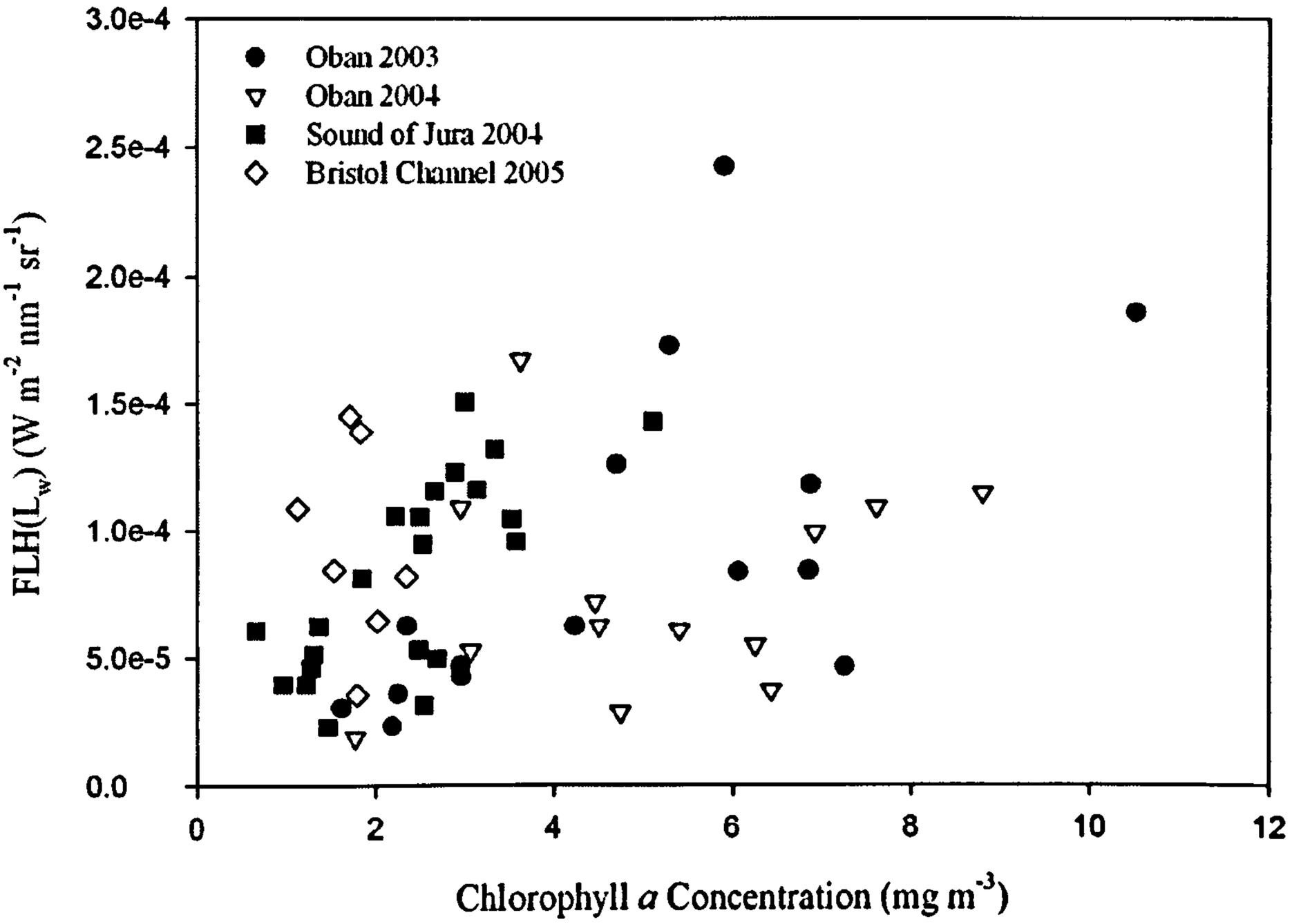

Figure 8.2. FLH versus chlorophyll *a* concentration in coastal waters. The FLH has been calculated from the water leaving radiance, L_w, spectra for the stations occupied. The figure illustrates that FLH cannot be used as an indicator of chlorophyll *a* concentration in coastal waters.

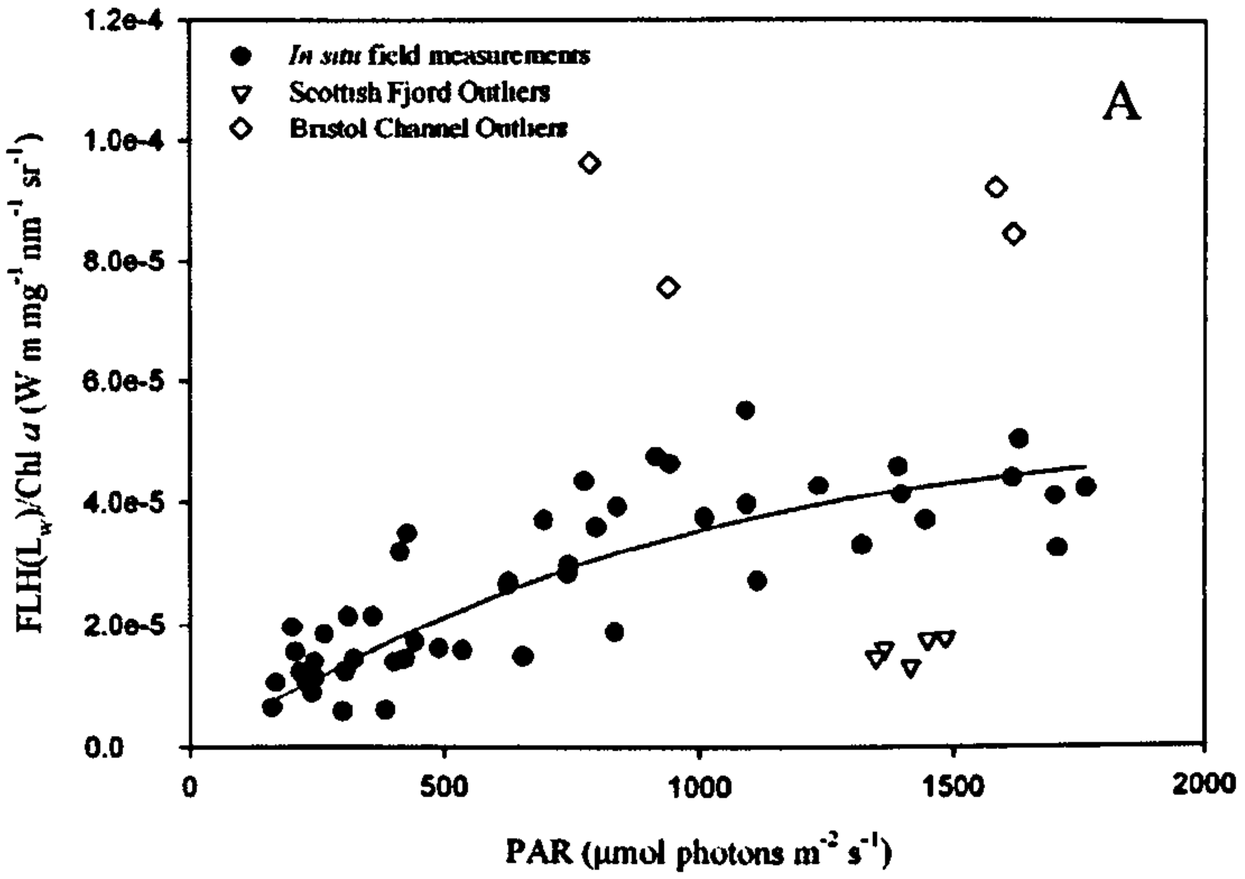

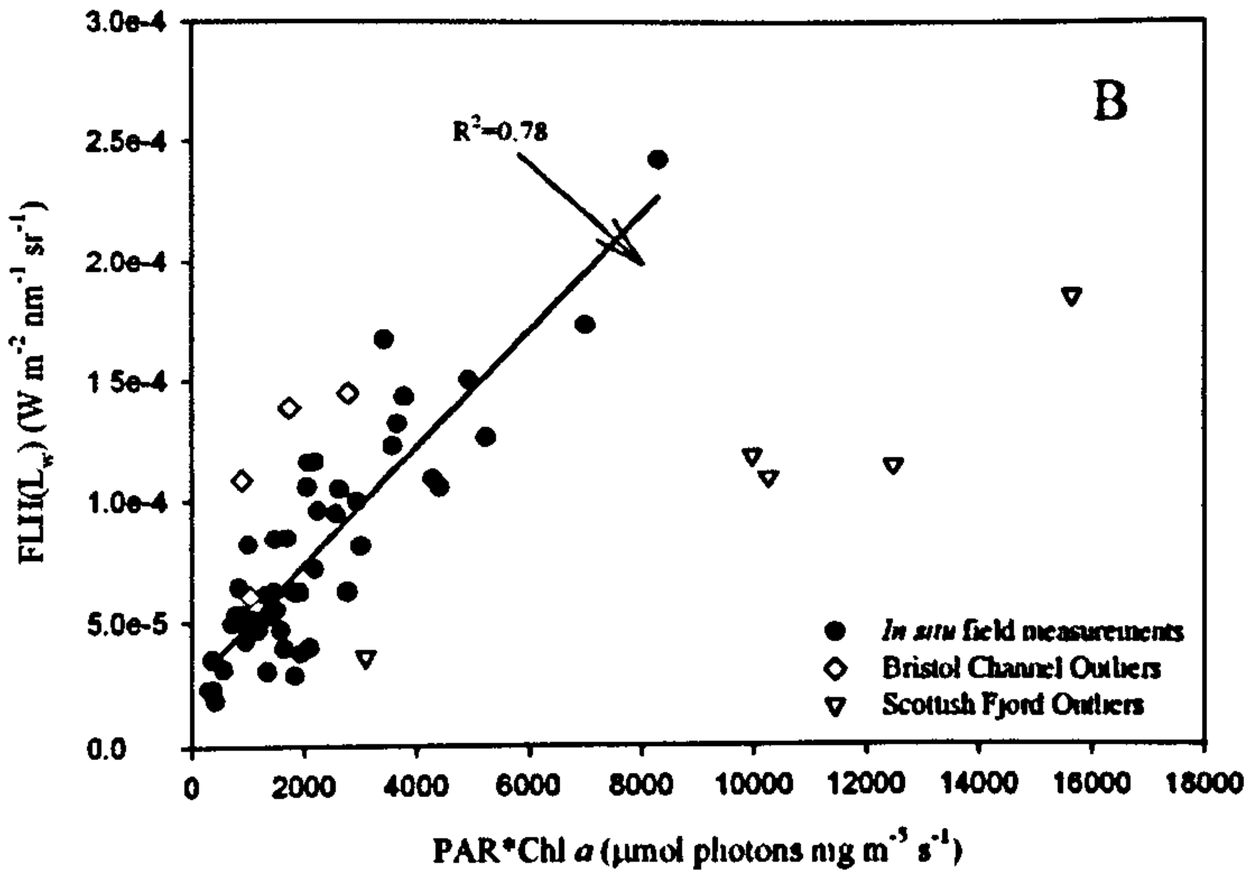

Figure 8.3. Panel (A) illustrates (FLH/Chl) plotted against PAR. The outliers were found to occur in the Bristol Channel, upper Loch Etive and Loch Creran (open symbols). A similar relationship to Letelier *et al* (1997) was found in panel (A). Panel (B) shows FLH plotted against the product of PAR and chlorophyll *a*, producing a linear relationship with the exception of the outliers found in the Scottish fjords.

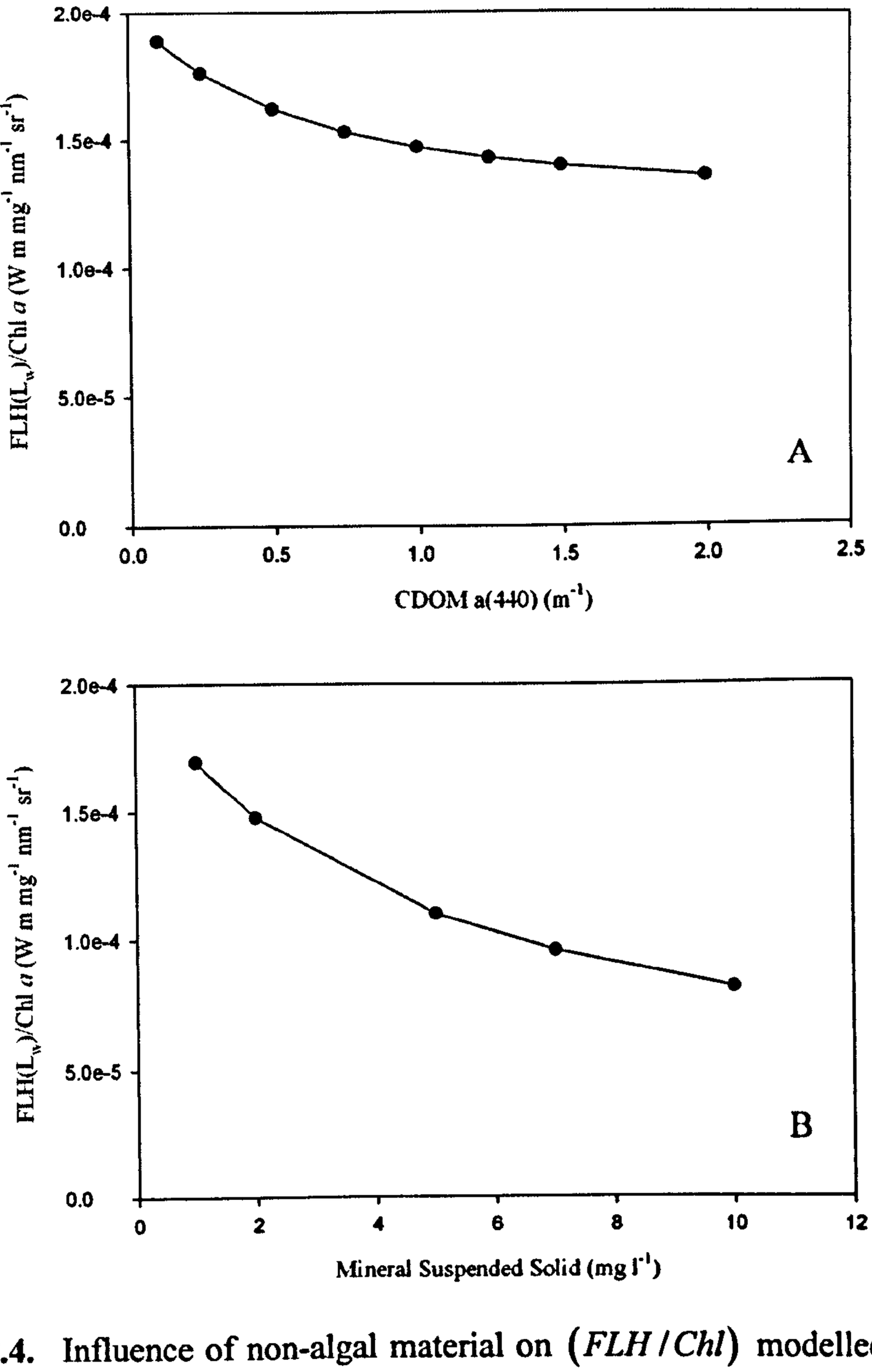

Figure 8.4. Influence of non-algal material on (FLH/Chl) modelled using the Hydrolight computer package. Panel (A) illustrates how (FLH/Chl) varies as the CDOM concentration is increased. Panel (B) illustrates the effect of increasing the MSS. All other parameters (e.g. chlorophyll concentration, solar angle and incident irradiation) were held constant.

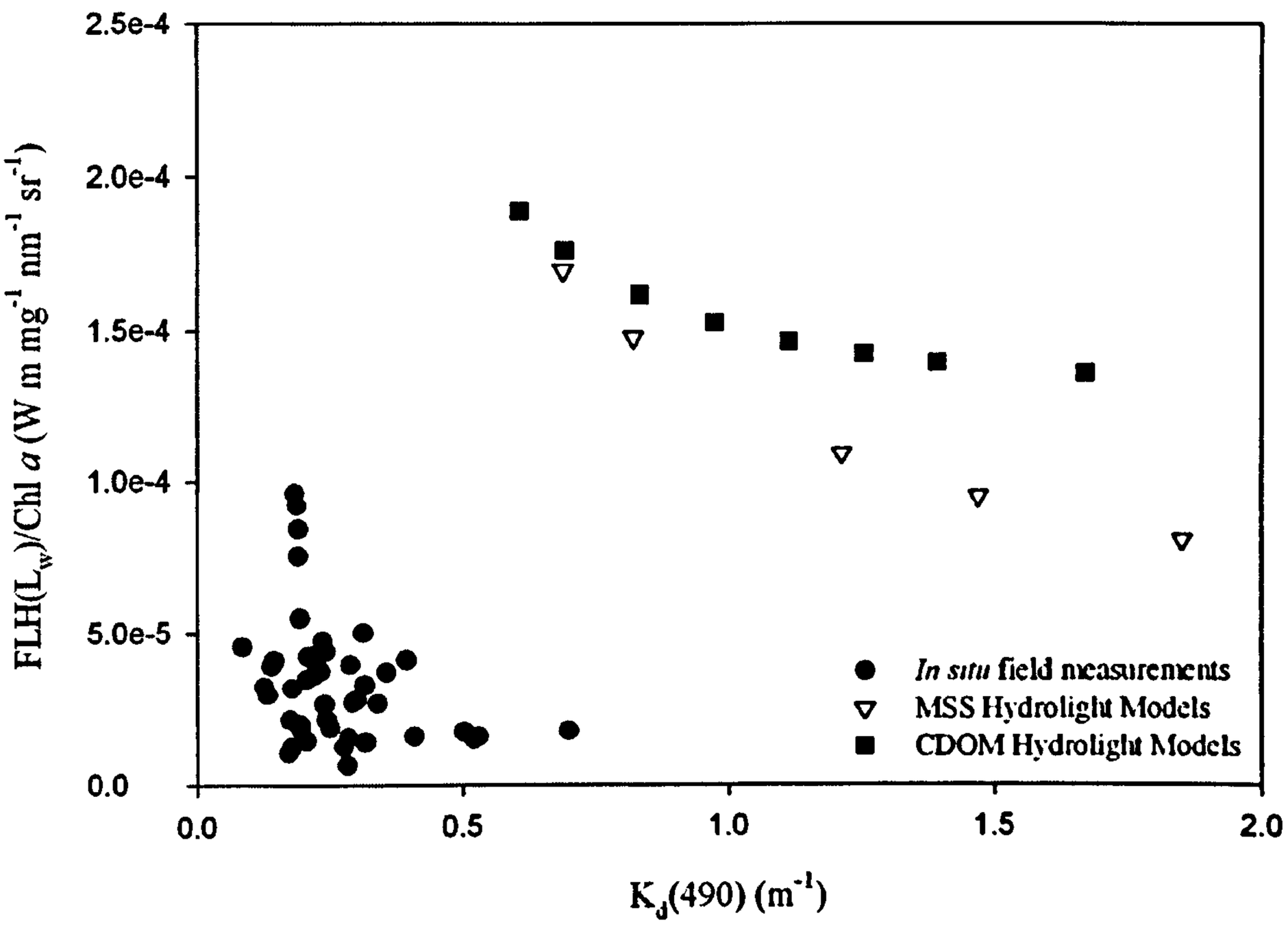

Figure 8.5. Variation of (FLH/Chl) with $K_d(490)$. The Hydrolight models show that (FLH/Chl) generally decreases as $K_d(490)$ increases. For a given $K_d(490)$, MSS has a greater attenuating effect than CDOM. *In situ* measurements (also shown) are subject to the effects of other factors, such as varying solar angle and PAR values.

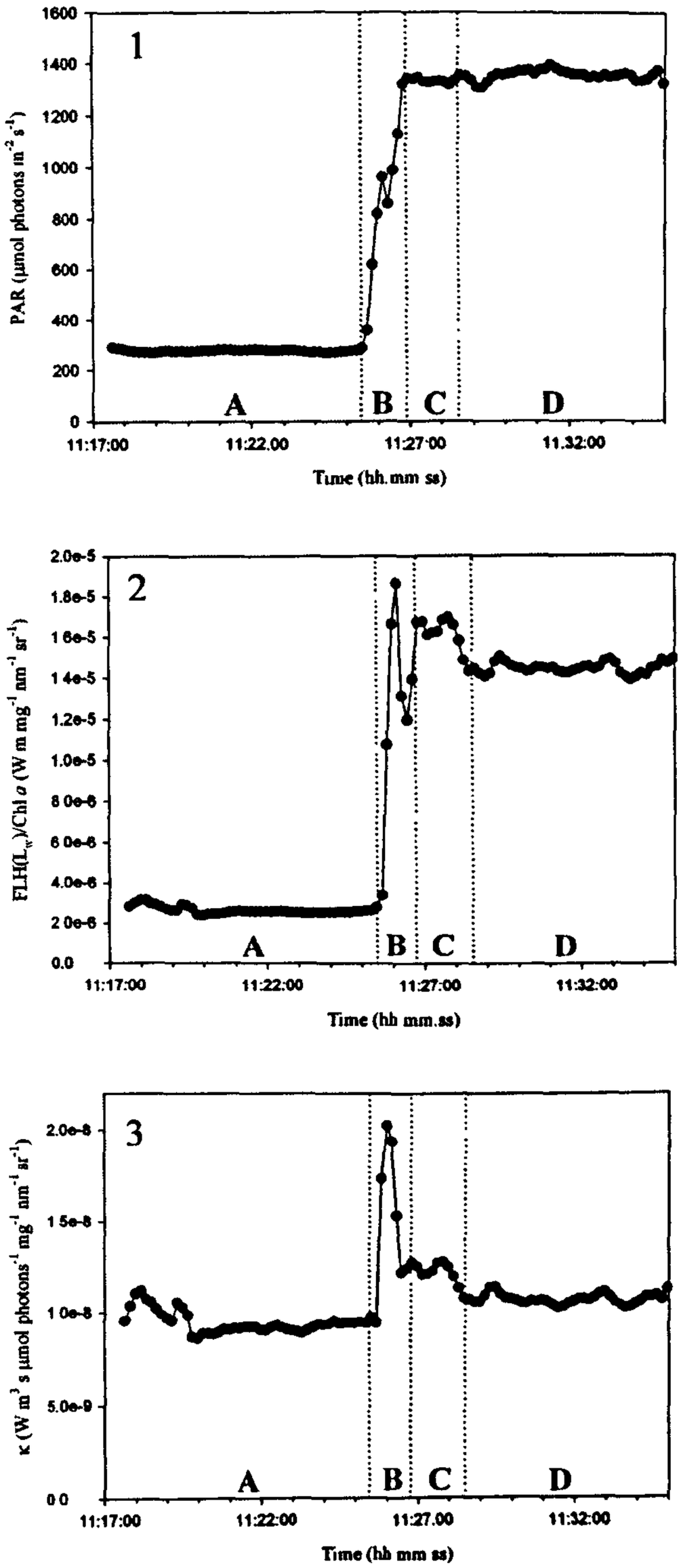

Figure 8.6. Station 13, Oban 2004. Panel (1) illustrates the time dependence of PAR, (2) (FLH/Chl) and (3) κ $(FLH/(Chl \times PAR))$. As the PAR levels increase so does the (FLH/Chl). With the exception of the transitional stage κ remains relatively constant with time being only slightly elevated under clear bright sky conditions.

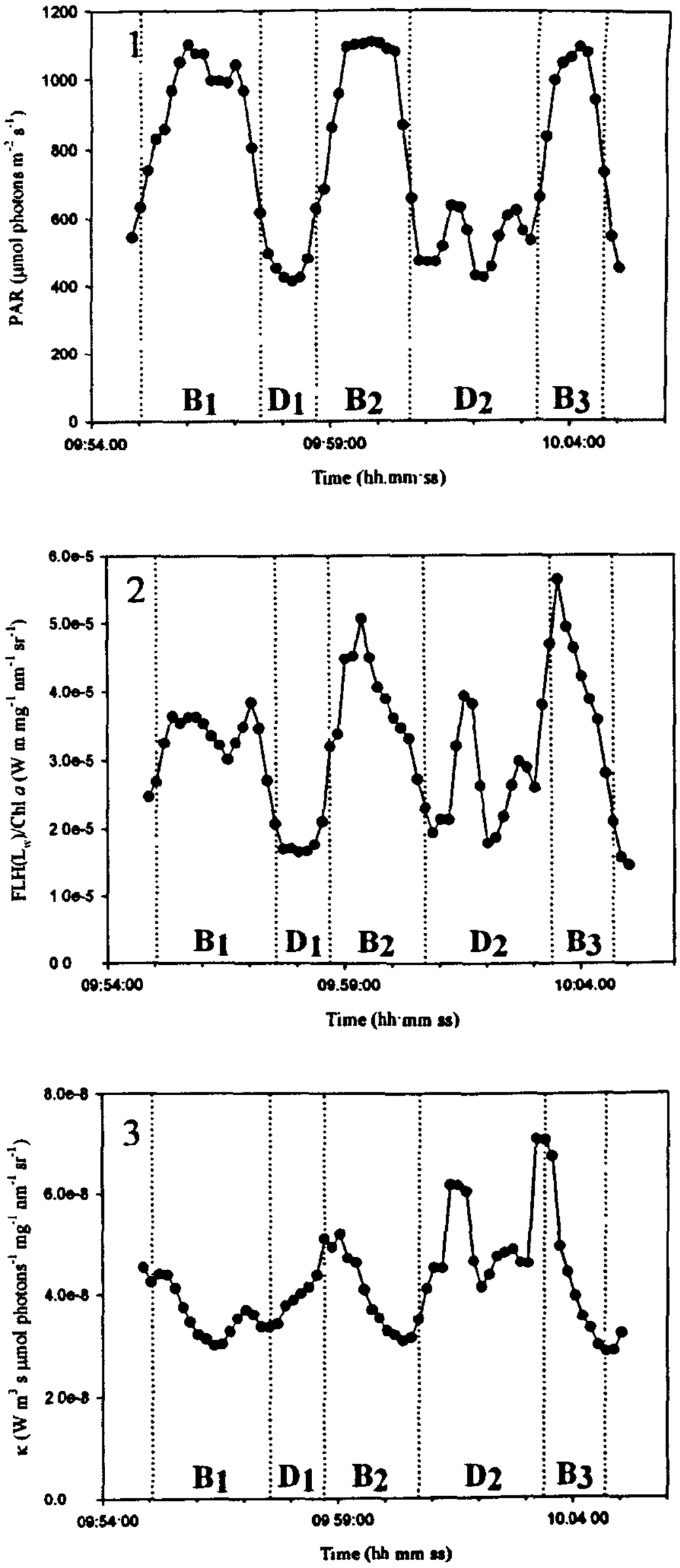

Figure 8.7. Station 12, Oban 2004. Panel (1) illustrates the time dependence of PAR, (2) (FLH/Chl) and (3) κ $(FLH/(Chl \times PAR))$. The variation in (FLH/Chl) maps onto the variation in PAR levels. In bright sunlight conditions (i.e. periods of high PAR) the (FLH/Chl) is reduced by non-photochemical quenching as the phytoplankton cells adapt to the bright light conditions.

Chapter 9: Discussion, Conclusions and Recommendations for Further Work

9. 1. Summary of the Work Conducted

Hyperspectral radiometric data were measured in a variety of water types and for a wide range of geographic locations. This produced a unique hyperspectral dataset which encompassed the oceanic waters of the Atlantic, the clear waters of the South Atlantic gyre, the chlorophyll dominated waters of the North African Upwelling, the turbid sediment dominated waters of the Bristol Channel and the diverse waters of the West coast of Scotland. Information on the IOPs and composition of the seawater were also collected during field trips. As technology improves it seems likely that hyperspectral profiling instrumentation will become more feasible.

Hyperspectral radiometric data successfully collected at the surface allowed the following questions to be investigated:

- Do inelastic processes affect the hyperspectral $R_{rs}\left(0^{+}\right)$ spectra?
- Are there significant discrepancies between hyperspectral and multispectral spectra?
- Can information on the composition of the water body be extracted using hyperspectral data?
- Can binned hyperspectral data be used to test remote sensing algorithms for a variety of ocean colour sensors in coastal waters?
- Does the increased resolution of FLH provided by hyperspectral sensors provide information on mechanisms determining its variation in coastal waters?

9. 2. Main Conclusions

Hyperspectral $R_{rs}(0^+)$ spectra were investigated using the Hydrolight radiance transfer computer package and by examination of field spectra.

9. 2. 1. Radiance Transfer Modelling of Inelastic Processes

A batch of Hydrolight runs were conducted to investigate the effects of inelastic scattering processes on the $R_{rs}(0^+)$. The following observations were made:

a. The effect of Raman scattering on the $R_{rs}(0^+)$ spectra was small, though it may be of importance deeper down in the water column.

b. CDOM fluorescence can be an important feature of the $R_{rs}(0^+)$ spectra at high CDOM concentrations and low levels of chlorophyll and MSS. Due to the spectral location of CDOM fluorescence the signal was susceptible to attenuation by other in-water constituents.

c. Chlorophyll fluorescence generates a peak in the $R_{rs}(0^+)$ spectra in the red, though this peak can be attenuated by CDOM and MSS.

9. 2. 2. Comparison of Hyperspectral and Multispectral Reflectance Data

A programme of Hydrolight radiance transfer modelling was carried out for case 1 and case 2 water types. A variety of case 2 water types were investigated for water bodies containing different constituents, representative of the concentrations found in West of Scotland coastal water. Integration of normalised spectra into SeaWiFS, MODIS and MERIS wavebands allowed the differences in hyperspectral and multispectral spectra to be investigated.

There was loss of detail and fine structure in the spectrum due to the binning process and linear interpolation between wavebands. Some spectral areas were under sampled in the multi-waveband spectra with the main area being the region between 560 and 670nm. Variations in the peak position were not indicated due to

the spacing of the wavebands and the presence of secondary peaks was also missed. The hyperspectral spectra showed more subtle changes in the $R_{rs}(0^+)$ spectra and variation in the peak position.

9. 2. 3. Hyperspectral Shape Analysis

Using the normalised hyperspectral radiance transfer models and the hyperspectral $R_{rs}(0^+)$ field measurements the possibility of using high resolution data to obtain information on the water body or as a water type classification tool was investigated. The approach adopted was to smooth and differentiate the $R_{rs}(0^+)$ spectra to find out if any features were identifiable. Derivative methods have been successfully applied to absorption spectra data (Aguirre-Gomez *et al*, 2001(a); Aguirre-Gomez *et al*, 2001(b)), therefore this method of analysing the reflectance spectra was attempted. Due to the large amount of data in hyperspectral datasets it was decided that using spectral features may prove helpful when analysis of the differentiated spectra was being attempted. The differentiation process was limited to the first order as higher order derivative's proved difficult to interpret due to noise. The following points were found:

a. The same differentiated spectral features were found in field measurements that were observed in modelled data.

b. A correlation test revealed that none of the hyperspectral features were solely related to the in-water constituents. Therefore, constituent concentration could not be retrieved from the hyperspectral derivative features.

c. The extent to which the hyperspectral features could be used as a water type classifier was investigated. The sign of the integral was shown to differentiate between open ocean and other water types.

d. Coastal water analysis was more complicated and cluster analysis was used as an exploratory tool which grouped stations with similar features together. Cluster analysis of the hyperspectral features revealed four high level clusters which were linked to the composition of the water body. The normalised

spectral shape of stations contained within these clusters was generally representative of the composition of the water body.

9. 2. 4. Assessment of Remote Sensing Algorithms in Coastal Waters

A number of remote sensing algorithms were tested on the coastal water dataset and the four clusters identified in the hyperspectral derivative features allowed the extent to which algorithms worked in the different water types identified to be investigated.

a. None of the chlorophyll *a* algorithms tested proved successful at retrieving accurate estimates of the chlorophyll concentration for this coastal water dataset. Clusters 3 and 4, the highly turbid clusters, produced large overestimates in the chlorophyll *a* concentration using band ratio algorithms. Removing these clusters improved the agreement between measured and calculated (algorithm) values.

b. The MODIS $a_{phyto}(675)$ performed poorly for all clusters, and underestimated this value when compared to *in situ* data.

c. The MODIS $a_{CDOM}(400)$ algorithm worked well for this dataset, and provided accurate estimates of the CDOM absorption at 400nm. It appeared that the retrieval of $a_{CDOM}(400)$ was possible in coastal waters using remote sensing algorithms.

d. The SeaWiFS $K_d(490)$ algorithm performed badly, and underestimated $K_d(490)$ values. Two branches were found to occur which corresponded to (A) clusters 1 and 4, and (B) clusters 2 and 3. Considering these two branches separately a tuned dual algorithm was obtained which allowed $K_d(490)$ to be successfully retrieved.

e. The four hyperspectral feature clusters helped explain why the remote sensing algorithms failed.

9. 2. 5. Fluorescence Line Height Variation in Coastal Waters

Using the increased resolution of FLH measured in coastal waters the following points were found:

a. FLH was not correlated with chlorophyll *a* concentration for the coastal waters sampled.

b. Regressing (FLH/Chl) against PAR a function similar to that obtained by Letelier *et al* (1997) was found. However, this did not explain all of the variation observed in FLH measurements.

c. CDOM and MSS were found to have a diminishing effect on (FLH/Chl).

d. Time series measurements of (FLH/Chl) under varying irradiance conditions showed that (FLH/Chl) was not uniquely determined by PAR. In bright light conditions the (FLH/Chl) decreased as the phytoplankton cells photo-adapted, probably due to non-photochemical quenching. During periods of darkness the (FLH/Chl) recovered.

9. 3. Possible Further Work

At present most of the applications of hyperspectral remote sensing reflectance deal with issues related to land, possibly due to the fact that the land is a stronger reflector. However, it is probable that in the future hyperspectral remote sensing technology will extend to ocean science. The work carried out in this thesis highlights some of the benefits to be gained using hyperspectral data rather than discrete bandwidths. The methodology used to deal with hyperspectral data was to normalise and differentiate the spectra. Alternative methods for analysing the hyperspectral reflectance spectra for oceanic waters warrant further research. It is possible that analysis of absolute magnitude spectra may prove useful, or a combination of normalised and absolute magnitude spectra, when attempting to derive information about the water body in question. Incorporating IOP measurements into the data analysis may also prove fruitful. Though the dataset used in this thesis was extensive it lacked stations which contained high chlorophyll

values, both in coastal and open ocean water. Incorporation of this data may reveal some interesting results. Hyperspectral remote sensing techniques would also allow for a greater variety of algorithms to be implemented by any single ocean colour sensor and the possibility of developing new algorithms from hyperspectral data requires further investigation.

Work carried out in this thesis was restricted to surface leaving signals, however, investigation into hyperspectral profiles of the underwater light field would be of interest. For example, the role that inelastic processes play on modulating the light field at depth could be further investigated.

References

E. Aas (2000), Spectral Slope of Yellow Substances: Problems Caused by Small Particles, Ocean Optics XV, Monaco.

M. R. Abbott, and R. M. Letelier, "Algorithm Theoretical Basis Document: Chlorophyll Fluorescence (MODIS Product Number 20)" (NASA, 1999).

R. Aguirre-Gomez, S. R. Boxall, A. R. Weeks (2001(a)). Detecting Photosynthetic Algal Pigments in Natural Populations Using a High-Spectral-Resolution Spectroradiometer, *International Journal of Remote Sensing* **22**, 2867-2884.

R. Aguirre-Gomez, A. R. Weeks, S. R. Boxall (2001 (b)). The Identification of Phytoplankton Pigments from Absorption Spectra, *International Journal of Remote Sensing* **22**, 315-338.

K. Allali, A. Bricaud, M. Babin, A. Morel, P. Chang (1995). A New Method for Measuring Spectral Absorption Coefficients of Marine Particles, *Limnology and Oceanography* **40**, 1526-1532.

R. W. Austin, "Air-Water Radiance Calibration Factor Technical Memorandum MI-76-004t" (Visibility Laboratory, Scripps Institute of Oceanography, 1976).

R. W. Austin, G. Halikas, "The Index of Refraction of Seawater" (Visibility Laboratory, Scripps Institute of Oceanography, 1976).

R. W. Austin, T. J. Petzold, The Determination of the Diffuse Attenuation Coefficient of Sea Water Using the Coastal Zone Colour Scanner, in *Oceanography from Space* J. F. R. Gower, Ed. (Plenum Press, New York, 1981).

N. R. Baker, P. Horton, Chlorophyll Fluorescence Quenching During Photoinhibition, in *Photoinhibition* D. J. Kyle, C. B. Osmond, C. J. Arntzen, Eds. (Elsevier, Amsterdam, 1987) pp. 145-168.

J. S. Bartlett, K. J. Voss, S. Sathyendranath, A. Vodacek (1998). Raman Scattering by Pure Water and Seawater, *Applied Optics* **37**, 3324-3332.

J. L. Bezy, S. Delwart, M. Rast (2000). MERIS - a New Generation of Ocean-Colour Sensor Onboard Envisat, *ESA Bulletin-European Space Agency*, 48-56.

C. E. Binding, D. G. Bowers, E. G. Mitchelson-Jacob (2003). An Algorithm for the Retrieval of Suspended Sediment Concentrations in the Irish Sea from SeaWiFS Ocean Colour Satellite Imagery, *International Journal of Remote Sensing* **24**, 3791-3806.

C. E. Binding, D. G. Bowers, E. G. Mitchelson-Jacob (2005). Estimating Suspended Sediment Concentrations from Ocean Colour Measurements in Moderately Turbid Waters; the Impact of Variable Particle Scattering Properties, *Remote Sensing of Environment* **94**, 373-383.

D. Blondeau-Patissier, G. H. Tilstone, V. Martinez-Vicente, G. F. Moore (2004). Comparison of Bio-Physical Marine Products from SeaWiFS, MODIS and a Bio-Optical Model with in Situ Measurements from Northern European Waters, *Journal of Optics a-Pure and Applied Optics* **6**, 875-889.

D. G. Bowers, S. Gaffney, M. White, P. Bowyer (2002). Turbidity in the Southern Irish Sea, *Continental Shelf Research* **22**, 2115-2126.

A. Bricaud, A. Morel, V. Barale (1999). MERIS Potential for Ocean Colour Studies in the Open Ocean, *International Journal of Remote Sensing* **20**, 1757-1769.

A. Bricaud, A. Morel, L. Prieur (1981). Absorption by Dissolved Organic-Matter of the Sea (Yellow Substance) in the UV and Visible Domains, *Limnology and Oceanography* **26**, 43-53.

A. Bricaud, A. Morel, L. Prieur (1983). Optical-Efficiency Factors of Some Phytoplankters, *Limnology and Oceanography* **28**, 816-832.

A. Bricaud, D. Stramski (1990). Spectral Absorption-Coefficients of Living Phytoplankton and Nonalgal Biogenous Matter - a Comparison between the Peru Upwelling Area and the Sargasso Sea, *Limnology and Oceanography* **35**, 562-582.

R. P. Bukata, *Optical Properties and Remote Sensing of Inland and Coastal Water* (CRC Press, 1995, ed.).

B. Bulgarelli, G. Zibordi (2003). Remote Sensing of Ocean Colour: Accuracy Assessment of an Approximate Atmospheric Correction Method, *International Journal of Remote Sensing* **24**, 491-509.

W. L. Butler (1962). Absorption of Light by Turbid Materials, *J. Opt. Sco. Am* **52**, 292-299.

N. A. Campbell, J. B. Reece, L. G. Mitchel, *Biology* (Addison Wesley, 1987, ed. Fifth).

K. L. Carder, F. R. Chen, Z. Lee, S. K. Hawes, J. P. Cannizzaro, "MODIS Algorithm Theoretical Basis Document 19: Case 2 Chlorophyll *A*" (NASA, 2003).

K. L. Carder, F. R. Chen, Z. P. Lee, S. K. Hawes, D. Kamykowski (1999). Semianalytic Moderate-Resolution Imaging Spectrometer Algorithms for Chlorophyll a and Absorption with Bio-Optical Domains Based on Nitrate-Depletion Temperatures, *Journal of Geophysical Research-Oceans* **104**, 5403-5421.

K. L. Carder, R. G. Steward, G. R. Harvey, P. B. Ortner (1989). Marine Humic and Fulvic-Acids - Their Effects on Remote-Sensing of Ocean Chlorophyll, *Limnology and Oceanography* **34**, 68-81.

G. Chang, K. Mahoney, A. Briggs-Whitmire, D. D. R. Kohler, C. D. Mobley, M. Lewis, M. A. Moline, E. Boss, M. Kim, W. Philpot, T. D. Dickey (2003). Coastal Ocean Optics and Dynamics: The New Age of Hyperspectral Oceanography, *Oceanography* **17**.

R. F. Chen, J. L. Bada (1992). The Fluorescence of Dissolved Organic-Matter in Seawater, *Marine Chemistry* **37**, 191-221.

D. K. Clark, H. R. Gordon, K. J. Voss, Y. Ge, W. Broenkow, C. Trees (1997). Validation of Atmospheric Correction over the Oceans, *Journal of Geophysical Research-Atmospheres* **102**, 17209-17217.

M. E. Culver, M. J. Perry (1997). Calculation of Solar-Induced Fluorescence in Surface and Subsurface Waters, *Journal of Geophysical Research-Oceans* **102**, 10563-10572.

A. Cunningham (1996). Variability of in-Vivo Chlorophyll Fluorescence and Its Implications for Instrument Development in Bio-Optical Oceanography, *Scientia Marina* **60**, 309-315.

G. Dall'Olmo, A. A. Gitelson, D. C. Rundquist, B. Leavitt, T. Barrow, J. C. Holz (2005). Assessing the Potential of SeaWiFS and MODIS for Estimating Chlorophyll Concentration in Turbid Productive Waters Using Red and near-Infrared Bands, *Remote Sensing of Environment* **96**, 176-187.

M. Darecki, S. Kaczmarek, J. Olszewski (2005). SeaWiFS Ocean Colour Chlorophyll Algorithms for the Southern Baltic Sea, *International Journal of Remote Sensing* **26**, 247-260.

K. Demchak (2005). Flourishing Phytoplankton Hint at Global Climate Change, *Frontiers in Ecology and the Environment* **3**, 125-125.

T. Dickey, M. Lewis, G. Chang (2006). Optical Oceanography: Recent Advances and Future Directions Using Global Remote Sensing and in Situ Observations, *Reviews of Geophysics* **44**.

D. Doxaran, R. C. N. Cherukuru, S. J. Lavender (2004). Estimation of Surface Reflection Effects on Upwelling Radiance Field Measurements in Turbid Waters, *Journal of Optics a-Pure and Applied Optics* **6**, 690-697.

D. Doxaran, R. C. N. Cherukuru, S. J. Lavender (2005). Use of Reflectance Band Ratios to Estimate Suspended and Dissolved Matter Concentrations in Estuarine Waters, *International Journal of Remote Sensing* **26**, 1763-1769.

W. E. Esaias, M. R. Abbott, I. Barton, O. B. Brown, J. W. Campbell, K. L. Carder, D. K. Clark, R. H. Evans, F. E. Hoge, H. R. Gordon, W. M. Balch, R. Letelier, P. J. Minnett (1998). An Overview of MODIS Capabilities for Ocean Science Observations, *IEEE Transactions on Geoscience and Remote Sensing* **36**, 1250-1265.

J. G. Field, G. Hempel, C. P. Summerhayes, *Ocean 2020: Science, Trends, and the Challenge of Sustainability*, The Intergovernmental Oceanographic Commission (Island Press, Washington, 2002, ed.).

E. A. Gallie, P. A. Murtha (1992). Specific Absorption and Backscattering Spectra for Suspended Minerals and Chlorophyll-a in Chilko Lake, British-Columbia, *Remote Sensing of Environment* **39**, 103-118.

R. J. Geider, E. H. Delucia, P. G. Falkowski, A. C. Finzi, J. P. Grime, J. Grace, T. M. Kana, J. La Roche, S. P. Long, B. A. Osborne, T. Platt, I. C. Prentice, J. A. Raven, W. H. Schlesinger, V. Smetacek, V. Stuart, S. Sathyendranath, R. B. Thomas, T. C.

Vogelmann, P. Williams, F. I. Woodward *(2001). Primary* Productivity of Planet Earth: Biological Determinants and Physical Constraints in Terrestrial and *Aquatic* Habitats, *Global Change Biology* **7**, 849-882.

B. Genty, J. M. Briantais, N. R. Baker (1989). The Relationship between the Quantum Yield of Photosynthetic Electron-Transport and Quenching of Chlorophyll Fluorescence, *Biochimica Et Biophysica Acta* **990**, 87-92.

A. Gershun (1936). The Light Field, *Journal of Mathematics and Physics* **18**, 51-151.

H. R. Gordon (1979). Diffuse Reflectance of the Ocean - Theory of Its Augmentation by Chlorophyll-a Fluorescence at 685-nm, *Applied Optics* **18**, 1161-1166.

H. R. Gordon (1997). Atmospheric Correction of Ocean Colour Imagery in the Earth Observing System Era, *Journal of Geophysical Research-Atmospheres* **102**, 17081-17106.

H. R. Gordon (1999). Contribution of Raman Scattering to Water-Leaving Radiance: A Re-examination, *Applied Optics* **38**, 3166-3174.

H. R. Gordon (2003). Pitfalls in Atmospheric Correction of Ocean Colour Imagery: How Should Aerosol Optical Properties Be Computed?: Comment, *Applied Optics* **42**, 542-544.

J. F. R. Gower, L. Brown, G. A. Borstad (2004). Observation of Chlorophyll Fluorescence in West Coast Waters of Canada Using the MODIS Satellite Sensor, *Canadian Journal of Remote Sensing* **30**, 17-25.

J. F. R. Gower, R. Doerffer, G. A. Borstad (1999). Interpretation of the 685 nm Peak in Water-Leaving Radiance Spectra in Terms of Fluorescence, Absorption and Scattering, and it's Observation by MERIS, *International Journal of Remote Sensing* **20**, 1771-1786.

S. A. Green, N. V. Blough (1994). Optical-Absorption and Fluorescence Properties of Chromophoric Dissolved Organic-Matter in Natural-Waters, *Limnology and Oceanography* **39**, 1903-1916.

W. W. Gregg, K. L. Carder (1990). A Simple Spectral Solar Irradiance Model for Cloudless Maritime Atmospheres, *Limnology and Oceanography* **35**, 1657-1675.

M. X. He, Z. S. Liu, K. P. Du, L. P. Li, R. Chen, K. L. Carder, Z. P. Lee (2000). Retrieval of Chlorophyll from Remote-Sensing Reflectance in the China Seas, *Applied Optics* **39**, 2467-2474.

S. B. Hooker, W. E. Esaias, G. C. Feldman, W. W. Gregg, C. R. McClain. (NASA Technical Memorandum, 104566, Vol 1, NASA Goddard Space Flight Centre, Greenbelt, Maryland, 1992).

P. Horton, J. R. Bowyer, Chlorophyll Fluorescence Transients, in *Methods in Plant Biochemistry*. (Academic Press Ltd, 1990), vol. 4, pp. 259-296.

C. M. Hu, K. J. Voss (1997). In Situ Measurements of Raman Scattering in Clear Ocean Water. *Applied Optics* **36**, 6962-6967.

Y. Huot, C. A. Brown, J. J. Cullen (2005). New Algorithms for MODIS Sun-Induced Chlorophyll Fluorescence and a Comparison with Present Data Products, *Limnology and Oceanography-Methods* **3**, 108-130.

S. W. Jeffery, G. F. Humphrey (1975). New Spectrophotometric Equations for Determining Chlorophylls *a*, *b*, *c* and *c2* in Higher Plants, Algae and Natural Phytoplankton, *Biochem. Physiol. Pflanzen* **167**, 191-194.

S. W. Jeffery, R. F. C. Mantoura, S. W. Wright, *Phytoplankton Pigments in Oceanography* (UNESCO, Paris, 1997).

N. G. Jerlov, *Marine Optics* (Elsevier, Amsterdam, 1976).

J. T. O. Kirk, *Light and Photosynthesis in Aquatic Ecosystems* (Cambridge University Press, Cambridge, 1986).

M. Kishino, S. Sugihara, N. Okami (1984). Influence of Fluorescence of Chlorophyll *a* on the Underwater Upward Irradiance Spectrum, *Mer* **22**, 224-232.

M. Kishino, M. Takahashi, N. Okami, S. Ichimura (1985). Estimation of the Spectral Absorption Coefficients of Phytoplankton in the Sea, *Bulletin of Marine Science* **37**, 634-642.

G. H. Krause, E. Weis (1991). Chlorophyll Fluorescence and Photosynthesis - the Basics, *Annual Review of Plant Physiology and Plant Molecular Biology* **42**, 313-349.

A. Laisk, V. Oja (2000). Alteration of Photosystem Ii Properties with Non-Photochemical Excitation Quenching, *Philosophical Transactions of the Royal Society of London Series B-Biological Sciences* **355**, 1405-1418.

S. J. Lavender, M. H. Pinkerton, J. M. Froidefond, J. Morales, J. Aiken, G. F. Moore (2004). SeaWiFS Validation in European Coastal Waters Using Optical and Bio-Geochemical Measurements, *International Journal of Remote Sensing* **25**, 1481-1488.

D. W. Lawlor, *Photosynthesis - Molecular, Physiological and Environmental Processes* (Longman Scientific and Technical, 1993, ed. Second).

Z. Lee, K. L. Carder (2000). Band-Ratio or Spectral-Curvature Algorithms for Satellite Remote Sensing? *Applied Optics* **39**, 4377-4380.

Z. P. Lee, K. L. Carder (2002). Effect of Spectral Band Numbers on the Retrieval of Water Column and Bottom Properties from Ocean Colour Data, *Applied Optics* **41**, 2191-2201.

Z. P. Lee, K. L. Carder, S. K. Hawes, R. G. Steward, T. G. Peacock, C. O. Davis (1994). Model for the Interpretation of Hyperspectral Remote-Sensing Reflectance, *Applied Optics* **33**, 5721-5732.

R. M. Letelier, M. R. Abbott, D. M. Karl (1997). Chlorophyll Natural Fluorescence Response to Upwelling Events in the Southern Ocean, *Geophysical Research Letters* **24**, 409-412.

I. Levin, E. Levina, G. Gilbert, S. Stewart (2005). Role of Sensor Noise in *Hyperspectral Remote Sensing* of Natural Waters: Application to Retrieval of Phytoplankton Pigments, *Remote Sensing of Environment* ***95, 264-271.***

S. E. Lohrenz (2000). A Novel Theoretical Approach to Correct for Pathlength Amplification and Variable Sampling Loading in Measurements of Particulate Spectral Absorption by the Quantitative Filter Technique, *Journal of Plankton Research* **22**, 639-657.

H. Loisel, A. Morel (1998). Light Scattering and Chlorophyll Concentration in Case 1 Waters: A Re-examination, *Limnology and Oceanography* **43**, 847-858.

C. J. Lorenzen (1967). Determination of Chlorophyll and Phaeopigments Spectrophotometirc Equations, *Limnology and Oceanography* **12**, 343-346.

R. A. Maffione, D. R. Dana (1997). Instruments and Methods for Measuring the Backward-Scattering Coefficient of Ocean Waters, *Applied Optics* **36**, 6057-6067.

S. Maritorena, A. Morel, B. Gentili (2000). Determination of the Fluorescence Quantum Yield by Oceanic Phytoplankton in Their Natural Habitat, *Applied Optics* **39**, 6725-6737.

B. R. Marshall, R. C. Smith (1990). Raman-Scattering and in-Water Ocean Optical-Properties, *Applied Optics* **29**, 71-84.

B. G. Mitchell (1990), Algorithms for Determining the Absorption Coefficients of Aquatic Particulates Using the Quantitative Filter Technique (QFT), Ocean Optics X.

B. G. Mitchell, D. A. Kiefer (1988). Chlorophyll-Alpha Specific Absorption and Fluorescence Excitation-Spectra for Light-Limited Phytoplankton, *Deep-Sea Research Part a-Oceanographic Research Papers* **35**, 639-663.

C. D. Mobley, *Light and Water: Radiative Transfer in Natural Waters* (Academic Press, London, 1994).

C. D. Mobley (1999). Estimation of the Remote-Sensing Reflectance from above-Surface Measurements, *Applied Optics* **38**, 7442-7455.

A. Morel, and B. Gentili (1996). Diffuse Reflectance of Oceanic Waters. 3. Implication of Bidirectionality for the Remote-Sensing Problem. *Applied Optics* **35**, 4850-4862.

A. Morel, and S. Maritorena (2001). Bio-Optical Properties of Oceanic Waters: A Reappraisal. *Journal of Geophysical Research-Oceans* **106**, 7763-7780.

A. Morel, L. Prieur (1977). Analysis of Variations in Ocean Colour, *Limnology and Oceanography* **22**, 709-722.

J. R. Morrison (2003). In Situ Determination of the Quantum Yield of Phytoplankton Chlorophyll a Fluorescence: A Simple Algorithm, Observations, and a Model, *Limnology and Oceanography* **48**, 618-631.

J. L. Mueller, "SeaWiFS Postlaunch Calibration and Validation Analysis, Part 3" (NASA Technical Memorandum, 104566, Vol 11, 2000).

J. L. Mueller, R. W. Austin, "Ocean Optics Protocols for SeaWiFS Validation (NASA Technical Memo 104566)" (NASA GSFC, 1995).

J. L. Mueller, C. Trees, "Case Studies for SeaWiFS Calibration and Validation, Part 4" (NASA Technical Memorandum, 104566, Vol 41, 1997).

R. A. Neville, J. F. R. Gower (1977). Passive Remote-Sensing of Phytoplankton Via Chlorophyll-Alpha Fluorescence, *Journal of Geophysical Research-Oceans and Atmospheres* **82**, 3487-3493.

T. Ohde, H. Siegel (2003). Derivation of Immersion Factors for the Hyperspectral TriOS Radiance Sensor, *Journal of Optics a-Pure and Applied Optics* **5**, L12-L14.

J. E. O'Reilly, S. Maritorena, B. G. Mitchell, D. A. Siegel, K. L. Carder, S. A. Garver, M. Kahru, C. McClain (1998). Ocean Colour Chlorophyll Algorithms for SeaWiFS, *Journal of Geophysical Research-Oceans* **103**, 24937-24953.

J. E. O'Reilly, S. Maritorena, D. A. Siegel, B. C. O'Brian, D. Toole, B. G. Mitchell, M. Kahru, F. P. Chavez, P. Strutton, G. Cota, S. B. Hooker, C. McClain, K. L. Carder, F. E. Muller-Karger, L. Harding, D. Magnuson, D. Phinney, G. F. Moore, J. Aiken, K. R. Arrigo, R. Letelier, M. E. Culver, "SeaWiFS Postlaunch Calibration and Validation, Part 3" (NASA Technical Memorandum, 104566, 2000).

T. R. Parsons, Y. Maita, C. M. Lalli, *A Manual of Chemical and Biological Methods for Seawater Analysis* (Pergamon Press, Oxford, 1992).

W. S. Pegau, J. S. Cleveland, W. Doss, C. D. Kennedy, R. A. Maffione, J. L. Mueller, R. Stone, C. C. Trees, A. D. Weidemann, W. H. Wells, J. R. V. Zaneveld (1995). A Comparison of Methods for the Measurement of the Absorption-Coefficient in Natural-Waters, *Journal of Geophysical Research-Oceans* **100**, 13201-13220.

W. S. Pegau, D. Gray, J. R. V. Zaneveld (1997). Absorption and Attenuation of Visible and near-Infrared Light in Water: Dependence on Temperature and Salinity, *Applied Optics* **36**, 6035-6046.

R. M. Pope, E. S. Fry (1997). Absorption Spectrum (380-700 nm) of Pure Water .2. Integrating Cavity Measurements, *Applied Optics* **36**, 8710-8723.

R. W. Preisendorfer, *Hydrologic Optics* (Pacific Mar. Environ. Lab/NOAA, Seattle, WA, 1976).

L. Prieur, S. Sathyendranath (1981). An Optical Classification of Coastal and Oceanic Waters Based on the Specific Spectral Absorption Curves of Phytoplankton Pigments, Dissolved Organic-Matter, and Other Particulate Materials, *Limnology and Oceanography* **26**, 671-689.

J. A. Raven, P. G. Falkowski (1999). Oceanic Sinks for Atmospheric Co2, *Plant Cell and Environment* **22**, 741-755.

A. Rees, "Atlantic Meridional Transect: AMT 15 Cruise Report" (Natural Environment Research Council, 2004).

C. S. Roesler (1998). Theoretical and Experimental Approaches to Improve the Accuracy of Particulate Absorption Coefficients Derived from the Quantitative Filter Technique, *Limnology and Oceanography* **43**, 1649-1660.

C. S. Roesler, M. J. Perry, K. L. Carder (1989). Modelling *in Situ* Phytoplankton Absorption from Total Absorption Spectra in Productive Inland Marine Waters, *Limnology and Oceanography* **34**, 1510.

S. Sathyendranath, R. Arnone, M. Babin, J. F. Berthon, R. P. Bukata, J. Campbell, C. O. Davis, R. Doerffer, M. D. Dowell, H. R. Gordon, N. Hoepffner, C. M. Hu, J. T. O. Kirk, M. Kishino, O. Kopelevich, H. Krawczyk, A. Neumann, J. Parslow, P. Schlittenhardt, A. Tanaka, "Remote Sensing of Ocean Colour in Coastal and Other Optically Complex Waters" *Tech. Report No. 3* (International Ocean Colour Coordinating Group, 2000).

S. Sathyendranath, G. Cota, V. Stuart, H. Maass, T. Platt (2001). Remote Sensing of Phytoplankton Pigments: A Comparison of Empirical and Theoretical Approaches, *International Journal of Remote Sensing* **22**, 249-273.

M. Schroeder, H. Barth, R. Reuter (2003). Effect of Inelastic Scattering on Underwater Daylight in the Ocean: Model Evaluation, Validation, and First Results, *Applied Optics* **42**, 4244-4260.

D. A. Siegel, S. Maritorena, N. B. Nelson (2005). Independence and Interdependencies among Global Ocean Colour Properties: Reassessing the Bio-Optical Assumption, *Journal of Geophysical Research-Oceans* **110**.

H. Siegel, M. Gerth, T. Ohde, T. Heene (2005). Ocean Colour Remote Sensing Relevant Water Constituents and Optical Properties of the Baltic Sea, *International Journal of Remote Sensing* **26**, 315-330.

E. L. Smith (1936). Photosynthesis in Relation to Light and Carbon Dioxide, *Proceedings of the National Academy of Sciences, USA* **22**, 504-511.

K. Stamnes, W. Li, H. Eide, J. J. Stamnes (2005). Challenges in Atmospheric Correction of Satellite Imagery, *Optical Engineering* **44**.

M. Stramska, D. Stramski (2005). Effects of a Nonuniform Vertical Profile of Chlorophyll Concentration on Remote-Sensing Reflectance of the Ocean, *Applied Optics* **44**, 1735-1747.

D. Stramski, A. Bricaud, A. Morel (2001). Modelling the Inherent Optical Properties of the Ocean Based on the Detailed Composition of the Planktonic Community, *Applied Optics* **40**, 2929-2945.

S. Sugihara, M. Kishino, N. Okami (1984). Contribution of Raman Scattering to Upward Irradiance in the Sea, *Journal of Oceanography Society of Japan* **40**, 397-404.

S. Tassan, G. M. Ferrari (1998). Measurement of Light Absorption by Aquatic Particles Retained on Filters: Determination of the Optical Pathlength Amplification by the 'Transmittance-Reflectance' Method, *Journal of Plankton Research* **20**, 1699-1709.

M. S. Twardowski, E. Boss, J. B. Macdonald, W. S. Pegau, A. H. Barnard, J. R. V. Zaneveld (2001). A Model for Estimating Bulk Refractive Index from the Optical Backscattering Ratio and the Implications for Understanding Particle Composition in Case I and Case Ii Waters, *Journal of Geophysical Research-Oceans* **106**, 14129-14142.

A. Vodacek, S. A. Green, N. V. Blough (1994). An Experimental-Model of the Solar-Stimulated Fluorescence of Chromophoric Dissolved Organic-Matter, *Limnology and Oceanography* **39**, 1-11.

J. Wang, G. F. Cota (2003). Remote-Sensing Reflectance in the Beaufort and Chukchi Seas: Observations and Models, *Applied Optics* **42**, 2754-2765.

P. Ward, S. Thorpe, JR 116 Southern Shelf and Production. Dynamoe Cruise 116; Season Dec 2004/ Jan 2005 (British Antarctic Survey, 2005).

C. Werhli, "Extraterrestrial Solar Spectrum" (Physikalish-Meterologisches Observatorum Davos and World Radiation Centre, 1985).

K. Weston, L. Fernand, D. K. Mills, R. Delahunty, J. Brown (2005). Primary Production in the Deep Chlorophyll Maximum of the Central North Sea, *Journal of Plankton Research* **27**, 909-922.

S. B. Wozniak, D. Stramski (2004). Modelling the Optical Properties of Mineral Particles Suspended in Seawater and Their Influence on Ocean Reflectance and Chlorophyll Estimation from Remote Sensing Algorithms, *Applied Optics* **43**, 3489-3503.

C. S. Yentsch (1962). Measurements of Visible Light Absorption by Particulate Matter in the Ocean, *Limnology and Oceanography* **7**, 207-217.

J. R. V. Zaneveld, J. C. Kitchen, C. Moore (1994), The Scattering Error Correction of Reflecting Tube Absorption Metres, Ocean Optics XII.